Liquefaction-Induced Downdrag on Piles: Centrifuge and Numerical Modeling, and Design Procedures

By

SUMEET KUMAR SINHA
DISSERTATION

Submitted in partial satisfaction of the requirements for the degree of

DOCTOR OF PHILOSOPHY

in

Civil and Environmental Engineering

in the

OFFICE OF GRADUATE STUDIES

of the

UNIVERSITY OF CALIFORNIA

DAVIS

Approved:

Katerina Ziotopoulou, Chair

Bruce L. Kutter

Ross W. Boulanger

Committee in Charge

2022

This dissertation is

dedicated to my beloved family and the memory of my grandparents and dear uncle

Nand Kishore Prasad

“Bade Papa”

ABSTRACT

Pile foundations are designed to transfer superstructure loads through positive skin friction and tip resistance while undergoing acceptable settlements. However, when liquefaction-induced soil settlement occurs, it causes drag load and settlement in piles. For such cases, estimating the axial load distribution and pile settlement becomes an important criterion for designing and evaluating the performance of piles in liquefiable soils. Most of the challenges related to the liquefaction-induced downdrag phenomenon are the incomplete understanding of the different mechanisms that affect drag load and pile settlement. The interrelationships between mechanisms affecting negative skin friction (pore pressure generation and dissipation patterns, the sequencing of settlements and reconsolidation of liquefied soils, as well as gapping and softening of soils around the piles) are currently not accounted for in current practice, leading to over-conservative or unsafely designed piles. This dissertation describes the liquefaction-induced downdrag mechanisms through a series of centrifuge model tests, the development of a numerical modeling approach incorporating the observed mechanism and proposes a displacement-based design procedure for designing axially loaded piles subject to seismic loading and liquefaction-induced downdrag. The redistribution of high pore pressures from liquefiable to adjacent non-liquefiable deposits impacted pile performance significantly. Therefore, a procedure for estimating the redistribution of excess pore pressure is also studied.

EXECUTIVE SUMMARY

Pile foundations are designed to transfer superstructure loads through positive skin friction and tip resistance while undergoing acceptable settlements. However, when liquefaction-induced soil settlement occurs, it causes drag load and settlement in piles. For such cases, estimating the axial load distribution and pile settlement becomes an important criterion for designing and evaluating the performance of piles in liquefiable soils. Most of the challenges related to the liquefaction-induced downdrag phenomenon are the incomplete understanding of the different mechanisms that affect drag load and pile settlement. The interrelationships between mechanisms affecting negative skin friction (pore pressure generation and dissipation patterns, the sequencing of settlements and reconsolidation of liquefied soils, as well as gapping and softening of soils around the piles) are currently not accounted for in current practice, leading to over-conservative or unsafely designed piles. This dissertation describes the liquefaction-induced downdrag mechanisms through a series of centrifuge model tests, the development of a numerical modeling approach incorporating the observed mechanism, and proposes a displacement-based design procedure for designing axially loaded piles subject to seismic loading and liquefaction-induced downdrag. The redistribution of high pore pressures from liquefiable to adjacent non-liquefiable deposits impacted pile performance significantly. Therefore, a procedure for estimating the redistribution of excess pore pressure is also studied.

A series of densely instrumented large centrifuge model tests were performed to study liquefaction-induced downdrag on piles and understand the interplay and effects of (i) pile embedment and pile-head load, (ii) excess pore pressure generation and dissipation; and (iii) reconsolidation and ground settlement on pile response during and post shaking. The tests included five heavily instrumented piles installed in two different layered soil profiles. The pile tips were embedded at different depths (0, 3 pile diameters, and 5 pile diameters) into a dense sand (bearing) layer below a liquefiable layer. The piles were loaded with different head loads resulting in a static factor of safety ranging from 1.6 to 12.4. The models were shaken with multiple scaled Santa Cruz earthquake motions of different intensities, and the mechanism behind liquefaction-induced downdrag was investigated. For each shaking event, the drag load on the piles first decreased during shaking and then increased during reconsolidation, exceeding its pre-shaking value. With multiple shaking events, the net drag load on the piles increased and approached the value estimated from negative skin friction equal to the drained interface shear strength of the pile. Larger drag loads and smaller settlements were observed for the pile with smaller head load or embedded deep in the dense sand layer. Most of the pile settlement occurred during shaking when the shaft and tip capacities decreased from excess pore pressures around the pile. During reconsolidation, the pile settlement was less than 10 mm (0.2% of the pile's diameter). The settlement in piles was generally smaller than the free-field soil settlements except for the case when the pile plunged in soil due to very high excess pore pressure near its tip. Results showed that complete liquefaction (r_u = 1.0) is not necessary for developing significant drag loads. Soil settlement (relative to the pile) in the order of 1% of pile diameter was found enough to mobilize significant negative skin friction at the interface. Medium shaking events with r_u as low as 50% caused enough soil settlement resulting in significant drag loads.

A TzQzLiq numerical model is developed to model the mechanism of liquefaction-induced downdrag on piles observed in centrifuge model tests. The numerical model consists of the existing TzLiq and a new QzLiq material (implemented in OpenSees), which accounts for the changes in the pile's shaft and the tip capacity as free-field excess pore pressures develop/dissipate in soil. Soil settlement (estimated from inverse analysis) and excess pore pressure profiles (directly measured from the centrifuge test) account for sequencing and pattern of excess pore pressure dissipation and soil settlement. The model also accounts for initial drag load on piles. The developed numerical model is validated against centrifuge tests, and the procedure for obtaining the necessary information for running the TzQzLiq analysis is described. Additionally, a sensitivity study on TzLiq and QzLiq material properties is performed to study their effect on the developed drag load and pile settlement. Analyses results showed that the proposed TzQzLiq numerical model could reasonably predict the time histories of axial load distribution and settlement of axially loaded piles in liquefiable soils both during shaking and reconsolidation.

An approximate procedure is developed to evaluate the effects of redistribution of excess pore pressures from consolidating liquefied layers to the adjacent non-liquefiable layers. Results from centrifuge model tests show that non-liquefiable soils could be subject to large excess pore pressure developments due to redistribution effects. Accounting for the redistributed excess pore pressures is thus crucial for quantification of consequences of liquefaction, including the effect of liquefaction on the capacity of deep foundations. Excess pore pressures that migrate from a liquefied layer toward the pile tip could significantly reduce the pile's tip capacity, even if the tip is embedded in a deposit that is not considered liquefiable. On the other hand, if redistribution can reduce excess pore pressures in the liquefiable layers, the risk associated with liquefaction-related failures is also reduced. A criterion is developed to evaluate the thicknesses of the liquefiable layer below which redistribution could prevent liquefaction in the layer deemed liquefiable according to the liquefaction-triggering procedures. Finally, the proposed approximate procedure is applied on selected shakings of centrifuge tests, and results are compared. The predictions from the approximate procedure matched decently with the results from the centrifuge test.

A displacement-based design procedure for designing axially loaded piles subject to seismic loading and liquefaction-induced downdrag was developed using the TzQzLiq analysis methodology. The procedure uses the pile settlement and the maximum load acting on the pile compared to its structural strength as the criteria for designing the piles. The proposed displacement-based design method offers several advancements to the state of practice (AASHTO 2020) forced-based design procedure. The proposed design method reasonably accounts for all the mechanisms observed in centrifuge tests on an axially loaded pile during and post shaking. It accounts for the initial drag load on the pile, redistribution effects resulting in large excess pore pressures in the non-liquefiable layers, reduction in the pile's shaft and tip capacity from excess pore pressures around the pile, and estimation of pile settlement and axial load distribution during shaking and reconsolidation. The procedure includes design steps to estimate absolute and differential (relative to the free-field soil settlement) pile settlement and drag load for varying pile lengths. The length of the piles is then selected based on the serviceability criteria on relative and absolute pile settlement and the pile's structural strength. The proposed design procedure is applied on the piles used in centrifuge tests, and the results are compared. Results show that the new design procedure reasonably predicted the seismic settlement, downdrag settlement, and the drag load on the piles. An example design problem is provided to illustrate the application of the proposed design procedure in practice.

Recommendations from this study on pile design are summarized below.

- Liquefaction-induced downdrag is not the controlling mechanism for pile settlement during a shaking event. End bearing piles with sufficient embedment in dense sand layer sustains the drag loads undergoing small settlements (< 2% of pile diameter). The leading cause of pile

settlement during a shaking event is the reduction of the pile's shaft and tip capacity from the excess pore pressures in the soil.

- The drag load on the pile should be estimated with negative skin friction in the liquefiable and non-liquefiable layers equal to the interface shear strength. Results from the centrifuge test showed that the negative skin friction in a pile eventually reaches the interface shear strength with multiple shaking events.
- The effect from the increase of excess pore pressure in the non-liquefiable layer due to the redistribution of pore pressures from the adjacent liquefiable layer should be considered in design procedures for piles. Redistribution of excess pore pressures to the bearing layer can significantly decrease the pile tip capacity and cause large settlement, even if the tip is sufficiently embedded in the bearing layer. The dissertation describes a procedure (validated against the centrifuge test results) for estimating the excess pore pressures in non-liquefiable layers following redistribution and the reduced pile tip capacity in liquefiable soils.
- Redistribution can be beneficial in increasing the liquefaction resistance of liquefiable layers. It can even prevent liquefaction if the thickness of a layer is smaller than a limiting thickness. The dissertation describes a criterion to evaluate the maximum thicknesses of the liquefiable layer below which redistribution would prevent liquefaction in the layer deemed liquefiable according to the liquefaction-triggering procedures. Preventing liquefaction in a deep thin liquefiable layer could prove extremely valuable in reducing the risk of liquefaction-related failures and the cost associated with the remediation.
- A displacement-based procedure accounting for the reduction in pile shaft and tip capacity from excess pore pressures, changes in drag load from the relative movement between the soil

and the pile, and evaluation of pile settlement as the performance criteria should be used for design. The dissertation describes a displacement-based design procedure using the TzQzLiq analysis methodology for designing axially loaded piles for seismic loading and liquefaction-induced downdrag. It also accounts for the effects of excess pore pressures in liquefiable and non-liquefiable layers.

- There should be separate serviceability criteria for total pile settlement and differential settlement (relative to the free-field soil settlement) to ensure the post-earthquake functionality of the structure. In some cases, especially where settlements are of the order of inches, settlement of piles close to free-field soil settlements may improve post-earthquake functionality of the superstructure (for example, in bridges). It is possible that if free-field settlement is (let us say) about 4 inches, the bridge would be functional if the pile settlement was 2 inches. However, the bridge would be closed if the pile settlement was 0 inches – due to the differential settlement between the bridge and the approach slab.

ACKNOWLEDGEMENTS

The work in this dissertation was funded by the California Department of Transportation (Caltrans) under Agreement 65A0688 with the project titled “Validation of Design for Liquefaction-Induced Downdrag on Piles.” The experiments were carried out at the UC Davis Center for Geotechnical Modeling supported by National Science Foundation (NSF) under award number CMMI 1635307. The content of this dissertation does not constitute a standard, specification, or regulation. Any opinions, findings, conclusions, or recommendations expressed in this material are those of the author(s), and they do not necessarily reflect the organizations’ views mentioned above.

The work in this dissertation has been the result of the research performed as a graduate student at the University of California Davis. It would have been impossible without much support, assistance, mentorship, and encouragement from family, friends, peers, and professors. I am incredibly thankful to the Department of Civil and Environmental Engineering and the Geotechnical Graduate Student Society (GGSS) for the excellent academics, scholarship, fellowship, and leadership opportunities, resulting in my overall professional development and, above all, creating a wonderful experience at UC Davis.

I am incredibly grateful to have worked with Professor Katerina Ziotopoulou and Professor Emeritus Bruce Lloyd Kutter. Their wisdom, intellect, enthusiasm, work ethic, hard work, humility, and kindness have constantly inspired me and made me grow in ways I would have never imagined to become a better researcher, educator, and individual. Professor Ziotopoulou’s excellent teaching and writing style, presenting complex technical concepts into simple language, attention to detail, humility, and approachability have been inspiring. I admire Professor Kutter’s

curiosity, enthusiasm, persistence, and knowledge of theoretical and experimental mechanisms. Both Professor Ziotopoulou and Kutter collectively formed a solid and diverse foundation of support and inspiration for my doctoral work. Their collective mentorship and guidance have significantly improved the quality and presentation of my work by challenging me to think critically, creatively, beyond the box, and present work in a simpler, concise, and efficient manner. Most notably, they have served as excellent role models. I hope to carry forward their teaching and values in the future. Additionally, I would like to thank Professor Ross Boulanger, Professor Jason Dejong, and Professor Alejandro Martinez for the academic support and feedback on my research. I am incredibly grateful to Professor Boris Jeremić for being instrumental in developing my numerical and computational skills and Professor Bruce Kutter for developing my experimental abilities resulting in a holistic understanding of geotechnical engineering.

I would like to acknowledge colleagues in GGSS for their generous help on my research. I am fortunate to have lovely colleagues and friends: Dr. Barry (Bao Li) Zheng, Professor Srikanth Madabhushi, and Professor Mohammad Khosravi, who have been patient in teaching me (who had never run even a lab test before) the intricacies of running a centrifuge test and have always been available for any kind of help. I am also thankful to my centrifuge buddies: Brian Morales, James Heins, Soham Banerjee, Evan To, Scott Proctor, and Jared May, for being generous with their help in my centrifuge tests. Additionally, I am also very thankful to Dan Wilson and the staff (Chad Justice, Anatoliy Ganchenko, and Tom Kohnke) at the Center for Geotechnical Modeling for their advice and inputs in making the centrifuge tests successful. I had a great time working, collaborating, and learning with Professor Ziotopoulou's research group: Maya Kortbawi, Renmin Pretell, Francisco Humire, Rachel Reardon, Hussain Alshawaf, Brian Morales, and James Heins. I am very grateful to have found incredible friends and future collaborators: Mandeep Basson, Francisco Humire, Han Yang, Hexiang Wang, Renmin Pretell, Patrick Bassal, and their spouses. Their company has always been fun, delightful, and rejuvenating, and above all, they have always been considerate in having some veggies on the menu :P.

I am grateful to have found an excellent Indian community at Davis through my association with the Indian Graduate Student Association (IGSA). I have found a strong connection and a family within the group members: Aritra Bej, Sukanya Mazumder, Arka Maity, Aditya Jhunjhunwala, Aadarsh Venugopal, Anirudh Gaur, Rakhi Sharma, Gregory Philip, Soukhin Das, Shubham Pandey, Rohan Sogani, Mahesh Sharma, Satyabrata Sarangi, Mandeep Basson, A.V. Krishnan, Subodh Kolwankar, and Tanya Arora. They have been the constant source of support, motivation, warmth, and encouragement throughout the ups and downs of my journey and made my stay enjoyable at Davis.

Special mention to Davis's Temple Coffee Roasters café for their fantastic coffee and lovely upbeat ambiance. I have spent countless hours at the café working on presentations, research, assignments, and even writing this dissertation. My friends would know I was likely at Temple :) if not at home.

Finally, I would like to thank my family back in India for their unconditional love, care, and support at all times. They have always supported my decisions in my career or otherwise and have been a constant source of motivation and encouragement. I would especially like to remember and dedicate this dissertation to my late uncle Nand Kishore Prasad, "Bade Papa," who supported my education since childhood and made me what I am today. I wish he was alive today to witness the fruits of the tree he planted.

TABLE OF CONTENTS

LIST OF TABLES

LIST OF FIGURES

CHAPTER 1:

INTRODUCTION

1.1 Background and Motivation

Pile foundations are typically designed to transfer axial loads at the pile head to deeper layers through upward (positive) interface shear stress (skin friction) and end bearing resistance [Figure 1.1 (a)]. However, if a soil layer around the pile settles more than the pile does, downward (negative) interface shear stress (skin friction) can develop [Figure 1.1 (d)]. Among other causes, ground settlement may result from reconsolidation following the earthquake-induced liquefaction of a soil layer. The net downward force due to negative skin friction, also called drag load (Q_d), increases the axial load in a pile beyond the pile head load, Q_f [Figure 1.1 (f)]. Consequently, both the positive skin friction below the liquefied layer and the load at the pile tip increases, and the pile settles until enough resistance is mobilized and force equilibrium is re-established. Pile settlement caused by the drag load is known as downdrag (Fellenius 2006). The depth at which the relative velocity (or relative movement in time Δt) of the soil and pile is zero is known as the neutral plane (Wang and Brandenberg 2013) [Figure 1.1 (e)]. Alternatively, the neutral plane is the depth at which the skin friction on the pile is zero. Above the neutral plane, the relative movement of soil is more than the pile resulting in the development of negative skin friction (drag load); below the neutral plane, the relative movement of the pile is more than the soil resulting in the development of positive skin friction (Fellenius 2006). The resulting load distribution from the said negative and positive skin friction developed along the pile is maximized at the neutral plane [Figure 1.1 (f)].

Most of the challenges related to the phenomenon of liquefaction-induced downdrag of piles relate to the timing and depth distribution of pore pressure generation and dissipation and reconsolidation settlements (Rollins 2017). In terms of its effects on resistance, liquefaction in the vicinity of the pile shaft leads to reduction (or loss for full liquefaction) of skin friction, while the presence of high excess pore pressures in the vicinity of the pile tip leads to reduction of end bearing resistance and its stiffness and result in large pile settlements [Figure 1.1 (b)]. Fellenius and Siegel (2008) used the unified pile design method (Fellenius 1984, 2004) to evaluate the influence of liquefaction on the overall axial behavior of piles:

- During shaking, if liquefaction and the associated post-liquefaction reconsolidation settlement occur above the initial static neutral plane (i.e., the neutral plane that exists before liquefaction), there is a minor effect on the axial load distribution and settlement of the pile. However, suppose partial or complete liquefaction occurs below the initial static neutral plane. In that case, more loads will be transferred to the pile's shaft and tip below the liquefied layer, causing settlement of the pile.
- Post shaking, excess pore pressures dissipate, soil regains its shear strength, and post-liquefaction reconsolidation strains lead to settlements in the liquefied layer and the layers above it, causing the development of negative skin friction and thus drag load on the pile. If post-liquefaction settlement occurs below the initial static neutral plane, it shifts the neutral plane downward and increases drag load on the pile. Correspondingly, the increased drag load extra load is balanced by mobilizing larger positive skin friction and tip resistance with a further pile settlement [Figure 1.1 (c)]. If it occurs above the initial static neutral plane, the increase in the drag load and settlement of the pile is small.

While the mechanisms presented above are reasonable based on our current understanding, the overall timing between the rate of excess pore pressure generation/dissipation and soil settlement can affect the development of downdrag and drag loads. If most of the soil settlement occurs when effective stresses are low, the developed negative skin friction and, thus, the drag are smaller compared to a case with higher effective stresses. A small amount of soil settlement toward the end of reconsolidation (when effective stresses are high) might be enough to mobilize full negative skin friction in the reconsolidated soil. Sinha et al. (2019) performed multiple t-z analyses to study the effect of reconsolidation settlements and pile tip conditions on liquefaction-induced settlement of piles. The study found that the downdrag settlement and drag load increased with reconsolidation settlements occurring deeper in the soil layers and around the pile's tip. End bearing piles developed larger drag loads than the floating piles; however, the resulting downdrag settlement was smaller. Coelho et al. (2004) performed dynamic centrifuge tests on uniform deposits of saturated sands and showed that the mechanisms of excess pore pressure generation and liquefaction are similar in dense and loose sand, with the rate of excess pore pressure generation being slower in dense sand. Centrifuge tests of pile groups by Knappett and Madabhushi (2009) and Stringer and Madabhushi (2010, 2013) observed substantial settlements of piles during shaking when the excess pore pressures were high around the shaft and near the tip. After shaking, as soil reconsolidated and drag load developed, the resulting settlement in the piles was much smaller.

The hydraulic boundary conditions can also significantly affect the overall response of the soil-pile system: the presence of cracks and interface gaps if they develop around the pile [Figure 1.1 (c)] can speed up reconsolidation and influence the downdrag phenomenon. Interface gaps essentially result in zero shaft resistance and provide a hydraulic exit to the fluid resulting in ejecta at the surface, while the movement of the fluid through interface gaps can erode the soil and further reduce the drag loads. Interbedded soil deposits can bring additional complexities due to entrapment and slow dissipation of excess pore pressures through low permeable layers.

Estimating the drag load for pile design requires estimating the mobilized negative skin friction on the pile in the liquefiable and non-liquefiable layers above the neutral plane. Downdrag is then estimated as the pile settlement needed to mobilize the positive skin friction and tip resistance that balance the drag load. The current state of practice follows recommendations from AASHTO (2020) as well as findings from other advanced research in this field (e.g., Boulanger and Brandenberg (2004), Rollins and Strand (2006), Fellenius and Siegel (2008), Hannigan et al. (2016), Muhunthan et al. (2017)). AASHTO (2020), in particular, uses a criterion on soil settlement or the neutral plane solution approach to determine the location of the neutral plane and the associated drag load. The general approach of AASHTO is to assume negative skin friction equal to a residual soil strength in the liquefiable zone and non-liquefied skin friction in the non-liquefiable layers above the zone of liquefaction. Boulanger and Brandenberg (2004) modified the neutral plane method to account for the timing of the soil settlement with the dissipation of excess pore pressures during reconsolidation. In their method, Boulanger and Brandenberg (2004) assumed mobilization of interface shaft friction as a linear function of excess pore pressure ratio ($1-r_u$). Through blast-induced liquefaction tests performed on driven piles, Rollins and Strand (2006) recommended the negative skin friction in the fully reconsolidated layer to be taken as approximately 50% of the mobilized positive skin friction before liquefaction. Other blast-induced liquefaction studies conducted on auger-cast piles (Nicks 2017; Rollins and Hollenbaugh 2015), and micro piles (Lusvardi 2020; Rollins et al. 2019) observed similar results. While these recommendations are consistent, there have been cases within these studies (Elvis 2018; Rollins and Hollenbaugh 2015; Rollins and Strand 2007) where the developed negative skin friction in the reconsolidated layer was greater than 50% of the positive skin friction before liquefaction. For sites with earthquake drains installed, Rollins and Strand (2007) observed the development of negative skin friction equal to 100% of the mobilized positive skin friction before liquefaction. Blast-induced liquefaction studies by Elvis (2018) on driven steel piles and drilled piles found the mobilized negative skin friction, respectively, to be 50-75% and 75-90%, of the positive skin friction before liquefaction. Fellenius and Siegel (2008) used a zero negative skin friction in the fully liquefied zone to estimate liquefaction-induced drag load. Vijayaruban et al. (2015), Muhunthan et al. (2017), and Fellenius et al. (2020) used the neutral plane method with zero negative skin friction in the fully liquefied zone for studying the liquefaction-induced downdrag for the Juan Pablo II bridge at the 2010 Maule Earthquake in Chile. They found that the settlement caused by the downdrag was relatively small and that the cause of failure was liquefaction of the soil below the pile tip. The Federal Highway Administration (FHWA) (Hannigan et al. 2016) recommend the use of neutral plane methods with soil behavior models (t-z and q-z models) calibrated from field tests to determine the drag load.

While the studies mentioned above have improved our understanding of liquefaction-induced downdrag, some confusion still exists in estimating the negative skin friction in the liquefiable layer and pile settlement. More testing is thus required to understand the development of drag load and pile settlement in liquefiable layers. Also, improvements are required in the current design procedure to model the mechanism of liquefaction-induced downdrag, which can be further used to study and identify the controlling factors affecting the magnitude of drag load and pile settlement.

1.2 Organization of Chapters

The dissertation has six chapters. The problem statement and motivation for the scope of research are described in Chapter 1. Chapters 2 to 5 are the main chapters describing the research outcome. Chapter 2 describes the experimental investigation of the mechanism behind liquefaction-induced downdrag on axially loaded piles. Chapter 3 describes the development of a numerical modeling approach for modeling liquefaction-induced downdrag and its validation with the centrifuge data. Chapter 4 describes the development of an analytical procedure to study excess pore pressure redistribution on liquefiable and non-liquefiable layers and its effect on increased excess pore pressure in the non-liquefiable layers and increased liquefaction resistance in the liquefiable layers. Chapter 5 describes the development of a displacement-based design procedure for designing piles in liquefiable soil for extreme loading events such as seismic and liquefaction-induced downdrag. Finally, Chapter 6 describes the summary and conclusion from all the four main chapters and lists some future work. A summary of each of the main chapters (including references) is described below.

Chapter 2: Experimental Investigation

This chapter describes a series of centrifuge model tests that were performed to investigate the factors affecting the magnitude of liquefaction-induced drag loads of piles and the settlements experienced in a pile. The centrifuge model tests included piles with a diameter of 635 mm passing through a thick liquefiable layer, embedded at different depths within an underlying deeper dense layer. The piles were heavily instrumented to monitor the axial load distribution, enabling the assessment of the skin friction distribution along the length of the pile. The models were shaken with a sequence of scaled realistic earthquake motions with different intensities. The effects of excess pore pressure generation/dissipation, soil settlement, pile tip embedment, and pile head load on liquefaction-induced downdrag were studied. Finally, implications for the design of axially loaded piles in liquefiable soils are summarized.

References

- Sinha, S. K., Ziotopoulou, K., and Kutter, B. L. (2021). "Centrifuge Model Tests of Liquefaction-Induced Downdrag on Piles in Uniform Liquefiable Deposits." *Journal of Geotechnical and Geoenvironmental Engineering*. Accepted.
- Sinha, S. K., Kutter, B. L., and Ziotopoulou K. (2022). Centrifuge Study of Downdrag on Axially Loaded Piles in Liquefiable Soils. In *20th International Conference on Soil Mechanics and Geotechnical Engineering.* Sydney, Australia: International Society for Soil Mechanics and Geotechnical Engineering.
- Sinha, S. K., Kutter, B. L., Wilson, D. W., Carey, T., and Ziotopoulou, K. (2021a). *Use of Photron Cameras and TEMA Software to Measure 3D Displacements in Centrifuge Tests*. UCD/CGM - 21/01. Davis, CA: Center for Geotechnical Modeling, University of California Davis. https://ucdavis.box.com/s/6hndp2m7mcy5cz8r9g0y6wokzj00hbfb
- Sinha, S. K., Kutter, B. L., and Ziotopoulou, K. (2021b). "Measuring Vertical Displacement Using Laser Lines and Cameras." *International Journal of Physical Modelling in Geotechnics*. https://doi.org/10.1680/jphmg.21.00038
- Sinha, S. K., Ziotopoulou, K., and Kutter, B. L. (2019). "Parametric Study of Liquefaction Induced Downdrag on Axially Loaded Piles." In *7th lnternational Conference on Earthquake Geotechnical Engineering*. Rome, Italy: International Society for Soil Mechanics and

Geotechnical Engineering.

- Sinha, S. K., Ziotopoulou, K., and Kutter, B. L. (2021c). *Centrifuge testing of liquefaction-induced downdrag on axially loaded piles : Data Report for SKS02*. UCD/CGMDR - 21/01. Davis, CA. Center for Geotechnical Modeling, University of California Davis. https://doi.org/10.17603/ds2-d25m-gg48
- Sinha, S. K., Ziotopoulou, K., and Kutter, B. L. (2021d). *Centrifuge Testing of Liquefaction-Induced Downdrag on Axially Loaded Piles : Data Report for SKS03*. UCD/CGMDR - 21/02. Davis, CA. Center for Geotechnical Modeling, University of California Davis. https://doi.org/10.17603/ds2-wjgx-tb78
- Sinha, S. K. (2021). DAQData v2.5: A Python Module to Read Recordings From Centrifuge Test Conducted at the Center for Geotechnical Modeling Facility at the University of California Davis. Electronic: https://github.com/SumeetSinha/DAQData. https://doi.org/10.5281/zenodo.5770981
- Sinha, S. K. (2021). DAQData_Matlab v2.5: Matlab Functions to read and plot binary data files of centrifuge tests conducted at Center for Geotechnical Modeling at the University of California Davis. Electronic: https://github.com/SumeetSinha/DAQData_Matlab/. https://doi.org/10.5281/zenodo.5770993
- Sinha, S. K. (2021). Rplot v2.0: Matplotlib style sheet to create scientific journal figures. Electronic: https://github.com/SumeetSinha/Rplot/. https://doi.org/10.5281/zenodo.5770993.

Chapter 3: Numerical Modeling and Validation

This chapter describes the development and validation of the TzQzLiq numerical model for modeling liquefaction-induced downdrag on piles. The TzQzLiq model uses zero-length elements and the existing TzLiq material and a new QzLiq material to account for changes in the shaft and tip capacity of the pile and their stiffness as free-field excess pore pressures develop/dissipate in the soil. The model also accounted for the modeling of initial drag loads on the pile. The developed numerical model was validated against data from the centrifuge tests conducted. The procedure for obtaining the necessary information to perform a TzQzLiq analysis is described. Additionally, a sensitivity study on TzLiq material and QzLiq material properties were performed to study their effect on the developed drag load and pile settlement. Analyses results show that the proposed numerical model can reasonably predict the time histories of axial load distribution and settlement of axially loaded piles in liquefiable soils both during and post shaking.

References

- Sinha, S. K., Ziotopoulou, K., and Kutter, B. L. (2021). “Numerical Modeling of Liquefaction-Induced Downdrag : Validation from Centrifuge Tests.” *Journal of Geotechnical and Geoenvironmental Engineering*. Under Review.
- Sinha, S. K. (2021). “QzLiq1 Material”. In *OpenSees Documentation*. Electronic. https://opensees.github.io/OpenSeesDocumentation/user/manual/material/uniaxialMaterials/QzLiq1.html.

Chapter 4: Effects of Excess Pore Pressure Redistribution on Liquefiable and Non-Liquefiable Layers

This chapter studies the effect of excess pore pressure redistribution on liquefiable and non-liquefiable layers. While redistribution increases excess pore pressure in non-liquefiable layers, it decreases excess pore pressures in the liquefiable layer. An approximate analytical procedure is developed to study redistribution effects and the associated excess pore pressures developed in the soil layers. A criterion is also developed to evaluate the thicknesses of the liquefiable layer below which redistribution could prevent liquefaction in the layer deemed liquefiable according to the liquefaction-triggering procedures. Finally, the proposed approximate procedure is applied on selected shakings of centrifuge tests involving liquefaction of layered soil profiles, and results were compared. The predictions from the approximate procedure matched satisfactorily with the centrifuge test results.

References

- Sinha, S. K., Ziotopoulou K., and Kutter, B. L. (2021). "Effects of Excess Pore Pressure Redistribution on Liquefiable and Non-Liquefiable Layers". *Journal of Geotechnical and Geoenvironmental Engineering*. In Preparation.

Chapter 5: Displacement-Based Design Procedures

This chapter describes a displacement-based design procedure using the developed TzQzLiq analysis methodology for designing axially loaded piles for earthquake loading and liquefaction-induced downdrag. The new design procedure accounts for initial drag load on the pile, excess pore pressures in the non-liquefiable layers following redistribution from the liquefied layers, and the reduction of the shaft and tip capacity from excess pore pressures in the soil. Design steps are provided to estimate the input properties required for running a TzQzLiq analysis. Finally, the proposed design procedure is applied to the piles used in centrifuge model tests, and results are compared. Analyses results show that the new design procedure reasonably predicts the seismic settlement, downdrag settlement, and the drag load in the piles. An example design problem is then considered to illustrate the application of the proposed design procedure in practice for designing piles in liquefiable soils.

References

- Sinha, S. K., Ziotopoulou K., and Kutter, B. L. (2021). "Displacement-Based Design of Axially Loaded Piles for Seismic Loading and Liquefaction-Induced Downdrag". *Journal of Geotechnical and Geoenvironmental Engineering*. In Preparation.

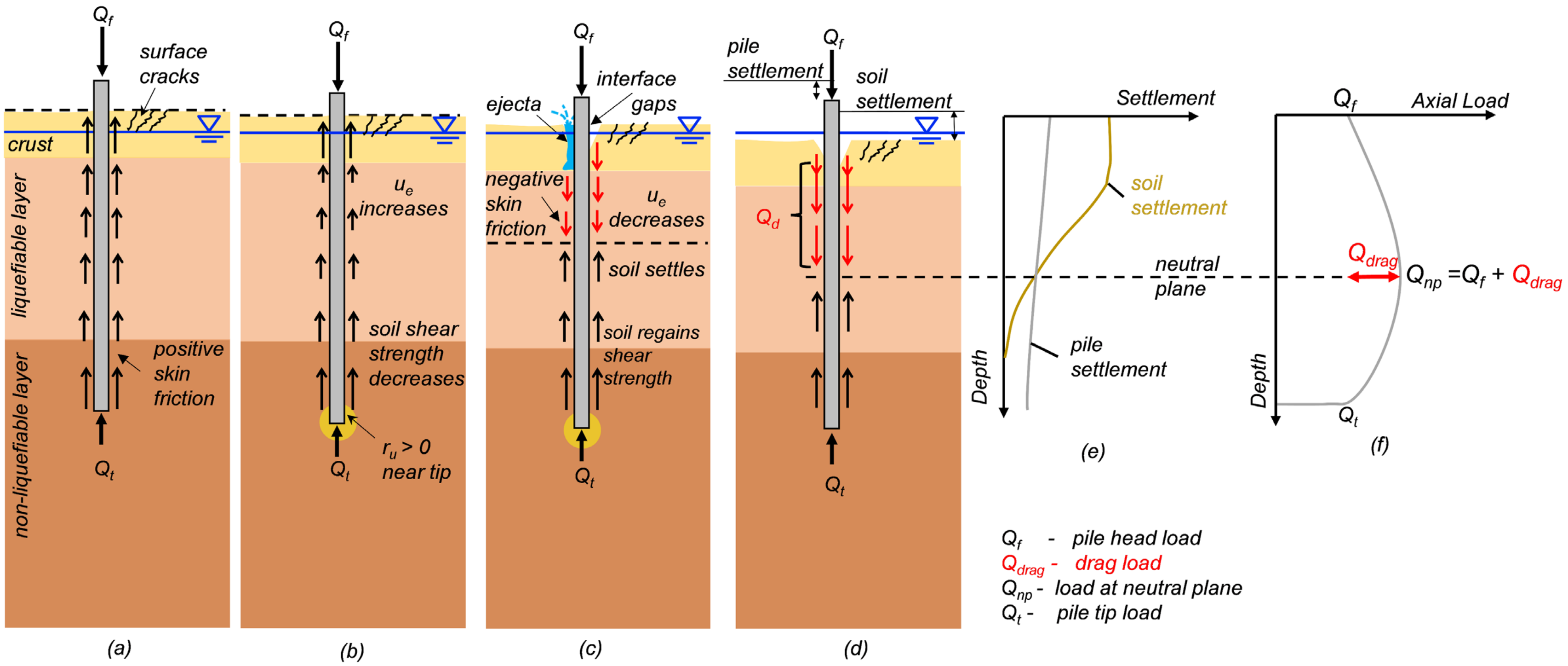
Qf
surface cracks
crust
liquefiable layer
non-liquefiable layer
positive skin friction
Qt
(a)
Qf
ue increases
soil shear strength decreases
ru > 0 near tip
Qt
(b)
Qf
ejecta
interface gaps
negative skin friction
ue decreases
soil settles
soil regains shear strength
Qt
(c)
pile settlement
Qf
soil settlement
Qd
Qt
(d)
Settlement
soil settlement
neutral plane
pile settlement
Depth
(e)
Qf
Axial Load
Qdrag
Qnp =Qf + Qdrag
Depth
Qt
(f)
Qf - pile head load
Qdrag - drag load
Qnp - load at neutral plane
Qt - pile tip load

CHAPTER 2:

EXPERIMENTAL INVESTIGATION

Two centrifuge model tests: SKS02 (Sinha et al. 2021c) and SKS03 (Sinha et al. 2021d), were performed on the 9-m radius centrifuge at the Center for Geotechnical Modeling at the University of California Davis. The tests were performed in a flexible shear beam container (FSB2) consisting of a rigid base plate and five rings, with internal dimensions of 1.651 m x 0.787 m x 0.553 m in length, width, and depth, respectively. Ilankatharan (2008) describes this container in more detail. The model tests included identical instrumented piles of outer diameter 365 mm passing through a thick liquefiable layer, embedded at different depths within an underlying deeper dense layer. The models were shaken with a sequence of realistic earthquake motions, and the mechanism of liquefaction-induced downdrag was investigated. The pile dimensions and the soil layers used in centrifuge tests were selected based on the parametric study of liquefaction-induced downdrag on piles by Sinha et al. (2019). The details of the centrifuge model tests SKS02 and SKS03 and their recordings from the sensors are summarized in the data reports by Sinha et al. (2021c) and Sinha et al. (2021d), respectively. In addition, the data from the tests are curated and made available publically through DesignSafe under Project PRJ-2828.

This chapter summarizes the two centrifuge tests and describes the observed mechanism of liquefaction-induced downdrag in selected shaking events. The chapter also describes the effects of excess pore pressure generation/dissipation, soil settlement, pile tip embedment, and pile head load on liquefaction-induced downdrag. Finally, implications for the design of axially loaded piles in liquefiable soils are summarized. Both model tests were performed at the centrifugal acceleration of 40 g. All quantities presented in this chapter have been converted to prototype units according to the scaling laws described by (Garnier et al. 2007) unless explicitly mentioned otherwise.

2.1 Configuration of Centrifuge Model Test SKS02

Model Description

The SKS02 model consisted of a layered soil profile of a 9 m-thick loose liquefiable Ottawa F-65 sand ($D_R \approx$ 42-44%) layer sandwiched between 4 m of an over-consolidated coarse kaolin clay layer (σ'_p =100 kPa) at the top and an 8 m-thick dense Ottawa F-65 sand layer ($D_R \approx$ 86-88%) [Figure 2.1]. Table 2.1 summarizes the thicknesses, relative densities, and total densities of the constructed soil profile. Using the minimum and maximum density procedures developed as part of the Liquefaction Experiments and Analyses Project LEAP (Carey et al. 2019), several tests were performed to measure the mean grain size diameter (D_{50}), the maximum and minimum void ratios (e_{max} and e_{min}), and the grain size distribution for the Ottawa F-65 batch used in the test. The index properties of all the soils used in the test are provided in Table 2.2. The critical state friction angle (ϕ'_{cv}) of Ottawa F-65 soil is approximately 30 degrees (Bastidas 2016). Details on soil properties and model construction are described in the data report by Sinha et al. (2021a).

The model included two instrumented piles with an outer diameter (D) of 635 mm and an inner diameter of 564 mm named “0DPile” and “5DPile”. The “5DPile” was embedded until its tip was five diameters into the dense sand. The “0DPile” tip was placed at the top of the dense sand. Both the piles (0DPile and 5DPile) were initially loaded with a pile head mass that, after spinning up the centrifuge, represented an axial load of 500 kN. The cross-section properties, instrumentation, installation, and static capacity of piles are described in Section 2.3.

Table 2.1. Soil layer properties used in centrifuge model test SKS02.

Soil Layers	***Relative Density^a, D_R (%)***	***Thickness (m)***	***Saturated Density (kg/m^3)***	***Permeability^b, k (cm/s)***
Monterey Sand	*95*	*1*	*2054*	*0.04*
Clay Layer	*-*	*4*	*1713*	*0.000312*
Loose Sand	*42-44*	*9*	*1968*	*0.026*
Dense Sand	*86-88*	*7.2*	*2060*	

[a] *measured during model construction*
[b] *scaled to prototype scale*

Table 2.2. Index properties of soils used in the centrifuge model test SKS02.

Properties	***Ottawa F-65 Sand***	***Monterey Sand***	***Coarse Kaolin Clay***
Specific Gravity, G_s	*2.65^a*	*2.64^a*	*2.58^b*
Grain Size, D_{50}	*0.2 mm^a*	*0.95 mm^a*	*4 μm^b*
Minimum Void Ratio, e_{min}	*0.52^a*	*0.536^a*	*-*
Maximum Void Ratio, e_{max}	*0.83^a*	*0.843^a*	*-*
Liquid Limit, LL	*-*	*-*	*46.8%^{b}*
Plasticity Index, PI	*-*	*-*	*18.5%^{b}*
USCS	*SP*	*SP*	*ML*

[a] Sinha et al. (2021c)

[c] Stringer et al. (2013)

Model Instrumentation

The model was instrumented with accelerometers (sensor names beginning with “A”), pore pressure transducers (names beginning with “P”), linear potentiometers (names beginning with “LP”), and settlement markers (names beginning with “SM”) [Figure 2.1]. Accelerometers: AH-

0D, AV-0D, AH-5D, and AV-5D installed on the pile head mass were used to measure horizontal and vertical accelerations of 0DPile and 5DPile. An accelerometer (BASE) was attached at the base of the container to measure the applied shaking. The linear potentiometers (SM-1, SM-2) and (LP-0D, LP-5D) measured soil and pile settlements, respectively. In addition, a new non-contact displacement sensing methodology was developed using line lasers and cameras to measure soil and pile settlement (Sinha et al. 2021b). The method used video recording of projected laser lines on target objects to measure static and dynamic settlements. More details on processing the recordings from sensors can be found in the data report by Sinha et al. (2021c).

Cone penetration tests (CPT), centrifuge pile penetration tests (CPPT), and vane shear tests (VST) were performed to determine the state of the model at different phases of the test. The cone penetration test was performed using a 6 mm diameter (model scale) cone with an apex angle of 60 degrees. The CPT probe had a load cell to measure tip load. The stroke of the CPT characterized soil up to the depth of 12 m (prototype units). For characterizing the deeper layers, a custom penetration test (CPPT) was designed, where a 10 mm diameter (model scale) solid steel pile with an apex angle of 120 degrees (same as the instrumented pile) was pushed with the help of a hydraulic actuator to a depth of 18 m (prototype scale). The CPPT probe was initially embedded at 1 g to the depth of 12 m and then pushed to 18 m while in flight at 40 g. An external load cell attached to its head measured the total pile load (skin friction and end bearing) in the CPPT. Hand vane shear tests using a 33 mm (model scale) blade were used to measure the undrained shear strength of the clay layer between spins.

Details on processing the CPT, CPPT, and VST data are described by Sinha et al. (2021a). The external load cell results obtained from the pile load test were corrected for the cone tip apex angle and skin friction effect to obtain the cone tip resistance (q_c) in the dense layer (Sinha et al. 2021a).

Hand vane shear tests and the measured water content at 1 g were used to obtain the undrained shear strength (s_u) profile in the clay layer (Sinha et al., 2021c). $CPPT_1$, CPT_1, and VST_6-VST_8 were conducted before EQM_1 to characterize the model's initial (pre-shaking) state.

Testing Sequence and Shaking Events

Testing was performed over two days, and the test sequence is shown in Table 2.3. On the first day of testing, the dead load on both the piles was 500 kN. On the second day, the load on the 0DPile was increased to 1000 kN. The model was spun up on the centrifuge and shaken with six scaled Santa Cruz earthquake motions (EQM_1 to EQM_6), with peak base accelerations (PBA) ranging from 0.025 to 0.4 g, as summarized in Table 2.3. The waveforms of the applied earthquake motions and their response spectra are also shown in Figure 2.2. EQM_6 was a long-duration motion composed of one strong Santa Cruz motion followed by five small magnitudes of Santa Cruz motions. CPTs and CPPTs were performed while spinning the model at 40g. The VSTs on the clay layer were performed at 1 g after spinning down the centrifuge. Enough time was allowed between each shaking event to completely dissipate the excess pore pressures from all the layers. Dissipating excess pore pressures from the clay layer took the longest time. For medium shaking events (EQM_2 and EQM_4), it took about 3 hours (4.5 minutes model scale) to completely dissipate (greater than 90%) of the excess pore pressures from the clay layer. For the strong shaking events (EQM_3, EQM_5, EQM_6), complete dissipation took up to 5 hours (7.5 minutes in model scale).

The predominant period of the motions was designed to avoid the first fundamental period of the piles to control the magnitude of lateral pile head loads. It was desirable to limit the lateral loads because they produce bending moments in the piles, which in turn affected the axial load measurements due to the cross-axis sensitivity of the axial load strain gauges. For shaking event EQM_3, Figure 2.2 shows the spectral acceleration of the applied earthquake motion. It shows the obtained spectral acceleration for EQM_3 at the soil surface, 0DPile mass, and 5DPile mass. The spectra show that the input motions had a predominant period between 0.3-0.4 seconds [Figure 2.2(b)] and were away from the piles' first fundamental period of 1.2-1.4 seconds [Figure 2.2(c)].

Table 2.3. The testing sequence in centrifuge model test SKS02.

Events	***Description***	***Measurements***
Day 1		
VST_6	*Hand Vane Shear Test*	*s_u = 22 kPa*[a]
$CPPT_1$	*Centrifuge Pile Penetration Test*	Figure 2.3 *(a)*
VST_7-VST_8	*Hand Vane Shear Test*	*s_u = 22 kPa*[a]
Spin Up		
CPT_1	*Cone Penetration Test*	Figure 2.3 *(a)*
EQM_1	*Small Santa Cruz*	*PBA = 0.026 g*
EQM_2	*Medium Santa Cruz*	*PBA = 0.14 g*
CPT_2	*Cone Penetration Test*	Figure 2.3 *(a)*
EQM_3	*Large Santa Cruz*	*PBA = 0.24 g*
Spin Down		
VST_9-VST_{10}	*Hand Vane Shear Test*	*s_u = 25 kPa*[a]
Day 2		
$CPPT_2$[b]	*Centrifuge Pile Penetration Test*	Figure 2.3 *(a)*
VST_{11}[b]	*Hand Vane Shear Test*	*s_u = 25 kPa*[a]
Spin Up		
CPT_3[b]	*Cone Penetration Test*	Figure 2.3 *(a)*
EQM_4[b]	*Medium Santa Cruz*	*PBA = 0.14 g*
EQM_5[b]	*Large Santa Cruz*	*PBA = 0.32 g*
CPT_5[b]	*Cone Penetration Test*	Figure 2.3 *(a)*
EQM_6[b]	*Large EJM01*[c] *Motion*	*PBA = 0.40 g*
Spin Up		
VST_{12}[b] *- VST_{13}*[b]	*Hand Vane Shear Test*	*s_u = 37 kPa*[a]

[a] *peak undrained shear strength (s_u) measured at the middle of the clay layer*

[b] *load on 0DPile was increased from 500 kN to 1000 kN*

[c] *Malvick et al. (2002)*

PBA- peak acceleration measured at the base of the container

State of the Model During Test

Cone tip resistance (q_c), relative density (D_R), and soil shear strength interpreted from cone penetration tests (CPT), centrifuge pile penetration tests (CPPT), and vane shear tests (VST) for different shaking events are shown in Figure 2.3. The initial D_R of the sand layer interpreted from the CPT and CPPT matched quite well with the pluviated D_R's, i.e., about $D_R \approx$ 44-46% in the loose sand layer and $D_R \approx 90\%$ in the dense sand layer. The initial undrained shear strength in the middle of the clay layer was estimated to be about $s_u = 22$ kPa. After shaking the model with a medium (EQM_2) and a large (EQM_3) earthquake motion, the liquefaction-induced settlement increased D_R in the loose sand layer to $D_R \approx 49\%$. The undrained shear strength in the clay layer increased to $s_u \approx 25$ kPa. The increase of the peak undrained shear strength of the clay layer resulted from the consolidation strains after shaking. On the second day and after the two large shaking events, EQM_5 and EQM_6, the D_R in the loose sand increased to $D_R \approx 58\%$, whereas the undrained shear strength in the clay layer increased to $s_u \approx 37$ kPa.

Results from CPTs, CPPTs, and VSTs were used to obtain the shear strength of the soil layers. Figure 2.3 (d) shows the undrained shear strength in the clay layer and drained interface shear strength in the loose sand layer. VSTs were used to obtain undrained shear strength in the clay layer. The drained interface shear strength in the sand layer was estimated with a lateral stress coefficient, K =1 (as for a driven cast-in-situ pile (Fleming et al. 2008)) with an interface friction angle of $\delta = 30^{\circ}$. Here, K is defined as the ratio of effective radial stress at the pile's interface to effective vertical stress. The shear strength presented in Figure 2.3 (d) was later used to estimate the limit load curve for the piles described later in Section 2.3.

2.2 Configuration of Centrifuge Model Test SKS03

Model Description

Model SKS03 (Sinha et al. 2021d) included six distinct soil layers. The soil profile consisted of 1 m of Monterey sand, 2 m of clay crust ($s_u \approx 35$ kPa), 4.7 m of loose liquefiable sand ($D_R \approx 40\%$), 1.3 m of clayey silt (20% Kaolin clay and 80% non-plastic silt), 4 m of medium dense sand ($D_R \approx 60\%$) and dense sand ($D_R \approx 83\%$) beneath it (Figure 2.4). The clay crust was prepared from a lightly cemented Yolo Loam slurry with a water content of w = 50%, soil cement ratio of 3%, and cured for about two weeks underwater before the test. The sand layers were constructed from Ottawa F-65 sand. The index properties of all the soils used in the test are provided in Table 2.2. Table 2.4 summarizes the thicknesses, relative densities, and total densities of the as-constructed soil profile. More details on soil properties and model construction are described in Sinha et al. (2021d).

Table 2.4. Soil layer properties used in centrifuge model test SKS03.

Soil Layers	***Relative Density[a], D_R (%)***	***Thickness (m)***	***Saturated Density (kg/m^3)***	***Permeability[b], k (cm/s)***
Monterey Sand	*95*	*1*	*2054*	*0.04*
Clay Crust	*-*	*2*	*1700*	*0.000312*
Loose Sand	*40*	*4.7*	*1971*	*0.026*
Clayey Silt	*-*	*1.3*	*2000*	*0.00036*
Medium Dense Sand	*60*	*4*	*2019*	*0.022*
Dense Sand	*83*	*8*	*2051*	

[a] *measured during model construction*

[b] *scaled to prototype scale*

The model included three identical instrumented piles with an outer diameter (D) of 635 mm and an inner diameter of 564 mm (3DPileS, 3DPileM, and 3DPileL), loaded with 500kN, 1500 kN, and 2400 kN, respectively. The "3D" at the beginning of the pile names indicates that the pile tips were embedded three pile diameters into the dense sand layer. The cross-section properties, instrumentation, installation, and static capacity of piles are described in Section 2.3.

Model Instrumentation

The model was instrumented with accelerometers (A#), pore pressure transducers (P#), and cameras [Figure 2.4]. Accelerometers: (AH-3DS and AV-3DS), (AH-3DM and AV-3DM), and (AH-3DL and AV-3DL) installed on the pile head masses measured (horizontal and vertical) accelerations of 3DPileS, 3DPileM, and 3DPileL, respectively. An accelerometer (BASE) was attached to the base of the container to measure the applied base shaking. Cameras with target markers were used to obtain 3-D movements of the model surface and the piles. Sinha et al. (2021a) describe the procedure of using cameras with digital image correlation (DIC) techniques to obtain 3-D movements in centrifuge tests. In addition, the model also used lasers and cameras to quickly estimate settlement during the test (Sinha et al. 2021d; b). More details on processing the recordings from sensors can be found in the data report by Sinha et al. (2021d).

Cone penetration tests (CPT), pile load tests (PLT), and vane shear tests (VST) were performed to determine the state of the model at different phases of the test. The cone penetration test was performed using a 6 mm diameter (model scale) cone with an apex angle of 60 degrees. The probe used was of Liquefaction Experiments and Analysis Projects' (LEAP-2017) design (Carey et al. 2018). The CPT probe had a load cell attached to the tip, which measured the tip stress as it penetrated the soil. The stroke of the CPT characterized soil up to the depth of about 16 m (prototype scale). Pile load tests (PLT) were conducted on 3DPileS to estimate the static pile load capacity of the 3DPiles. A constant rate of penetration test (ASTM D1143 2016) was used to push 3DPileS at a penetration rate of 1 mm/minute. Hand vane shear tests using a 33 mm (model scale) blade were used to measure the undrained shear strength of the clay crust layer between spins. The data processing from the soil investigation tests (CPT, PLT, and VST) to obtain the strength properties of the soil layers and the piles is described in detail in the data report by Sinha et al. (2021d).

Testing Sequence and Shaking Events

Testing was performed over two days. The test sequence is shown in Table 2.5. The first day of testing involved establishing the initial state of the model. The model was spun up to 40 g, followed by performing a cone penetration test (CPT_1) and a pile load test (PLT_1). Then the model was shaken with a small Santa Cruz earthquake motion (EQM_1) with a PBA of 0.09 g, followed y another cone penetration test CPT_2. On the second day of testing, the model was shaken with medium (EQM_2, EQM_3) and large (EQM_4 and EQM_5) scaled Santa Cruz earthquake motions with peak base accelerations (PBA) ranging from 0.13 g to 0.61 g [Figure 2.5]. The time histories of the applied earthquake motions and their response spectra are shown in Figure 2.5. EQM_4 and EQM_5 were the long-duration motion of strong Santa Cruz motion followed by five small magnitude Santa Cruz motions. CPTs (CPT_3-CPT_5) were performed in between the shaking events. The VSTs were measured by hand at 1g at the beginning and after spinning down the centrifuge. Enough time was allowed between successive shaking events to completely dissipate the excess pore pressures from all the layers. A second pile load test, PLT_2, was performed at the end of all shaking events.

Like the centrifuge model test SKS02, the predominant period of the motions was designed to be away from the first fundamental period of the piles to ensure that the piles would not undergo strong horizontal movements generating large moments, which might affect the accuracy of the axial load measurements. For shaking event EQM_4, Figure 2.5 shows the spectral acceleration of the applied earthquake motion. It also shows spectral acceleration obtained from the EQM_4 shaking event at the soil surface and on 3DPiles masses. The spectra show that the input motions had a predominant period between 0.3-0.4 seconds [Figure 2.5 (b)] and were away from the piles' first fundamental period of 1-2 seconds [Figure 2.5 (c)].

Table 2.5. The testing sequence in centrifuge model test SKS03.

Events	***Description***	***Measurements***
Day 1		
VST_1-VST_2	*Hand Vane Shear Test*	*$s_u \approx 35kPa^a$*
Spin Up		
CPT_1	*Cone Penetration Test*	Figure 2.6 *(a)*
PLT_1	*Pile Load Test*	Figure 2.7 (a)
EQM_1	*Small Santa Cruz*	*PBA = 0.09g*
CPT_2	*Cone Penetration Test*	Figure 2.6 *(a)*
Day 2		
VST_3-VST_4	*Hand Vane Shear Test*	*$s_u \approx 35kPa^a$*
Spin Up		
EQM_2	*Medium Santa Cruz*	*PBA = 0.13 g*
CPT_3	*Cone Penetration Test*	Figure 2.6 *(a)*
EQM_3	*Large Santa Cruz*	*PBA = 0.18 g*
CPT_4	*Cone Penetration Test*	Figure 2.6 *(a)*
EQM_4	*Large EJM01^b Motion*	*PBA = 0.45 g*
EQM_5	*Large EJM01^b Motion*	*PBA = 0.60 g*
PLT_2	*Pile Load Test*	Figure 2.7
CPT_5	*Pile Load Test*	Figure 2.6 *(a)*
Spin Down		
VST_5 - VST_8	*Hand Vane Shear Test*	*$s_u \approx 37\ kPa^a$*

^{a} peak undrained shear strength (s_u) measured at the middle of the clay layer

^{b} Malvick et al. (2002)

PBA- peak acceleration measured at the base of the container

State of the Model During Test

Cone tip resistance (q_c), relative density (D_R), and soil shear strength interpreted from cone penetration tests (CPT), and vane shear tests (VST) for different shaking events are shown in Figure 2.6. The initial D_R of the sand layer interpreted from the CPT matched quite well with the pluviated D_R's, i.e., about $D_R \approx 40\%$ in the loose sand layer, $D_R \approx 60\%$ in the medium dense sand layer, and $D_R \approx 85\%$ in the dense sand layer. The initial undrained shear strength (VST_1-VST_8) in the middle of the clay crust layer was estimated to be about $s_u \approx 35$ kPa, which remained almost constant throughout the test. At the end of the test, the clay crust layer's undrained shear strength (VST_9-VST_{11}) increased to $s_u \approx 37$ kPa.

Soil reconsolidation from liquefaction increased the relative density of the sand layers [Figure 2.6 (c)]. The small shaking event EQM_1 only liquefied the loose sand layer, which, after reconsolidation, increased relative density to $D_R \approx 42.5\%$. At the end of the medium shaking events (EQM_2 and EQM_3), the relative density of the loose sand layer increased to $D_R \approx 50\%$. The small and medium shaking events only liquefied the loose sand layers with small excess pore pressure generation in the clayey silt, medium dense, and dense sand layers. The large shaking events (EQM_4 and EQM_5) liquefied the loose sand layer and part of the medium dense sand layer. At the end of large shaking events, the relative density in the loose sand layer increased to $D_R \approx 60\%$, and in the medium dense sand layer, it increased to $D_R \approx 75\%$.

Results from PLTs and VSTs were used to obtain the shear strength profile of the soil layers. Figure 2.6 (d) shows the undrained shear strength in the clay layer and drained interface shear strength in the sand layers. VSTs were used to obtain undrained shear strength in the clay layer. The drained interface shear strength in the sand layers was estimated from the pile load tests performed on 3DPileS (Sinha et al. 2021d). Figure 2.7 shows the results from the pile load tests

PLT_1 and PLT_2, respectively. In the PLT_1 test, the pile was pushed in 0.12 pile diameters (0.12 D). The pile was pushed in an additional 0.5 D in PLT_2. Figure 2.7 also shows the axial load distribution in the 3DPileS at different penetration levels during the PLT_2 test. As described in more detail by Sinha et al. (data report), the axial load distribution from the PLT_2 test during loading at large head loads (such as 50 MN) was used to estimate the limit load curve (show later in Figure 2.9) and interface shear strength in the soil layers [Figure 2.6 (d)].

2.3 Pile Properties for SKS02 and SKS03

The centrifuge model test included 1/40 scale models of Aluminum 6061 closed-ended piles with an outer diameter (D) of 635 mm and an inner diameter of 564 mm. For obtaining maximum drag loads on piles, the outer surface of the pile was machined to achieve an average roughness (R_a) of 0.04 to 0.06 mm. The achieved interface profile is shown in Figure 2.8 (c). According to Martinez and Frost (2017), this roughness was sufficient to mobilize the interface friction angle (δ) equal to the drained soil friction angle of $\phi'_{cv} = 30^o$ [Figure 2.8 (d)]. A summary of pile instrumentation, installation, static capacity, and limit load curve is given below. A more detailed description can be found in Sinha et al. (2021c) and Sinha et al. (2021d).

Instrumentation

The piles were instrumented internally to measure the axial load distribution. While instrumenting the outer surface would be easier, it would be challenging to secure the sensor wires while achieving a uniform diameter and roughness profile. Therefore, the instrumentation was attached along the inner diameter of the pile, keeping the strain gages and their wires secured from abrasion and making the pile reusable for multiple tests. The pile's outer and inner diameters at the model scale were approximately 15.9 mm and 14.1 mm, respectively. Nine strain gage bridges were installed with a spacing of about 5.08 cm (i.e., about 2 m at prototype scale) [Figure 2.8 (a)]. The gages were labeled 1 to 9 from bottom to top [Figure 2.8 (a)]. The axial strain gages in 0DPile, 5DPile, 3DPileS, 3DPileM, and 3DPileL were correspondingly numbered as $G1^{0D} – G9^{0D}$, $G1^{5D} – G9^{5D}$, $G1^{3D\text{-}S} – G9^{3D\text{-}S}$, $G1^{3D\text{-}M} – G9^{3D\text{-}M}$, and $G1^{3D\text{-}L} – G9^{3D\text{-}L}$, respectively, starting from the pile's tip to its head [Figure 2.8 (a), Figure 2.1, Figure 2.4]. The bottommost gage in the piles was placed 3.18 cm (i.e., 1.27 m in the prototype scale) from the tip. Although the strain gages were wired in a full-bridge configuration to measure axial load, the bridges had some cross-sensitivity to bending moments. Therefore, two-point bending moment tests on different loading axes were conducted on the piles to determine the orientation corresponding to the minimum cross-axis sensitivity. During the test, the piles were oriented about those axes to minimize the error in axial load measurements arising from the bending moments generated during shaking. Sinha et al. (2021c) performed p-y analyses of the piles using the expected lateral loads and found the error in the axial load measurements to be within 15%. The fully assembled pile is shown in Figure 2.8 (b). The bottom of the pile was plugged with an O-ring sealed tip [Figure 2.8 (b)] to keep the sensors safe from water seeping from the bottom. More details on the pile design can be found in Sinha et al. (2021c).

Installation

The piles were pushed at 1 g to their target depths in soil layers. A crane with a heavy mass was slowly lowered to push the pile in the soil. The apex angle of the pile tip was designed to be 120 degrees to facilitate pile installation [Figure 2.8 (b)]. A split mass (Sinha et al. 2021c) was clamped to the pile to produce the desired axial load. The bottom of the pile mass was set at 1 m above the ground surface. A gap of 1 m above the ground was considered large enough to permit large settlements of the pile head and small enough to limit the magnitude of shaking-induced bending moments. Minimizing bending moments is desirable to minimize errors in axial load measurements. More details regarding pile installation are described in Sinha et al. (2021c).

Static Pile Capacity

The total static pile capacity for the 0DPile and 5DPile estimated from the cone penetration and centrifuge pile penetration tests [Figure 2.3] was about 2700 kN (shaft: 1200 kN + tip: 1500 kN) and 6200 kN (shaft: 2300 kN + tip: 3900 kN), respectively (Sinha et al. 2021c). The piles (0DPile and 5DPile) under the initial load of 500 kN had a static factor of safety of 5.4 and 12.4, respectively. When the load on 0DPile was increased to 1000 kN on the second day of testing, the associated static factor of safety got reduced to 2.7.

For the centrifuge model test SKS03, PLT_2 was used to estimate the static pile load capacity of the piles. The static pile capacity estimated from PLT_2 was about 4550 kN (shaft: 1950 kN + tip: 2600 kN) (Sinha et al. 2021d), resulting in a static factor of safety of 8, 2.6, and 1.6 for the 3DPileS, 3DPileM, and 3DPileL, respectively.

Limit Load Curves

The limit load curve is defined as the axial load distribution of the pile corresponding to the maximum drag load the pile can develop. Assuming the pile mobilizes negative skin friction equal to its interface shear strength, the maximum drag load is estimated. Alternatively, the limit load curve for a pile can be defined as the sum of pile head load and its cumulative shaft capacity with depth. The limit load curves for the piles obtained for both the centrifuge model tests (SKS02 and SKS03) for zero pile head load are shown in Figure 2.9. The limit load curve for the centrifuge model test SKS03 was obtained directly from the axial load distribution recorded during the PLT_2

test (Sinha et al. 2021d). For centrifuge model test SKS02, the limit load curve was estimated from the measured undrained shear strength in the clay layer and drained shear strength in the sand layers. Interface shear strength in the clay layer was estimated using the α method of AASHTO (2020) with an undrained shear strength (s_u) of 20 kPa. The interface shear strength in the loose sand layer was estimated as $\tau = K\sigma'_v \tan(\delta)$ with an interface friction angle of $\delta=30^o$ and an average lateral stress coefficient K=1 [Figure 2.3 (d)].

2.4 Centrifuge Spin-up Induced Drag Load

The spinning up of the centrifuge resulted in drag loads [as shown later in Figure 2.16 and Figure 2.17]. As the centrifuge spun up, the increase of gravity resulted in excess pore pressures in soil. The dissipation of these pore pressures resulted in soil consolidation settlements and hence negative skin friction and drag load on the pile. At the end of centrifuge spin-up, the 0DPile and the 5DPile developed drag loads of about 250 kN and 700 kN, respectively [as shown later in Figure 2.16]. Their initial static neutral planes were about 11 m and 14 m deep, respectively [as shown later in Figure 2.17]. In the centrifuge model test SKS03, centrifuge spin-up resulted in drag loads of about 300 kN in 3DPileS and 3DPileM. The consolidation settlement from centrifuge spin-up that caused the development of drag loads could not be precisely measured. The consolidation of the clay layer and the unknown settlement of the racks connected to the settlement sensors under increasing gravity made it difficult to obtain settlements precisely. In centrifuge model test SKS02, the soil settlement during spin-up one was estimated qualitatively (using the stiffness of the racks and the clay layer calibrated from multiple spin-up and spin-down measurements) to be about 20-30 mm in the sand layers and about 10-15 mm in piles.

2.5 Mechanism of Liquefaction-Induced Downdrag

During several shaking events: EQM_3, EQM_5, and EQM_6 in centrifuge model test SKS02 and EQM_1-EQM_5 in centrifuge model test SKS03, liquefaction occurred in portions of the loose and medium dense sand layers; significant excess pore pressures were also measured in the dense sand layer. On the other hand, there were shaking events: EQM_2 and EQM_4 in centrifuge model test SKS02 which did not cause liquefaction but did produce measurable small excess pore pressures. However, the dissipation of these small excess pore pressures and reconsolidation caused enough soil settlement to cause drag loads and downdrag settlements of the piles. Figure 2.10 (a,b) and Figure 2.11 (a,b) shows the time histories of excess pore pressure (u_e) and soil and pile settlement for shaking event EQM_3 in centrifuge model test SKS02 and EQM_4 in centrifuge model test SKS03, respectively. The figures also show the isochrones of u_e in the soil layers [Figure 2.10 (e), Figure 2.11 (e)] and axial load distribution in 0DPile [Figure 2.10 (f)], 5DPile [Figure 2.10 (g)], 3DPileS [Figure 2.11 (f)], 3DPileM [Figure 2.11 (g)], and 3DPileL [Figure 2.11 (h)]. The figures also show the mobilized tip load and pile settlement as free-field effective stress changed at the pile's tip depth [Figure 2.10 (c,d), Figure 2.11 (c,d)]. Appendix B and Appendix C show similar plots for all the shaking events of centrifuge model tests SKS02 and SKS03, respectively. Appendix A and Appendix B show similar plots for all the shaking events of centrifuge model tests SKS02 and SKS03, respectively.

The mechanisms observed during shaking and reconsolidation for the liquefaction-induced downdrag phenomenon were similar across all the shaking events in the two centrifuge model tests. Thus, they are mainly described below, referring to the shaking event EQM_3 of centrifuge model test SKS02 [Figure 2.10]. Furthermore, whenever needed, Figure 2.11 is also referred to illustrate the similarities between the observed mechanism between the two centrifuge model tests.

The EQM_3 shaking event liquefied the top 7 m of the loose sand layer (i.e., depths 5 – 12 m). The mobilized interface shear stress, the mobilized pile tip stress, and the soil and pile settlement in response to the excess pore pressure ratio (r_u) in the liquefied layer and near the pile's tip for the shaking event EQM_3 are shown in Figure 2.12. In what follows, the mechanisms of liquefaction-induced downdrag during shaking and reconsolidation are described with reference to Figure 2.10, Figure 2.12, and Figure 2.11.

During Shaking

At the beginning of shaking (t = 0 sec), the piles had an initial drag load, and correspondingly an initial static neutral plane developed from the negative skin friction either from centrifuge spin-up or past shaking events [Figure 2.10 (f,g), Figure 2.11 (f,g,h)]. For the shaking event EQM_3 (t = 0 sec) in centrifuge model test SKS02, the piles had an initial drag load developed from past shaking events EQM_1 and EQM_2. Similarly, for the shaking event EQM_4 in centrifuge model test SKS03, 3DPiles had initial drag load developed from past shaking events EQM_1, EQM_2, and EQM_3. At the beginning of the shaking (i.e., even before soil started developing excess pore pressures), a small reduction of negative skin friction [Figure 2.12 (c)] and a compensating increase in the mobilized pile tip stress [Figure 2.12 (d)] occurred. This initial decrease in skin friction could have resulted from the relaxation of shear stresses from the disturbance caused by the shaking. At the beginning of the shaking, some soil (surface) settlements occurred in the models [Figure 2.10 (b), Figure 2.11 (b), Table 2.6, Table 2.7]. The initial surface settlement could have resulted from undrained soil movement caused by the tendency of the flat ground surface to conform to the curved g-field in the centrifuge.

Excess pore pressures generated in the soil layers during shaking decreased skin friction, decreasing drag loads, and thus axial loads in the piles. At t = 5 s, excess pore pressures in soil started to develop. As a result, the negative skin friction and drag loads [Figure 2.12 (c)] decreased. In addition, the r_u build-up and strength loss throughout the model [Figure 2.10 (a,d)] also decreased positive skin friction and the tip resistance below the initial static neutral plane. The decrease in drag load caused a decrease in axial loads in the piles [Figure 2.10 (f,g), Figure 2.11 (f,g,h)]. Typically, the decrease in drag load surpassed the decrease in shaft resistance below the neutral plane resulting in a decrease of the pile tip load [Figure 2.10 (c), Figure 2.11 (c)]. However, when large excess pore pressures developed around the heavily loaded pile 3DPileL, the loss of shaft resistance surpassed the loss of drag loads, resulting in mobilization of larger pile tip loads [Figure 2.11 (c)].

When the soil liquefied, the drag load was reduced to zero, and high excess pore pressures were generated in the dense sand layer. At the peak of shaking, the loose sand layer liquefied between the depths of 5 and 12 m while generating high excess pore pressures of $u_e \approx 80$ kPa in the dense sand layer [Figure 2.12 (a)]. In shaking event EQM_4 of centrifuge model test SKS03, high excess pore pressures equal to $u_e \approx 80$ kPa also developed in the dense sand layer. While the dense sand is expected to exhibit small earthquake-induced excess pore pressures, water migration from the loose sand layer to the dense layer resulted in increased excess pore pressures. The magnitude of pore pressure increase in the dense layer depends on the relative thicknesses of the layers and drainage boundary conditions. This issue is examined in some detail in Chapter 4. When the loose sand layer was fully liquefied (between the depths of 5-12 m), the interface skin friction for the 5DPile in the liquefied layer was reduced to zero, and consequently, the drag load vanished [Figure 2.12 (c)]. The constant axial load profile of the 5DPile in the depth of 5-12 m demonstrates the vanishing of the drag load in the liquefied soil [Figure 2.10 (g)]. Similar observations were made for the 0DPile [Figure 2.12 (f)] and 3DPiles [Figure 2.11 (f,g,h)]. However, for 0DPile and 3DPileL, the axial loads in the liquefied soil were not constant. 0DPile and 3DPileL were the same instrumented pile (used in both the centrifuge model tests), which had the greatest aforementioned cross-sensitivity in the axial gages. In the centrifuge model test SKS02, during the post-testing model dissection, the 0DPile was found inclined vertically by about 1.4 degrees in the shaking direction. This inclination might have also introduced residual moments in the 0DPile affecting its residual axial load measurements. In the centrifuge model test SKS03, axial load measurements in 3DPileL were severely affected [shown later in Figure 2.17]. It is assumed that deterioration of axial gages from multiple shaking events from centrifuge test SKS02 and the moment generated from the large head load of 3DPileL may have further increased their cross-sensitivity to bending moments, affecting the axial load measurements. While the axial load measurements were affected in 0DPile and 3DPileL, the pile settlement was accurate. Although not as accurate as one would wish, the recorded axial loads provided valuable indications of the change in axial load distribution during shaking and reconsolidation. While presenting the axial load distribution profiles for 0DPile and 3DPileL, results from some gages were removed from the plot because they were deemed inaccurate. Please note that the data reports by Sinha et al. (2021c; d) show the recorded data for all the gages in piles.

Even though the drag load decreased the pile's tip load during shaking, the pile settled [Figure 2.10 (d), Figure 2.11 (d)]. The pile settlement occurred because the excess pore pressures generated around the pile decreased the pile's shaft and tip capacity causing settlement until enough resistance was mobilized to achieve force equilibrium. During shaking event EQM_3, very high excess pore pressures developed around the shaft and near the tip resulting in significant pile settlement [Figure 2.12 (b)]. For the deeply embedded 5DPile with a smaller load and a higher tip capacity, the resulting pile settlement was small (< 10 mm) [Figure 2.12 (b)]. For the shaking event EQM_4 of the centrifuge model test SKS03, all the piles underwent some settlement due to the development of excess pore pressures around the pile [Figure 2.11 (d)]. The heavily loaded 3DPileL with a large tip load and smaller free-field effective stress near tip ($\sigma'_v = 60$ kPa) caused the pile to plunge by 200 mm in soil [Figure 2.11 (d)]. On the other hand, the lightly loaded piles (3DPileS and 3DPileM) with smaller pile head loads suffered comparatively small settlements.

Post Shaking

After shaking, excess pore pressures dissipated, and consequently, the soil reconsolidated. The clay and silt layers in the centrifuge tests contributed to interesting effects such as drainage impedance and equalization of excess pore pressures. In the centrifuge model test SKS02, the presence of the low permeability clay layer (with effective stress of $\sigma'_{vo} = 38$ kPa at its bottom) hindered the drainage of water coming to the soil surface, leading to an equalization of excess pore pressures in the layers beneath to $u_e \approx 38$ kPa at $t \approx 2.5$ minutes [Figure 2.10 (a)]. The hindrance of drainage led to a water film formation beneath the clay-sand interface (also observed in other tests with impermeable interfaces, e.g., Malvick et al. (2002)). The surface settlement remained almost constant with small, probably localized, heaving during this period, as shown in Figure 2.10 (b). The heaving must have resulted from the redistribution of the water film (Fiegel and Kutter 1994), which eventually drained through leakage from cracks in the clay layer and along the sides of the centrifuge model container. At about t = 8 minutes, the water film layer had fully disappeared. During this period ($t \approx 2.5 – 8$ minutes), the model surface settled by about 45 mm at a constant excess pore pressure of $u_e \approx 34$ kPa [Figure 2.10 (a)] and $r_u = 52\%$ [Figure 2.12 (a)]. Once the water film fully dissipated (t > 8 minutes), excess pore pressure in the soil started to dissipate faster from gaps created in the clay layer or from the sides of the container [Figure 2.10 (a)]. Video recordings showed water coming to the surface along the sides of the container. In the centrifuge model test SKS03, no such sequences of surface settlements were observed. The soil surface kept continuously settling during reconsolidation due to dissipation from the cracks present in the clay crust layer [Figure 2.11 (b)]. However, the relatively low permeability of the clayey silt and the clay layer slowed down the dissipation and equalized the excess pore pressures in the soil layers beneath [Figure 2.11 (a,e)]. The excess pore pressures in the loose sand layer first equalized to $u_e \approx 20$ kPa, approximately equal to the effective stress at the bottom of the clay layer. The excess pore pressures in the medium dense sand and dense sand first equalized to $u_e \approx 76$ kPa, equal to the effective stress at the bottom of the clayey silt layer. Sinha et al. (2021e) developed a numerical model (described in Chapter 3) to investigate and study the development of water film formation, which was used to understand the pattern of surface settlement in centrifuge model tests SKS02 and SKS03. For centrifuge model test SKS02, full reconsolidation (> 98%) was generally achieved within 45-60 minutes. For centrifuge model test SKS03, cracks in the clay crust layer finished reconsolidation in the loose sand layer within 45-60 minutes [Figure 2.11 (b)]. However, the clayey silt layer's low permeability took more than 3 hours to complete reconsolidation in the medium dense and dense sand layers beneath [Figure 2.11 (b)].

During reconsolidation, as excess pore pressures dissipated and the soil settled, the negative skin friction and hence the drag loads increased on the piles [Figure 2.12 (c), Figure 2.10 (f,g), Figure 2.11 (f,g,h)]. The decrease in excess pore pressure and correspondingly increase in drag load and axial load in the piles at t = 1 minute, t = 3 minutes, and t = 1 hour for the shaking event EQM_3 of centrifuge test SKS02 is shown in Figure 2.10 (e,f,g). Between t = 0.5 – 2.5 minutes, while the surface did not settle [Figure 2.10 (b), Figure 2.12 (a)], the negative skin friction in the reconsolidating liquefied layer kept on increasing [Figure 2.12 (c)]. The increase in negative skin friction can be explained by the reconsolidation (dissipation of excess pore pressures by about 45%) occurring within the liquefied layer; however, it did not show up as the surface settlement because the water expelled in this process produced the water film layer under the clay. Consequently, the load at the shaft and the tip below the neutral plane also increased [Figure 2.10 (d,f,g), Figure 2.11 (d,f,g,h), and Figure 2.12 (d)]. However, the resulting pile settlement was smaller as the piles regained their tip capacity and stiffness [Figure 2.10 (d), Figure 2.11 (d)]. During reconsolidation, the settlement in the piles was less than 10 mm (i.e., 1.6% of pile diameter) [Table 2.6, Table 2.7].

After complete reconsolidation ($r_u = 0$), the achieved drag load was higher than the initial drag load before shaking, while the neutral plane depths remained unchanged [Figure 2.10 (f,g), Figure 2.11 (f,g,h)]. The increase in drag load resulted from the increased mobilized negative skin friction [Figure 2.12 (c)] above the neutral plane caused either 1) due to the increased soil displacement at the interface or 2) due to increased lateral stresses from densification. For the 5DPile, the negative interface skin friction in the liquefiable layer increased from -20 kPa to -40 kPa [Figure 2.12 (c)]. Ganainy et al. (2014) and Kokkali et al. (2018) used tactile pressure sensors in centrifuge model tests and observed the lateral stresses after reconsolidation higher than their initial value before shaking. After complete reconsolidation, the drag load on the 0DPile and 5DPile for shaking event EQM_3 increased from 250 to 500 kN and from 700 to 1100 kN, respectively [Figure 2.10 (f,g)]. Consequently, the mobilized tip stress (and tip load) in the 0DPile and 5DPile increased from 1.5 to 2.2 MPa and from 2.2 to 3.0 MPa, respectively [Figure 2.12 (d), Figure 2.10 (c)]. Similarly, for shaking event EQM_4 in centrifuge model test SKS03, after complete reconsolidation, the drag load, and the tip load in 3DPileS, 3DPileM, and 3DPileL increased [Figure 2.11 (c,e,f,g)].

2.6 Discussion on Pile Settlement

Most of the settlements in the piles occurred during shaking when the excess pore pressures around the pile's shaft and tip were high. On the other hand, the pile settlement (or downdrag settlement) during reconsolidation from liquefaction-induced downdrag was typically small (< 2% of the pile's diameter). The settlement of piles during shaking and reconsolidation for all the shaking events from centrifuge model tests SKS02 and SKS03 is summarized in Table 2.6 and Table 2.7, respectively. Figure 2.13 summarizes the pile settlement during shaking as an effect of free field-field excess pore pressure ratio (r_u) near the pile's tip. Pile settlement from all shaking events [Table 2.6, Table 2.7] shows that pile settlements mainly occurred during shaking. The leading cause for the large settlement of the piles was the decrease in pile tip capacity and stiffness from increased excess pore pressures near the tip resulting in settlement of the piles. Centrifuge tests showed that even if the bearing layer (in which the pile tip is embedded) is non-liquefiable, redistribution of excess pore pressures from the nearby liquefied layers and the generated earthquake-induced excess pore pressures can cause large excess pore pressure developments in the bearing layer. These large excess pore pressure near the tip significantly reduced the tip capacity and caused settlement in the piles. With the increase in the magnitude of the shaking events, the free-field excess pore pressures developed near the pile's tip increased, and correspondingly the pile settlement also increased. In the centrifuge model test SKS02, for each successive shaking event EQM_1, EQM_2, EQM_3, EQM_5, and EQM_6, the free-field excess pore pressure ratio (r_u) at the 0DPile and 5DPile tip increased. This increased excess pore pressure caused an increase in pile settlements [Figure 2.13 (a)]. Likewise, in centrifuge model test SKS03, the settlement of the piles increased in each successive shaking event (EQM_1 - EQM_5) due to the progressive increase of excess pore pressure ratio near the pile's tip [Figure 2.13 (b)]. During reconsolidation, while the drag loads increased, the shaft and tip capacity and stiffness also increased, producing small pile settlements. As a result, for every event (except for 5DPile and 3DPileS for small shaking events), the pile settlement during reconsolidation was much smaller than the settlement caused during shaking. The settlement of the piles during reconsolidation (i.e., downdrag settlement) from all the shaking events in the two centrifuge model tests SKS02 and SKS03 was less than 10 mm (i.e., 1.6% of pile diameter) [Table 2.6 and Table 2.7]. Smaller downdrag settlement shows that drag loads do not control the pile's performance unless structurally overloaded. It is the pile settlement during shaking that governs the performance of the pile.

The piles plunged when the mobilized tip load was near or exceeded the reduced pile tip capacity due to the increased free-field excess pore pressures near the tip. For example, the large shaking events EQM5 and EQM6 in centrifuge model test SKS02 generated relatively large free-field excess pore pressures near the 0DPile's tip, causing plunging of the pile into the soil [Figure 2.13 (a)]. Similarly, in centrifuge model test SKS03, the heavily loaded 3DPileL (during shaking event EQM_3 and EQM_5) and medium loaded 3DPileM (during shaking event EQM_4) plunged in soil [Figure 2.13 (b)]. This plunging failure in the piles occurred when the tip load exceeded the reduced tip capacity. Knappett and Madabhushi (2009) used load measurements from a series of centrifuge tests on liquefiable soils and proposed an empirical model [Equation 2.1] to estimate the reduced pile tip capacity in liquefying soil $\left(Q_{t,ult}^{r_u}\right)$ as a nonlinear function of free-field excess pore pressure ratio (ru) in near pile's tip.

$$Q_{t,ult}^{r_u} = Q_{t,ult}^{o}(1 - r_u)^{\alpha_t}$$

$$\alpha_t = \frac{3 - sin\phi'}{3(1 - sin\phi')} \qquad 2.1$$

where $Q^{o}_{t,ult}$ is the ultimate tip capacity when $r_u = 0$, α_t is a constant that, according to Knappett and Madabhushi (2009), depends only on ϕ', the effective friction angle of the soil at the tip. In the performed centrifuge model tests, the effective friction angle of the soil at the tip was $\phi' = 30^o$ which resulted in constant $\alpha_t = 0.55$. Figure 2.14 shows the mobilized pile tip load (Q_t) and the associated settlement in piles as a result of the reduced pile tip capacity $\left(Q^{r_u}_{t,ult}\right)$ from the increased free-field excess pore pressure ratio (r_u) near the tip for all the shaking events of centrifuge model tests SKS02 and SKS03. From the figure, it can be observed that when the mobilized pile tip load (Q_t) was within the reduced pile tip capacity $\left(Q^{r_u}_{t,ult}\right)$, the associated settlement in piles were small. However, when the mobilized tip load (Q_t) was near the reduced tip capacity $\left(Q^{r_u}_{t,ult}\right)$, the piles plunged and suffered significant settlements [Figure 2.14]. For example, for the heavily loaded 3DPileL for shaking events EQM_4 and EQM_5, the mobilized tip load exceeded the reduced pile tip capacity resulting in plunging of the pile [Figure 2.14, Figure 2.13 (b)]. On the other hand, for the lightly loaded piles 3DPileS and 5DPile, the mobilized tip load was always within the reduced pile tip capacity and thus suffered smaller settlements during shaking.

The magnitude of pile settlement was less than free-field settlement in all cases except when the tip load approached the reduced tip capacity, i.e., when pore pressures increased, in the end, bearing stratum. Figure 2.15 compares total soil and pile settlement at the end of each shaking event of the centrifuge model tests SKS02 and SKS03. For most of the shaking events, the settlement of the piles was smaller than the ground settlement. Only for large shaking events when the tip capacity significantly reduced and caused plunging of the piles, the pile settlement was greater than the soil.

Table 2.6. Summary of soil and pile settlements (during shaking, during reconsolidation, and total settlement) for all the shaking events of centrifuge model test SKS02.

Events	*During Shaking* [a]			*During Reconsolidation*			*Total Settlement*		
	Surface	*0DPile*	*5DPile*	*Surface*	*0DPile*	*5DPile*	*Surface*	*0DPile*	*5DPile*
EQM_1	2	0	0	1	0	0	3	0	0
EQM_2	14	6	3	6	0	0	20	6	3
EQM_3	13	10	1	57	2	2	70	12	3
EQM_4	12	4	1	5	1	1	17	5	2
EQM_5	14	114	2	57	9	2	71	123	4
EQM_6	19	54	7	53	6	2	72	60	9

[a] *about 30 seconds for EQM_1-EQM_5 and about 70 seconds for EQM_6*

Table 2.7. Summary of soil and pile settlements (during shaking, during reconsolidation, and total settlement) for all the shaking events of centrifuge model test SKS03.

Events	*During Shaking* [a]				*During Reconsolidation*				*Total Settlement*			
	Surface	*3DPileS*	*3DPileM*	*3DPileL*	*Surface*	*3DPileS*	*3DPileM*	*3DPileL*	*Surface*	*3DPileS*	*3DPileM*	*3DPileL*
EQM_1	27	0	2	5	11	4	6	6	38	4	8	11
EQM_2	40	4	6	16	16	4	4	4	56	8	10	20
EQM_3	55	4	8	28	20	0	4	2	75	4	12	30
EQM_4	45	2	30	200	35	6	5	8	80	8	35	208
EQM_5	46	5	220	700	34	5	10	10	80	10	230	710

[a] *about 30 seconds for EQM_1-EQM_3 and about 70 seconds for EQM_4-EQM_5*

2.7 Discussion on Drag Loads

With multiple shakings, the magnitude of drag load was observed to increase in these centrifuge tests. For each shaking event, the drag load on the piles first decreased during shaking and increased during reconsolidation, eventually exceeding the value before shaking [Figure 2.10 (f,g), Figure 2.11 (f,g,h)]. The pile head load (Q_f), load at the neutral plane (Q_{np}), drag load (Q_{drag}), and tip load (Q_t) for 0DPile and 5DPile after each shaking event and centrifuge spin up are summarized in Figure 2.16. The axial load profiles in the piles after each shaking event in centrifuge model test SKS02 and SKS03 are shown in Figure 2.17. It can be seen from the figures that while the initial static neutral plane depth in the piles remained almost the same across all shaking events, the drag loads kept on increasing [Figure 2.16, Figure 2.17]. For example, shaking events (EQM_1, EQM_2, and EQM_3) in centrifuge model test SKS02, after Spin up 1, increased drag loads from 250 kN to 500 kN in the 0DPile and 700 kN to 1100 kN in the 5DPile. The increased drag loads also increased the mobilized pile tip load [Figure 2.16, Figure 2.17]. This increase in drag load could be due to the gradual increase of the effective lateral stress during reconsolidation. It remains to be confirmed whether the increase in lateral stress is due to dilatancy of the soil adjacent to the pile producing increased lateral stresses locally around the pile or an artifact of the centrifuge model container flexibility. Another possible mechanism could be the increased stiffness of tip (due to soil stronger or increase in embedment from pile settlement) in each successive event resulting in small downdrag settlement and larger drag load. The mechanism of the increase of drag loads with successive shaking events should continue to be investigated. Shaking events (EQM_4, EQM_5, and EQM_6) after Spin Up 2 also increased drag loads in the piles. It increased from 150 kN to 500 kN in the 0DPile and about 700 kN to 1100 kN in the 5DPile. However, for the 5DPile, the drag load and the axial load distribution for shaking events EQM_5

and EQM_6 remained almost the same [Figure 2.16, Figure 2.17 (a)]. The drag load for the 5DPile may have achieved saturation at about 1100 kN, which could have resulted from the full mobilization of interface skin friction and stabilization of lateral stresses. The developed drag load was higher for the deeply embedded or lightly loaded (resulting in higher static factors of safety) piles. The deeply embedded 5DPile developed a much higher drag load than 0DPile [Figure 2.16, Figure 2.17]. Among all the 3DPiles, 3DPileS with a higher static factor of safety developed the largest drag load [Figure 2.17].

Centrifuge spin down and spin up changed drag load on the piles. After shaking event EQM_3, the centrifuge was stopped, and the pile head mass for the 0DPile was increased (from 500 kN to 1000 kN). The model was then left overnight, causing the soil to rebound at 1-g. The next day after spinning up the centrifuge (spin up 2), the drag loads developed in the 0DPile and 5DPile were less than they were after the shaking event EQM_3, while the neutral plane depth developed at the same depth as before. The decrease in drag load from centrifuge spin down and spin up can be explained by changes in the lateral stresses caused by stopping and starting the centrifuge. As may be expected, for the 0DPile, the increase in pile head load from 500 kN to 1000 kN resulted in a smaller developed drag load during spin up 2 than during Spin up 1. The developed drag load in the 0DPile after Spin up 2 was about 150 kN compared to 250 kN after Spin up 1. On the other hand, for the 5DPile (with no head load changed), the developed drag load was 700 kN, equal to the drag load after Spin up 1.

While estimating the exact lateral stresses developed at the interface is difficult, the results suggest that liquefaction-induced downdrag can mobilize negative skin friction equal to the interface shear strength. A conceptual limit load curve (see description in Section 2.3) was drawn to compare the axial load profile of the piles obtained after complete reconsolidation [Figure 2.17].

The conceptual limit load curve (indicated by dashed continuous lines) was found to envelop all the piles' axial load profiles. Please note that the discrepancy that appears for 3DPileL is likely due to the inaccurate axial load measurements being severely affected by the aforementioned cross-sensitivity in the axial gages as described in Section 2.5 [Figure 2.17 (b)]. Such large development of shear stresses in the clay layer and loose sand layer is practically impossible.

The development of negative skin friction requires small relative movements (about 5 millimeters) between the soil and pile (Rituraj and Rajesh 2022). The medium shaking events EQM_2 and EQM_4 of centrifuge model test SKS02, even though they did not fully liquefy the loose sand layer ($r_u \approx 50\%$), resulted in the development of negative skin friction and thus the drag loads on piles [Figure 2.16, Figure 2.17 (a)]. However, the increase in the drag load was smaller in magnitude when compared to the large shaking events (EQM_3, EQM_5, and EQM_6) [Figure 2.16]. The total soil settlement caused by the medium shaking events was about 15-20 mm [Table 2.6]. In centrifuge model test SKS03, about 20-30 mm of soil settlement (during reconsolidation) achieved full drag load on piles [Table 2.7]. During the pile load test [Figure 2.7], the penetration of the pile by about 20 mm (i.e., about 3% of pile's diameter) completely removed the initial drag load on 3DPileS. Fleming et al. (2008) suggest that displacements of 0.5% to 2% of the pile's diameter are required to mobilize skin friction completely. Results from pile load tests, particularly on drilled shafts (of diameter < 2 m), show that the skin friction is fully mobilized at a relatively small displacement in the order of 10 to 30 mm, depending on the soil's D_R (O'Neill 2001). The above results show that even when the soil layers do not fully liquefy, settlements caused by the dissipation of excess pore pressures, exceeding a small percentage of the pile diameter, would be enough to mobilize negative skin friction and thus drag loads in a pile. Viewed another way, the 20 mm of soil settlement also corresponds to a displacement equal to 2.5 times the median grain diameter (D_{50}) of sand used in the test. DeJong and Westgate (2009) and Martinez and Frost (2017) suggested an interface shear band thickness of 5–7 particle diameters adjacent to the interface. Assuming that the elastic settlement in the shear band with respect to the free field soil settlement is small, a displacement of 2.5 D_{50} would produce a shear strain of 50% (assuming a shear band thickness of 5 D_{50}) which would likely be enough to mobilize the significant negative skin friction at the pile's interface.

2.8 Summary and Conclusions

Two large centrifuge model tests were conducted to study liquefaction-induced downdrag on piles. The models contained a total of five heavily instrumented piles with an outer diameter of 635 mm, and their tips embedded different distances below a liquefiable layer into an end-bearing stratum of dense sand. Nine strain gages were installed inside the inner diameter to measure the axial load distribution along the length of the piles. The piles were made rough to achieve maximum interface shear strength. The models consisted of two different soil profiles with liquefiable layers and interbedded deposits. The model was shaken with multiple scaled (small, medium, and large) Santa Cruz earthquake motions, and the developed downdrag was monitored. Results from these experiments presented in this chapter illuminate the mechanisms and sequences of the evolution of liquefaction-induced downdrag, drag load, and soil and pile settlement.

Some interesting pore pressure dissipation patterns were observed due to the interbedded soil layering (sand and clay/silt layers). During reconsolidation, the excess pore pressure quickly equalized within the sand layer. However, the overlying impermeable clay layer hindered the drainage and led to the formation of a water film beneath it. At this state, excess pore pressures in the soil at all depths "equalized" at a value equal to the effective stress beneath the clay layer.

Ultimately, the water film dissipated, and excess pore pressures returned to zero within the next 45 – 60 minutes.

Some of the main findings from the centrifuge model tests, which should be accounted for in pile design, are described below.

- Settlements in the order of 1 - 3% of the pile diameter in the soil relative to the pile are sufficient to mobilize significant negative skin friction.
- Complete liquefaction ($u_e = \sigma'_v$, $r_u = 1.0$) is not a prerequisite to the development of significant drag loads. Significant drag loads were developed for shaking events that produced excess pore pressures as low as 50% of the initial effective stress (i.e., $r_u \approx 0.5$). Results showed that after reconsolidation, the developed negative skin friction could equal the interface shear strength ($\tau = K\, \sigma'_v \tan(\delta)$) for both the non-liquefied ($r_u < 1.0$) as well as liquefied soils ($r_u = 1.0$). These conclusions are different from those reported by Rollins and Strand (2006). From a limited number of blast-induced liquefaction field tests, they observed the magnitude of the negative skin friction in the reconsolidated liquefied (i.e., $r_u = 1.0$) layer to be 50% of the positive skin friction before shaking. They do not provide any physics-based explanation as to why negative skin friction should be limited. Furthermore, their recommendations are countermanded by the centrifuge tests on five piles with different end bearing conditions, each subject to multiple ground motions and different extents of liquefaction reported herein. Therefore, we recommend that the negative skin friction taken as equal to 50% of mobilized positive skin friction should not be considered and extrapolated to the entire domain of design scenarios.
- During shaking, excess pore pressures generated in the liquefiable layer reduced the negative skin friction, decreasing the drag loads and ultimately diminishing it to zero at complete

liquefaction ($u_e \approx \sigma'_v$). However, as pore pressures dissipated, the drag loads again increased, approaching or surpassing the drag load that existed before shaking.

- Most of the pile settlement occurred during shaking when the excess pore pressures in the soil around the pile resulted in the loss of shaft and tip capacity and their stiffness. As such, the 5DPile embedded deep into the dense sand layer suffered tiny settlements throughout all shaking events. On the other hand, the 0DPile embedded barely in the dense sand layer suffered significant settlements in each shaking event. Among the 3DPiles, the 3DPileL with the largest head load settled the most. Comparatively, the post-shaking settlement of the piles was small (< 10 mm). For design, it would be recommended to check the settlement of piles for both the scenarios (1) for the generated inertial loads during shaking with the reduced shaft and tip resistance from the excess pore pressures present near the shaft and the tip even if full liquefaction does not occur (i.e., $0 < r_u < 1$); and (2) from the development of drag load following soil reconsolidation combined with applicable structural loads. Furthermore, since most of the pile settlement occurs during shaking, if feasible, piles can be embedded deep into the bearing layer and thus maximizing their resistance and minimizing their settlement during shaking. Therefore, compared to liquefaction mitigation strategies, increasing the embedment of the pile could provide a cost-effective strategy to reduce pile settlements.
- Pile settlements are generally smaller than the free-field soil settlement if the tip capacity does not significantly decrease due to increased pore pressures near the pile's tip in the bearing layer. While designing piles in liquefiable soils, pile settlement should also be considered in the context of free field settlements. In some cases, especially where settlements are of the order of inches, settlement of piles close to free-field soil settlements may improve post-earthquake functionality of the superstructure (for example, in bridges). It is possible that if

> free-field settlement is (let us say) about 4 inches, the bridge would be functional if the pile settlement was 2 inches. However, the bridge would be closed if the pile settlement was 0 inches – due to the differential settlement between the bridge and the approach slab. Perhaps there should be separate serviceability criteria for total and differential pile settlement.

Results from the centrifuge model tests illuminated the mechanics of liquefaction-induced downdrag on piles through a simplified soil profile and allowed for some important conclusions to be made about how the various processes in this phenomenon interact and affect each other. The next chapter describes the development and validation of a numerical modeling approach for modeling liquefaction-induced downdrag on piles.

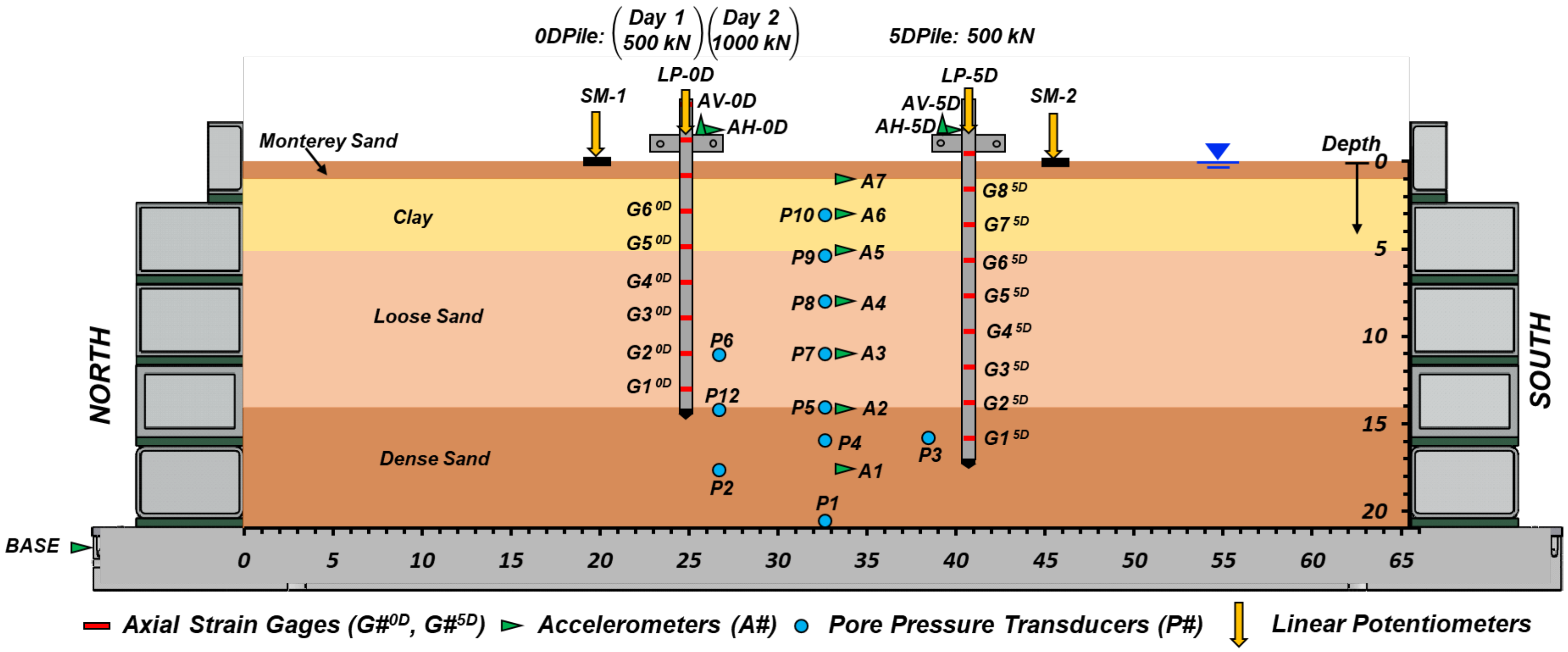

Figure 2.1. Cross-section view of the centrifuge model test SKS02.

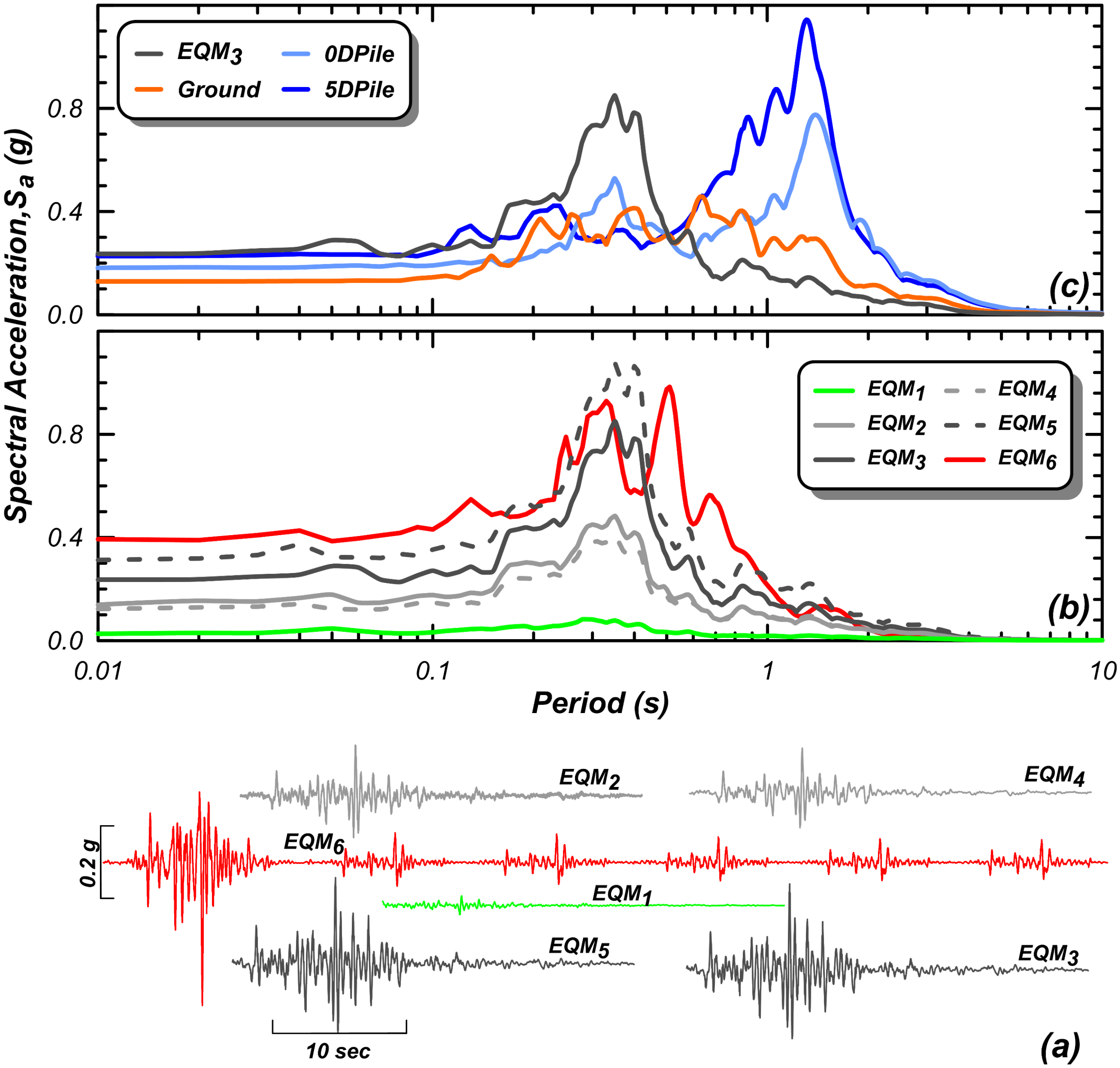

Figure 2.2. Earthquake motions used in centrifuge model test SKS02: (a) time histories of applied earthquake motions, (b) spectral accelerations of applied earthquake motions, and (c) spectral accelerations recorded for input motion (EQM_3) at the base of the model, the model surface, and the 0DPile and 5DPile.

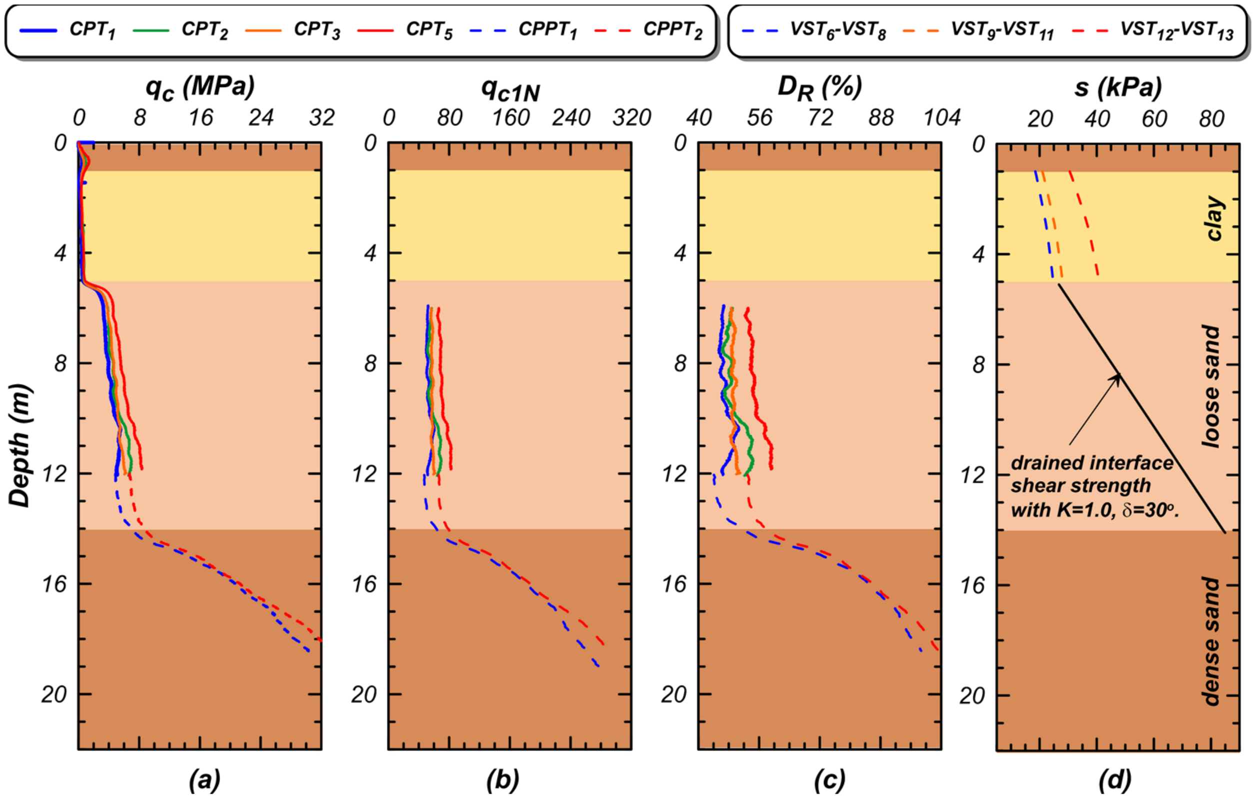

Figure 2.3. Results from soil investigation conducted on centrifuge model test SKS02 at various times (see Table 2.3) during the test.: (a) Cone tip resistance (q_c), (b) normalized overburden corrected cone tip resistance (q_{c1N}), relative density (D_R) and shear strength (s) interpreted from cone penetration tests (CPT), centrifuge pile penetration test (CPPT), and vane shear tests (VST).

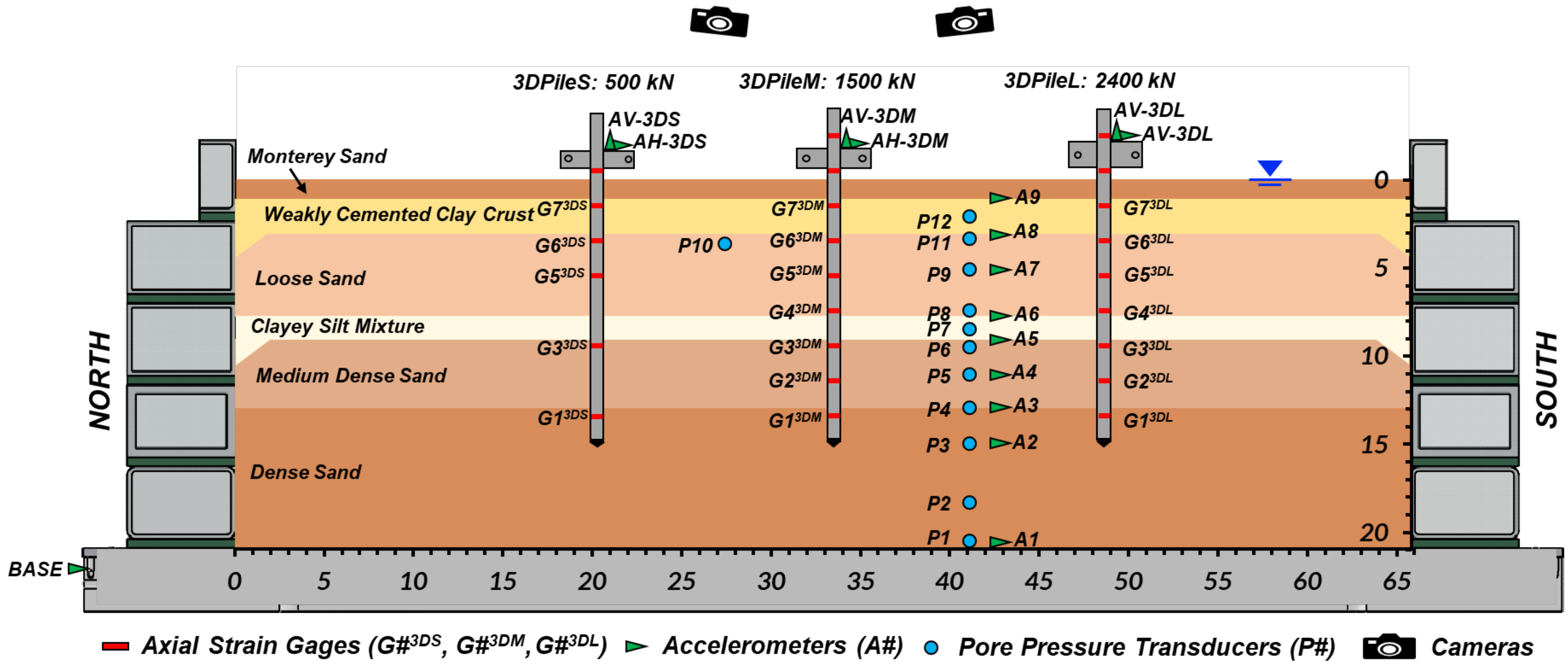

Figure 2.4. Cross-section view of the centrifuge model test SKS03.

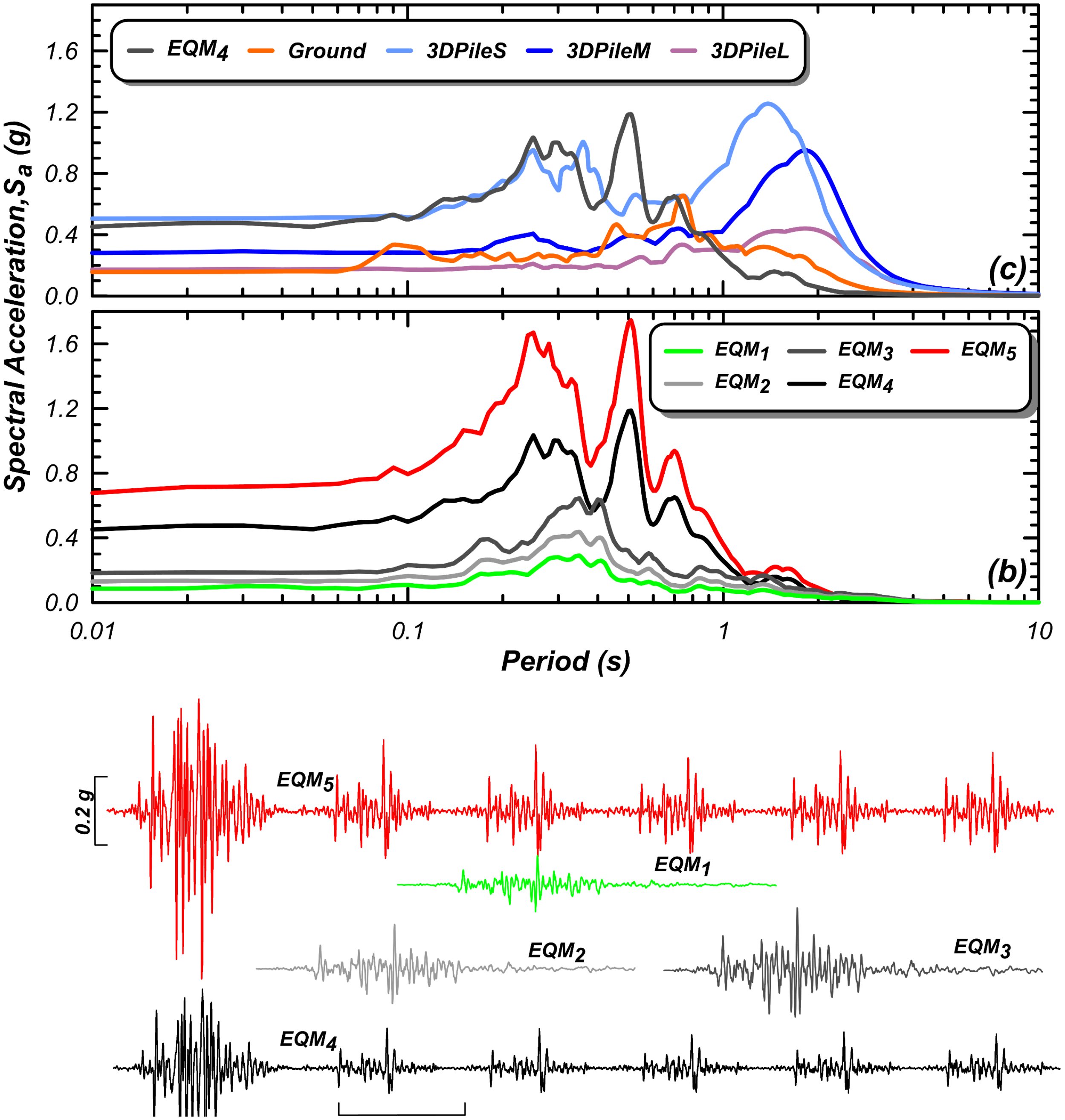

Figure 2.5. Earthquake motions used in centrifuge model test SKS03: (a) time histories of applied earthquake motions, (b) spectral accelerations of applied earthquake motions, and (c) spectral accelerations recorded for input motion (EQM4) at the base of the model, the model surface, and the 3DPileS, 3DPileM, and 3DPileL.

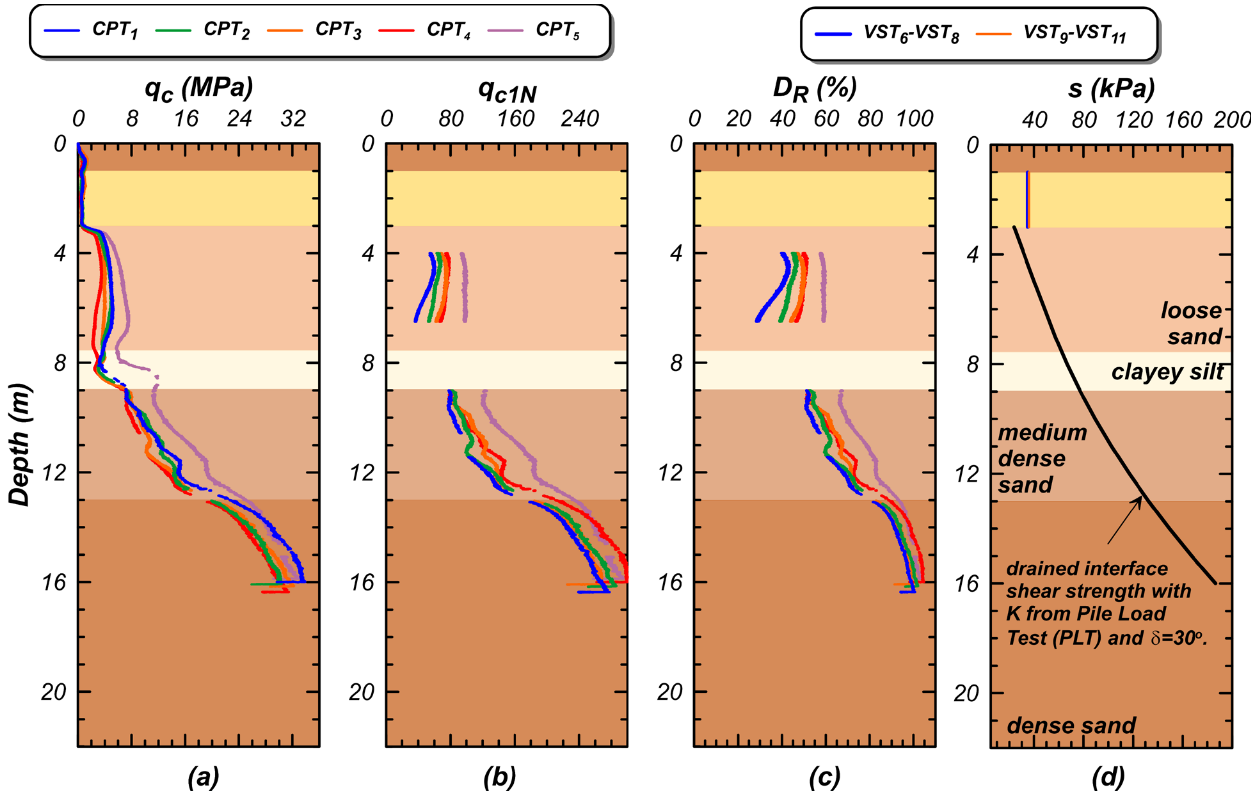

Figure 2.6. Results from soil investigation conducted on centrifuge model SKS03 at various times (see Table 2.5) during the test.: (a) Cone tip resistance (q_c), (b) normalized overburden corrected cone tip resistance (q_{c1N}), relative density (D_R) and shear strength (s) interpreted from cone penetration tests (CPT), pile load test (PLT), and vane shear tests (VST).

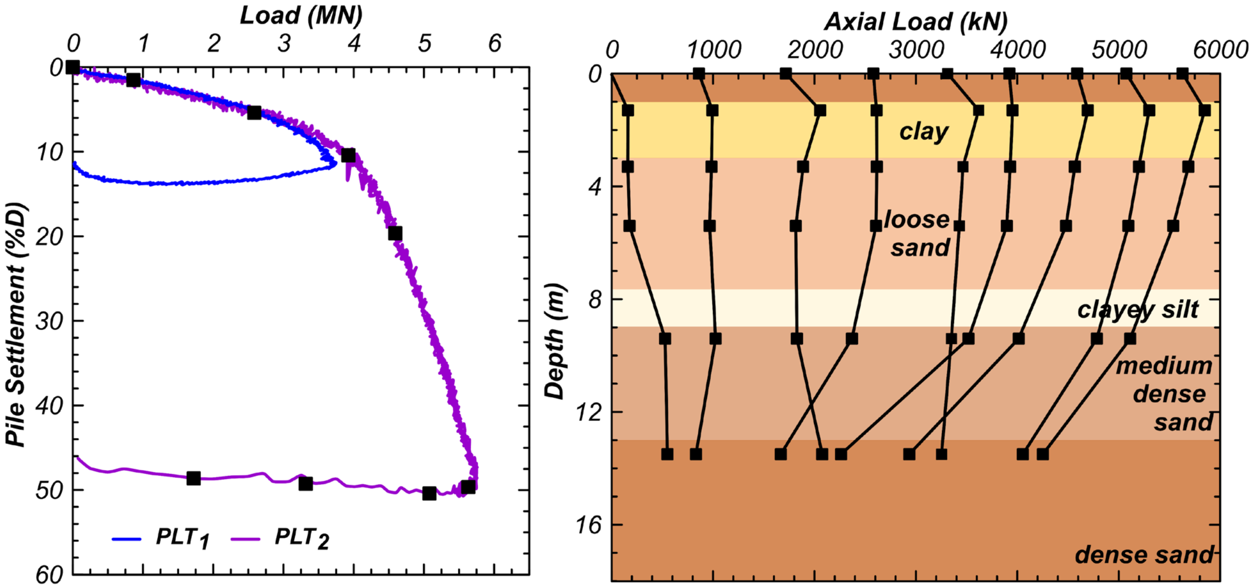

Figure 2.7. Results from pile load tests (PLT$_1$ and PLT$_2$) performed on 3DPileS during centrifuge model test SKS03.

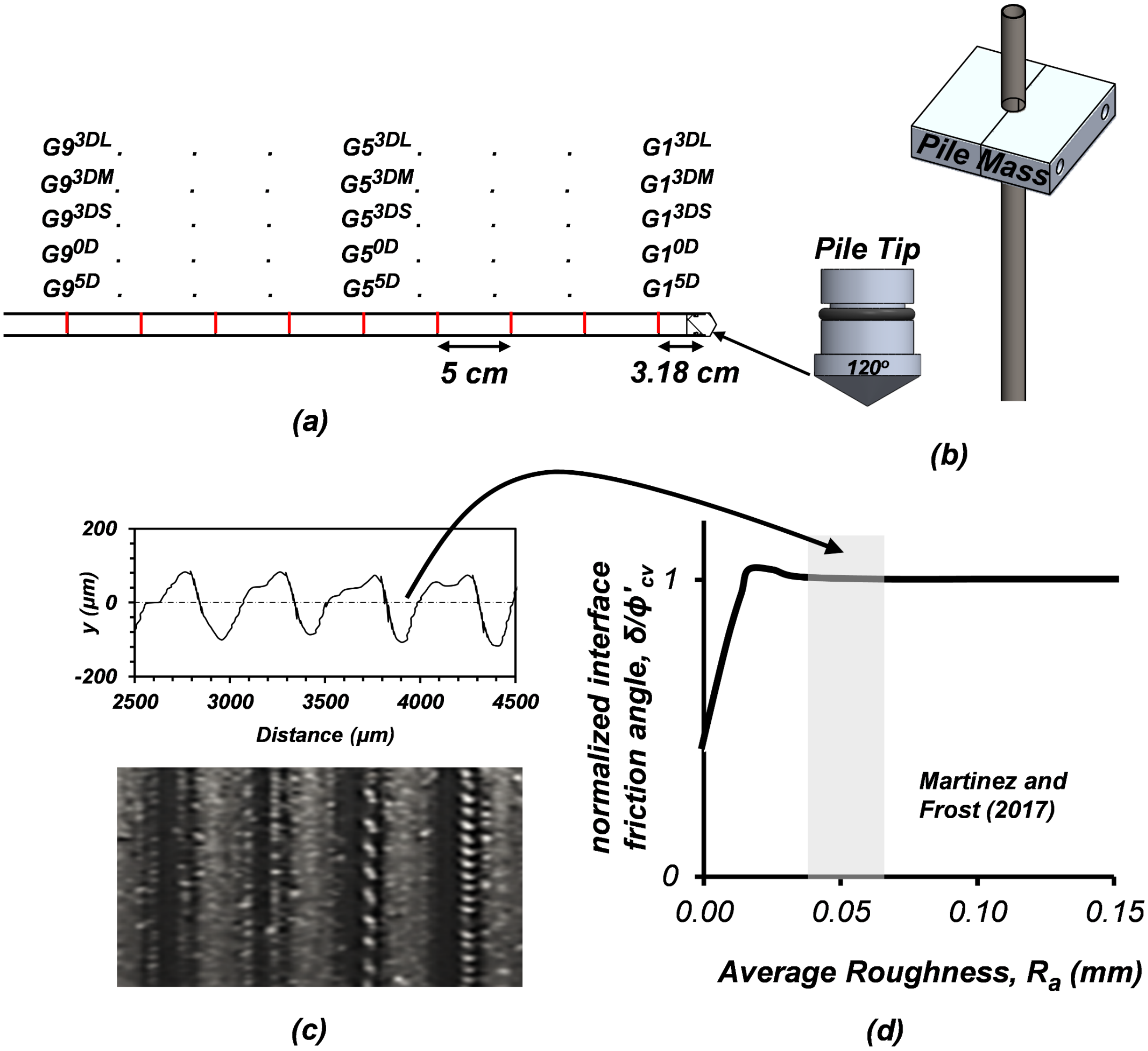

Figure 2.8. Instrumented model pile (a) with nine internally installed full-bridge axial strain gages, (b) model pile mass and pile tip apex angle of 120°, and (c) machined average interface average roughness (R_a) of 0.04 -0.06 mm enough to mobilize the (d) interface friction angle (δ) equal to the drained soil friction angle (ϕ'_{cv}).

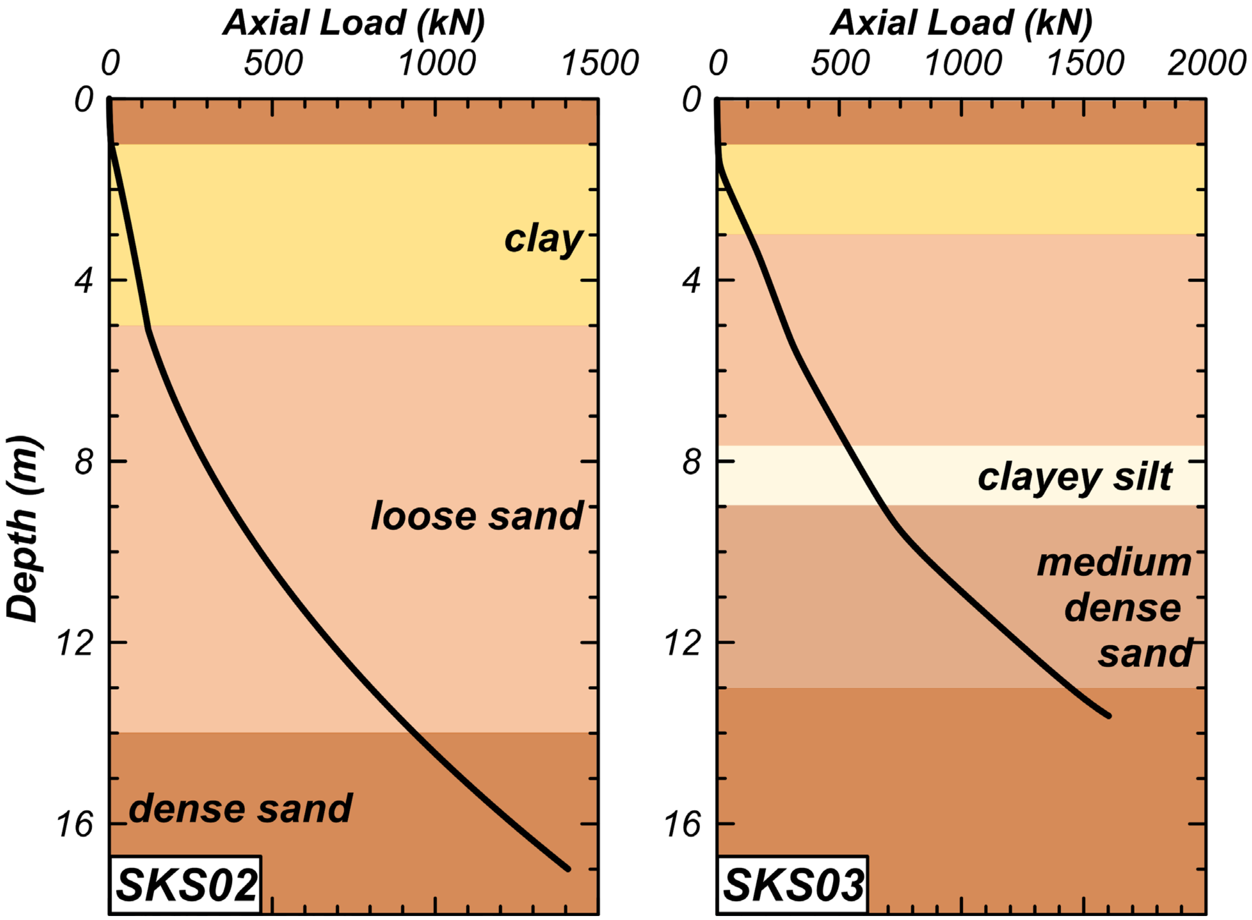

Figure 2.9. The limit load curves for the piles used in the centrifuge model tests SKS02 and SKS03 for zero pile head load.

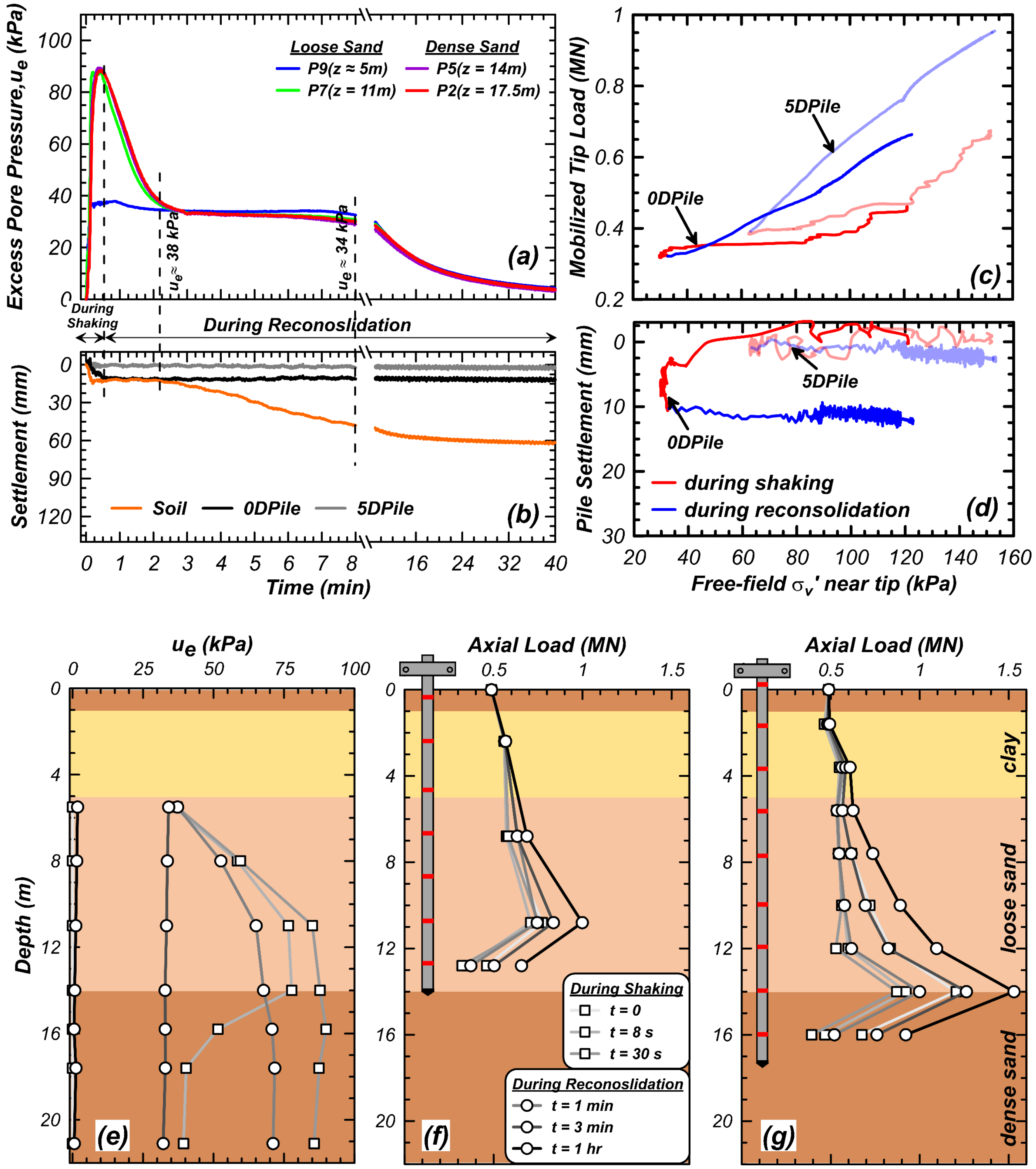

Figure 2.10. Results from shaking event EQM3 of centrifuge model test SKS02: Time histories of (a) excess pore pressures (u_e) and (b) soil and pile settlement. (c) Mobilized tip load and (d) pile settlement as free-field effective stress (σ'_v) changed near pile's tip. Isochrones of (e) u_e profile and axial load distribution in (f) 0DPile and (g) 5DPile during shaking and reconsolidation.

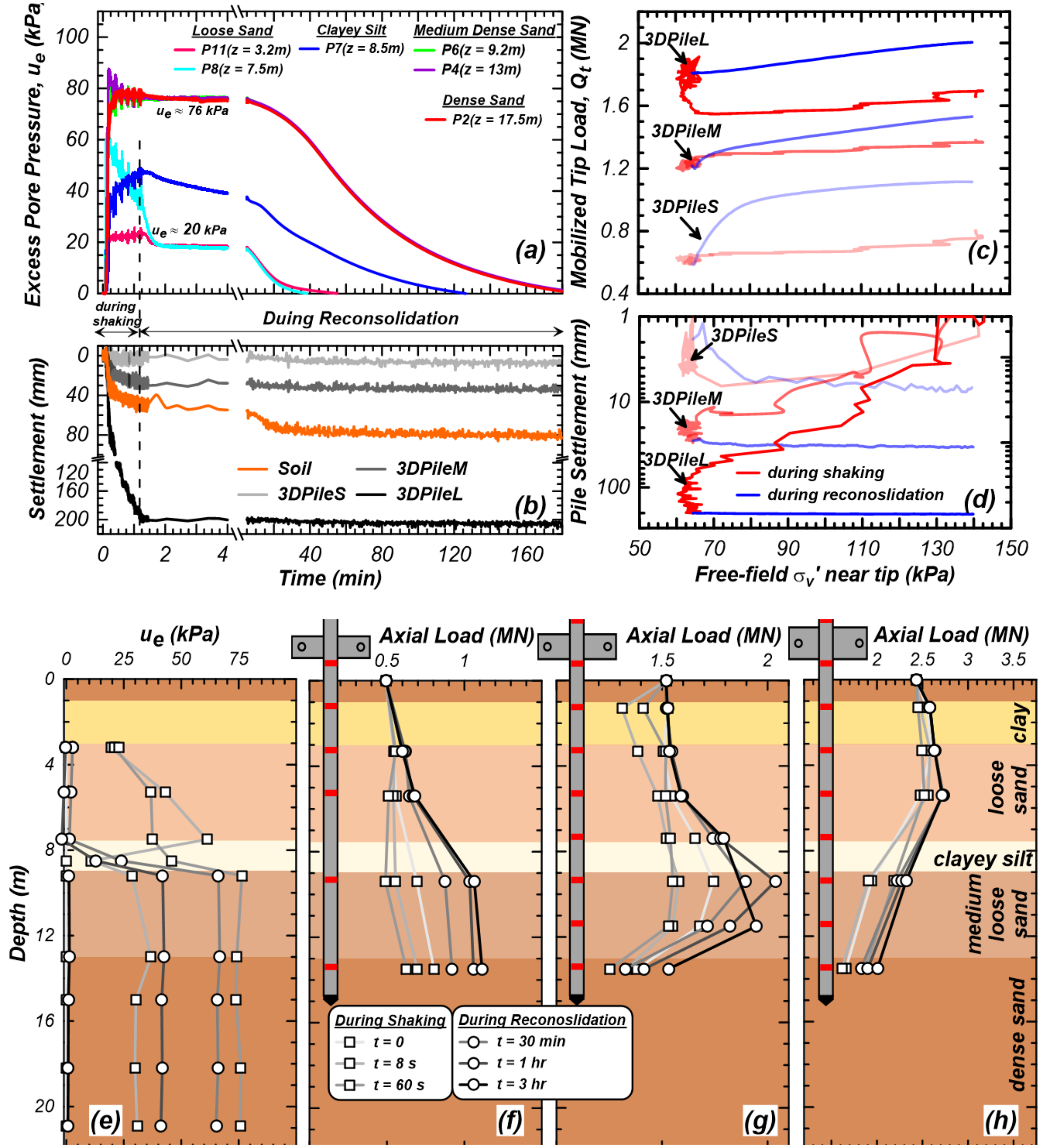

Figure 2.11. Results from shaking event EQM4 of centrifuge model test SKS03: Time histories of (a) u_e and (b) soil and pile settlement. (c) Mobilized tip load (Q_t) and (d) pile settlement as free-field effective stress (σ'_v) changed near the pile's tip. Isochrones of (e) u_e profile and axial load distribution in (f) 3DPileS, (g) 3DPileM, and (h) 3DPileL during shaking and reconsolidation.

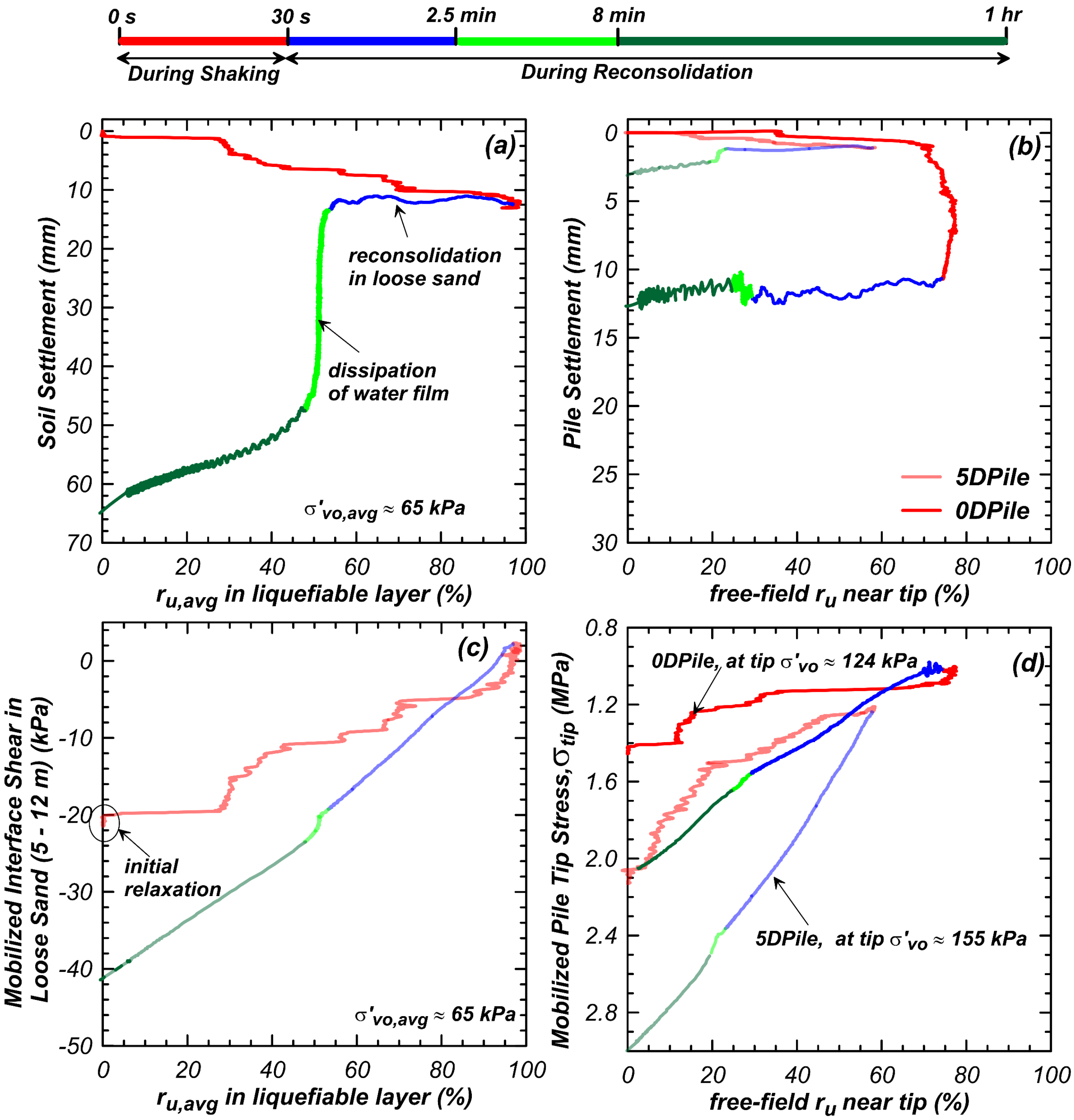

Figure 2.12. Development of (a) soil and (b) pile settlement, (c) average mobilized interface shear stress in the liquefiable layer (5-12 m), and (d) pile tip stress in the presence of excess pore pressure in the soil during and after event EQM$_3$. Shaking ends at (t = 30s), equalization of excess pore pressures ($u_e \approx$ 38 kPa) is first achieved at t ≈ 2.5 minutes, the water film beneath the clay layer disappears at t ≈ 8 minutes, and complete reconsolidation (>98%) is achieved at about t = 1 hr.

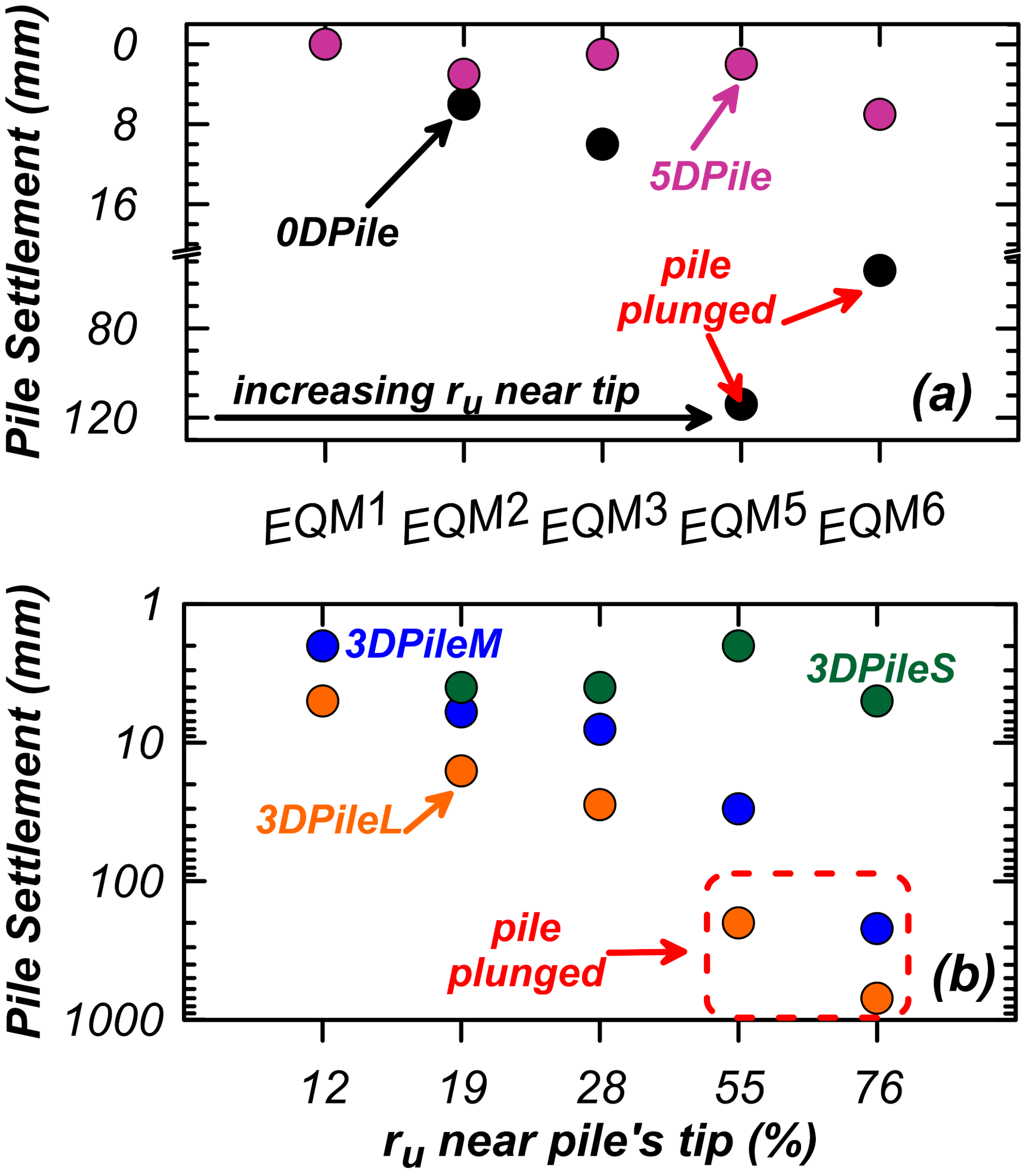

Figure 2.13. Summary of pile settlement during shaking as an effect of free-field excess pore pressure ratio (r_u) near the pile's tip for centrifuge model tests: (a) SKS02 and (b) SKS03.

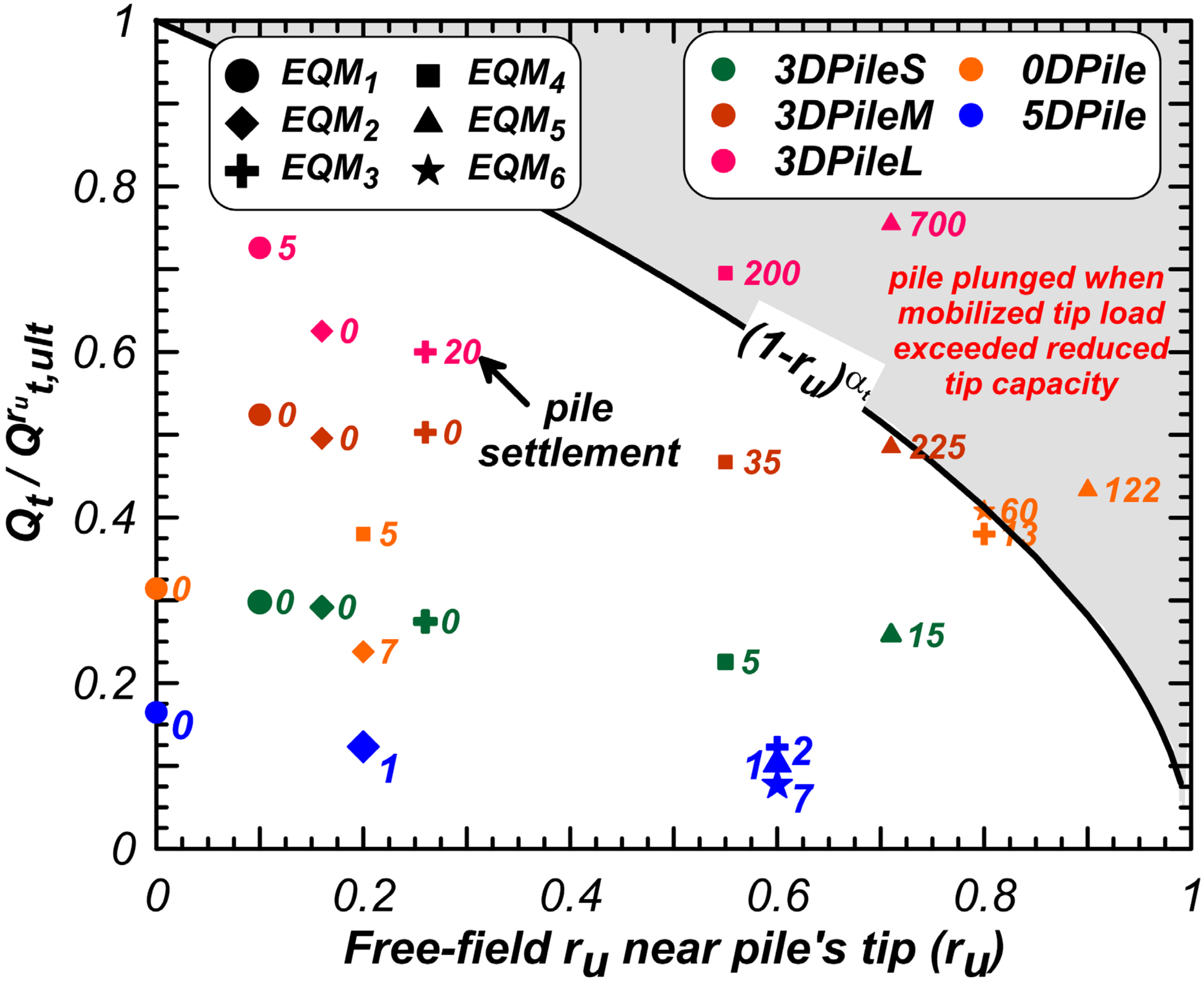

Figure 2.14. Summary of pile settlement during shaking resulting from the mobilization of tip load (Q_t) and reduced tip capacity ($Q_{t,ult}^{r_u}$) caused from increased free-field excess pore pressure ratio (r_u) near the pile's tip during shaking events of centrifuge model tests: SKS02 and SKS03.

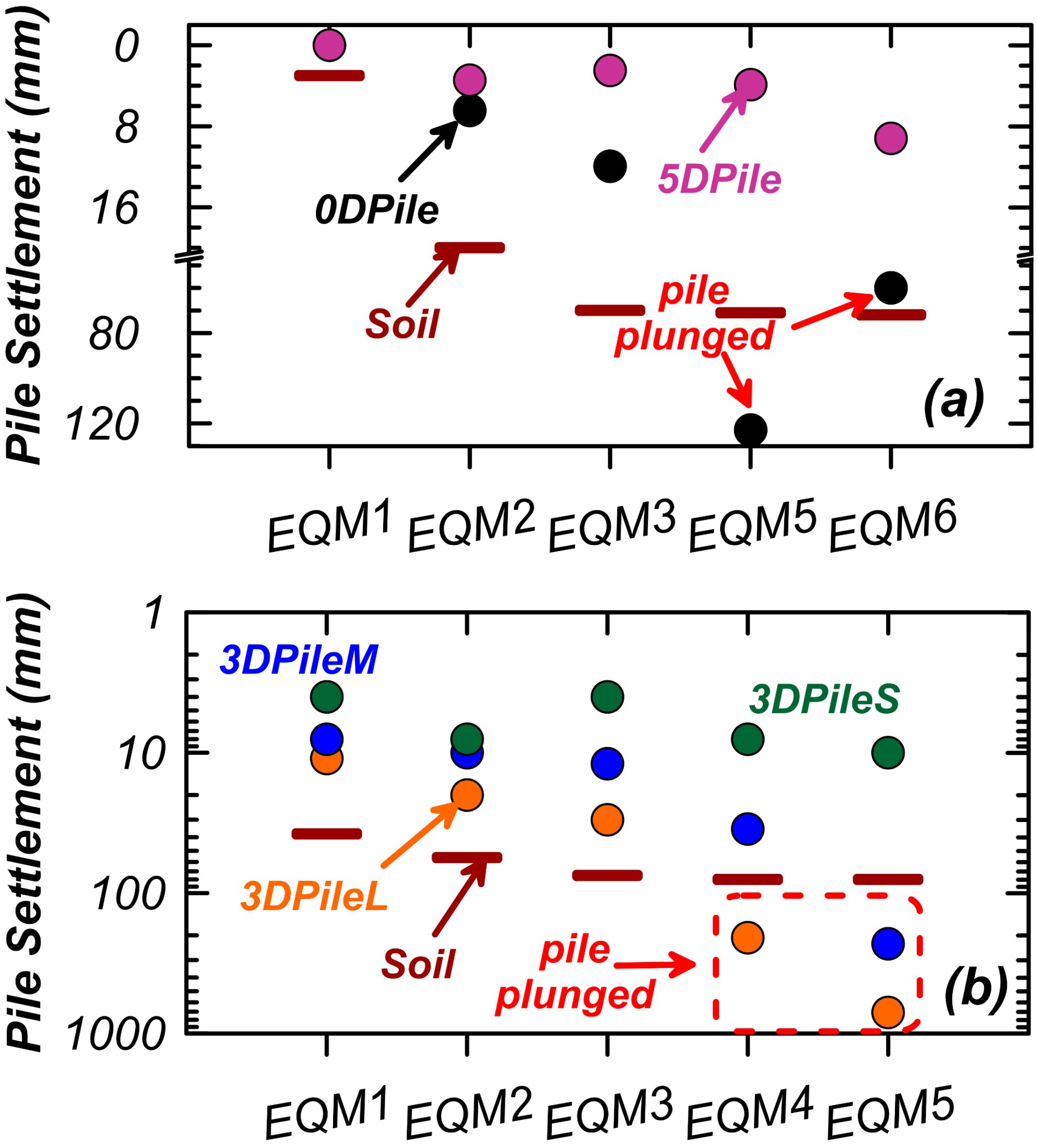

Figure 2.15. Summary of the total pile and soil settlement at the end of each shaking events of centrifuge model tests: SKS02 and SKS03.

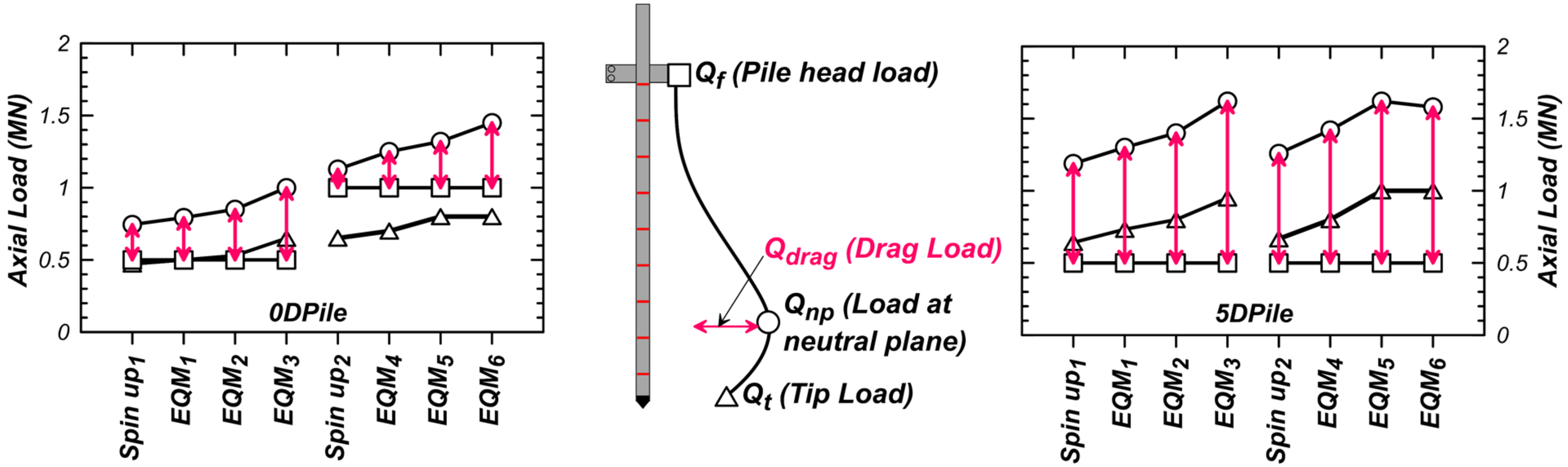

Figure 2.16. Summary of axial load distribution in piles for centrifuge model test SKS02: Pile head load (Q_f), developed drag load (Q_d), and mobilized pile tip load (Q_{tip}) after reconsolidation from centrifuge spin up (1 and 2) and reconsolidation from shaking events EQM$_1$-EQM$_6$.

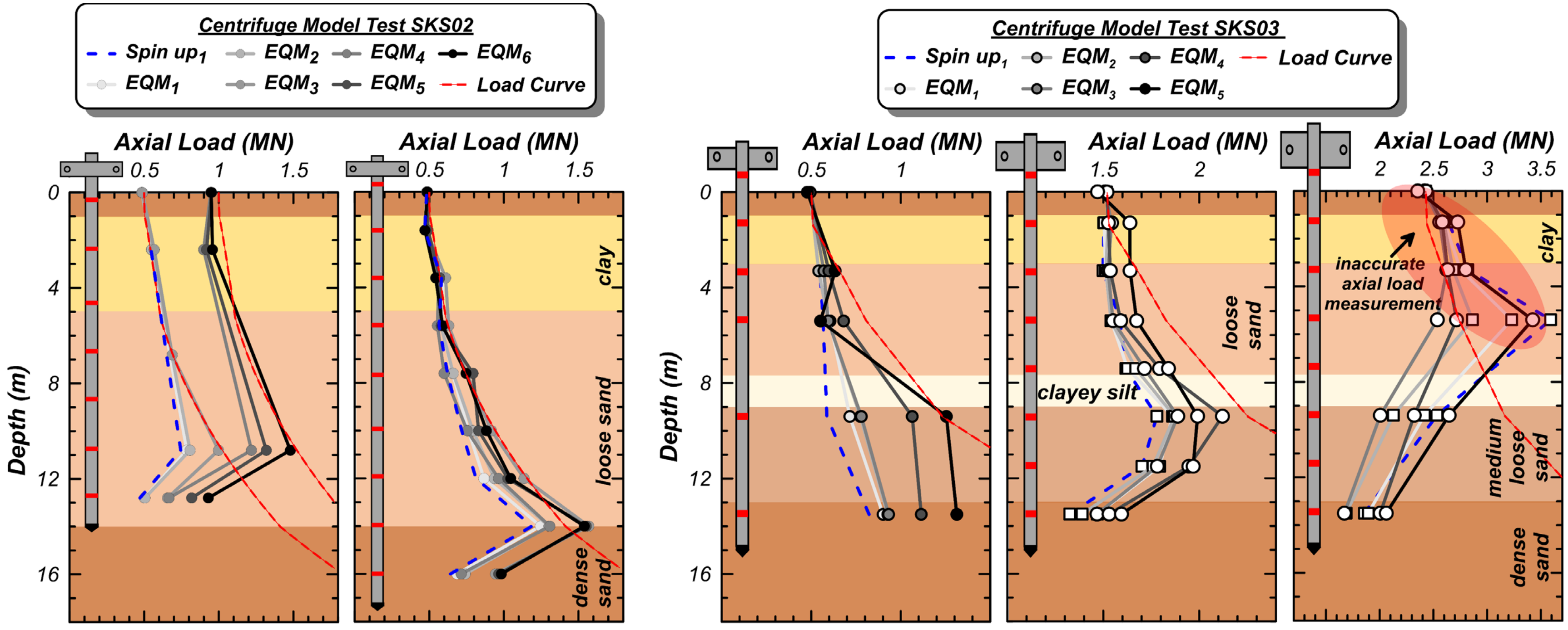

(a) (b)

Figure 2.17. Summary of axial load distribution in piles for centrifuge mode tests (a) SKS02 and (b) SKS03 after consolidation from centrifuge spin up and reconsolidation from shaking events EQM_1-EQM_6.

CHAPTER 3:

NUMERICAL MODELING AND VALIDATION

3.1 Introduction

Various methods have been developed to account for the development of drag loads and estimate pile settlement in liquefiable deposits. Out of all, the neutral plane solution method (Fellenius 1972) has been most widely used. Fellenius and Siegel (2008), Vijayaruban et al. (2015), Muhunthan et al. (2017), and Fellenius et al. (2020) used the unified pile design method (Fellenius 2004) with zero negative skin friction in the liquefied zone to model liquefaction-induced drag load. In this method, the mobilized negative skin friction in the non-liquefiable layer is taken as equal to the interface shear strength. Rollins and Strand (2006) recommend taking the negative skin friction in the liquefiable layer as 50% of the positive skin friction before shaking. AASHTO (2020) and Caltrans (2020) recommend taking the negative skin friction equal to the "residual soil strength" in the liquefiable layer. The Federal Highway Administration (FHWA – Hannigan et al. 2016) recommends using the neutral plane method with t-z and q-z springs calibrated from field tests. All the methods described above model the liquefiable layer as a consolidating layer with a defined strength without considering the effects of the event sequencing and the pattern of excess pore pressure dissipation, the soil settlement, and the evolution of soil shear strength during reconsolidation. Boulanger and Brandenberg (2004) modified the neutral plane method to account for the timing of the soil settlement and dissipation of excess pore pressures in liquefiable layers. The method accounted for the changes of shaft friction in the reconsolidating liquefied layer as a linear variation of excess pore pressures (1-ru). However, it did not provide a model to account for changes in the tip resistance as excess pore pressures develop and dissipate in the soil around the tip. As such, improvements are required to be able to model the mechanism of liquefaction-induced downdrag which can be further used to study and identify the controlling factors affecting the magnitude of drag load and pile settlement.

This chapter describes the development and validation of a TzQzLiq numerical model for capturing liquefaction-induced downdrag on piles. The TzQzLiq model uses zero-length elements and the existing TzLiq material and a new QzLiq material to account for changes in the shaft and tip capacity of the pile and their stiffness as free-field excess pore pressures develop/dissipate in the soil. The paper first describes the selection of input parameters, the development of the QzLiq material, and the calibration process. Results from a series of centrifuge model tests on piles with different tip embedments and pile head loads are then introduced. The mechanism of liquefaction-induced downdrag on piles and the effect of an impermeable soil layer on the dissipation of excess pore pressure causing the impedance of drainage, equalization of excess pore pressures, and water film formation is illustrated. Procedures for obtaining the necessary information from the test data are described, which are later used to model the centrifuge test piles and validate the numerical model against the corresponding centrifuge data. Additionally, a sensitivity study of the properties of the TzLiq and QzLiq materials is performed to study their effect on the developed drag load and pile settlement.

3.2 Description of TzQzLiq Numerical Model

A TzQzLiq numerical model using TzLiq and new QzLiq materials [Figure 3.1 (a)] with zero-length elements is developed to model the response of piles in liquefiable soils. The model accounts for changes in the shaft (using a TzLiq material) and tip capacity (using a QzLiq material) of the pile as free-field excess pore pressures develop and dissipate in soil [Figure 3.1 (b)]. A dynamic time history analysis is performed using the effective stress [Figure 3.1 (c)] and soil settlement [Figure 3.1 (d)] profiles to simulate the response of the pile. The results of the model include the time histories of axial load distribution [Figure 3.1 (e)] and settlement of the pile [Figure 3.1 (f)]. The overall numerical modeling process is illustrated in Figure 3.1. The model input parameters (pile cross-section and material properties, pile head loads (Q_f), TzLiq and QzLiq material properties, effective stress (σ'_v) profiles, soil settlement profiles, and stages of modeling are described in the subsections below.

Pile Properties and Loads

The pile cross-section, its material properties, and the superstructure dead load acting on the pile are the required inputs for the model. If the pile experiences cyclic axial loads during earthquake shaking, then those can be considered by applying a time series load on the pile. A separate analysis of the superstructure response under the design earthquake is required to estimate those cyclic axial loads. AASHTO (2020) suggests methods for determining seismic loads on bridges and their foundations. For the present study, a linear elastic beam element is used to model the piles. If the axial loads exceed the elastic structural capacity of the pile, then nonlinear beam elements would be needed without affecting the remainder of the herein presented procedure.

TzLiq Material Properties

Boulanger et al. (1999) developed TzLiq material to model the reduction of the shaft capacity and shaft stiffness as a linear function of excess pore pressure ratio ($1-r_u$) [Equation 3.1].

$$t^{r_u}_{ult} = t^{o}_{ult}(1 - r_u) \qquad 3.1$$

where t^{o}_{ult} is the ultimate shaft capacity when $r_u = 0$, and r_u is the free-field excess pore pressure ratio around the shaft. The TzLiq material response is modeled as the constitutive response of t-z material scaled in proportion to the excess pore pressure ratio ($1-r_u$) (Boulanger et al. 1999). The initial elastic stiffness of the material is defined as $t^{o}_{ult}/2z_{50}$, where the constant z_{50} is the displacement required to mobilize 50% of the ultimate shaft capacity (t^{o}_{ult}). The constant z_{50} is kept independent of r_u resulting in the changes in the stiffness of the TzLiq material directly proportional to the change in its capacity ($t^{r_u}_{ult}$). Boulanger and Brandenberg (2004) used the TzLiq material to study the liquefaction-induced downdrag on piles in liquefiable soils.

The ultimate shaft capacity (t^{o}_{ult}) in soil layers can be obtained empirically using equations and correlations provided in AASHTO (2020) or can be calibrated from tests on interface shear strength and pile load tests. The z_{50} parameter essentially defines the stiffness of the shaft resistance. According to Fleming et al. (2008), displacements of 0.5% to 2% of pile diameter are required to mobilize the shaft resistance fully. Sinha et al. (2021f) performed a series of centrifuge model tests and found that small displacements in the order of 1-3% of the pile's diameter were sufficient to mobilize full skin friction in soil. The nonlinear backbone curve for t-z material (Boulanger et al. 1999; Mosher 1984; Reese and O'Neil 1987) is a hyperbolic curve that takes displacement equal to about four times z_{50} to mobilize >90% of the ultimate capacity (t^{o}_{ult}). Thus, a z_{50} of 0.2% – 0.5% of the pile diameter can be assumed for modeling the stiffness of the TzLiq material.

QzLiq Material Properties

During shaking, loss of tip capacity and stiffness from excess pore pressures in the soil can cause settlements of piles. During reconsolidation, any settlement at the tip affects the development of drag load. Knappett and Madabhushi (2009) used load measurements from a series of centrifuge tests on piles in liquefiable soils and proposed an empirical model [Equation 3.2] to estimate the pile tip capacity in liquefying soil ($q_{t,ult}^{r_u}$) as a nonlinear function of the free-field excess pore pressure ratio (r_u) at the depth of pile's tip.

$$q_{t,ult}^{r_u} = q_{t,ult}^{o}(1 - r_u)^{\alpha_t}$$

$$\alpha_t = \frac{3 - sin\phi'}{3(1 + sin\phi')} \qquad 3.2$$

where $q_{t,ult}^{o}$ is the ultimate tip capacity when $r_u = 0$, α_t is a constant that, according to Knappett and Madabhushi (2009), depends only on ϕ', the effective friction angle of the soil at the tip. Following Equation 2 and the implementation of the TzLiq material (Boulanger et al. 1999), a QzLiq material was developed and implemented in OpenSees (McKenna et al. 2010). The documentation on the QzLiq material is available at https://opensees.github.io/OpenSeesDocumentation.The material models change in the pile's tip capacity and stiffness in the presence of excess pore pressures. Similar to the TzLiq material, the QzLiq material response is modeled as the constitutive response of a q-z material (Boulanger et al. 1999; Gajan et al. 2010) scaled in proportion to the excess pore pressure ratio $(1 - r_u)^{\alpha_t}$. The material has an ultimate load ($q_{t,ult}^{r_u}$) in compression related to the bearing capacity of the pile and a zero strength in tension. The properties of the QzLiq material include the ultimate tip capacity (q_{ult}^{o}), the displacement (z_{50}) at which 50% of q_{ult}^{o} is mobilized, the exponent (α_t) approximated from Equation 3.2, and a time series data of free-field effective stress (σ'_v) at the pile's tip depth. The element internally evaluates the excess pore pressure ratio (r_u) from the provided mean effective stress data.

Unlike shaft friction, the tip does not have an ultimate bound on its strength, especially for end-bearing piles. As penetration increases, the tip resistance increases. Displacements of the order of 10% of the pile diameter are required to significantly mobilize the pile tip capacity (Fleming et al., 2008). In the absence of pile load test data, the tip capacity (estimated from empirical correlations with soil characterization data) is usually taken as the mobilized resistance for tip penetration equal to 10% of the pile diameter. Vijivergiya (1977) describes the nonlinear backbone curves for tip response in dense sand; where z_{50} is taken equal to 0.125 times the displacement required to mobilize the tip capacity. A pile load test could circumvent the need to assume values for the properties (q^{o}_{ult}, z_{50}) of the QzLiq material.

Effective Stress and Soil Settlement Profiles

Time series of effective stress as a function of depth σ'_v (z, t) and settlement s (z, t) are required to perform the proposed analysis of downdrag. For design purposes, these time series may be obtained from a 1-D or 2-D site response analysis following a reconsolidation analysis with a finite element or a finite-difference software capable of capturing the salient features of the problem. For validation purposes, the time series can also be determined from measurements of a suitably instrumented field or model test.

Stages of Modeling

The simulation is performed with two analysis stages. Dead loads are applied in Stage 1, and the result of the analysis is the initial (at t = 0) axial load distribution [Figure 3.1 (e)] for Stage 2. Stage 2 is a dynamic time history analysis of the piles [Figure 3.1] stepping through the time series σ'_v (z, t) and s (z, t) applied to the TzLiq and QzLiq interface elements. In the case of seismic loads, a time series axial load is also applied to the piles.

3.3 Numerical Modeling of Piles used in Centrifuge Test

The piles (0DPile, 5DPile, 3DPileS, 3DPileM, and 3DPileL) used in the centrifuge model tests SKS02 and SKS03 (described in Chapter 2) were modeled for selected shaking events. For the centrifuge model test SKS02, the large shaking event EQM_3 was selected. For centrifuge model test SKS03, the large shaking event EQM_4 was selected. EQM_3 was a scaled Santa Cruz (Northridge 1994 earthquake) motion with a peak base acceleration (PBA) of 0.24 g [Figure 2.2]. EQM_4 was a long-duration modified Santa Cruz motion (Malvick et al. 2002) consisting of one large pulse followed by five small pulses, scaled to produce a PBA of 0.45 g [Figure 2.5]. Time histories of excess pore pressures (u_e) and soil and pile settlement profiles and isochrones of u_e profile and axial load distribution in piles during shaking and reconsolidation for the two shaking events EQM_3 and EQM_4 are shown in Figure 2.10 and Figure 2.11, respectively. The initial and final axial load distribution in the piles for the two shaking events and their limit load curves is shown in Figure 3.2. The mechanism of liquefaction-induced downdrag phenomenon with excess pore pressure generation and dissipation pattern, and sequencing and timing of soil and pile settlement are described in Section 2.5 in Chapter 2.

The following subsection describes the numerical modeling approach to estimate soil settlement profiles using an inverse analysis of measured excess pore pressures arrays during shaking events. Following that, the TzQzLiq analysis of the piles used in centrifuge tests is described.

Inverse Analysis of Measured Excess Pore Pressures to Obtain Soil Settlement Profiles

An inverse analysis of the recorded excess pore pressures was performed to obtain the time history of soil settlement profiles which were later used as an input in the numerical modeling of the centrifuge test piles for liquefaction-induced downdrag. In addition, a numerical model was developed to study the development of the water film at the sand-clay interface and its effect on surface settlements [as described earlier in Section 2.5 in Chapter 2]. Results from the analysis were later used to study the development of reconsolidation strains, surface settlement, and water film as excess pore pressures dissipated in the model (see the discussion on the soil settlement in Section 3.4). This section describes the numerical modeling approach used for the inverse analysis and modeling of the water film at the sand-clay interface.

Following Malvick et al. (2008), inverse analyses of the measured excess pore pressures along the pore pressure transducer arrays [Figure 2.10 (a), Figure 2.11 (b)] were performed to estimate reconsolidation strains within the soil layers. The method used Darcy's law and 1-D consolidation theory [Equation 3.3] to calculate the rate of reconsolidation strains ($\dot{\varepsilon_v}$).

$$\mathrm{i} = \frac{\partial u_e(t)}{\gamma_w \partial z}$$

$$\dot{\varepsilon_v} = \frac{k}{\gamma_w}\frac{\partial^2 u_e(t)}{\partial z^2} \qquad 3.3$$

where k is the permeability of the soil, γ_w is the unit weight of water, z is the layer depth, and $u_e(t)$ is the excess pore pressure at the time (t). A numerical smoothing function [Equation 3.4] was designed to numerically fit the measured excess pore pressures profiles.

$$u_e(t) = \frac{a_0}{2a_1} log(t^2+1) \; - \; \frac{a_0}{a_1} t \; tan^{-1} t + a_3 z + a_4) \qquad 3.4$$

$$t \; = \; (a_2 - a_1 z)$$

where a_0, a_1, a_2, a_3, and a_4 are the constants determined at each time (t) to numerically fit the experimental excess pore pressure profiles along with the boundary constraints. The impermeable boundary condition at the bottom of the container was enforced by making the hydraulic gradient zero ($i = 0$). Reconsolidation strain rates were integrated with time to obtain time histories of reconsolidation strains and soil settlements. The permeabilities of different soil layers used of centrifuge model tests SKS02 and SKS03 are summarized in Table 2.1 and Table 2.4, respectively.

The formation of the water film layer at the sand-clay interface was calculated as the difference in the velocity (q) of water entering ($q_{in} = k_{in}\ i_{in}$) and exiting ($q_{out} = k_{out}\ i_{out}$) the interface, where the permeabilities (k_{in} and k_{out}) and hydraulic gradient (i_{in} and i_{out}) are for the soil layers below and above the interface. A net inflow (q_{in} - $q_{out} > 0$) models increase of water film thickness, whereas a net outflow (q_{in} - $q_{out} < 0$) models drainage of the water film. In the centrifuge model test SKS02, the creation of favorable drainage paths from the sides of the model container (starting at t ≈ 2 min) [Figure 2.10 (a,b)] was modeled by increasing the permeability of the clay layer, which from calibration of the numerical results of surface settlement with measurements from centrifuge test was found to have increased by a factor of 35.

TzQzLiq Analysis of Piles

The TzQzLiq analysis of centrifuge model test piles was performed for the two large shaking events: EQM_3 in the centrifuge model test SKS02 and EQM_4 in the centrifuge model test SKS03. The ultimate capacity of the TzLiq material at different depths along the length of the pile was obtained from the limit load curves [Figure 2.9, Figure 3.2]. Backbone curves from Reese and O'Niel (1987) and Mosher (1984) were used to model the load transfer behavior of sections of piles in sand and clay layers, respectively. The parameter z_{50} of TzLiq material was taken as 0.3% of the pile diameter in the clay, silt, loose sand, and medium dense sand layers and 0.15% of the pile diameter in the dense sand layer (see also Section 3.2 on TzLiq and QzLiq Material Properties). The q-z load transfer behavior was modeled with backbone curves from Vijivergiya

(1977). Results from pile load tests were used to calibrate the properties (q^{o}_{ult}, z_{50}) of QzLiq material [shown later in Figure 3.6 (a)]. The numerical and the centrifuge test pile load test curves match quite well with the selected TzLiq and QzLiq material properties [Figure 3.6 (a)]. The constant (α_t) was taken as 0.55 calculated using Equation 3.2 with an effective friction angle of $\phi' = 30^{o}$. Table 3.1 summarizes the properties of the TzLiq and the QzLiq material used in the numerical analysis. Time history of effective stress was obtained directly from the measurements of excess pore pressures in the centrifuge test. The time history of the soil settlement profile was obtained from the inverse analysis (as described in the previous section).

The TzQzLiq analysis of the piles was performed in OpenSees (McKenna et al. 2010) with a mesh discretization of 0.1 m. The latest version of OpenSees (available from the GitHub repository at https://github.com/OpenSees/OpenSees) with QzLiq material model implemented was used to perform the analysis. Stage 1 modeled the initial axial load distribution in the piles [Figure 3.2] by applying the pile head load and iteratively finding the required soil settlement to develop the initial shear stresses. Stage 2 modeled liquefaction-induced downdrag on piles. Time histories of axial load distribution and pile settlement obtained from the analysis were compared to the results from the centrifuge tests to validate the numerical model. Additionally, a sensitivity study on the effect of the QzLiq constant (α_t) and stiffness of TzLiq materials in loose and dense sand ($z_{50,loose}$ and $z_{50,dense}$) was performed to evaluate their effect on the obtained drag load, neutral plane depth, pile settlement, and mobilized tip load. The study was performed by selecting the values of parameters (α_t, $z_{50,loose}$, and $z_{50,dense}$) one higher and one lower than the one selected for numerical analysis ($\alpha_t = 0.55$, $z_{50,loose}$= 0.3% D, and $z_{50,dense}$= 0.15% D).

Table 3.1. TzLiq and QzLiq material properties used in the TzQzLiq analysis of piles.

TzLiq*[a] *Material Properties		***QzLiq Material Properties***			
Soil Layers	***z_{50} (%D*[b]*)***	***Piles***	***z_{50} (%D*[b]*)***	***q^o_{ult} (kN)***	***α_t***
Clay and Silt Layers	*0.31*	*0DPile*	*7*	*2745*	*0.55*
Loose, Medium Dense Sand	*0.31*	*5DPile*	*7*	*7137*	
Dense Sand	*0.15*	*3DPiles*	*9*	*4576*	

[a] *t^o_{ult} at different depths along the length of the pile is obtained from the limit load curve shown in Figure 2.9*

[b] *diameter of the pile*

3.4 Comparison of Numerical Model Results with Centrifuge Test Data

Soil Settlement

While most of the soil settlements occurred during reconsolidation, the soil layers suffered some immediate settlements during shaking. For shaking event EQM_3 in centrifuge model test SKS02, surface settlements were observed until t = 30 s [Figure 2.10 (b)]. For shaking event EQM_4 in the centrifuge model test SKS03, the immediate settlement in soil layers occurred in the first 15 seconds of the shaking [Figure 2.11 (b)]. Contours of surface settlement at the end of shaking (~ 70 s) and after complete reconsolidation (~ 3 hr) of shaking event EQM_4 are shown in Figure 3.3. The figure also shows the time histories of soil settlement near the piles (3DPiles, 0DPile, and 5DPile) for the shaking events EQM_3 and EQM_4 [Figure 3.3 (b,c)]. The contours indicate larger settlements at the model's center compared to its boundaries. Investigations following the test suggested that in the curved g-field, the leveled surface of the Monterey sand layer and the layers beneath could be responsible for more immediate settlement at the center than at the boundaries [Figure 3.3 (a)]. The measured surface settlement was corrected by offsetting these immediate settlements during shaking ($t \approx 30$ s for both EQM_3 and $t \approx 15$ s for EQM_4) because it did not represent settlement from the dissipation of excess pore pressures. Corrected soil settlements were found similar across the model [Figure 3.3 (b,c)]. In the centrifuge model test SKS03, settlements measured at three distinct locations near the individual piles matched well with each other [Figure 3.3 (b)]. In the SKS02 model, the corrected settlements at two distinct locations (SM_1 and SM_2) still had some differences [Figure 3.3 (c)]. It is possible that the presence of the water film at the sand-clay interface could have resulted in non-uniform settlements of the overlying soil (Fiegel and Kutter (1994)). The mean of the corrected surface settlement was compared with the results from the inverse analysis.

Isochrones of excess pore pressure and reconsolidation strain rate profiles at selected times and the time histories of reconsolidation strain and soil settlement at selected depths for shaking events EQM_3 and EQM_4 are shown in Figure 3.4 and Figure 3.5, respectively. The plots show that the numerical smoothing function [Equation 3.4] used in the inverse analysis fitted the measured excess pore pressure profiles well [Figure 3.4 (a), Figure 3.5 (a)]. The surface settlements obtained from inverse analysis matched quite well with the surface measurements recorded in the centrifuge tests [Figure 3.4 (d), Figure 3.5 (d)]. The time histories of reconsolidation strains and soil settlement obtained from the inverse analysis helped understand the dissipation of excess pore pressures and observed surface settlement.

In the centrifuge model test SKS02, the analysis results showed water film formation at the sand-clay interface [Figure 3.4]. Results show that even though the impermeable clay layer hindered drainage, dissipation of excess pore pressures within the loose sand layer developed reconsolidation strains. The reconsolidation strains in the loose sand can be seen increasing with time [Figure 3.4 (c)]. During $t < 2$min, the water produced from the reconsolidation could not drain to the surface and resulted in the formation of a water film at the sand-clay interface [Figure 3.4 (d)]. Consequently, during this period, no surface settlement occurred. The maximum thickness of the water film formed was about 0.5 mm (in model scale). At t ≈ 2 minutes, the water film drained once it formed a clear drainage path from the sides of the container. As the water film drained, the soil surface settled [Figure 3.4 (d)]. By about 6 minutes, the water film had entirely dissipated while the reconsolidation continued and lasted for more than an hour. Most of the volume change occurred in the loose sand layer with an average reconsolidation strain of $\varepsilon_v \approx 0.56\%$. The average reconsolidation strain in the dense sand layer was $\varepsilon_v \approx 0.1\%$. The results also show some settlements occurring at the pile's tip depth [Figure 3.4 (d)]. Soil settlement of about 7 mm and 3 mm was calculated at the tip of the 0DPile and 5DPile, respectively.

For centrifuge model test SKS03, results from the inverse analysis provided insights on sequencing and timing of soil settlement [Figure 3.5]. During shaking, the cracks in the weakly cemented crust layer provided quick drainage for the loose sand layer, resulting in soil settlement during and post shaking. As expected from the observation of surface settlement, the numerical analysis result also did not show any water film formation at the sand-clay interface. Complete reconsolidation of the loose sand layer was completed within 20 minutes [Figure 3.5 (c)]. Reconsolidation in the medium dense sand layer started much later (about 20 minutes) and took more than 2 hours to achieve complete reconsolidation. Results from the inverse analysis show that the loose sand and medium dense sand layers developed average reconsolidation strains of 0.75% and 0.48%, respectively. In comparison, the dense sand layer developed an average reconsolidation strain of 0.03%. The results also showed soil settlement of about 1.5 mm at the pile's tip depth [Figure 3.5 (d)].

Axial Load Distribution and Drag Load

Axial load distributions at selected times obtained from the TzQzLiq analyses were compared against results from the centrifuge tests in Figure 3.6, Figure 3.7, and Figure 3.8. Results from the pile embedded 3 diameters in dense sand with a small pile head load, 3DPileS, are compared in Figure 3.6; results from the pile with medium load (3DPileM) and large load (3DPileL) are compared in Figure 3.7. Results for the 0DPile and 5DPile are compared in Figure 3.8. The free-field effective stress and soil settlement profiles at selected times are also presented in Figure 3.6 (a,b) and Figure 3.8 (a,b). Time histories of axial load for the piles at selected depths from the TzQzLiq analysis are compared against results from centrifuge tests in Figure 3.6 (f), Figure 3.7 (d), and Figure 3.8 (f). The initial axial load distribution in the TzQzLiq analysis matched the centrifuge test results quite well [t = 0 s in Figure 3.6 (d), Figure 3.7 (a), and Figure 3.8 (a)]. The initial axial load distribution of 3DPileL [Figure 3.8 (b)] did not match well. An investigation found that some gages of the 3DPileL (which had already been used as 0DPile in the SKS02 model) might have become unreliable. The gages of the pile were found to be sensitive to bending moments and were found not to have performed well in the previous centrifuge model test SKS02 (Sinha et al. 2021c) as well. The issue is discussed in Section 2.5 in Chapter 2. Regardless, it was thought useful to numerically model and study the response of 3DPileL while keeping in mind the lower reliability of the comparisons for 3DPileL.

The axial load in piles decreased during shaking; however, post-shaking, when the excess pore pressures dissipated and the soil settled, it again increased. For the centrifuge model test SKS03, the axial loads in 3DPileS and 3DPileM at different depths and times matched quite well with the measured loads from the centrifuge tests [Figure 3.6 (d,f) and Figure 3.7 (a,d)]. For 3DPileM, the load near its tip (at a depth of 13.5 m) [Figure 3.7 (d)] estimated by the numerical model was found higher than the measured loads. However, the increments of axial load post shaking (during reconsolidation, t > 70 s) were found similar. The difference in the axial load was found to be most apparent during shaking (i.e., t < 70 s). The post-shaking axial load distribution in 3DPileL followed a similar load distribution profile as 3DPileM. Similar results were observed from the numerical modeling of SKS02 piles. The disagreement between the axial load increments in the 0DPile and 3DPile is apparent during shaking [Figure 3.8 (f)]. During reconsolidation, the increments in the axial loads from the numerical analysis were similar to those from the centrifuge test. Not modeling the dynamic changes in lateral stresses could have resulted in some difference between the numerical and centrifuge test results. Overall, the axial load distribution in the piles matched reasonably well with the centrifuge test data [Figure 3.6 (d), Figure 3.7 (a,b), and Figure 3.8 (c,d)].

An increase in excess pore pressure during shaking decreased drag load and correspondingly resulted in a shallow neutral plane (i.e., the depth of maximum axial load). However, as excess pore pressures dissipated and the soil settled, the drag load again increased, and correspondingly the neutral plane deepened. Results from the numerical analysis on time histories of drag load and neutral plane depth for all the piles are shown in Figure 3.9. For heavily loaded piles (3DPileM and 3DPileL) and piles with shallow embedment (0DPile), drag load decreased to zero during shaking, and correspondingly the neutral plane reached the ground surface. Changes in the neutral plane for 5DPile and 3DPileS were small. For all the piles, only a few minutes (< 2-3 minutes) after shaking, the neutral plane came back close to the initial depth before shaking; however, the increase in drag load was small. During this period, the soil had settled about 10-20 mm. This shows that a small amount of soil settlement during reconsolidation is enough to bring back the neutral plane close to the initial depth before shaking. As reconsolidation progressed, drag load and depth of neutral plane both increased. After complete reconsolidation, the drag load was greater for the deeply embedded (5DPile) and the lightly loaded pile (3DPileS). The drag loads on 3DPileM and 3DPileL were equal [Figure 3.9 (b)], which was also confirmed by the similar axial load distribution during reconsolidation [Figure 3.7 (a,b)]. The neutral plane depth was greater for piles with deeper embedment. 5DPile developed the deepest neutral plane (14 m). Regardless of different head loads, all the 3DPiles of centrifuge model test SKS03 resulted in the same neutral plane depth of ~10.5 m after complete reconsolidation. However, the developed drag load on lightly loaded pile (3DPileS) was 15% (about 100 kN) greater than the other piles (3DPileM and 3DPileL).

Pile Settlement

Settlement time histories of the piles (0DPile, 5DPile, and 3DPiles) from the numerical analysis matched quite well with recorded settlements. The comparisons between the recordings from centrifuge test and numerically simulated time histories of pile settlements for 3DPileS, (3DPileM and 3DPileL), and (0DPile and 5DPiles) are shown in Figure 3.6 (e), Figure 3.7 (c), and Figure 3.8 (e), respectively. During shaking, while the axial loads in piles at all depths decreased because of the decrease in the initial drag loads from the increased excess pore pressures, the loss of the shaft and tip capacity and its stiffness resulted in settlement of the piles [Figure 3.6 (e,f), Figure 3.7 (c,d), and Figure 3.8 (e,f)]. During reconsolidation, as effective stresses increased and the soil settled, the re-development of drag load resulted in an additional settlement of the piles. Piles that had a large ratio of static axial capacity to the applied head load (5DPile and 3DPileS) settled < 2 mm during shaking and < 5 mm during reconsolidation [Figure 3.6 (e) and Figure 3.8 (e)]. The 0DPile recorded settlement of about 10 mm both during shaking and during reconsolidation. However, during reconsolidation, since the soil at the tip settled by 7 mm [Fig. 8

(d)], the penetration of the ODPile in soil was effectively < 5 mm. Heavily loaded piles (3DPileM and 3DPileL) suffered large settlements during shaking (> 20 mm). Settlement time histories of 3DPileS, 3DPileM, 0DPile, and 5DPile matched the recorded settlement quite well [Figure 3.6 (e), Figure 3.7 (c), and Figure 3.8 (e)] both during shaking and reconsolidation. For 3DPileL, there were some differences in the numerical and centrifuge test results. While both the numerical analysis and centrifuge test showed plunging of 3DPileL during shaking, the numerical model underestimated the settlement of 3DPileL during shaking by about 40% [Figure 3.7 (c)]. The numerical analysis showed the settlement of the pile to be about 120 mm (i.e., ~19% of the pile's diameter) compared to about 200 mm (~31% of the pile's diameter) in the centrifuge test. A possible explanation for the difference could be the limitation of the constitutive model of the QzLiq material in accurately modeling the realistic behavior of the tip. The exponent (α_t) which was assumed constant $(\alpha_t = 0.55)$ throughout the analysis may not be a constant; for example, it may increase to 1.0 during failure. The settlement of 3DPileL during reconsolidation (about 10 mm) matched quite well with the centrifuge test results. The slope of the pile settlement during reconsolidation can be seen parallel to the centrifuge test results [Figure 3.7 (c)]. Overall, the numerical model with the newly developed QzLiq material reasonably modeled the movement of piles in liquefiable soils both during shaking and reconsolidation. Results showed that the pile settlement mainly occurred during shaking when the excess pore pressures were high. During reconsolidation, the tip penetration in soil was small (< 10 mm). The piles with smaller head loads (3DPileS and 5DPile) suffered settlements less than 10 mm. Other piles settled more than about 20 mm.

3.5 Sensitivity Study of TzLiq and QzLiq Material Properties

A sensitivity study on TzLiq and QzLiq material properties was performed in order to exercise and further increase our understanding of the numerical modeling of liquefaction-induced downdrag on piles. The study showed that the QzLiq material stiffness greatly affected pile settlement, whereas the TzLiq material stiffness controlled drag load. Changes in the stiffness of the TzLiq material in the soil below the neutral plane showed minimal effect on the magnitude of drag load and pile settlement. Results from the sensitivity study of QzLiq exponent (α_t) and TzLiq parameter (z_{50}) on the developed drag load, neutral plane depth, pile settlement, and mobilized tip load after complete reconsolidation are shown in Figure 3.10. An increase in the QzLiq constant (α_t) (from $\alpha_t = 0.30$ to $\alpha_t = 0.8$) resulted in larger pile settlement [Figure 3.10 (c)] and decreased drag load [Figure 3.10 (a)]. Correspondingly, the mobilized tip load [Figure 3.10 (d)] and the neutral plane depth [Figure 3.10 (b)] also decreased. Increasing the QzLiq constant (α_t) decreased the tip capacity ($q_{t,ult}^{r_u}$) and stiffness nonlinearly [Equation 3.2]. A smaller tip capacity and stiffness (i.e., larger α_t) resulted in a larger settlement and a smaller drag load. As expected, the heavily loaded piles (3DPileM and 3DPileL) experienced greater changes in pile settlement than the lightly loaded piles (0DPile, 5DPile, and 3DPileS) as the exponent (α_t) changed [Figure 3.10 (c)]. The increase in settlement of lightly loaded piles resulted in the decrease of drag load. However, any further increase in pile settlement for heavily loaded piles did not cause any significant change in drag load [Figure 3.10 (a)]. The decrease in the stiffness of TzLiq material ($z_{50,loose} = 0.3\%\,D$ to $z_{50,loose} = 0.6\%\,D$) in the loose sand layer significantly decreased drag load [Figure 3.10 (a)]. Correspondingly, the neutral plane depth [Figure 3.10 (b)] and mobilized tip load [Figure 3.10 (d)] also decreased. For the lightly loaded piles (0DPile and 3DPileS) that had their neutral plane in the loose sand layer and thus had a significant contribution of shaft friction in resisting the pile; the decrease of stiffness of TzLiq material resulted in more load transferred to the tip [Figure 3.10 (d)]. For the heavily loaded piles (3DPileM and 3DPileL) and the piles with a neutral plane below the loose sand layer (5DPile), the decrease in stiffness of TzLiq material decreased the overall load at the neutral plane, causing smaller mobilization of load at the tip [Figure 3.10 (d)]. The increase in the stiffness of TzLiq material in dense sand layer ($z_{50,dense} = 0.30\%\ D$ to $z_{50,dense} = 0.15\%\ D$) showed minimal effect on the drag load [Figure 3.10 (a)] and pile settlement [Figure 3.10 (c)]. The dense sand layer being below the neutral plane did not contribute to drag load. For the 5DPile, a higher stiffness of TzLiq material mobilized greater shaft friction in the dense sand and resulted in a smaller load transferred to the tip [Figure 3.10 (d)]. For the piles that were not embedded very deep in dense sand, the increased TzLiq stiffness in dense sand had minimal effect.

3.6 Considerations for Practice

This chapter used the centrifuge test data to determine the effective stress and soil settlement profiles and TzLiq and QzLiq material properties. In practice, one would need to determine the pore pressure and free-field settlement distribution by other analysis procedures. For example, a 1-D site response analysis with pore pressure models (such as Chiaradonna et al. (2020)) with the design earthquake followed by a reconsolidation analysis could be a reasonable approach for predicting the effective stress and soil settlement distributions over the depth. The ultimate capacity of TzLiq and QzLiq materials can be obtained from the empirical correlations developed on data from soil investigation methods such as cone penetration tests, static penetration tests, and others. The stiffness of TzLiq material can be defined, considering that a small relative displacement of 10-30 mm or 1 - 3% of the pile's diameters is enough to mobilize the full shaft resistance in piles (Sinha et al. 2021f). Determining site-specific QzLiq material stiffness is important for accurately modeling pile settlement and drag load. The sensitivity study shows that the stiffness of the QzLiq material significantly affects the pile settlement. On the other hand, the drag load is affected by both the TzLiq and the QzLiq materials stiffnesses. Therefore, it is crucial to calibrate the initial capacity and stiffness properties of the QzLiq material against results from the pile load test. In the absence of test data, displacement equal to 10% of pile diameter can be taken as the tip penetration required to mobilize the capacity of QzLiq material (API 2000). Section 5.3 of Chapter 5 provides an empirical pile load test curve for large diameter (> 20 inches) cast-drilled-hole (CIDH) piles that can be used to calibrate the QzLiq materials properties in the absence of pile load test data. The constant (α_t) for the QzLiq material can be estimated from Equation 3.2. Additionally, a sensitivity study can be performed on the stiffness of the TzLiq and QzLiq material to determine their effect on pile settlement and drag load.

3.7 Summary and Conclusion

A TzQzLiq numerical analysis was performed to model liquefaction-induced downdrag on piles. Model input parameters included TzLiq and QzLiq material properties, time histories of soil settlement and effective stress profiles, and pile properties. A QzLiq material was developed and implemented in OpenSees to model the reduction of pile tip capacity and stiffness in the presence of excess pore pressures. Together, the TzLiq and the QzLiq materials account for changes in the shaft and the tip capacity of the pile as free-field excess pore pressures develop and dissipate in soil. The TzLiq and the QzLiq material properties were obtained and calibrated against the limit load curves and the pile load test results. The TzQzLiq analysis was validated against the results from a series of large centrifuge model tests conducted on piles embedded in layered and interbedded soil deposits with liquefiable layers. An inverse analysis was performed on the measured excess pore pressures arrays to obtain time histories of soil settlement profiles. Analyses results showed that the performed TzQzLiq analysis reasonably predicted the time histories of axial load distribution and settlement of piles.

A numerical model was developed and incorporated into the inverse analysis of the centrifuge model test to study the water film formation at the sand-clay interface. The formation/drainage of the water film was modeled as the net velocity of water (q_{in} - q_{out}) entering/leaving the interface. The results from the numerical model explained the mechanism behind the observed surface settlement in the centrifuge model test SKS02. While the impermeable clay layer hindered drainage, the dissipation of excess pore pressures (and reconsolidation) occurred in the loose sand layer resulting in the formation of the water film. During this period, no surface settlement occurred in the model. However, once the water established drainage paths through cracks or along edges of the model container, the water film started draining, and the surface settled. Time histories of the numerically simulated surface settlement matched well the recorded measurements from the centrifuge test.

The TzQzLiq numerical model presented in this chapter can model the response of piles during shaking and reconsolidation. The TzQzLiq analysis improves the traditional neutral plane solution method by accounting for changes in the stiffness and capacity of the pile’s shaft friction and tip resistance in liquefiable soils, offers complete modeling of the liquefaction-induced downdrag phenomenon, and provides time history of axial load distribution and settlement of piles. Analysis results on the axial load distribution, pile settlement, and drag load can aid in designing and evaluating the performance of piles in liquefiable soils. The maximum load obtained on the pile (Q_{np}) at the end of reconsolidation can be checked against the pile’s structural strength. In addition, the settlement of the pile at the end of shaking and after complete reconsolidation can be checked against the serviceability criteria. Chapter 5 describes a design procedure using TzQzLiq analysis for designing piles in liquefiable soils for extreme loading conditions (such as seismic loading and liquefaction-induced downdrag).

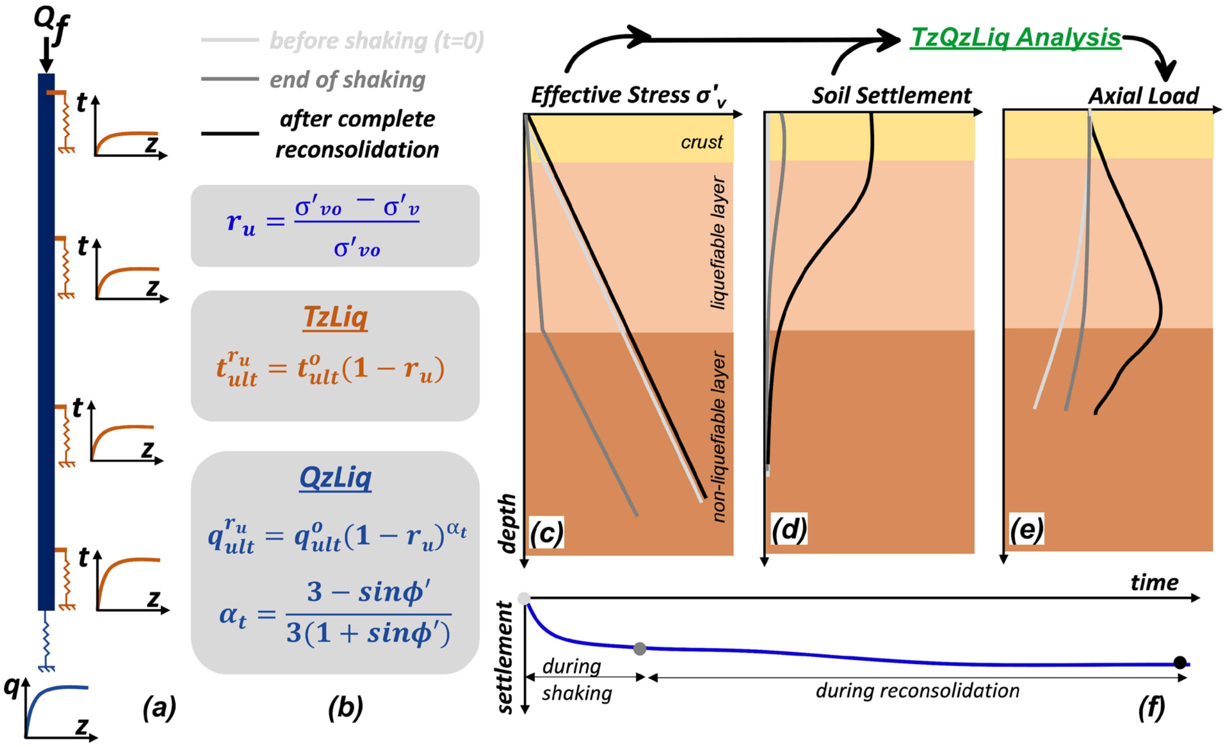

Figure 3.1. Illustration of the TzQzLiq numerical model for modeling liquefaction-induced downdrag on piles using (a) the zero thickness interface elements with TzLiq and QzLiq materials. Model input parameters include properties of the pile, (b) TzLiq and QzLiq material properties, (c) isochrones of effective stress, and (d) soil settlement profiles. Model results include time histories of (e) axial load distribution and (f) pile settlement.

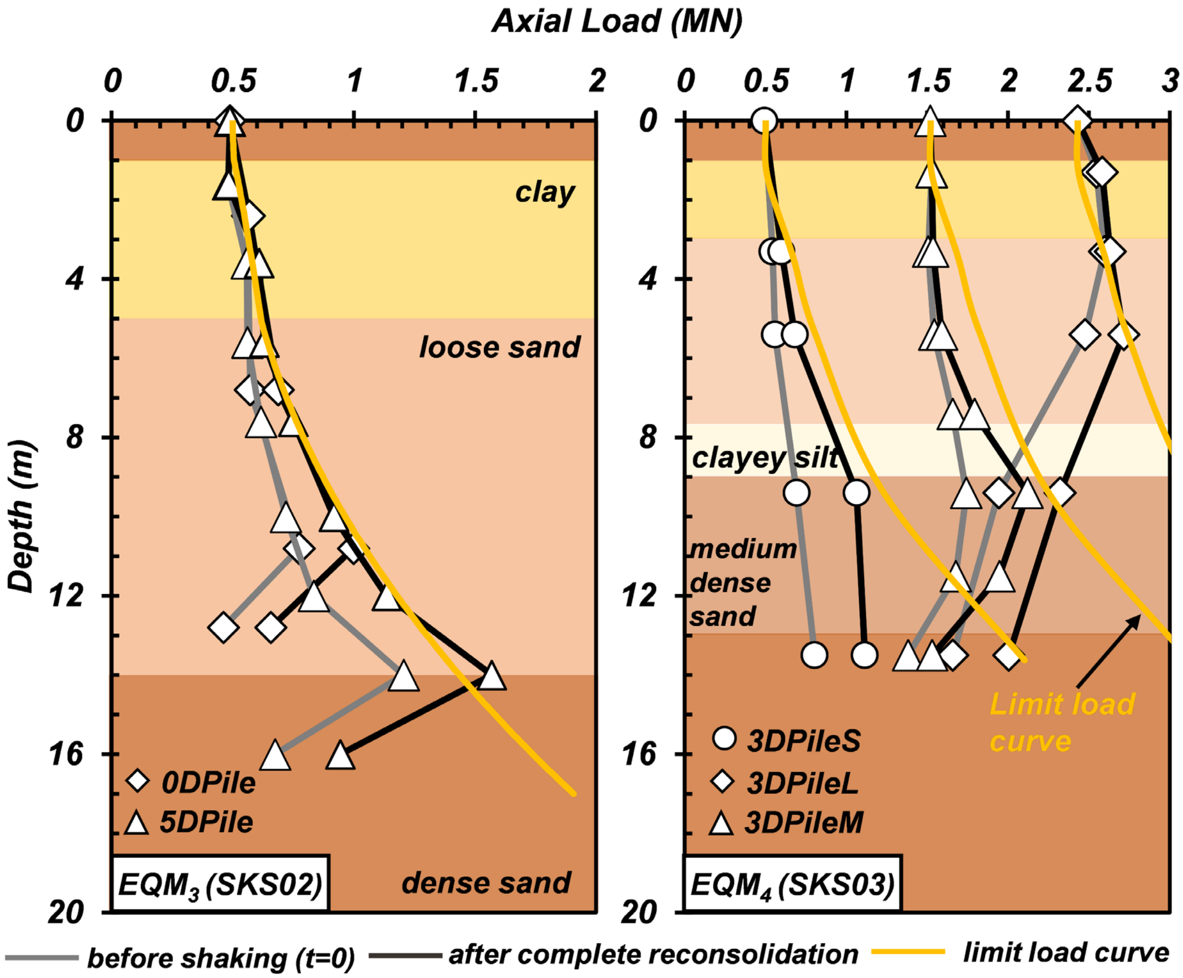

Figure 3.2. Axial load distribution in piles before and after shaking for shaking events EQM$_3$ (in centrifuge test SKS02) and EQM$_4$ (in centrifuge test SKS03) with their corresponding limit load curves.

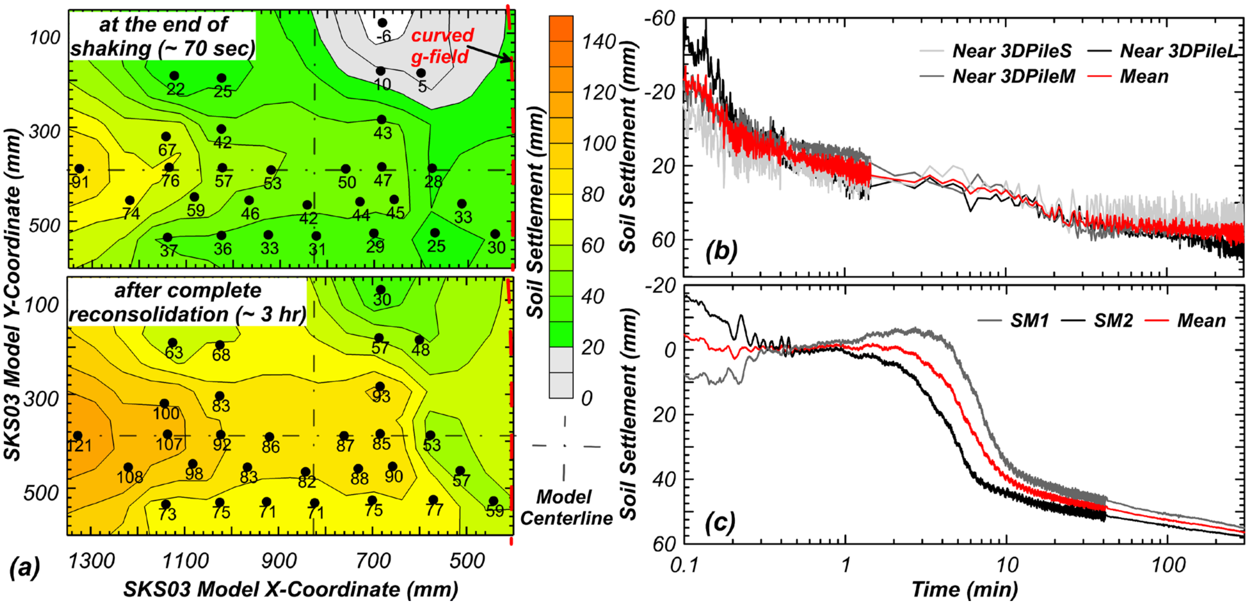

Figure 3.3. (a) Contours of measured surface settlement for event EQM4 of centrifuge test SKS03 towards the end of shaking (~ 70 s – top) and after complete reconsolidation (~ 3 hr – bottom). Time history of soil surface settlements and their mean after correcting them for their immediate settlement at t ≈ 15 s for shaking event EQM4 and t ≈ 30 s for shaking event EQM3 (in centrifuge test SKS02) in (b) and (c), respectively.

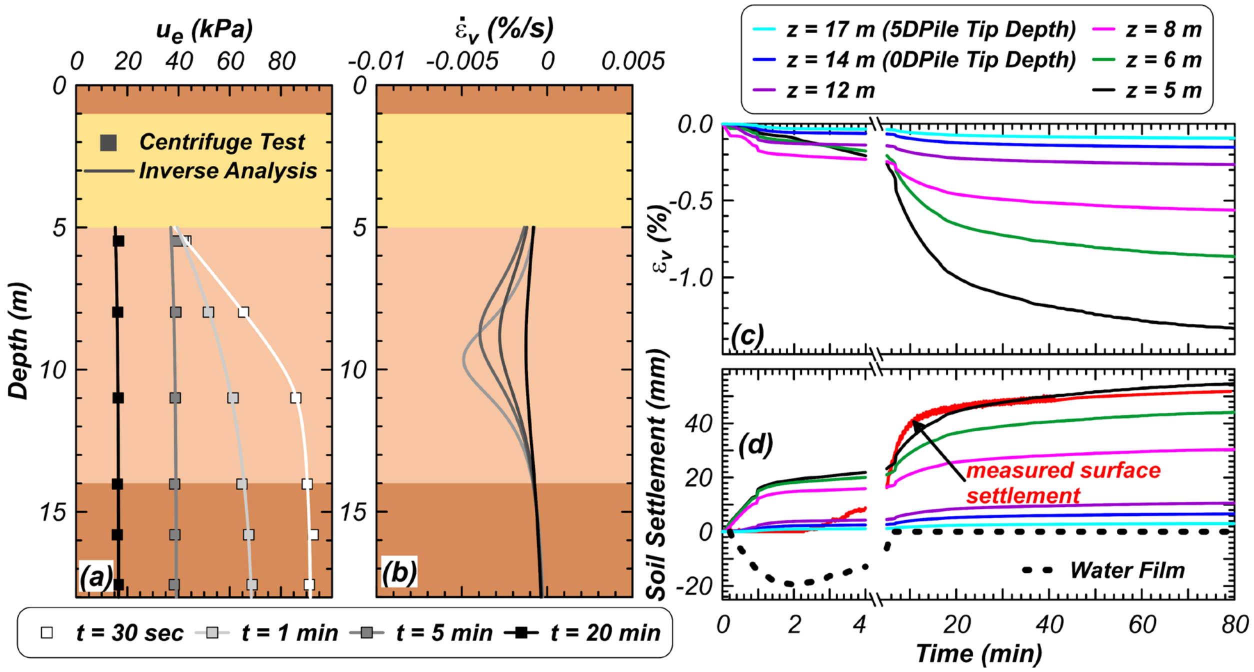

Figure 3.4**.** Inverse analysis of excess pore pressure arrays for shaking event EQM$_3$ of centrifuge model test SKS02. Isochrones of (a) excess pore pressure (u_e) and (b) reconsolidation strain rate ($\dot{\varepsilon_v}$) at selected times. Time histories of (c) reconsolidation strain (ε_v), (d) water film thickness, soil settlement at selected depths and at pile's tip loaction, and comparison of surface settlement from numerical analysis with centrifuge test results.

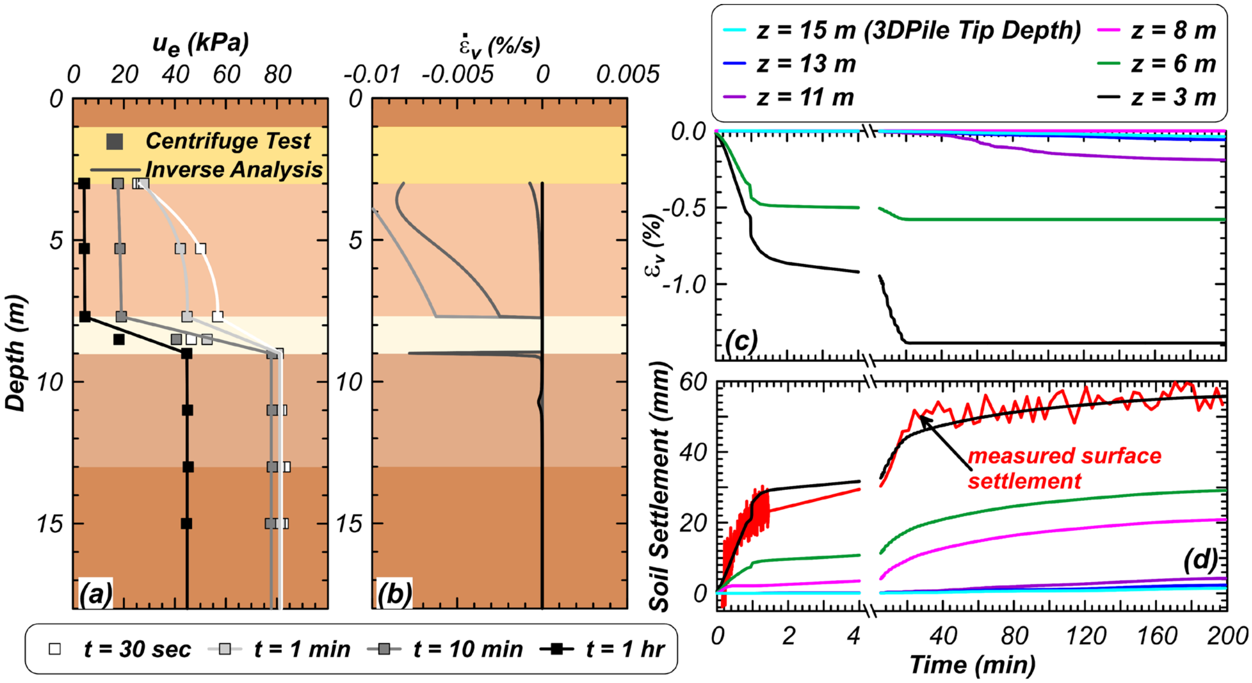

Figure 3.5. Inverse analysis of excess pore pressure arrays for shaking event EQM_4 of centrifuge model test SKS03. Isochrones of (a) excess pore pressure (u_e) and (b) reconsolidation strain rate ($\dot{\varepsilon_v}$) at selected times. Time histories of (c) reconsolidation strain (ε_v), (d) soil settlement at selected depths and at pile's tip location, and comparison of surface settlement from numerical analysis with centrifuge test results.

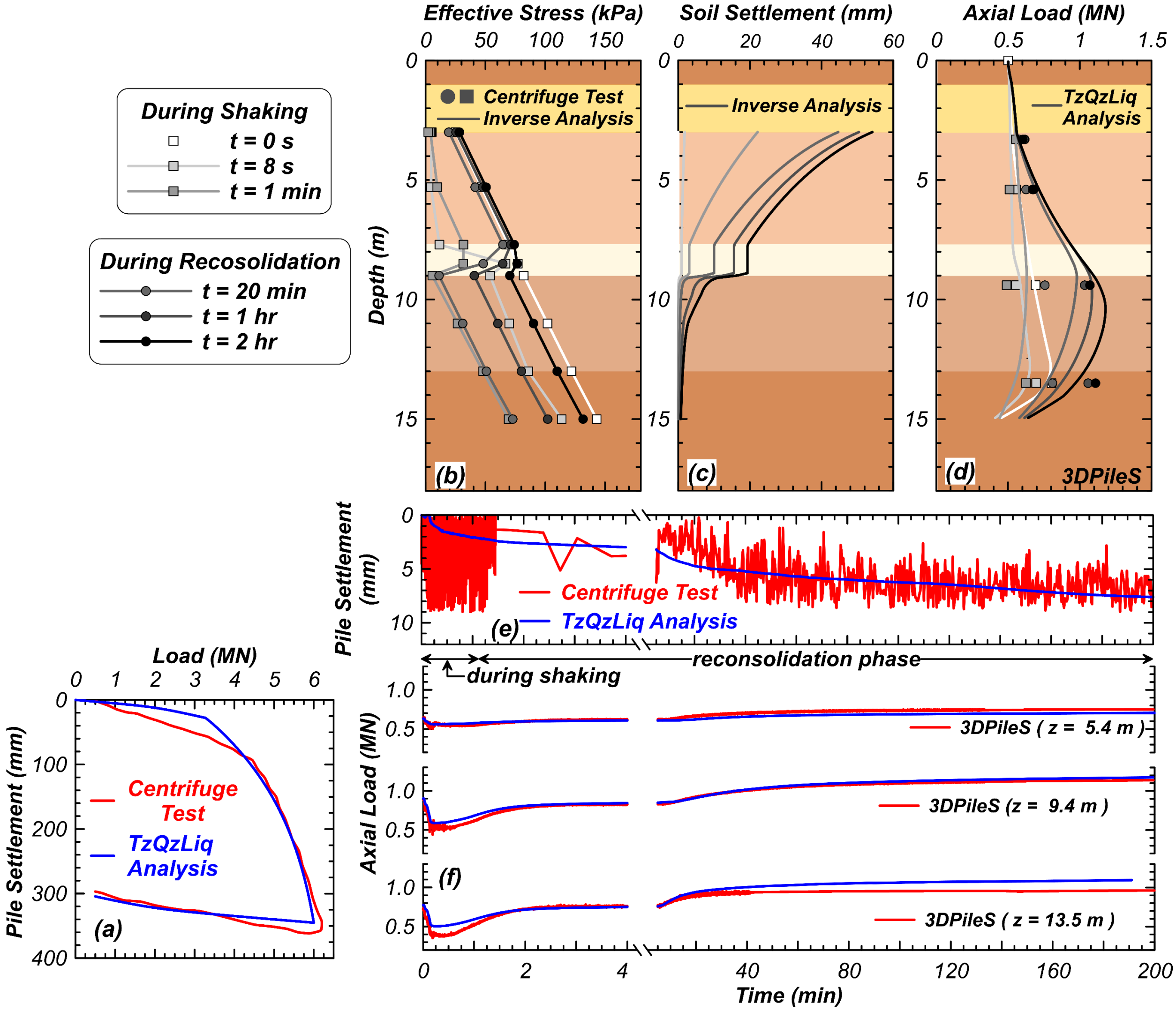

Figure 3.6. Validation of TzQzLiq analysis of 3DPileS for shaking event EQM4 in centrifuge model test SKS03: (a) Calibration of QzLiq material properties against pile load test data. Profiles of (b) effective stress, (c) soil settlement, and (d) axial load at selected times during shaking and reconsolidation. Time histories of (e) settlement and (f) axial load at the selected depths.

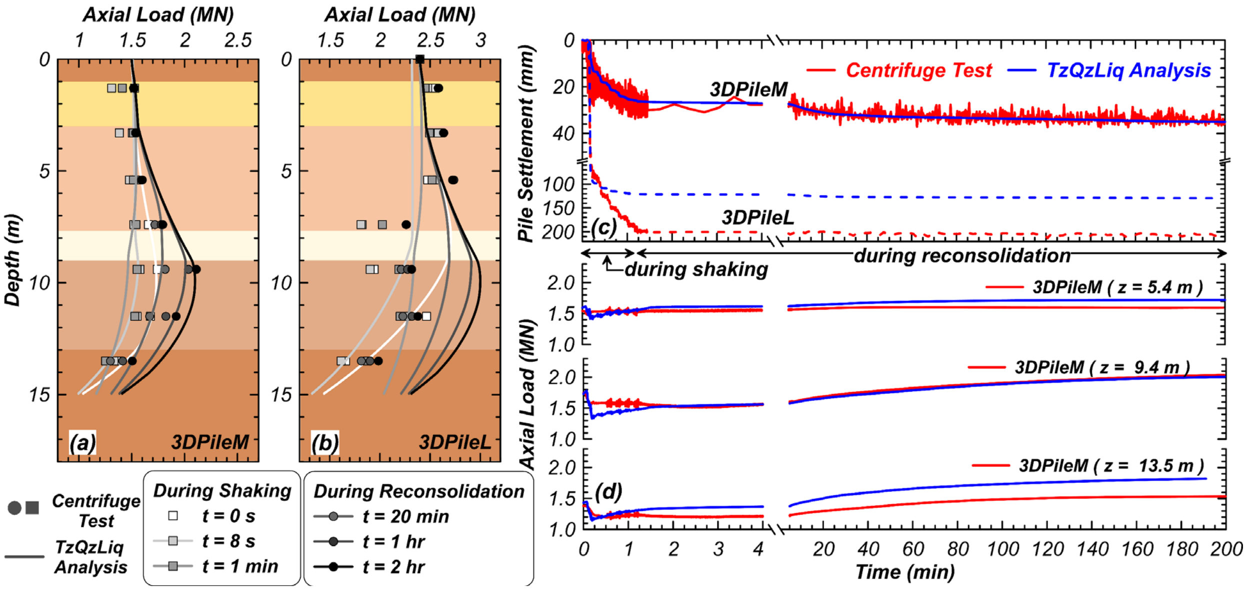

Figure 3.7. Validation of TzQzLiq analysis of 3DPileM and 3DPileL for shaking event EQM_4 in centrifuge model test SKS03: Axial load profiles of (a) 3DPileM and (b) 3DPileL at selected times during shaft and reconsolidation. Time histories of (c) settlement and (d) axial load of piles at the selected depths.

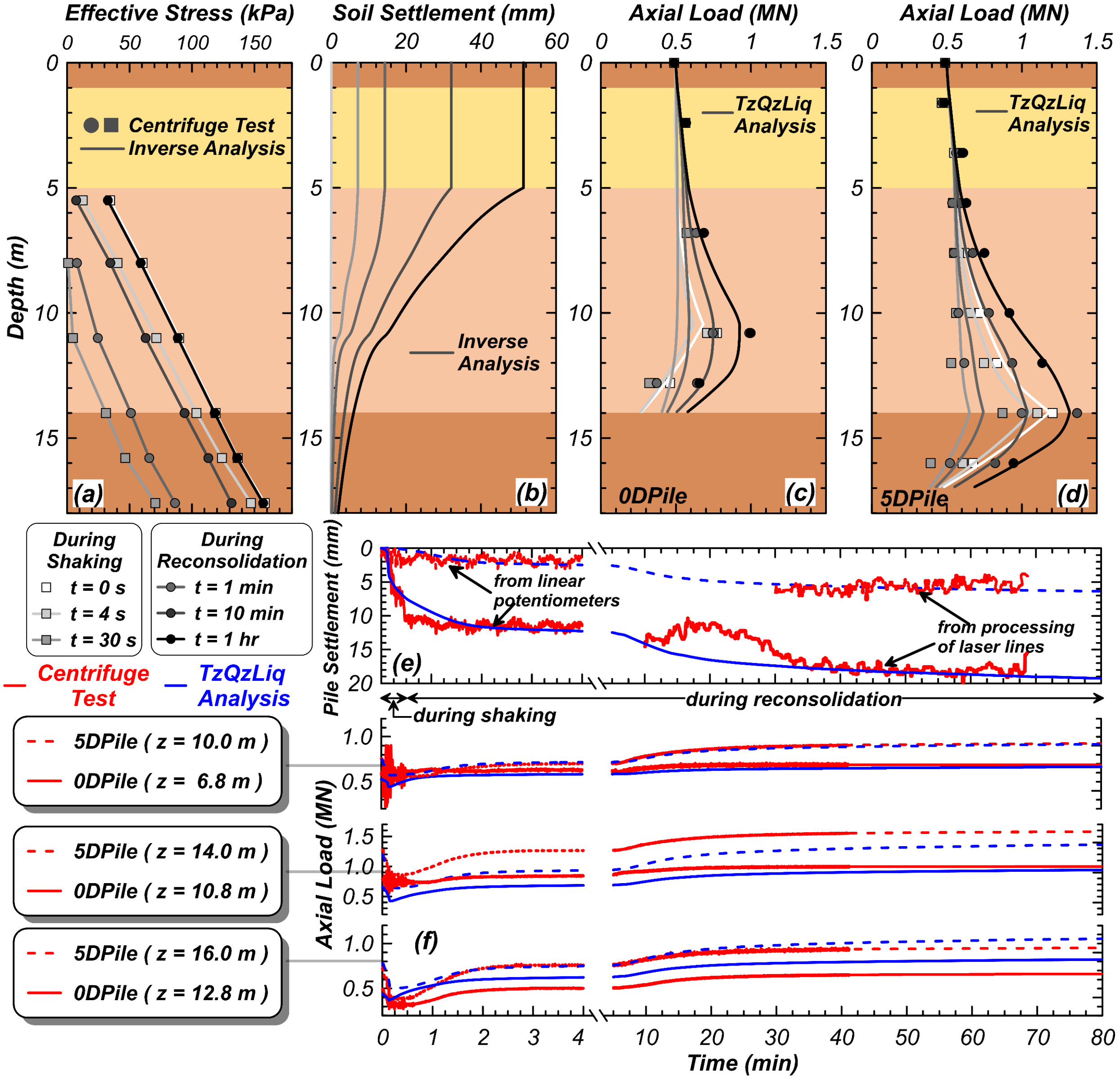

Figure 3.8. Validation of TzQzLiq analysis of 0DPile and 5DPile for shaking event EQM$_3$ in centrifuge model test SKS02: Profiles of (a) effective stress, (b) soil settlement, and axial load of (c) 0DPile and (d) 5DPile at selected times during shaking and reconsolidation. Time histories of (e) settlement and (f) axial load of piles at the selected depths.

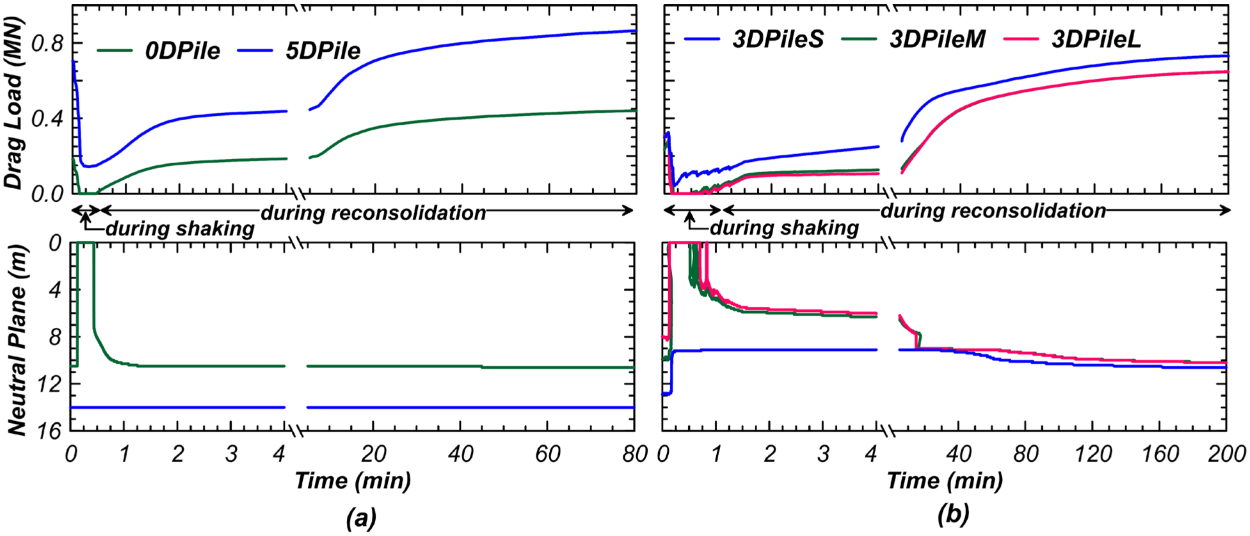

Figure 3.9. Results from the TzQzLiq analysis on time histories of drag load and neutral plane (depth of maximum load Q_{np}) for 0DPile, 5DPile, 3DPileS, 3DPileM, and 3DPileL.

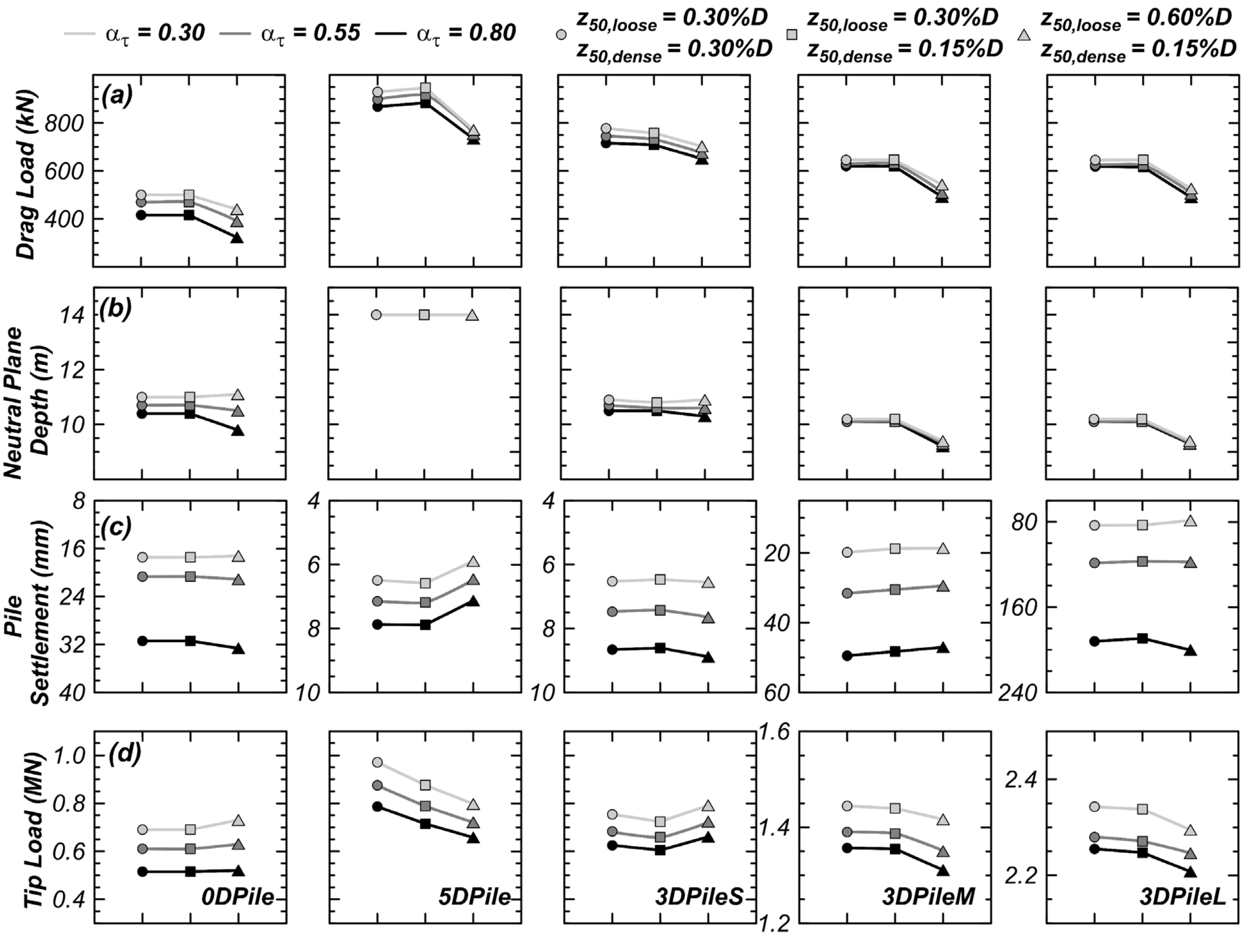

Figure 3.10. Results from the sensitivity study of QzLiq constant (α_t) and stiffness of TzLiq material in dense ($z_{50,dense}$) and loose sand ($z_{50,loose}$) on (a) drag load, (b) neutral plane depth, (c) pile settlement, and (d) mobilized tip load after complete reconsolidation for 0DPile, 5DPile, 3DPileS, 3DPileM, and 3DPileL for shaking events EQM$_3$ (in centrifuge model test SKS02) and EQM$_4$ (in centrifuge model test SKS03).

CHAPTER 4:

EFFECTS OF EXCESS PORE PRESSURE REDISTRIBUTION ON LIQUEFIABLE AND NON-LIQUEFIABLE LAYERS

4.1 Introduction

In recent years, significant progress has been made to develop simplified procedures (such as Idriss and Boulanger 2008; Youd et al. 2001) to evaluate the possibility of soil liquefaction during earthquakes or other types of cyclic loading conditions. In addition, analytical methods have been developed to estimate reconsolidation settlement (such as Tokimatsu and Seed (1984)), lateral spreading (Zhang et al. 2004), and excess pore pressures (u_e) in soil layers (Chiaradonna et al. 2018), which have been applied to study case histories (Bray and Macedo 2017; Chiaradonna et al. 2015; Seed and Seed 1967) for assessing the site performance under specified earthquake conditions. The foundation of the development of the above procedures is based on the undrained cyclic shear test on uniform soil specimens (for example, Lee and Albasia 1974; Nagase and Ishiharai 1988), where the effect of excess pore pressure dissipation and redistribution to the neighboring layers is neglected. Undrained tests on saturated specimens (e.g., cyclic triaxial compression or cyclic simple shear) have been used to determine the stress conditions under which the soil would generate excess pore pressure equal to the applied confining stress (initial liquefaction) and undergo large strains (cyclic mobility). For example, Ishihara and Yoshimine (1992) developed a methodology for estimating liquefaction-induced ground settlement based on many undrained cyclic simple shear tests on uniformly saturated specimens. However, natural soil deposits often consist of liquefiable and non-liquefiable layers where excess pore pressure migrates from one layer to another during and after shaking.

Redistribution can result in large excess pore pressures in the non-liquefiable layers and decreased excess pore pressures in the liquefiable layer. Accounting for the redistributed excess pore pressures is essential for quantification of consequences of liquefaction, including its effect on the capacity of pile foundations and liquefaction prevention in the liquefiable layers. During a shaking event, earthquake-induced excess pore pressures from the liquefiable layers would dissipate to the adjacent non-liquefiable layers, resulting in an increased excess pore pressure in non-liquefiable layers and decreased excess pore pressure in the liquefiable layers (Seed and Lee 1966). Yoshimi and Kuwabara (1973) studied excess pore pressure development from a non-liquefiable layer caused by redistributing excess pore pressures from an overlying reconsolidating liquefied layer. They found that as the liquefied soil reconsolidated, the excess pore pressures in the non-liquefiable layer increased and reached a peak value, after which the excess pore pressures in both layers together decreased. They also found that if the compressibility of the non-liquefiable layer was two orders magnitude smaller than the compressibility of the liquefied layer, very large excess pore pressure could be developed in the non-liquefiable layer. Seed et al. (1976) developed a numerical model to estimate excess pore pressures in the soil layers considering redistribution. The model accounted for excess pore pressures generation from cyclic loading and dissipation from reconsolidation. While these studies have made a significant contribution in understanding the distribution of excess pore pressure in the layers adjacent to liquefied soil, their usage in the simplified procedures has still been limited. Mele et al. (2021) developed a simplified model to estimate excess pore pressures in soil layers following liquefaction triggering procedures from Idriss and Boulanger (2008); however, they did not consider the redistribution effects. Considering redistribution would increase excess pore pressures in the non-liquefiable layers and decrease excess pore pressures in the liquefiable layer. The redistributed excess pore pressures in non-liquefiable layers could severely affect the performance of geotechnical structures. For example, high excess pore pressures around the pile and below the tip would reduce the pile’s shaft and tip resistance and cause settlement (Sinha et al. 2021f). On the other hand, a decrease of excess pore pressures within the liquefiable layers can increase its liquefaction resistance and potentially benefit the projects affected by thin and deep liquefiable soil layers by eliminating the need for ground improvement or other liquefaction mitigation efforts.

This chapter describes an approximate procedure for estimating peak excess pore pressures in the non-liquefiable layer following redistribution from the adjacent reconsolidating liquefied layer. It describes redistribution effects on two primary types of layered systems: non-liquefiable layer below the liquefied layer and non-liquefiable above the liquefied layer. The chapter also provides a criterion on the minimum thickness of the liquefiable layer below which redistribution would prevent liquefaction in that layer. Finally, the proposed approximate procedure is applied on selected shakings of centrifuge tests involving liquefaction of layered soil profiles, and results are compared.

4.2 Analytical Framework

When a soil layer liquefies (i.e., the excess pore pressure ratio $r_u = u_e/\sigma'_{vo} = 1$), the compressibility of the layer significantly increases depending upon the extent of liquefaction and initial relative density (Seed et al. 1976). The increase in the compressibility is due to two mechanisms: (1) the nonlinearity of the unloading-reloading compression curve, and (2) volume change that occurs due to sedimentation while the soil is liquefied (i.e., while $r_u = 1$) (Scott 1986). As soil sediments and reconsolidates, water moves from the reconsolidating liquefied layer (with high u_e) to the non-liquefiable layer (with small u_e). The water movement decreases u_e in the reconsolidating liquefied layer and increases u_e in the non-liquefiable layer achieving a peak value of excess pore pressure in the non-liquefiable layer. After that, u_e in the non-liquefiable layer starts to decrease together with the reconsolidating liquefied layer. The rate and amount of water movement between the two layers depend upon their permeability (k), compressibility (m_v), and hydraulic boundary conditions around them.

For assessing the excess pore pressure increase due to redistribution in a 1- dimensional layered deposit, the knowledge of soil permeability is not critical because it occurs after shaking, and time is essentially unlimited after shaking. The redistribution of excess pore pressures into non-liquefiable layers may be assumed to occur some uncertain and relatively unimportant amount of time after shaking. The magnitude of the pore pressure redistribution is much more important than the time required for pore pressure redistribution. For example, prediction of the time at which a pile's capacity would decrease is secondary in importance compared to predicting that the pile capacity would decrease. Determination of the peak excess pore pressure in the non-liquefiable layer from redistribution could be estimated by tracking the movement of water between the non-liquefiable layer and reconsolidating liquefied layers.

On the other hand, precluding liquefaction due to redistribution requires adequate permeability to produce significant drainage during generation (e.g., during earthquake shaking). Suppose the soil permeabilities are relatively large and the thickness of the liquefiable layer is smaller than the non-liquefiable layer. In that case, dissipation caused by redistribution could potentially prevent the initially assumed liquefiable layer from liquefying. Determining the maximum thickness of a layer that can be prevented from liquefying would require estimating the excess pore pressure generation and dissipation rates and then integrating them over the entire duration of shaking.

The following section describes the effects of redistribution in increasing excess pore pressures in the non-liquefiable layers and increasing liquefaction resistance in the liquefiable layers. Please note that the terms "liquefiable" (Lu) and "non-liquefiable" (NLu) for the soil layers in this chapter are described with reference to the state of soil layers under undrained cyclic loading. "Lu" corresponds to the soil layer that would liquefy due to undrained loading. Similarly, "NLu" refers to the soil layers that will not be liquefied due to undrained loading. Making a clear distinction about the description of soil layers as NLu and Lu was importation because potential all the soil layers can be made into the liquid state or prevented from becoming into the liquid state by either injecting or removing sufficient water. For example, as expected, the movement of water from redistribution can cause liquefaction in the NLu layers and, at the same time, can also prevent liquefaction in the Lu layers.

4.3 Redistributed Excess Pore Pressures in Two-Layered Systems

For simplicity, the redistribution of excess pore pressures is analyzed for two types of layered systems, depending on whether the Lu layer is above (Figure 4.1 (a)) or below (Figure 4.1 (b)) the NLu layer. For being conservative, the two-layered systems are assumed to be surrounded by impermeable layers, neglecting drainage outside these two layers. In both cases, the top of the NLu layer is defined at a depth Z. The results from these two primary layered systems act as a basis for estimating excess pore pressures in multi-layered soil profiles (described later in section 4.4). When the NLu is above the Lu layer, redistribution of excess pore pressures can potentially liquefy the NLu layer [Figure 4.1 (a)]. When the NLu layer occurs below the Lu layer, pore pressures will increase; however, full liquefaction will not occur because excess pore pressures from redistribution will not exceed the excess pore pressure in the overlying Lu layer [Figure 4.1 (b)]. The approximate possible redistributed excess pore pressure (u_e^d) profiles (at times when the redistributed excess pore pressure achieves its peak value in NLu layer) for the primary two-layered systems are shown by solid red lines in Figure 4.1. Please note that the redistributed excess pore pressure (u_e^d) profiles shown in Figure 4.1 approximate the actual excess pore pressures profiles. The average excess pore pressure ratio (r_u^d) in the NLu and Lu layers following redistribution can be obtained by assuming volume conservation between the impermeable boundaries. The conservation of volume can be written as

$$m_{v-Lu} H_{liq}\, \sigma'_{vo-Lu}\left(r_{u-Lu}^{u} - r_{u-Lu}^{d}\right) = m_{v-NLu} H_{NLu}\, \sigma'_{vo-NLu}\left(r_{u-NLu}^{d} - r_{u-NLu}^{u}\right) \qquad 4.1$$

where (H_{Lu} and H_{NLu}) is the thickness, (m_{v-Lu} and m_{v-NLu}) is the average compressibility, (σ'_{vo-Lu} and σ'_{vo-NLu}) is the average initial effective stress, and (r_{u-Lu}^{u} and r_{u-NLu}^{u}) is the average earthquake-induced excess pore pressure ratio for the (Lu and NLu) layers [Figure 4.1]. The term r_{u-NLu}^{d} represent the average peak redistributed excess pore pressure ratio in the NLu Layer, and r_{u-Lu}^{d} is the the corresponding redistributed excess pore pressure ratio in the Lu layer. Similarly, the terms (u_{e-Lu}^{u} and u_{e-NLu}^{u}) and (u_{e-Lu}^{d} and u_{e-NLu}^{d}) represent the average earthquake-induced ($u_e^u = r_u^u\, \sigma'_{vo}$) and redistributed ($u_e^d = r_u^d\, \sigma'_{vo}$) excess pore pressures in the (Lu and NLu) layers. In the excess pore pressures (u_e^u, u_e^d) and excess pore pressure ratio (r_u^u, r_u^d) terms, the superscript “u” refers to undrained loading conditions (such as earthquake loading), and “d” refers to the redistribution effect. Solving Equation 4.1 for the different excess pore pressure profiles for the primary two types of layered systems [Figure 4.1] can provide estimates of $r_{u-Lu}^{d}\ and\ r_{u-NLu}^{d}$ in the Lu and NLu layers, respectively. While solving Equation 4.1, the Lu layer is assumed to be a reconsolidating liquefied layer with $r_{u-Lu}^{u} = 1.0$.

NLu Layer Above a Lu Layer

When an NLu layer is above a Lu layer, the high compressibility of the Lu layer and comparatively lower initial effective stress (σ'_{vo-NLu}) of the NLu layer can lead to high r^d_{u-NLu}. For relatively thick Lu layers, r^d_{u-NLu} values may even reach 1 [Figure 4.1 (a).]. Yoshimi and Kuwabara (1973) note that the sub-surface NLu layer can get liquefied for a relatively high compressibility ratio (m_{v-Lu}/m_{v-NLu} in order of 10 or more) depending upon the relative thicknesses (H), earthquake-induced excess pore pressure ratios (r^u_u), and depth of the layers (Z). The possible redistributed excess pore pressures profiles corresponding to peak redistributed excess pore pressures in NLu layer are shown in Figure 4.1 (a). During reconsolidation, excess pore pressures would begin dissipating from the bottom of the Lu layer of a thickness (ℓ), as shown in u^d_e Profile 1 in Figure 4.1 (a). For thin NLu layers, redistribution can cause complete liquefaction in the NLu layer $\left(i.e., r^d_{u-NLu} = 1.0\right)$, if the redistributed excess pore pressure in Lu layer (u^d_{e-Lu}) is higher than the effective stress at the bottom of the non-liquefiable layer (i.e., for $\ell < H_{Lu}$ in u^d_e Profile 1 shown in Figure 4.1 (a)). The thickness (ℓ) of the Lu layer that will result in complete liquefaction of the NLu layer can be obtained by solving Equation 4.1 for the u^d_e Profile 1 [shown in Figure 4.1 (a)] as

$$\ell = H_{Lu}\sqrt{\frac{2\overline{H}}{\overline{m_v}}\,\frac{\sigma'_{vo-NLu}}{\gamma' H_{Lu}}\left(1 - r^u_{u-NLu}\right)} \qquad 4.2$$

where, $\overline{m_v} = \frac{m_{v-Lu}}{m_{v-NLu}}$ is the compressibility ratio, $\overline{H} = \frac{H_{NLu}}{H_{Lu}}$ is the thickness ratio, and γ' is the effective unit weight of the layer. For $\ell < H_{Lu}$, complete liquefaction is achieved in the NLu layer (i.e., r^d_{u-NLu}=1.0). As the thickness of the NLu layer increases, redistribution results in u^d_e Profile 2 as shown in Figure 4.1 (a). The peak redistributed excess pore pressure in the NLu layer (u^d_{e-NLu})

equals σ'_{vo} at its top and u^d_{e-Lu} at its bottom (Yoshimi and Kuwabara 1973). For a large thickness of the NLu layer, redistribution results in equalized excess pore pressures in both the Lu and NLu layers, as shown in u^d_e Profile 3 of Figure 4.1 (a). The resulting average peak redistributed excess pore pressure ratio (r^d_{u-NLu}) in the NLu layer and correspondingly the average redistributed excess pore pressure ratio (r^d_{u-Lu}) in the Lu layer obtained for the three different u^d_e Profiles [Figure 4.1 (a)] is shown in Equations 4.3 and 4.4. below.

$$r^d_{u-NLu} = \begin{cases} 1, & \dfrac{\ell}{H_{Lu}} < 1 \\ \dfrac{r^u_{u-NLu} + \dfrac{\overline{m_v}}{\overline{H}}\,\dfrac{\sigma'_{vo-Lu} + \sigma'_{vo-NLu} - \gamma' H_{NLu}/2}{\sigma'_{vo-NLu}}}{1 + 2\,\dfrac{\overline{m_v}}{\overline{H}}}, & 1 - \dfrac{\gamma' H_{NLu}/2}{\sigma'_{vo-NLu}} \leq r^d_{u-NLu} \leq 1.0 \\ \dfrac{r^u_{u-NLu} + \dfrac{\overline{m_v}}{\overline{H}}\,\dfrac{\sigma'_{vo-Lu}}{\sigma'_{vo-NLu}}}{1 + \dfrac{\overline{m_v}}{\overline{H}}}, & r^d_{u-NLu} \leq 1 - \dfrac{\gamma' H_{NLu}/2}{\sigma'_{vo-NLu}} \end{cases} \tag{4.3}$$

$$r^d_{u-Lu} = \begin{cases} 1 - \dfrac{\gamma' \ell/2}{\sigma'_{vo-Lu}}, & \dfrac{\ell}{H_{Lu}} \leq 1 \\ \dfrac{\dfrac{(2r^u_{u-NLu} - 1)\sigma'_{vo-NLu} + \gamma' H_{nliq}/2}{\sigma'_{vo-Lu}} + \dfrac{2\overline{m_v}}{\overline{H}}}{1 + 2\,\dfrac{\overline{m_v}}{\overline{H}}}, & \dfrac{\sigma'_{vo-NLu} - \gamma' H_{NLu}/2}{\sigma'_{vo-Lu}} \leq r^d_{u-Lu} \leq 1 - \dfrac{\gamma' H_{Lu}/2}{\sigma'_{vo-Lu}} \\ \dfrac{r^u_{u-NLu}\,\dfrac{\sigma'_{vo-NLu}}{\sigma'_{vo-Lu}} + \dfrac{\overline{m_v}}{\overline{H}}}{1 + \dfrac{\overline{m_v}}{\overline{H}}}, & r^d_{u-Lu} \leq \dfrac{\sigma'_{vo-NLu} - \gamma' H_{NLu}/2}{\sigma'_{vo-Lu}} \end{cases} \tag{4.4}$$

It can be observed from Equation 4.3 that as compressibility ratio ($\overline{m_v}$) increases, the peak redistributed excess pore pressure ratio (r_{u-NLu}^{d}) in the NLu layer also increases. Figure 4.2 shows the redistributed excess pore pressure ratio (r_u^d) of the NLu and Lu layer as a function of thickness ratio ($\overline{H}$) for a compressibility ratio of $\overline{m_v} = 50$, earthquake-induced excess pore pressure ratio (r_{u-NLu}^{u}) of 0, 0.5, and 0.9 and a unit thickness of the NLu layer ($H_{NLu} = 1\ m$) at a depth of $Z = 10\ m$. As expected, the redistributed excess pore pressure ratio (r_u^d) in both layers (Lu and NLu) decreases as the thickness ratio ($\overline{H}$) increases. For very large thickness ratio ($\overline{H}$), r_{u-NLu}^{d} asymptotically approaches to r_{u-NLu}^{u}, whereas r_{u-Lu}^{d} asymptotically approaches $\frac{r_{u-NLu}^{u}}{1+H_{NLu}/Z}$ [Figure 4.2]. Since u_e^d becomes uniform after excess pore pressures equalization and NLu is above the Lu Layer; r_u^d in both the layers decreases with depth (Z) and (r_u^d) in the NLu layer is greater than that in the Lu layer [Figure 4.2]. The midpoint of the transition curve occurs at a thickness ratio of about 50, consistent with the assumed compressibility ratio of about 50 used to create this figure. While redistribution increased excess pore pressure in the NLu Layer $\left(r_{u-NLu}^{d} > r_{u-NLu}^{u}\right)$, it decreased excess pore pressures in the Lu layer $\left(r_{u-Lu}^{d} < r_{u-Lu}^{u}\right)$. This decrease of excess pore pressures in the Lu layer from redistribution during shaking can produce significant drainage and increase its liquefaction resistance, especially for the deeply embedded thin Lu layers. The discussion on the effect of redistribution in increasing the liquefaction resistance of Lu layers is presented later in a separate section.

NLu Layer Below a Lu Layer

When an NLu layer is below a Lu layer, the movement of water from the Lu layer results in the equalization of excess pore pressures while forming a water-film layer at the impermeable boundary above the Lu layer (Sinha et al. 2021f) [Figure 4.1 (b)]. With the assumption that reconsolidation of the Lu layer results in water movement only in the NLu layer with no formation of the water film layer, Equation 4.1 can be solved to get the average peak redistributed excess pore pressure ratio (r_{u-NLu}^{d}) in the NLu layer and the corresponding r_{u-Lu}^{d} in the Lu layer. The approximate possible u_e^d Profiles (1 and 2) for the case of the NLu layer below a Lu layer are shown in Figure 4.1 (b). During reconsolidation, excess pore pressures would begin dissipating from the bottom of the Lu layer of a thickness (ℓ) as shown in u_e^d Profile 1 in Figure 4.1 (b). For a thin Lu layer, the maximum peak excess pore pressure that can get developed in the NLu layer is equal to the effective stress at the bottom of the Lu layer (i.e., $u_{e-NLu}^{d} = \sigma_{vo-Lu}' + \gamma' H_{Lu}/2 \; for \; \ell \rightarrow 0$). If the earthquake-induced excess pore pressure in the NLu layer is larger than the effective stress at the bottom of the Lu layer (i.e., $u_{e-NLu}^{d} > \sigma_{vo-Lu}' + \gamma' H_{Lu}/2$), no redistribution toward the NLu layer would occur. As the thickness of the NLu layer increases, the thickness of the liquefied layer (ℓ) contributing to redistribution increases [Figure 4.1 (b)]. For u_e^d Profile 1 in Figure 4.1 (b), the equalized excess pore pressure in the NLu layer (u_{e-NLu}^{d}) would then correspond to the excess pore pressure at a distance (ℓ) from the bottom of the Lu layer. For very thick non-liquefiable layers, the full thickness of the Lu layer ($\ell = H_{Lu}$) would contribute to redistribution and correspondingly will result in u_e^d Profile 2 as shown in Figure 4.1 (b). The thickness of the Lu layer contributing to redistribution can be obtained by solving Equation 4.1 for u_e^d Profile 1 [shown in Figure 4.1 (b)] as

$$\frac{\overline{m_v}}{2}\left(\frac{\ell}{H_{Lu}}\right)^2 + \overline{H}\frac{\ell}{H_{Lu}} - \overline{H}\left((1 - r_{u-NLu}^{u})\frac{\sigma_{vo-NLu}'}{\gamma' H_{Lu}} - \frac{\overline{H}}{2}\right) = 0 \qquad 4.5$$

where a solution of the thickness $\ell \leq H_{Lu}$ indicate that only a small thickness (ℓ) of the Lu layer participates in redistribution and results in u_e^d Profile 1 as shown in Figure 4.1 (b). Any other solution would indicate the participation of full-thickness ($\ell = H_{Lu}$) of Lu layer resulting in u_e^d

Profile 2 as shown in Figure 4.1 (b). The resulting average peak redistributed excess pore pressure ratio (r_{u-NLu}^{d}) in the NLu layer and correspondingly the average redistributed excess pore pressure ratio (r_{u-Lu}^{d}) in the Lu layer obtained for the two different u_e^d Profiles [Figure 4.1 (b)] is shown in Equations 4.6 and 4.7 on the following page.

It can be observed from Equations 4.6 and 4.7 that with the increase in compressibility ratio ($\overline{m_v}$) and the earthquake-induced excess pore pressure ratio (r_{u-NLu}^{u}), the peak redistributed excess pore pressure ratio in the NLu layer (r_{u-NLu}^{d}) also increases. Figure 4.3 shows the average redistributed excess pore pressure ratio (r_u^d) as a function of thickness ratio ($\overline{H}$) for a compressibility ratio of $\overline{m_v} = 50$, earthquake induced excess pore pressure ratio (r_{u-Nlu}^{u}) of 0, 0.5, and 0.9 and a unit thickness of the NLu layer (H_{NLu}=1 m) at a depth of Z = 10 m. As expected, as the thickness ratio ($\overline{H}$) increases, the r_u^d decreases, and asymptotically approaches to $r_{u-NLu}^{d} = r_{u-NLu}^{u}$ and $r_{u-Lu}^{d} = r_{u-NLu}^{u}\ (1 + 0.5H_{NLu}/Z)$ in the NLu and Lu layers, respectively. Again, since u_e^d becomes uniform after excess pore pressures equalization and Lu layer is above the NLu layer; r_u^d is higher in the Lu layer than the NLu layer (i.e., $r_{u-Lu}^{d} \geq r_{u-NLu}^{d}$). For this layered profile as well, redistribution resulted in decreased excess pore pressure in the LU layer $\left(r_{u-Lu}^{d} < r_{u-Lu}^{u}\right)$ and increased excess pore pressure in the NLu layer $\left(r_{u-NLu}^{d} > r_{u-NLu}^{u}\right)$. The resulting increase in liquefaction resistance of the Lu layer from redistribution is discussed later in a separate section.

$$r^{d}_{u-NLu} = \begin{cases} r^{u}_{u-NLu}, & r^{u}_{u-NLu} \geq 1 - \dfrac{\gamma' H_{NLu}/2}{\sigma'_{vo-NLu}} \\ 1 - \dfrac{\gamma'(\ell + \frac{H_{NLu}}{2})}{\sigma'_{vo-NLu}}, & \dfrac{\ell}{H_{Lu}} < 1, r^{u}_{u-NLu} \leq 1 - \dfrac{\gamma' H_{NLu}/2}{\sigma'_{vo-NLu}} \\ \dfrac{\frac{\overline{m_v}}{\overline{H}} \frac{\sigma'_{vo-Lu}}{\sigma'_{vo-NLu}} + r^{u}_{u-NLu}}{\left(1 + \frac{\overline{m_v}}{\overline{H}}\right)}, & r^{d}_{u-NLu} \leq \dfrac{\sigma'_{vo-Lu} - \gamma' H_{Lu}/2}{\sigma'_{vo-NLu}}, r^{u}_{u-NLu} \leq 1 - \dfrac{\gamma' H_{NLu}/2}{\sigma'_{vo-NLu}} \end{cases} \tag{4.6}$$

$$r^{d}_{u-Lu} = \begin{cases} 1.0, & r^{u}_{u-NLu} \geq 1 - \dfrac{\gamma' H_{NLu}/2}{\sigma'_{vo-NLu}} \\ 1 - \dfrac{\gamma' \ell/2}{\sigma'_{vo-Lu}}, & \dfrac{\ell}{H_{Lu}} < 1, r^{u}_{u-NLu} \leq 1 - \dfrac{\gamma' H_{NLu}/2}{\sigma'_{vo-NLu}} \\ \dfrac{\frac{\overline{m_v}}{\overline{H}} + r^{u}_{u-NLu} \frac{\sigma'_{vo-NLu}}{\sigma'_{vo-Lu}}}{\left(1 + \frac{\overline{m_v}}{\overline{H}}\right)}, & r^{d}_{u-Lu} \leq \dfrac{\sigma'_{vo-Lu} - \gamma' H_{Lu}/2}{\sigma'_{vo-Lu}}, r^{u}_{u-NLu} \leq 1 - \dfrac{\gamma' H_{NLu}/2}{\sigma'_{vo-NLu}} \end{cases} \tag{4.7}$$

4.4 Redistributed Excess Pore Pressure in Multi-Layered Systems

Redistributed excess pore pressures in the multi-layered system can be obtained by decomposing the multi-layered system into many primary layered systems of NLu layer above or below the Lu layer [Figure 4.4]. In multi-layered layered systems, redistribution of excess pore pressure in the NLu layer can occur from the Lu layer above and below it. Similarly, dissipation of excess pore pressures from the Lu layer can also occur in either direction: to the NLu layer above and below it. As described earlier, the maximum possible r_u^d in an NLu layer below a Lu layer equals the effective stress at the bottom of the Lu layer. On the other hand, if the NLu layer is above the Lu layer, redistribution can cause liquefaction in the NLu layer ($r_{u-NLu}^d = 1.0$). Thus, a reasonable and simple way to split the multi-layered system and prevent the double counting the redistribution effect in both (upward and downward) directions is to (wherever possible) decompose the multi-layered system into multiple units of the primary layered system of an NLu layer above a Lu layer [Figure 4.4].

The presence of an impermeable layer within the multi-layered system can result in two additional types of subsystems: an NLu layer sandwiched between two Lu layers and a Lu layer sandwiched between two NLu layers. For example, in the multi-layered system presented in Figure 4.4, the presence of the clay layer results in two subsystems: a Lu layer (# 4) sandwiched between the NLu layers (# 3 and 5) and an NLu layer (# 8) sandwiched between the Lu layers (# 7 and 9). Similarly, the no drainage condition beneath layer 14 results in a subsystem with a Lu Layer (# 13) sandwiched between two NLu layers (# 12 and 14). The following subsections describe the redistributed excess pore pressures for the two additional subsystems.

Lu Layer Sandwiched Between NLu Layers

For the subsystem of a Lu layer sandwiched between two NLu layers, the excess pore pressures in the NLu layer can be estimated conservatively by assuming full participation of the Lu layer in developing redistributed excess pore pressures in both NLu layers above and below it. An equivalent would be to decompose the subsystem into two primary systems: an NLu layer above the Lu layer and an NLu layer below the Lu layer. And then individually calculate the peak redistributed excess pore pressures in both the NLu layers. The redistributed excess pore pressure in the sandwiched Lu layer can be conservatively taken equal to the minimum of the u_{e-Lu}^{d} calculated from the two primary systems. For example, in Figure 4.4, the Lu layer (4) sandwiched between two NLu layers (# 3 and 5) is decomposed into the two primary layers: an NLu layer (# 3) above the Lu layer (# 4) and an NLu layer (# 5) below the Lu layer (# 4). In order to find the redistributed excess pore pressure in the NLu layers ($u_{e-NLu\#3}^{d}$ and $u_{e-NLu\#5}^{d}$) and Lu layer ($u_{e-Lu\#4}^{d}$), let's assume ($u_{e-NLu\#3}^{d-Lu\#4}$ and $u_{e-NLu\#5}^{d-Lu\#4}$) represent the u_e^d in NLu layers (# 3 and 5) from the adjacent Lu layer (#4) and ($u_{e-Lu\#4}^{d-NLu\#3}$ and $u_{e-Lu\#4}^{d-NLu\#5}$) represent the u_e^d in the Lu layer (#4) from the adjacent NLu layers (#3 and 5). Then, the u_e^d in the Lu and NLu layers are taken as $u_{e-NLu\#3}^{d} = u_{e-NLu\#3}^{d-Lu\#4}$, $u_{e-NLu\#5}^{d} = u_{e-NLu\#5}^{d-Lu\#4}$, and $u_{e-Lu\#4}^{d} = min(u_{e-Lu\#4}^{d-NLu\#3}, u_{e-Lu\#4}^{d-NLu\#5})$.

NLu Layer Sandwiched Between Lu Layers

For the subsystem of the NLu layer sandwiched between two Lu layers, the excess pore pressures in the NLu layers can be estimated conservatively by taking the contributions from both Lu layers. The steps involve estimating the redistributed excess pore pressures from the Lu layer above it and then assuming it as an earthquake-induced excess pore pressure to obtain the final redistributed excess pore pressure in the NLu layer from the Lu layer below it. For example, in

Figure 4.4, the redistributed excess pore pressure in the NLu layer (# 8) sandwiched between two Lu layers (# 7 and 9) is obtained by decomposing the subsystem into two primary systems: the NLu layer (# 8) below the Lu layer (# 7) and the NLu layer (# 8) above a Lu layer (# 9). First, the redistributed excess pore pressure ($u_{e-NLu\#8}^{d-Lu\#7}$) in the NLu layer (# 8) is evaluated from the Lu layer (# 7) above it. The obtained redistributed pore pressure is then taken as the earthquake-induced pore pressure (i.e., $u_{e-NLu\#8}^{u} = u_{e-NLu\#8}^{d-Lu\#7}$) to estimate the final redistributed excess pore pressure ($u_{e-NLu\#8}^{d} = u_{e-NLu\#8}^{d-Lu\#9}$) in the NLu layer from the Lu layer (# 9) below it. The redistributed excess pore pressure in the Lu layers is taken as $u_{e-Lu\#7}^{d} = u_{e-Lu\#7}^{d-NLu\#8}$ and $u_{e-Lu\#9}^{d} = u_{e-Lu\#9}^{d-NLu\#8}$. Later in this chapter section 4.7, the developed approximate procedure is applied on selected shakings of centrifuge test on multi-layered soil systems; and the predicted peak excess pore pressure in the soil layers are compared with measurements from pore pressure transducers.

4.5 Increased Liquefaction Resistance by Redistribution

This section evaluates the potential by redistribution on preventing liquefaction in the Lu layer (a layer that would be expected to liquefy during undrained loading). The analytical framework described in the above sections showed that for large thickness ratio ($\overline{H}$), redistribution can significantly reduce excess pore-pressures in the Lu layer. During shaking, a partially drained condition exists, where the undrained loading generates excess pore pressures in the Lu layer while redistribution decreases it. If the dissipation rate from redistribution is fast compared to the generation rate, it can eventually prevent liquefaction in the Lu layer. However, if redistribution occurs too slow, liquefaction may not be prevented in the Lu layer. Thus, determining the rate of excess pore pressure generation (from undrained loading) and dissipation (from redistribution) during shaking is essential to determine the conditions when redistribution can prevent liquefaction in the Lu layer. The net effect from generation and dissipation processes is the result of a partially drained ("pd") excess pore pressure ratio (r_{u-Lu}^{pd}) in the Lu layer.

Rate of Excess Pore Pressure Dissipation

In the previous sections, redistributed excess pore pressure ratio in the Lu layer (r_{u-Lu}^{d}) was calculated at the end of shaking when the Lu layer was reconsolidating from the liquefied state (i.e., $r_{u-Lu}^{u} = 1$) [Equations 4.4 and 4.7]. A simplified and conservative way of estimating the redistributed excess pore pressure ratio $r_{u-Lu}^{d}(t)$ at any time (t) during shaking is linear scaling of r_{u-Lu}^{d} with the partially drained excess pore pressure ratio ($r_{u-Lu}^{pd}(t)$) in the Lu layer [Equation 4.8].

$$r_{u-Lu}^{d}(t) = r_{u-Lu}^{pd}(t)\, r_{u-Lu}^{d} \qquad 4.8$$

The assumption of linear-scaling of the r_{u-Lu}^{d} with $r_{u-Lu}^{pd}(t)$ would be generally valid for the u_e^d Profiles (Profile 3 in Figure 4.1 (a) and Profile 2 in Figure 4.1 (b)) where the excess pore pressure is fully equalized between the Lu and the NLu layers. During shaking, since the excess pore pressures are still developing, redistribution would likely result in fully equalized u_e^d profiles. Furthermore, since we are primarily interested in increased liquefaction resistance of thin liquefiable layers adjacent to thick liquefiable layers, r_{u-Lu}^{d} would likely result from fully equalized u_e^d profiles. Suppose the r_{u-Lu}^{d} is the result from the other u_e^d profiles shown in Figure 4.1, the assumption of linear scaling would be conservative as those profiles would result in higher r_{u-Lu}^{d}(t).

With the estimated $r_{u-Lu}^{d}(t)$, the dissipation of the excess pore pressure ratio in the Lu layer from redistribution at any time (t) can be reasonably represented equivalent to the dissipation of uniform excess pore pressure ratio of ($r^{pd}_{u-Lu}(t) - r^{d}_{u-Lu}(t)$) with a single drainage boundary condition. The rate of dissipation ($\dot{r}^{d}_{u-Lu}(t)$) can then be estimated as

$$\begin{gathered} \dot{r}^{d}_{u-Lu}(t) = r^{pd}_{u-Lu}(t)\, \dot{r}^{d}_{u-Lu} \\ \dot{r}^{d}_{u-Lu} = \frac{\left(1 - r^{d}_{u-Lu}\right)}{t_d} \end{gathered} \qquad 4.9$$

where t_d is the dissipation time required to achieve the redistributed excess pore pressure ratio (r^{d}_{u-Lu}) in the reconsolidating liquefied Lu layer. As expected, the time required for dissipation (t_d) is larger for smaller r^{d}_{u-Lu}. Later in this chapter, Section 4.6 describes the procedure for estimating dissipation time (t_d).

Rate of Excess Pore Pressure Generation

The average rate of excess pore pressure ratio generation ($\dot{r}^{u}_{e-Lu}(t)$) in the Lu layer can be estimated from the rate of undrained loading (Seed et al. 1976) at an arbitrarily defined stress level (τ) as

$$\dot{r}^{u}_{u-Lu}(t) = \dot{r}^{u}_{u-Lu} = \left(\frac{N_u}{N_{Lu}}\right)\frac{1}{t_g} \qquad 4.10$$

where N_{Lu} is the number of shear stress (τ) cycles required to cause liquefaction, N_u is the equivalent number of shear stress (τ) cycles of undrained loading, and t_g is the loading duration. The cycle ratio $\left(\frac{N_u}{N_{Lu}}\right)$ can be substituted in terms FS_{Lu} defined as the factor of safety against liquefaction and the parameter b defined as the slope of cyclic resistance ratio (CRR) (Idriss and Boulanger 2008) as

$$\dot{r}^{u}_{u-Lu} = (FS_{Lu})^{-1/b}\,\frac{1}{t_g} \qquad 4.11$$

Partially Drained Excess Pore Pressure in Lu Layer

The partially drained excess pore pressure ($\dot{r}_{u-Lu}(t)$) in the Lu layer is given by the difference in the generation ($\dot{r}^{u}_{u-Lu}(t)$) and dissipation ($\dot{r}^{d}_{u-Lu}(t)$) rates, resulting in a first-order ordinary differential equation [Equation 4.12].

$$\dot{r}^{pd}_{u-Lu}(t) = \dot{r}^{u}_{u-Lu} - r^{pd}_{u-Lu}(t)\,\dot{r}^{d}_{u-Lu} \qquad 4.12$$

The differential equation can be solved for the boundary condition of $r^{pd}_{u-Lu}(t=0) = 0$ and integrated to get the partially drained excess pore pressure ratio in the Lu layer at any time during shaking $\left(r^{pd}_{u-Lu}(t)\right)$ as shown in Equation 4.13 below.

$$r^{pd}_{u-Lu}(t) = \frac{\dot{r}^{u}_{u-Lu}}{\dot{r}^{d}_{u-Lu}}\left(1 - e^{-\,\dot{r}^{d}_{u-Lu}\,t}\right), \qquad r^{pd}_{u-Lu}(t) < 1 \qquad 4.13$$

The partially drained excess pore pressure ratio at the end of shaking (r^{pd}_{u-Lu}) can be obtained from Equation 4.13 as

$$r^{pd}_{u-Lu} = (FS_{Lu})^{-1/b}\,\frac{1}{(1-r^{d}_{u-Lu})\bar{t}}\left(1 - e^{-\,(1-r^{d}_{u-Lu})\,\bar{t}}\right), \qquad r^{pd}_{u-Lu} < 1 \qquad 4.14$$

where the $\bar{t} = \frac{t_g}{t_d}$ is the ratio of the generation and dissipation times (t_g and t_d). A larger $\bar{t}$ (i.e., a smaller t_d) means redistribution results in comparatively faster dissipation of excess pore pressures than the generation from the undrained loading in the Lu layer. In Equation 4.14, FS_{Lu} < 1 model the extent of liquefaction in the Lu layer and its effect on r^{pd}_{u-Lu}. A Lu layer with a

$FS_{Lu} < 1$, even after considering redistribution could still develop huge excess pore pressures (r_{u-Lu}^{pd}). For soils with a larger b parameter, redistribution results in smaller r_{u-Lu}^{pd}. The average partially drained excess pore pressure ratio in the Lu layer at the end of shaking (r_{u-Lu}^{pd}) as a function of thickness and compressibility ratio ($\overline{H}/\overline{m_v}$) for a time ratio ($\bar{t}$) of (0.2, 1, and 5), $r_{u-NLu}^{u} = 0$ and 0.9, and a unit thickness of the NLu layer (H_{NLu}=1 m) at a depth of (Z = 10 m) for the primary two-layered systems are shown in Figure 4.5 and Figure 4.6, respectively. As expected, r_{u-Lu}^{pd} is smaller for larger thickness ratio ($\overline{H}$) and larger time ratio ($\bar{t}$). A smaller compressibility ratio ($\overline{m_v}$) and earthquake-induced excess pore pressure ratio in the NLu layer (r_{u-NLu}^{u}) leads to smaller r_{u-Lu}^{pd}. For very large thickness ratio ($\overline{H}$), r_{u-Lu}^{pd} asymptotically approaches to $r_{u-Lu}^{pd} = (FS_{Lu})^{-1/b} \frac{1}{\bar{t}(1-r_{u-Lu}^{d})} \left(1 - e^{-\bar{t}(1-r_{u-Lu}^{d})}\right)$.

The Criterion for Liquefaction Prevention in Lu Layer

Liquefaction can be conservatively assumed to be prevented in the Lu layer if the partially drained excess pore pressure ratio (r_{u-Lu}^{pd}) falls below 0.9. The criterion on the thickness and compressibility ratio ($\overline{H}/\overline{m_v}$) and the time ratio ($\bar{t}$) to prevent liquefaction in the Lu layer for a given undrained loading represented by $(FS_{Lu})^{-1/b}$ can be obtained by solving Equation 4.14 for $r_{u-Lu}^{pd}(t_o) = 0.9$. The minimum thickness and compressibility ratio ($\overline{H}/\overline{m_v}$) as a function of time factor ratio ($\bar{t}$) required to prevent liquefaction in the Lu layer for a unit thickness of NLu layer ($H_{NLu} = 1\ m$) at a depth of Z = 10 m for the primary two-layered systems are shown in Figure 4.7 and Figure 4.8, respectively. As expected, the minimum thickness ratio ($\overline{H}$) that can prevent liquefaction in Lu layer is larger for smaller time factor ratio ($\bar{t}$). A smaller $\bar{t}$ (i.e., a larger t_d) means that a longer time for dissipation (from redistribution) is required to prevent liquefaction in the Lu layer. The minimum thickness ratio ($\overline{H}$) is also larger for soils with smaller relative compressibility ($\overline{m_v}$), larger factor of safety against liquefaction or a larger b parameter (i.e., smaller $(FS_{Lu})^{-1/b}$), and smaller earthquake-induced pore pressure ratio in the NLu layer (r_{u-NLu}^{u}). A very large minimum thickness ratio ($\overline{H}$) means redistribution cannot prevent liquefaction in the Lu layer. For example, in Figure 4.7, for r_{u-NLu}^{u}= 0, $\overline{H}$ approaches infinity for $(FS_{Lu})^{-1/b} > 10$ and $\bar{t} \leq 10$. The figure also shows how large time ratios ($\bar{t}$) (i.e., reducing t_d by installing for example earthquake drains) can prevent liquefaction in the Lu layers. For the primary two-layered system with an NLu layer below the Lu layer, since redistribution does not occur for u_{e-NLu}^{u} greater than the effective stress at the bottom of the Lu layer, liquefaction cannot be prevented in the Lu layer (i.e., $r_{u-Lu}^{pd}(t_o) = 1.0$). For example, in Figure 4.8, for $r_{u-NLu}^{u} = 0.9$, the thickness and compressibility ratio ($\overline{H}/\overline{m_v}$) to prevent liquefaction in the Lu layer is very large, in the order of 10^5.

From the minimum thickness ratio ($\overline{H}$) estimated from Figure 4.7 and Figure 4.8 (or from Equation 4.14), the maximum thickness of the Lu layer that can be prevented from liquefaction can be computed as $H_{Lu} = H_{NLu}/\overline{H}$. For example in Figure 4.8, for $(FS_{Lu})^{-1/b} = 1$ and $r_{u-NLu}^{u} = 0$, and $\bar{t} = 1$, the thickness and compressibility ratio ($\overline{H}/\overline{m_v}$) is about 0.3. Assuming a compressibility ratio of $\overline{m_v} = 20$, the maximum thickness of the Lu layer that can be prevented from liquefaction is about 167 mm (i.e., equal to 16.6% of H_{NLu} = 1 m). Knowing a Lu layer cannot liquefy because of redistribution (as opposed to liquefiable under undrained loading with (FS_{Lu}<1) as predicted by the simplified liquefaction-triggering procedures) can prove to be extremely valuable in reducing the risk of liquefaction-related problems and their remediation costs.

4.6 Procedure For Estimating Redistribution Effects

Procedure for estimating redistributed effects in the soil layers involves three steps: (a) determination of Lu and NLu layers, (b) estimation of earthquake-induced excess pore pressures (u_e^u), and (c) estimation of redistributed excess pore pressures (u_e^d). The subsections below describe each of the steps in detail.

(a) Determination of Lu and NLu layers

A soil liquefaction hazard analysis of a site is performed to determine the soil layers, which are Lu and NLu. Among many methods (such as Youd et al. (2001), Idriss and Boulanger (2008), Robertson (2015), and Cetin et al. (2018)), the simplified procedure from Idriss and Boulanger (2008) is widely used for performing soil liquefaction hazard analysis for the assumed design earthquake loading. The site's design earthquake loading properties such as magnitude ($\mathrm{M_w}$) and peak ground acceleration (PGA) is first used to compute the cyclic stress ratio (CSR) in the soil layers. Then, liquefaction-triggering correlations developed on normalized overburden corrected "N value" for clean sand (N_{160cs}) obtained from static penetration test (SPT) investigations or normalized overburden corrected cone tip resistance for clean sand (q_{c1Ncs}) obtained from cone penetration test (CPT) investigations are used to estimate the cyclic resistance ratio (CRR) of the soil layers. In the end, a factor of safety against liquefaction $\left(FS_{Lu} = \frac{CRR}{CSR}\right)$ is computed to designate the layers as Lu and NLu under the design earthquake loading. If the soil layer has $FS_{Lu} \leq 1$, it is considered as an Lu layer. If $FS_{Lu} \geq 1$, the soils layer is considered as an NLu layer.

(b) Estimation of Earthquake-Induced Excess Pore Pressures ($\boldsymbol{u_e^u}$)

Earthquake-induced excess pore pressure in the soil layers is estimated using the simplified equations by Mele et al. (2021). The method uses the factor of safety against liquefaction (FS_{Lu}) computed in step (a) to estimate the earthquake-induced pore pressure ratios r_u^u in the soil layers as

$$r_u^u = \begin{cases} \frac{2.0}{\pi} arcsin\left(FS_{Lu}^{-\frac{1}{2b\beta}}\right),\ FS_{Lu} > 1 \\ 1.0,\ FS_{Lu} \leq 1 \end{cases} \quad 4.15$$

where $b\ and\ \beta$ are the parameters in terms of q_{c1Ncs} and N_{160cs} defined by Mele et al. (2021). The equation for Mele et al. (2021) was slightly modified to include liquefaction triggering condition of $r_u^u = 1.0$ for $FS_{Lu} \leq 1.0$ (instead of $r_u^u = 0.9$ for $FS_{Lu} = 1.0$). As expected, for Lu layers with $FS_{Lu} \leq 1$, $r_{u-Lu}^u = 1.0$ and for NLu layers with $FS_{Lu} > 1$, $r_{u-Lu}^u < 1.0$. The average excess pore pressure ratio (r_{u-Lu}^u) in the NLu layer is calculated by taking the ratio of the average earthquake-induced excess pore pressure (u_{e-NLu}^u) with the average initial mean effective stress ($\sigma_{vo-NLu}^{'}$).

(c) Estimation of Redistributed Excess Pore Pressures ($\boldsymbol{u_e^d}$)

The redistributed excess pore pressures in the Lu and NLu layer depends on the thickness ratio ($\overline{H} = \frac{H_{NLu}}{H_{Lu}}$), compressibility ratio $\left(\overline{m_v} = \frac{m_{v-Lu}}{m_{v-NLu}}\right)$, depth to the top of NLu layer (Z), average effective unit weight ($\boldsymbol{\gamma'}$) and average initial mean effective stress ($\sigma_{vo}^{'}$) of the soil layers, and the earthquake-induced pore pressure ratio (r_u^u) computed in step (b). The compressibility (m_v) of the Lu and NLu layers can be estimated using the relation by Seed et al. (1976), which approximates the lab test results from Lee and Albasia (1974). The relation models m$_v$ as a function of relative density (D$_R$) and earthquake-induced excess pore pressure ratio (r_u^u) as follows.

$$\frac{m_v}{m_{vo}} = \frac{exp(y)}{1 + y + y^2/2}$$

$$y = 5(1.5 - D_R)(r_u^u)^b \qquad 4.16$$

$$b = 3(4)^{-D_R}$$

where m$_{vo}$ is the compressibility at zero excess pore pressure $r_u^u = 0$. The compressibility (m$_{vo}$) of the normally consolidated sand at mean effective stress (σ'_{vo}) with $r_u^u = 0$ can be calculated using empirical correlations from Janbu (1985), as follows

$$m_{vo} = \frac{1}{m\sqrt{P_o\sigma'_{vo}}} \qquad 4.17$$

where m is the modulus parameter depending upon the porosity (n) of the sand layer (determined from Figure 4.9) and P$_o$ is a constant equal to the atmospheric pressure, i.e., P$_o$ =101.3 kPa.

The redistributed excess pore pressure ($u_e^d = r_u^d\sigma'_{vo}$) in the Lu and NLu layers are estimated using Equations 4.2-4.7 with the obtained input parameters ($\overline{H}, \overline{m_v}, \sigma'_{vo}, r_u^u, Z, \gamma'$). From the obtained u_e^d, the corresponding u_e^d Profile (as shown in Figure 4.1) can be used to estimate the redistributed excess pore pressure profile in Lu and NLu layers.

(d) Estimation of Partially Drained Excess Pore Pressures in the Lu Layer (u_{e-Lu}^{pd})

Estimation of partially drained excess pore pressure (u_{e-Lu}^{pd}) in the Lu layer requires estimating the time for excess pore pressure generation (t_g) and dissipation (t_d). The time for generation (t_g)

is taken as the duration of the undrained loading. The dissipation time (t_d) can be estimated from dimensionless time factor ($T_d = (c_v/H^2)\, t_d$) associated with the degree of consolidation $\left(U \ = \ 1 - r^{d}_{u-Lu}\right)$. Taylor (1948) describes the relation for estimating time factor (T_d) for a given degree of consolidation (U) as

$$T_d = \begin{cases} \frac{\pi}{4}\mathrm{U}^2, \ \mathrm{U} < 0.6 \\ 0.9332 \log_{10}(1 \ - \ \mathrm{U}) - 0.0851, \ \mathrm{U} \geq 0.6 \end{cases} \qquad 4.18$$

Since the rate of dissipation would depend upon the relative permeability (k), compressibility (c_v), and thickness of the layers (H), the ratio (c_v/H^2) can be conservatively taken equal to that of the (Lu or NLu) layer with the smaller ratio, i.e., the smaller of c_{v-Lu}/H^2_{Lu} or c_{v-NLu}/H^2_{NLu}. The coefficient of consolidation $c_v = k/(m_v\gamma_w)$ can be estimated from the permeability (k) and compressibility (m_v) (estimated from Equation 16 and 17) and the unit weight of water $\gamma_w = 10$ kPa/m. The partial drained excess pore pressure (u^{pd}_{e-Lu}) in the Lu layer is then estimated from Equation 14 using the estimated redistributed excess pore pressures (u^{d}_{e-Lu}) and the time ratio $\left(\bar{t} \ = \frac{t_g}{t_d}\right)$.

The maximum thickness of the Lu layer that can be prevented from liquefaction (for the assumed liquefaction prevention criteria of r^{pd}_{u-Lu}<0.9) can be obtained by solving Equation 14 iteratively for different H_{Lu} and the associated time ratio $\left(\bar{t} \ = \frac{t_g}{t_d}\right)$ and the average factor of safety against liquefaction (FS_{Lu}).

4.7 Application in Centrifuge Tests

Description of Centrifuge Model Tests

Selected shaking events: EQM_3 and EQM_4, respectively, from the two large centrifuge model tests, SKS02 (Sinha et al. 2021c) and SKS03 (Sinha et al. 2021d), were chosen to apply the developed approximate procedure to study redistribution effects on liquefiable and non-liquefiable layers. The centrifuge model tests (SKS02 and SKS03) were conducted on the 9-m radius centrifuge facility at the Center of Geotechnical Modeling at the University of California Davis at the centrifugal acceleration of 40 g. All the units reported for the centrifuge test are in the prototype scale following centrifuge scaling laws by Garnier et al. (2007). The models consisted of 21 m of soil with no drainage at the bottom of the layers (i.e., at 21 m) because of the impermeable base of the model container. The centrifuge model test SKS02 consisted of a 9 m-thick liquefiable loose sand layer ($D_R \approx 43\%$, $n \approx 0.41$) sandwiched between a 4 m thick layer of low permeable over-consolidated clay layer (with an undrained shear strength $s_u \approx 20$ kPa) on the top and dense sand layer ($D_R \approx 85\%$, $n \approx 0.36$) below [Figure 4.10]. The soil profile of centrifuge model test SKS03 consisted of 1 m of Monterey sand, 2 m of clay crust ($s_u \approx 28\text{-}35$ kPa), 4.7 m of the loose liquefiable sand layer ($D_R \approx 40\%$, $n \approx 0.41$), 1.3 m of a clayey silt layer (20% clay and 80% silt), 4 m of the medium dense sand layer ($D_R \approx 60\%$, $n \approx 0.39$), and a dense sand layer ($D_R \approx 83\%$, $n \approx 0.36$) [Figure 4.11]. The effective unit weight ($\boldsymbol{\gamma'}$) of the sand layers was about 10 kPa/m. The loose and medium dense sand layer's permeability (k) was about 0.026 and 0.022 cm/s, respectively. The models were shaken with scaled Santa Cruz earthquake motions of $M_w = 6.9$ from the Loma Prieta 1989 earthquake. The duration of shaking of the earthquake motion was about 30 seconds. The measured peak ground acceleration (PGA) for the shaking event EQM_3 and EQM_4 was about 0.12 g and 0.16 g, respectively. The measured normalized overburden corrected cone tip resistance

(q_{c1Ncs}) and peak excess pore pressure (u_e) generated in the soil layers during shaking are shown in Figure 4.10 (a,c) and Figure 4.11 (a,c).

Estimating Redistribution Effects in Lu and NLu layers

Results on the cyclic stress ratio (CSR), the factor of safety against liquefaction (FS_{Lu}), and earthquake-induced pore pressure for the selected shaking from SKS02 and SKS03 are shown in Figure 4.10 (b,c) and Figure 4.11 (b,c), respectively. The figures also show the categorization of soil layers as Lu and NLu layer depending on whether $FS_{Lu} \leq 1$ or $FS_{Lu} > 1$, respectively. In the centrifuge model test SKS02, the Lu layer consisted of the loose sand layer up to the depth of 14 m (i.e., H_{Lu} = 9 m). The NLu layer consisted of the dense sand layer from the depth of Z = 14 m up to 21 m (i.e., H_{NLu} = 7 m). The average effective stress in the soil layers was σ'_{vo-Lu} = 79.6 kPa and σ'_{vo-NLu} = 157.3 kPa. The average earthquake-induced excess pore pressure (u_e^u) in the soil layers was u_{e-Lu}^u = 79.6 kPa and u_{e-NLu}^u = 15.03 kPa, resulting in $r_{u-Lu}^u = 1.0$ and r_{u-NLu}^u = 0.096. In the centrifuge mode test SKS03 test, the Lu layer consisted of about 1.7 m of the medium dense sand layer below the relatively impermeable silt layer (i.e., H_{Lu} = 1.7 m). The NLu layer consisted of soils layers (2.3 m of medium dense sand and dense sand below it) below the depth of Z = 10.7 m up to 21 m (i.e., H_{NLu} = 10.3 m). The average earthquake-excess pore pressure ratio computed for the Lu and NLu layers was r_{u-Lu}^u = 1.0 and r_{u-NLu}^u = 0.24 estimated from the effective stress of σ'_{vo-Lu} = 89.54 kPa and σ'_{vo-NLu} = 151.8 kPa and earthquake-induced pore pressure of u_{e-Lu}^u = 89.54 kPa and u_{e-NLu}^u = 36.05 kPa, respectively. The compressibility ratio ($\overline{m_v}$) of the soil layers was estimated using Equations 4.16 and 4.17. The compressibility (m_{vo}) was computed by taking the mean value of the modulus parameter (m) for the sand layers [Figure 4.9]. The estimated compressibility ratio ($\overline{m_v}$) for the Lu and NLu layers in the SKS02 and SKS03 model was $\overline{m_v} =$ 20 and $\overline{m_v} = 12$, respectively.

The redistributed excess pore pressures in the soil layers were estimated using Equations 4.6 and 4.7. In both centrifuge models, the NLu layer is below the Lu layer with an impermeable clay or silt layer above the Lu layer and an impermeable boundary condition below the NLu layer. The redistributed excess pore pressure for the selected shaking events in the NLu layer in the SKS02 and SKS03 model was estimated to be u_{e-NLu}^{d}= 98 kPa and 75 kPa, respectively.

The thickness of the Lu layer for $r_u^{pd} < 0.9$ was found iteratively by solving Equation 14 for different thicknesses of Lu layer (H_{Lu}) and the associated dissipation time (t_d) (obtained using the time factor T_d from equation 18) with the estimated redistributed excess pore pressure of u_{e-Lu}^{d} in the Lu layer. The time for generation of excess pore pressures (t_g) was taken as 30 seconds, equal to the duration of shaking. The sand used in the centrifuge model tests was Ottawa F-65 with parameter "b" equal to 0.15 (Bastidas 2016). For the shaking event EQM_3 of centrifuge model test SKS02, the thickness of the Lu layer with $r_u^{pd} < 0.9$ was obtained 1.9 m from the bottom of the loose sand layer with time ratio of $\bar{t} = 42.3$. For the shaking event EQM_4 of centrifuge model test SKS03, redistribution resulted in $r_u^{pd} < 0.9$ in the 1.8 m thick medium dense sand Lu layer with the time ratio $\bar{t} = 10.7$.

Comparison of Results with Centrifuge Test

The excess pore pressure in the NLu layer considering redistribution matched quite well with the centrifuge test. The comparison of estimated excess pore pressure from redistribution with the measured excess pore pressures for the shaking event EQM_3 and EQM_4 in the centrifuge model test SKS02 and SKS03 are shown in Figure 4.10 (c) and Figure 4.11 (c), respectively. It can be seen from the figures that the earthquake-induced earthquake pore pressures (estimated without considering redistribution) significantly underestimate excess pore pressures in the NLu layers. In the SKS02 test [Figure 4.10 (c)], the average earthquake-induced excess pore pressure in the NLu layer was u_{e-NLu}^{u} = 15 kPa compared to measured excess pore pressure $u_e \approx 90$ kPa. Similarly, in the SKS03 test [Figure 4.11 (c)], u_{e-NLu}^{u} = 36 kPa compared to measured excess pore pressure $u_e \approx 76$ kPa. On the other hand, the estimated excess pore pressure in the N_{Lu} layer considering redistribution (u_{e-NLu}^{d} = 98 kPa and u_{e-NLu}^{d} = 75 kPa) matched reasonably well with the measured excess pore pressures in both the centrifuge model tests (SKS02 and SKS03).

While redistribution increased excess pore pressure in the N_{Lu} layers, it prevented liquefaction in the Lu layers. In the centrifuge model test SKS02 [Figure 4.10 (c)], the excess pore pressure in the loose sand layer between the depth of 11-14 m was found less than the layer's effective stress opposed to liquefaction prediction ($u_e^u = \sigma_{vo}^{'}$) under the undrained loading condition. The reason for $u_e < \sigma_{vo}'$ at the bottom 3 m of loose sand is due to the redistribution of excess pore pressures from the Lu layer to the bottom NLu layer below. In Figure 4.10 (c), the equalized excess pore pressure profile considering redistribution (u_e^d) predicted $u_e^d < \sigma_{vo}^{'}$ in the bottom 2.5 m of loose sand layer like the results from the centrifuge test. Similar observation can be seen in the results of EQM_4 in centrifuge model test SKS03, where redistribution prevented liquefaction in 1.8 m thick medium dense sand layer, which was initially predicted liquefiable with $FS_{Lu} \leq 1$ [Figure 4.11 (c)].

While redistribution increased excess pore pressure in the N_{Lu} layers, it prevented liquefaction in the Lu layers. The predicted thickness of the Lu layer where redistribution prevented liquefaction as opposed to initial liquefaction prediction from the undrained loading with $FS_{Lu} \leq 1$, matched decently with the observation from the centrifuge test. For the shaking event EQM_3 of centrifuge model test SKS02, the developed approximate procedure predicted prevention to liquefaction in the 1.9 m thickness of the loose sand layer from its bottom compared to the 3 m thickness of loose sand layer observed from the pore pressure transducers measurements in the centrifuge test [Figure 4.10 (c)]. The difference in the predicted thickness of the Lu layer being prevented from liquefaction could be due to the conservatism in the developed approximate procedure. For the shaking event EQM_4 of centrifuge model test SKS03, the developed approximate procedure predicted liquefaction prevention in the 1.8 thick medium dense sand Lu layer, similar to the observations from the centrifuge test [Figure 4.11 (c)].

4.8 Conclusions

This chapter described a new procedure to account for redistribution of excess pore pressures that will either increase excess pore pressures in layers determined to be non-liquefiable (NLu) under undrained conditions or decrease pore pressures in layers determined to be liquefiable (Lu) under undrained conditions. The development of the procedure involved studying redistributed excess pore pressures in two types of layered systems: an NLu below a Lu layer and an NLu layer above a Lu layer, which formed the basis to estimate redistributed excess pore pressures in multi-layered systems. While redistribution increased excess pore pressures in the NLu layer, it also decreased excess pore pressures in the Lu layers. Equations were provided to estimate the redistributed excess pore pressure in the Lu and NLu layers. The chapter also described the criterion on the maximum thickness of the Lu layer that can be prevented from liquefaction due to the redistribution effects (as opposed to liquefaction prediction by simplified procedures). Preventing liquefaction in a deep thin Lu layer due to redistribution of excess pore pressures to the adjacent NLu layers might prove extremely valuable in reducing the risk of liquefaction-related failures and the cost associated with the remediation. The developed approximate procedure was applied for estimating excess pore pressures in centrifuge tests. Comparing the estimated excess pore pressures considering redistribution with the measurements from pore pressure transducers showed that the developed analytical procedure reasonably predicted the peak excess pore pressures in the soil.

Several simplifying assumptions were used to present a complete procedure; many of these assumptions may be more conservative than necessary. For example, redistribution of excess pore pressures in the non-liquefiable layer assumed no water drainage outside the liquefied and non-liquefiable layers until redistribution was achieved. This condition would be applicable for the case when the surrounding soil layers are relatively impermeable (such as clay, silt, and sand silt mixtures). For the case of partially or fully drained hydraulic boundary conditions, the presented approximate procedure would result in conservative estimates of redistributed excess pore pressures. The procedure for extending the two-layer systems to multi-layer systems conservatively assumed that the Lu layer fully contributed to excess pore pressures above and below the layer. In the analytical study of increased liquefaction resistance in the Lu layer from redistribution, since the compressibility of soil increases, as pore pressure develops, the assumption of a constant compressibility ratio might be overly conservative. The compressibility ratio actually is nonlinear and maybe more accurately determined by an iterative procedure. On the other hand, factor such as duration of shaking and the extent of liquefaction is not well captured in the present analytical study and thus may result in underestimation of excess pore pressure estimates in the Lu and NLu layers. For longer duration shakings and with prominent liquefaction in the Lu layer, continuous redistribution can occur throughout the shaking resulting in very high excess pore pressures in soil layers. Future refinements of the procedure may be able to estimate redistribution effects better while avoiding some of the excessive conservatism. For sites where the above-listed factors may play an important role, an advanced 1-D or 2-D site response analysis with excess pore pressure generation/dissipation models can be performed to estimate realistic excess pore pressures in soil layers.

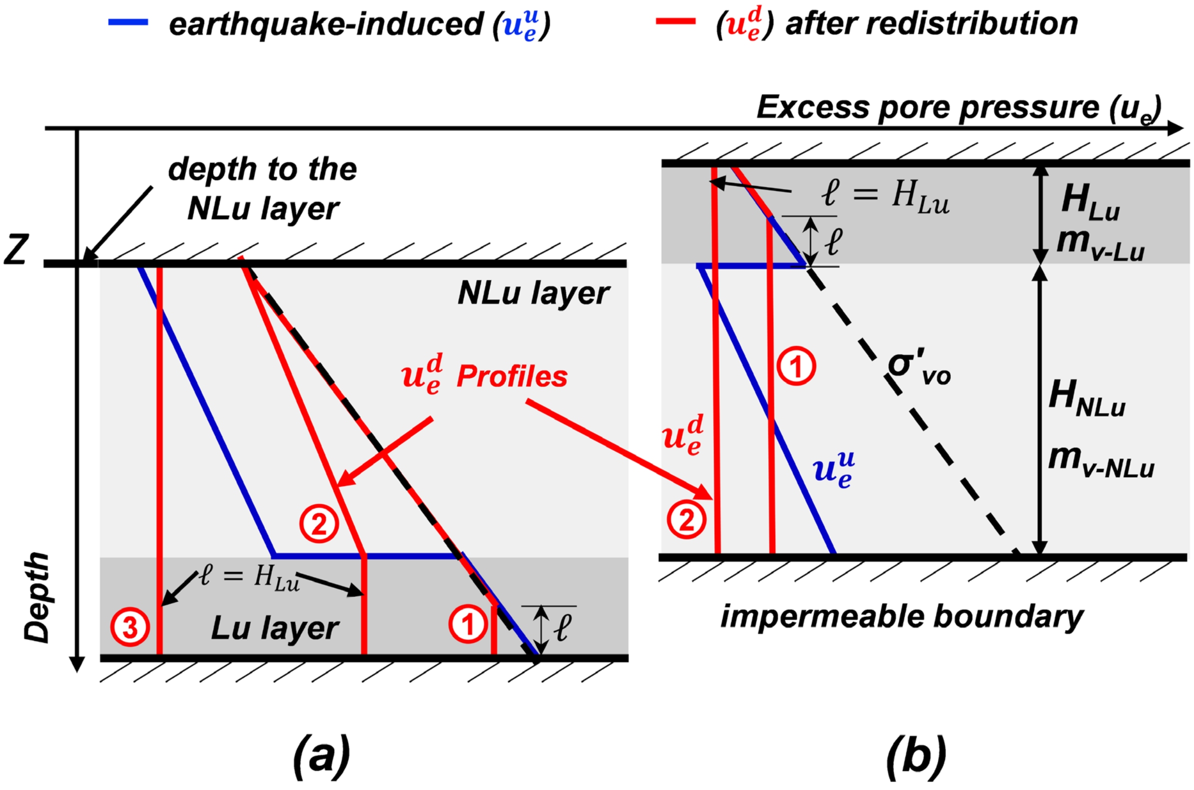

Figure 4.1. Illustration of possible excess pore pressures (u_e^d) profiles (corresponding to the time when peak u_e is developed in the NLu layer) due to redistribution of excess pore pressures from the reconsolidating Lu layer present (a) below and (b) above the NLu layer.

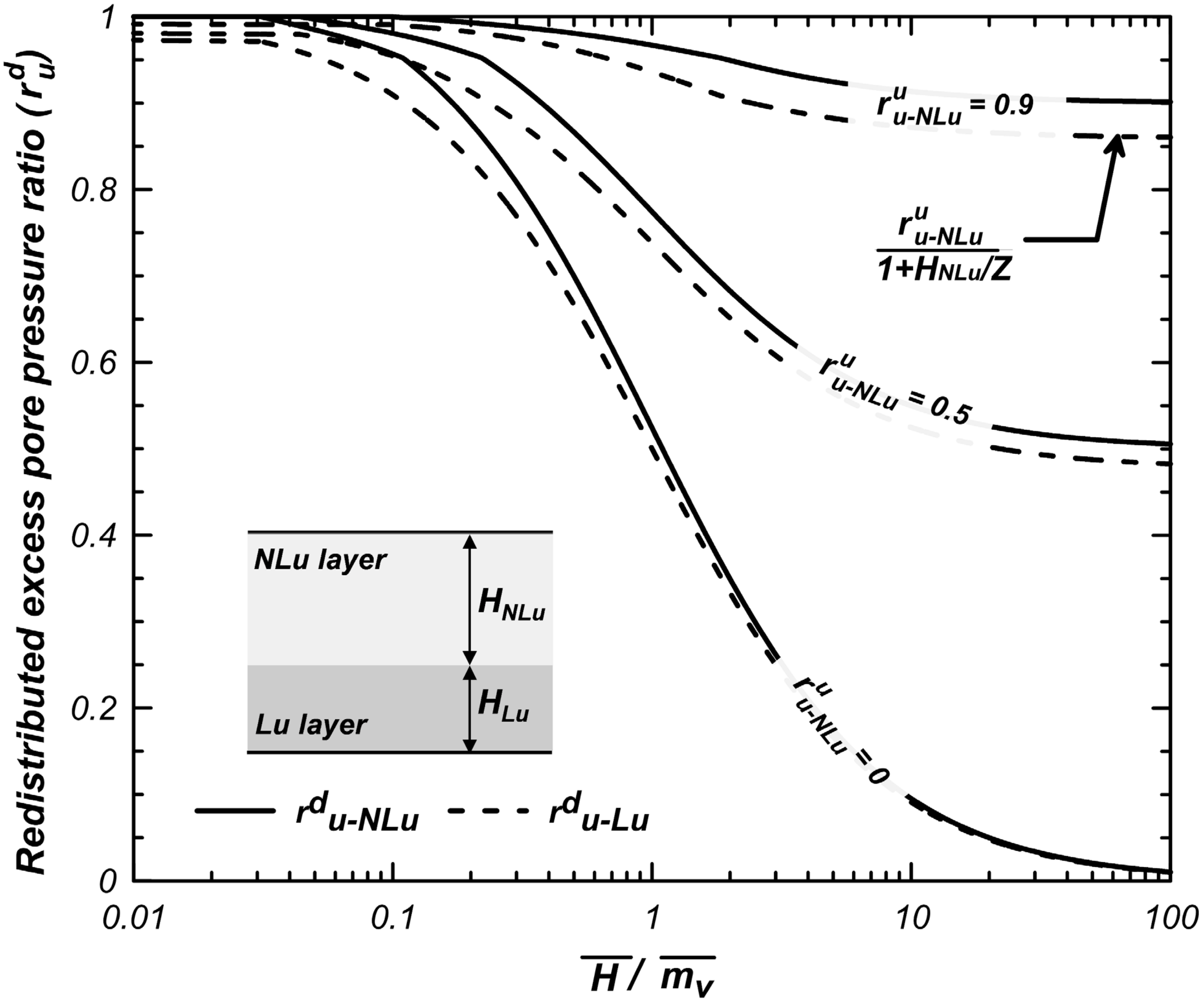

Figure 4.2. Redistributed excess pore pressure ratio (r_u^d) in the layered system with an NLu layer above a Lu layer as a function of thickness and compressibility ratio ($\overline{H}/\overline{m_v}$) for earthquake-induced excess pore pressure ratio (r_{u-NLu}^u) of 0, 0.5, and 0.9 and a unit thickness of the NLu layer ($H_{NLu} = 1\ m$) at a depth of $Z = 10\ m$.

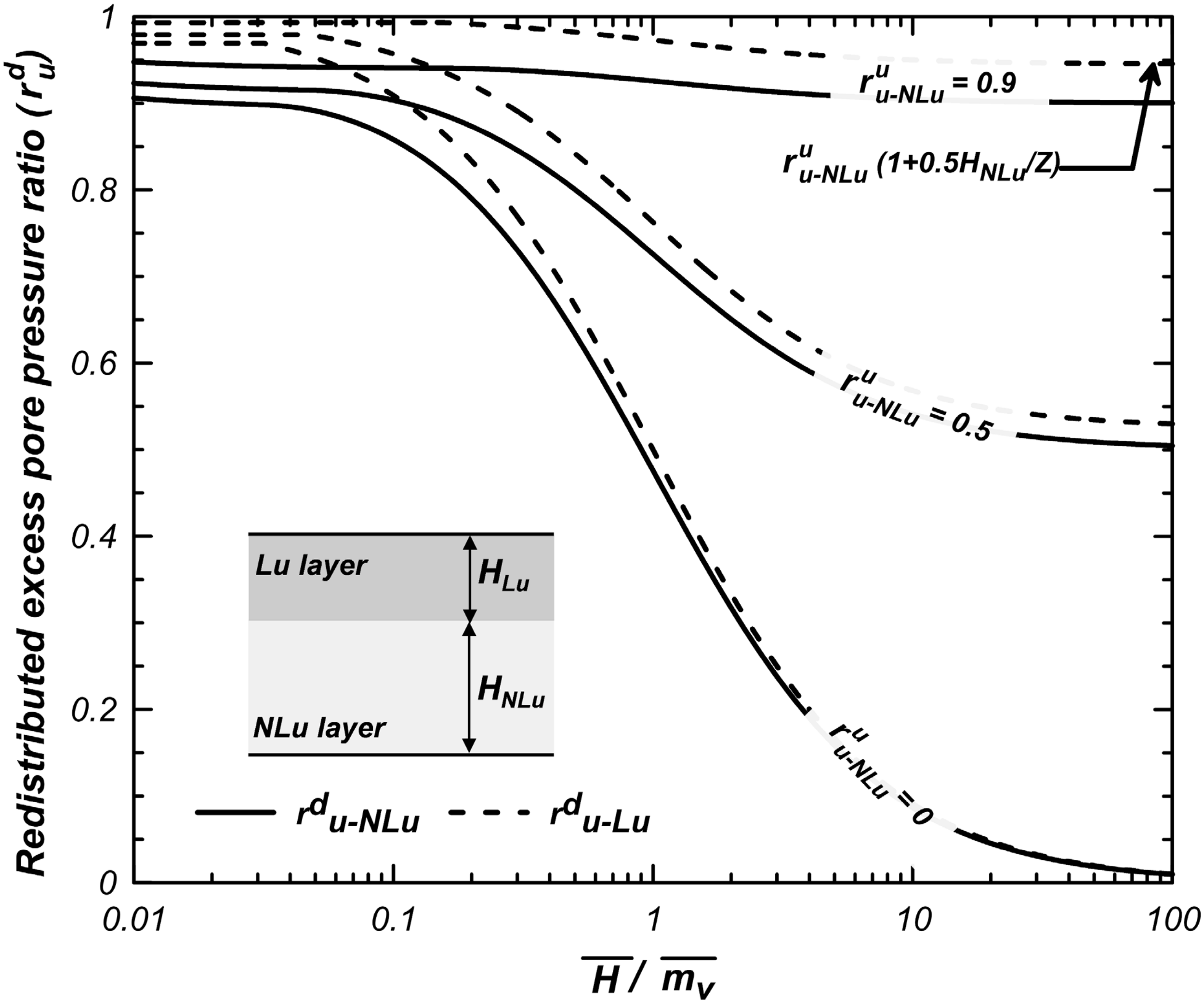

Figure 4.3. Redistributed excess pore pressure ratio (r_u^d) in the layered system with an NLu layer below a Lu layer as a function of thickness and compressibility ratio $(\overline{H}/\overline{m_v})$ for earthquake-induced excess pore pressure ratio (r_{u-NLu}^u) of 0, 0.5, and 0.9 and a unit thickness of the NLu layer $(H_{NLu} = 1\ m)$ at a depth of $Z = 10\ m$.

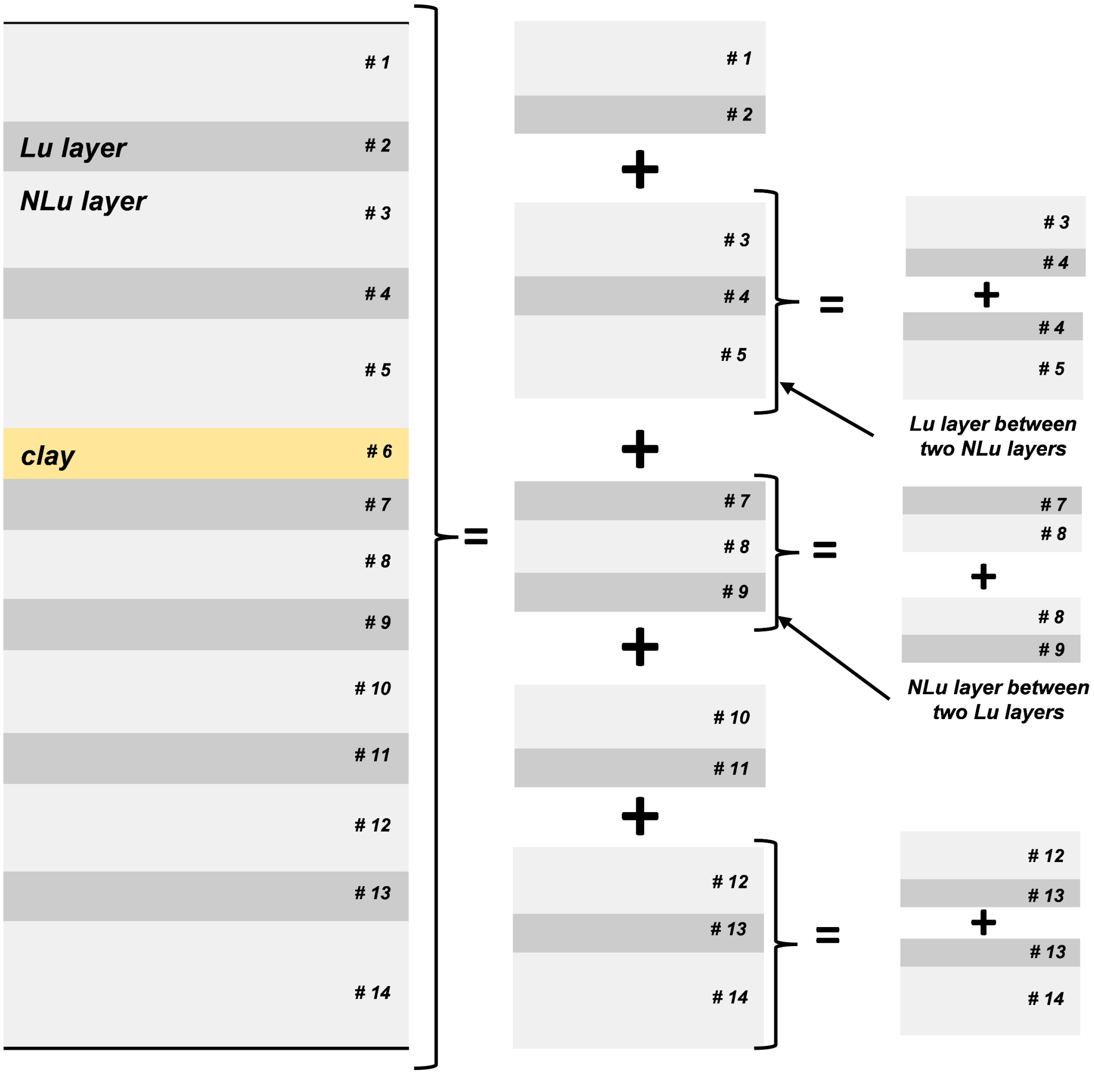

Figure 4.4. Illustration of the multi-layered soil systems decomposition into smaller units of the two primary layered soil systems of the non-liquefiable layer above/below a liquefied layer to estimate redistributed excess pore pressure in the non-liquefiable layers.

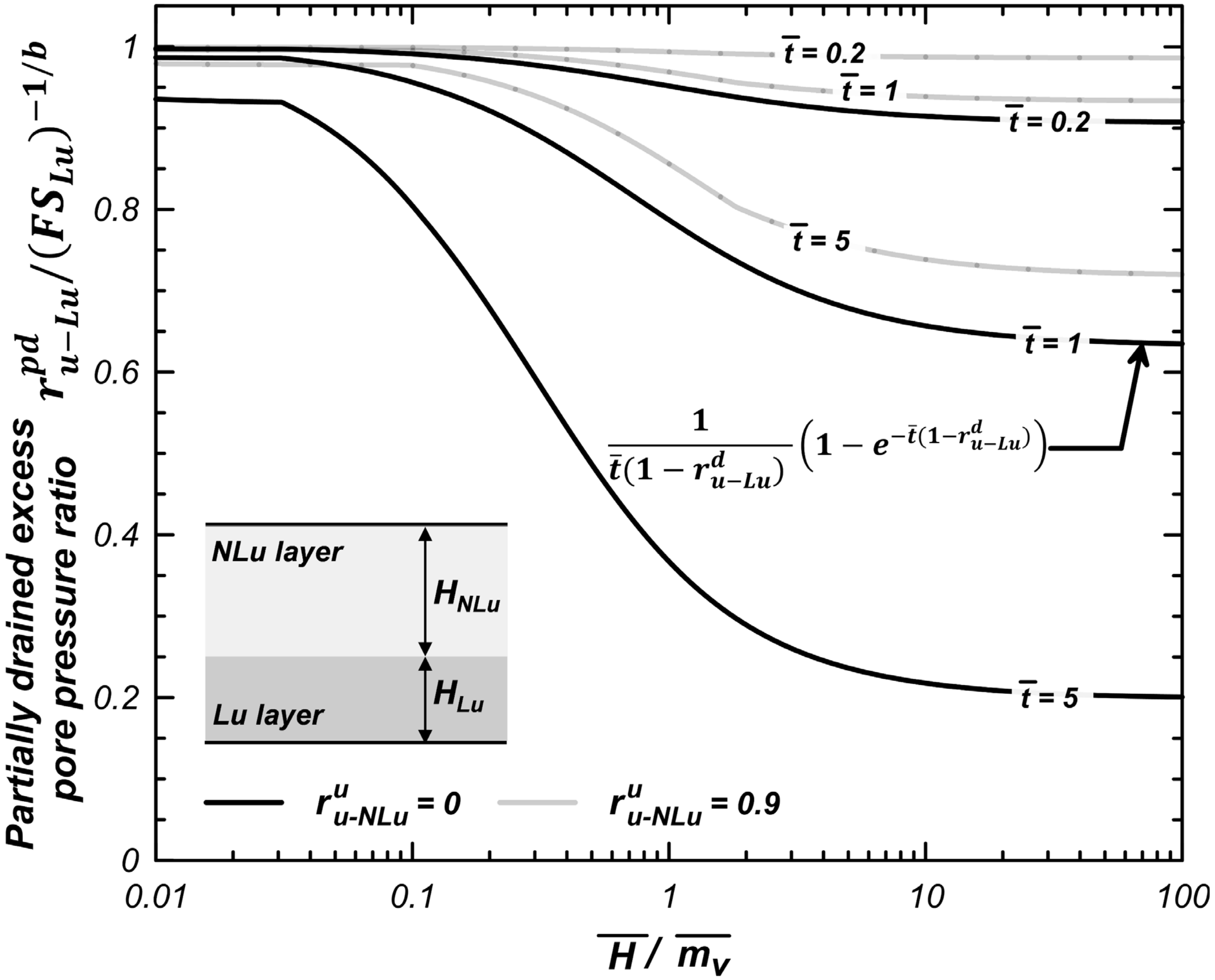

Figure 4.5. Partially drained excess pore pressure ratio in the Lu layer $\left(r^{pd}_{u-Lu}/(FS_{Lu})^{-1/b}\right)$ in the layered system with an NLu layer above a Lu layer as a function of thickness and compressibility ratio ($\overline{H}/\overline{m_v}$) for time ratio ($\bar{t}$) of 0.2, 1, and 5, earthquake-induced excess pore pressure ratio (r^u_{u-NLu}) of 0 and 0.9 and a unit thickness of the NLu layer ($H_{NLu} = 1\ m$) at a depth of $Z = 10\ m$.

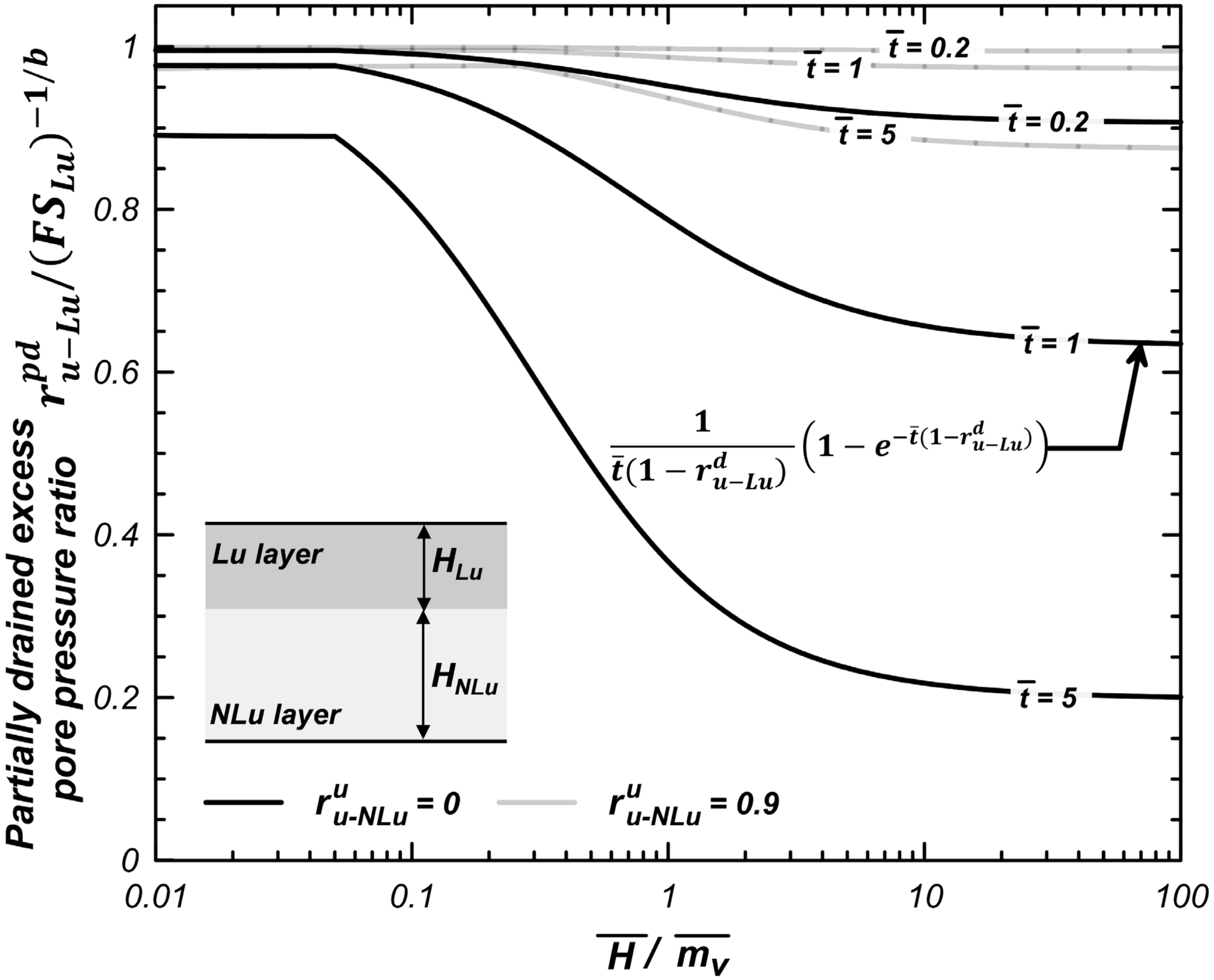

Figure 4.6. Partially drained excess pore pressure ratio in the Lu layer $\left(r_{u-Lu}^{pd}/(FS_{Lu})^{-1/b}\right)$ in the layered system with an NLu layer below a Lu layer as a function of thickness and compressibility ratio $(\overline{H}/\overline{m_v})$ for time ratio $(\bar{t})$ of 0.2, 1, and 5, earthquake-induced excess pore pressure ratio (r_{u-NLu}^{u}) of 0 and 0.9 and a unit thickness of the NLu layer $(H_{NLu}=1\ m)$ at a depth of $Z=10\ m$.

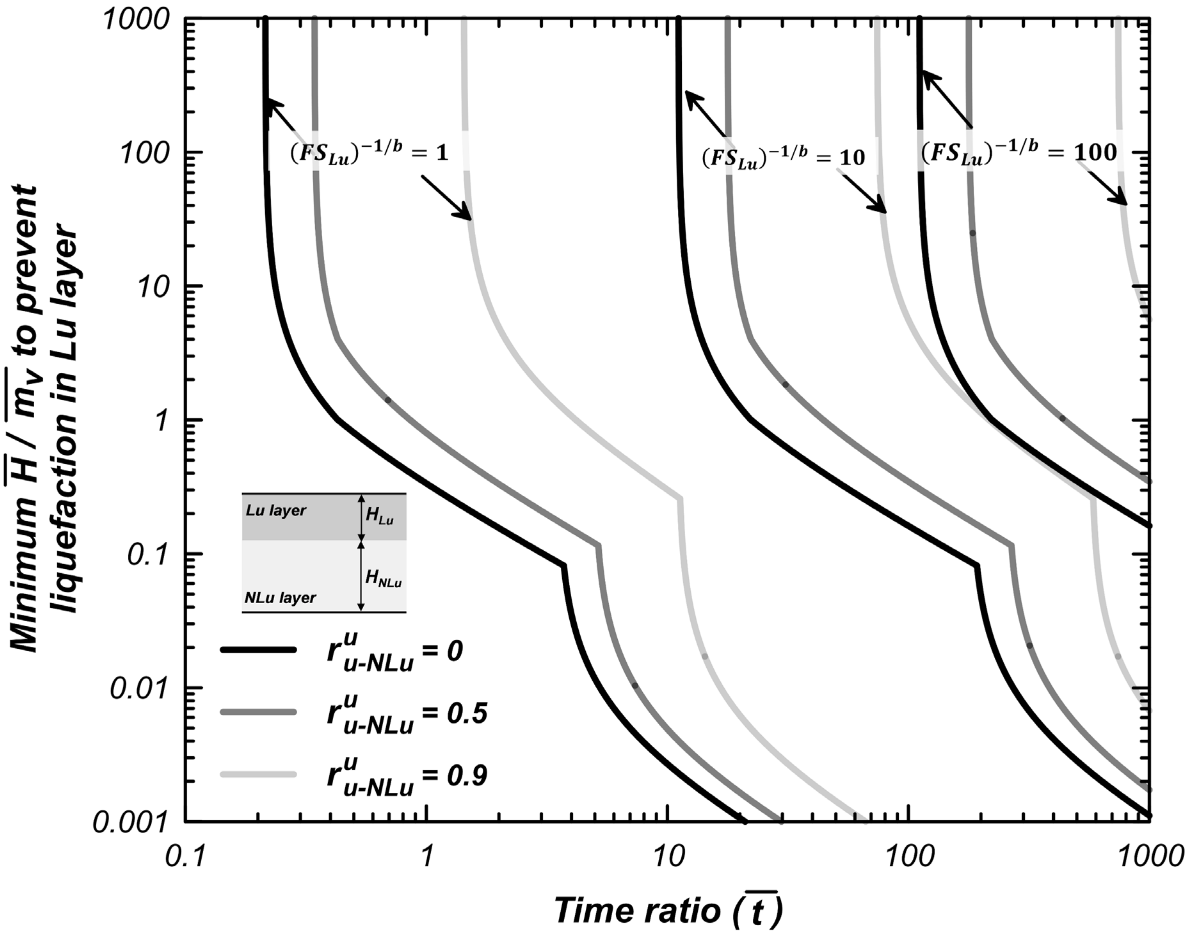

Figure 4.7. The minimum thickness and compressibility ratio ($\overline{H}/\overline{m_v}$) in the layered system with an NLu layer above a Lu layer as a function of time ratio ($\bar{t}$) for which liquefaction can be prevented in the Lu layer (i.e., $r_{u-Lu}^{pd} \leq 0.9$) having earthquake-induced excess pore pressure ratio (r_{u-NLu}^{u}) of 0, 0.5, and 0.9, and undrained loading represented by $(1/FS_{Lu})^{1/b}$ of 1,10, and 100.

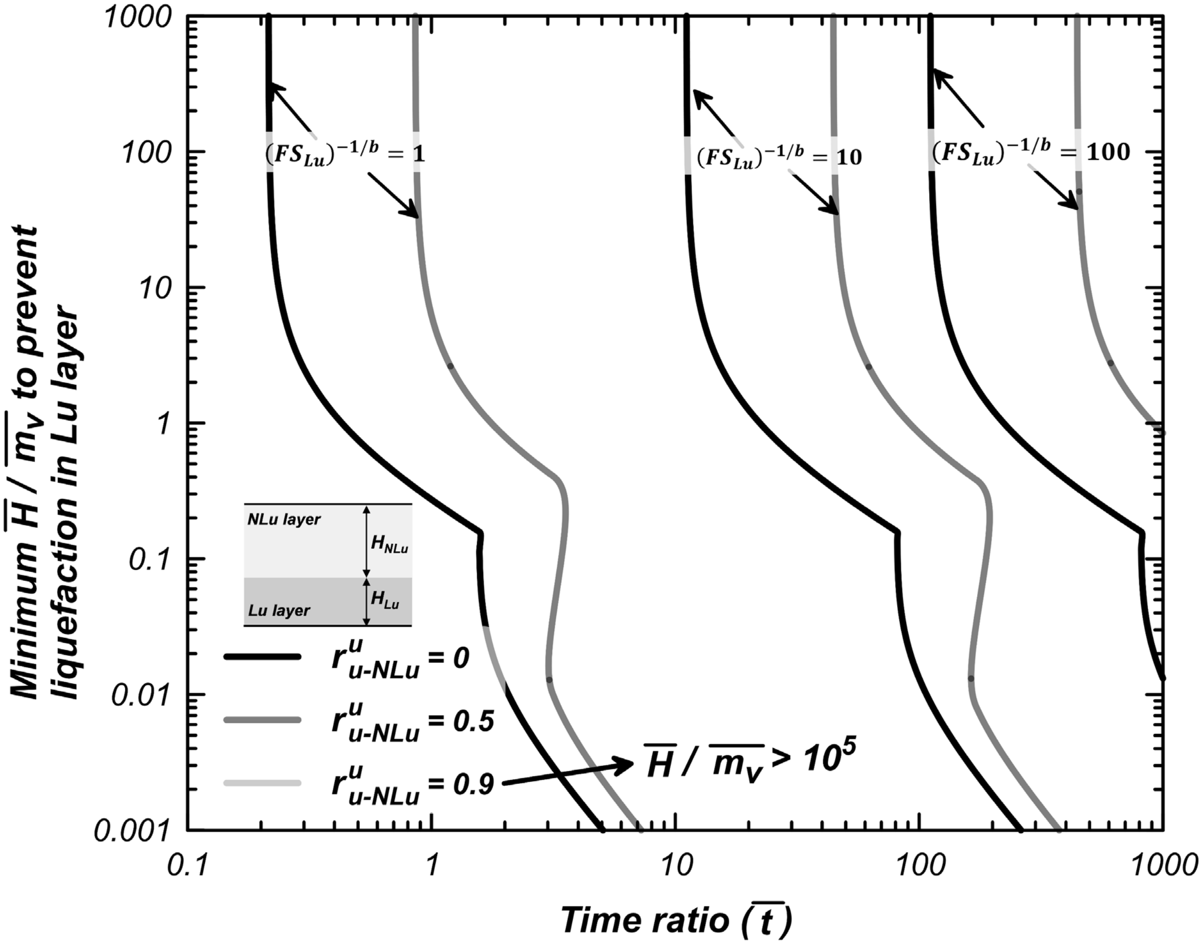

Figure 4.8. The minimum thickness and compressibility ratio ($\overline{H}/\overline{m_v}$) in the layered system with an NLu layer below a Lu layer as a function of time ratio ($\bar{t}$) for which liquefaction can be prevented in the Lu layer (i.e., $r^{pd}_{u-Lu} \leq 0.9$) having earthquake-induced excess pore pressure ratio (r^{u}_{u-NLu}) of 0, 0.5, and 0.9, and undrained loading represented by $(1/FS_{Lu})^{1/b}$ of 1,10, and 100.

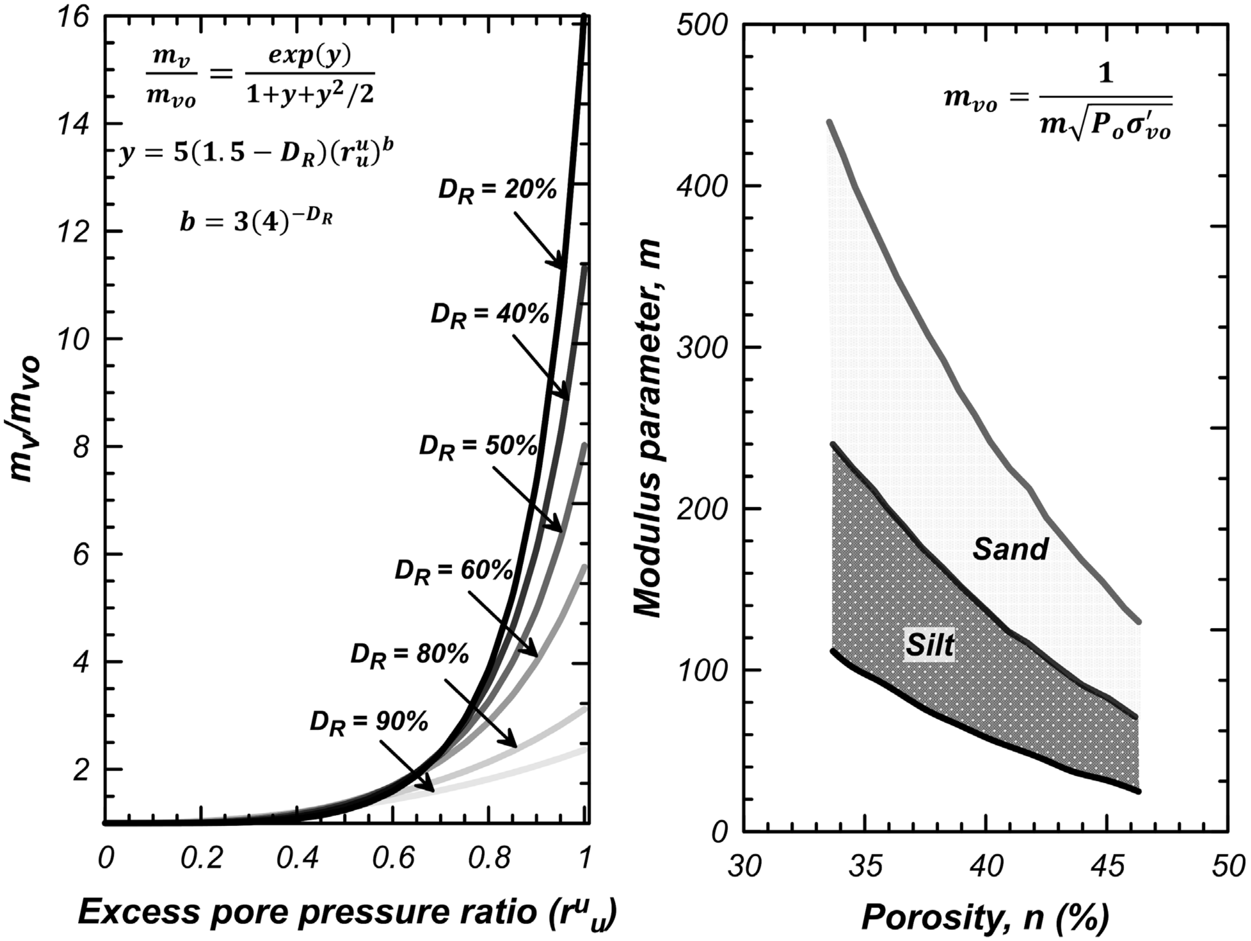

Figure 4.9. Estimation of compressibility (m_v) of liquefiable soils using (a) the compressibility ratio (m_v/m_{vo}) relation as a function of earthquake-induced excess pore pressure ratio (r_u^u) from Seed et al. (1976) and (b) compressibility (m_{vo}) of normally consolidated sand and silts at mean effective stress (σ'_{vo}) with $r_u^u = 0$ from Janbu (1985).

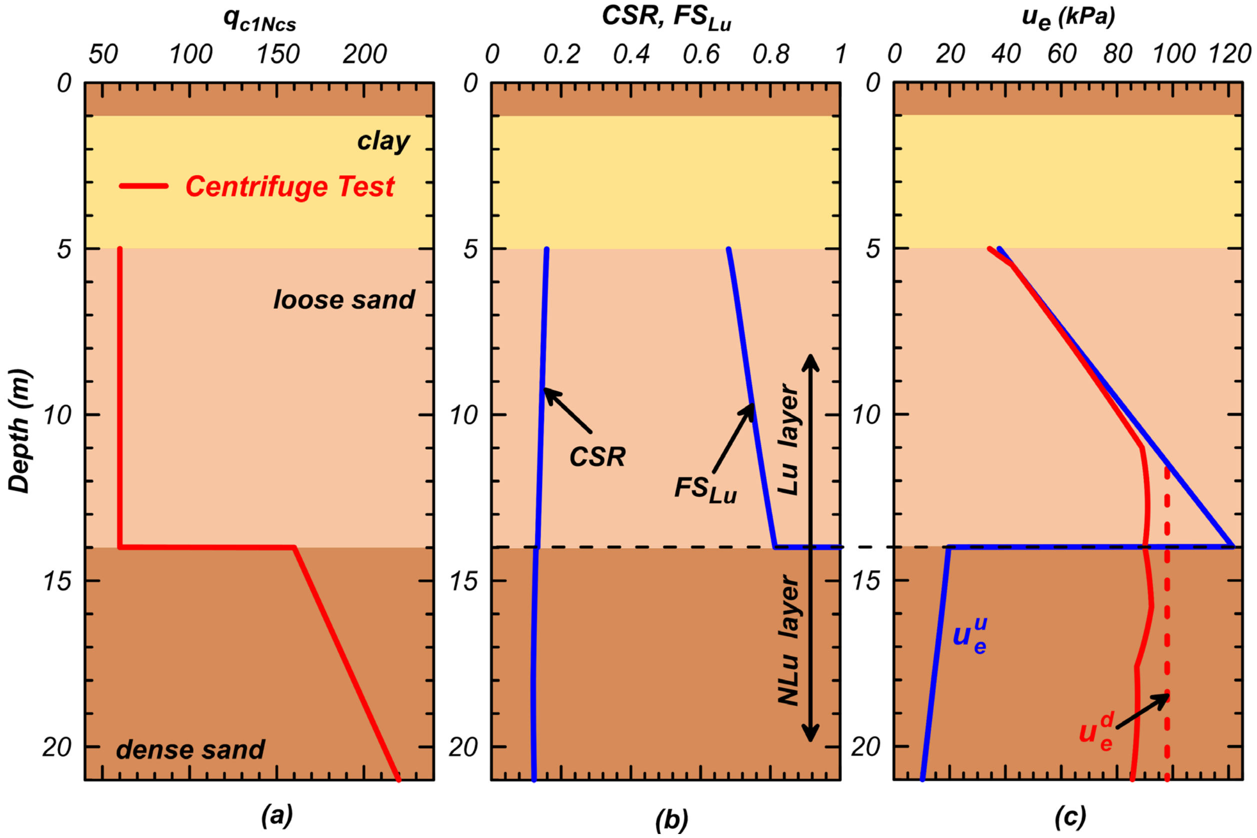

Figure 4.10. Redistribution effects for shaking event EQM$_3$ of centrifuge model test SKS02 (Sinha et al. 2021c): (a) Measured normalized overburden corrected cone tip resistance (q_{c1Ncs}). (b) Cyclic stress ratio (CSR) and factor of safety against liquefaction (FS_{Lu}). (c) Comparison of estimated earthquake-induced (u_e^u) and redistributed (u_e^d) excess pore pressures with the measured excess pore pressures.

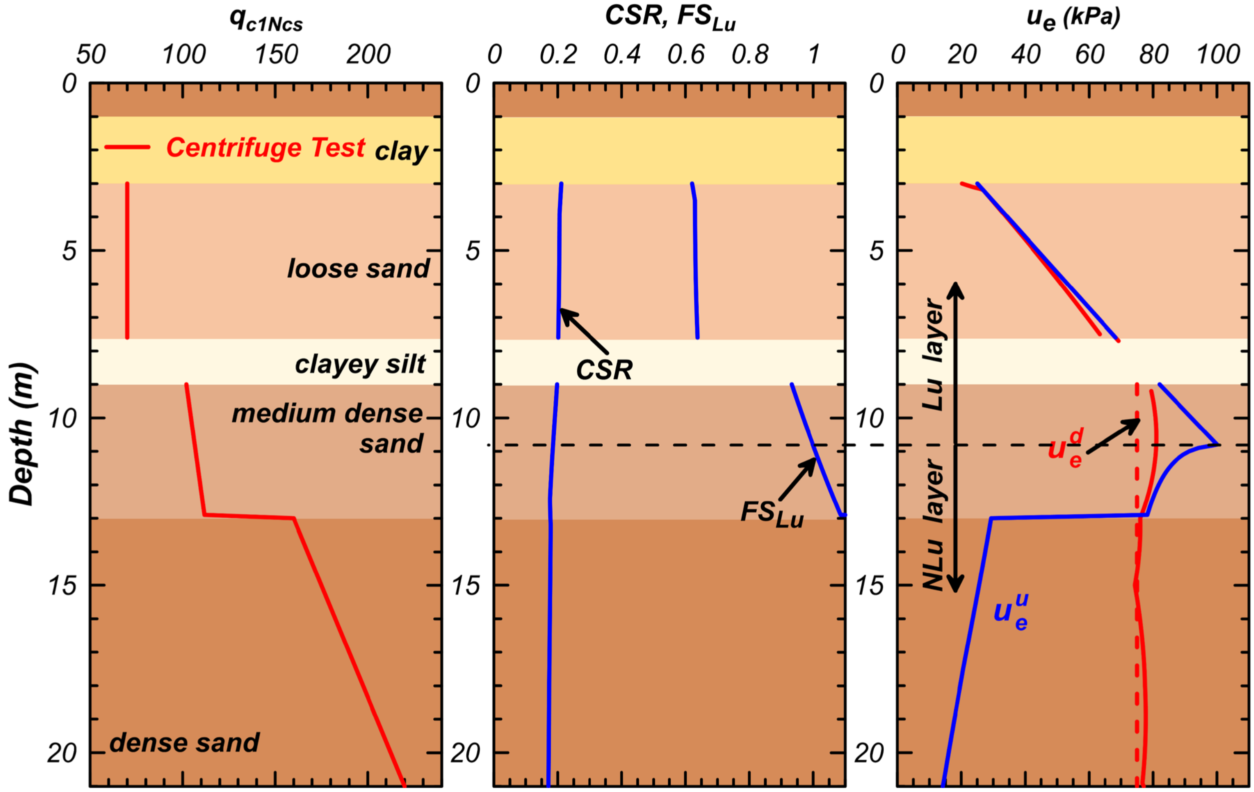

Figure 4.11. Redistribution effects for shaking event EQM$_4$ of centrifuge model test SKS03 (Sinha et al. 2021d): (a) Measured normalized overburden corrected cone tip resistance (q_{c1Ncs}). (b) Cyclic stress ratio (CSR) and factor of safety against liquefaction (FS_{Lu}). (c) Comparison of estimated earthquake-induced (u_e^u) and redistributed (u_e^d) excess pore pressures with the measured excess pore pressures.

CHAPTER 5:

DISPLACEMENT-BASED DESIGN PROCEDURE

5.1 Introduction

Axially loaded piles in liquefiable soils can undergo severe settlements from a shaking event. During shaking, the settlement is caused by the loss of shaft and tip resistance from the generated excess pore pressures in the soil and seismic loads on the pile. After shaking, soil settlement from reconsolidation results in the development of drag load leading to the additional settlement of the pile. The mechanism affecting the response of a pile in liquefiable soil is illustrated in Figure 5.1. Generally, a pile resists the dead load (Q_{dead}) (from the superstructure) by mobilizing positive skin friction (positive shaft resistance) and tip resistance [Figure 5.1 (a)]. During shaking, the generation of excess pore pressures and liquefaction around the pile reduces the positive skin friction in that layer, transferring load further down the shaft and to the tip. Moreover, the seismic load ($Q_{seismic}$) from the shaking of the superstructure cycles the load on the pile [Figure 5.1 (b)]. The pile resists the seismic load with the reduced shaft and tip capacity by undergoing settlement until enough resistance is mobilized to achieve the load equilibrium. In case of excess pore pressures development around the pile's tip, the tip capacity and stiffness are reduced, potentially causing pile settlements. At the end of shaking, the seismic load on the pile disappears, and only the dead load acts on the pile [Figure 5.1 (c)]. However, after shaking, soil settlement from reconsolidation causes a downdrag phenomenon, resulting in drag loads (from negative skin friction) on the pile [Figure 5.1 (c)]. The depth at which skin friction changes its direction from negative to positive is called the neutral plane (Fellenius 1984). Above the neutral plane, the soil settles more than the pile resulting in negative skin friction [Figure 5.1 (c,e)]. Below the neutral plane, the pile settles more than the soil and mobilizes positive skin friction [Figure 5.1 (c,e)]. The drag load increases the load on the pile and decreases the length of the portion of the pile, providing positive skin friction. As a result, more load is transferred to the shaft and tip below the neutral plane, and the pile settles [Figure 5.1 (c,d)]. After complete reconsolidation, a permanent drag load (Q_{drag}) may remain and the neutral plane moves deeper into the liquefiable layer [Figure 5.1 (d,e)]. Due to the development of drag load, the axial load on the pile increases from the pile's head to the neutral plane and then decreases below that [Figure 5.1 (f)]. At the neutral plane, the pile experiences the maximum axial load (Q_{np}) [Figure 5.1 (f)].

The existing procedures for designing piles in liquefiable soils do not fully account for the mechanisms observed during shaking and reconsolidation. The state of practice, AASHTO (2020), uses a forced-based approach to design piles in liquefiable soils. First, the total load acting on the pile is checked against the total resistance offered with appropriate load and resistance factors for service and strength limit design. Then, for extreme loading conditions such as the seismic loads during shaking and liquefaction-induced downdrag, the superstructure's survival is checked against the pile's total capacity and structural strength. For calculating the pile's capacity during shaking, the shaft capacity in the liquefied ($r_u = 1$) layer is assumed zero while assuming total shaft and tip capacity in the non-liquefiable layers ($r_u < 1$). AASHTO (2020) does not recommend evaluating the reduced shaft and tip capacities in the non-liquefiable layers due to increased excess pore pressures that may be generated due to shaking or transmitted to the non-liquefiable layers by redistribution from the liquefied layers. However, recent studies on axially loaded piles in liquefiable soils such as Knappett and Madabhushi (2009) and Sinha et al. (2021c; d; f) showed that estimating excess pore pressures in soil and their effect on reducing the pile's capacity is crucial for pile design. Knappett and Madabhushi (2009) found that the pile tip capacity and stiffness decreased as the excess pore pressures increased near the pile's tip. Sinha et al. (2021c;

d) found that most of the pile settlement in centrifuge model tests occurred during shaking when the high excess pore pressure in soil surrounding the pile reduced its shaft and tip capacity. Sinha et al. (2021f) also observed significant excess pore pressures developments in the non-liquefiable dense sand (bearing) layer due to the redistribution of excess pore pressure from the adjacent liquefiable layer (Seed et al. 1976; Yoshimi and Kuwabara 1973). The high excess pore pressures developed near the pile's tip caused large settlements of the piles. Sinha et al. (2021d) conducted centrifuge model tests on three identical axially loaded piles embedded at three diameters in a dense sand layer with small, medium, and large pile head loads (Q_f), resulting in a static factor of safety of 8, 2.6, and 1.6, respectively. Across multiple shaking events, the settlement of the pile increased as the excess pore pressure near the tip increased [Figure 5.2Figure 5.3]. When very large excess pore pressures developed near the tip, the piles with medium and large head loads plunged in soil [Figure 5.2]. For designing piles from liquefaction-induced downdrag, AASHTO (2020) recommends taking the neutral plane at the bottom of the lowest liquefiable layer or at the depth where soil settlement equals 10 mm. The drag load is calculated as the total negative skin friction above the neutral plane. AASHTO (2020) "conservatively" assumes the negative skin friction equal to the "residual shear strength" in the reconsolidated liquefied soil and non-liquefied shear strength (i.e., equal to the soil shear strength) in the non-liquefied soil. The factored drag load (Q_{drag}) is then added to the factored pile head load (Q_{dead}) and checked against total resistance offered by the length of the pile below the neutral plane [Figure 5.1 (d,f)], ignoring any movement of the pile. However, contrary to the force-based method, if the pile settles relative to the soil, the negative skin friction would change to positive skin friction, providing resistance to the pile. AASHTO (2020) also does not recognize the presence of initial (i.e., before shaking) drag load in the piles and its effect on the downdrag phenomenon. AASHTO (2020) also does not provide a method for calculating the settlement of the pile, and hence it cannot be used for displacement-based design.

A displacement-based design approach offers the advantage of direct evaluation of the performance of piles in terms of the pile settlement. Results from centrifuge studies by Sinha et al. (2021c; d) confirmed that while large drag loads could be caused by liquefaction-induced downdrag, the resulting pile settlement is small. Among various methods, the displacement-based approach using t-z and q-z springs analyses may be used to estimate the load distribution and settlement of the piles. The t-z material models the behavior of shaft resistance, and the q-z material models the tip resistance. Law and Wilson (2017) used a displacement-based design procedure using t-z and q-z materials and saved the pile length by 20% compared to the force-based design procedure from AASHTO (2020). Boulanger et al. (1999) developed a TzLiq material to account for shaft resistance and stiffness changes as excess pore pressures developed and dissipated in the soil around the pile. The TzLiq material modeled capacity and stiffness as a linear function of excess pore pressures in the adjacent soil. Boulanger and Brandenberg (2004) used the TzLiq material to model liquefaction-induced downdrag on axially loaded piles accounting for the dissipation of excess pore pressures with the associated soil settlement. Sinha et al. (2021e) developed QzLiq material to model tip behavior in liquefiable soils. The pile's tip capacity and stiffness was varied non-linearly with excess pore pressures at the tip $i.e. (1 - r_u)^{\alpha_t}$, where α_t is a constant defined by Knappett and Madabhushi (2009) that is a function of the soil's friction angle (ϕ). Sinha et al. (2021e) used the TzLiq and the QzLiq material and performed a TzQzLiq analysis to model the response of axially loaded piles in liquefiable soils and validated the numerical results against centrifuge test data. The numerical model accounted for initial drag load on piles, changes in the shaft and tip capacities, and their stiffnesses in the presence of excess pore pressures in soil and the timing of soil settlement and excess pore pressure distribution. The TzQzLiq analysis provided time histories of axial load distribution and settlement of piles during and after shaking. The TzQzLiq analysis provided a method to estimate pile settlement and axial load distribution.

This chapter presents a displacement-based design procedure using the TzQzLiq analysis methodology for designing axially loaded piles subject to seismic loading and liquefaction-induced downdrag. The new design procedure accounts for the initial drag load on the pile, excess pore pressures in the non-liquefiable layers following redistribution from the liquefied layers, and reduction in the pile's shaft and tip capacity from excess pore pressures in the soil. Design steps are provided to estimate the input properties required for running a TzQzLiq analysis. Results from the analysis are then used to obtain design curves describing the settlement and drag load on the pile with varying pile lengths, which are ultimately used for selecting the design length of the pile. Finally, the design procedure is applied to the piles used in centrifuge tests, and the results are compared. Towards the end, an example design problem is considered to illustrate the applicability of the new method in practice.

5.2 Displacement-Based Design Method

The extreme events considered in pile design include seismic loading conditions and liquefaction-induced downdrag. A TzQzLiq analysis of piles (Sinha et al. 2021e) (also described in Chapter 3) can be performed to obtain the axial load distribution and settlement of piles from these loading conditions. The TzQzLiq analysis is performed in three stages, as shown in Figure 5.3. Stage 1 applies a pile head load ($Q_f = Q_{dead}$) and simulates the initial axial load distribution on the pile. Stage 2 and Stage 3 model the extreme loading events (as described in subsections below). Results from the TzQzLiq analysis can be used to obtain design curves on drag load and pile settlement for varying pile lengths. The length of the pile can then be selected based on the serviceability criteria and checked against the structural strength of the pile. The serviceability criteria could be based on the total pile settlement or the differential pile settlement relative to the free field settlement.

Design for Seismic Loading

During shaking, excess pore pressures generated in the soil around the pile may decrease the shaft and tip capacity of the pile. At the same time, cyclic seismic loads $(Q_{seismic})$ may be developed on the pile from the shaking of the superstructure. These seismic loads can be estimated by analyzing the superstructure under the design earthquake load. AASHTO (2015) suggests methods for determining seismic loads on bridges and their foundations. Additionally, during shaking, liquefaction near the surface can cause surface manifestation around the piles causing a complete reduction of shaft resistance above the liquefied layer (Caltrans (2020)).

A conservative approach for estimating the settlement of piles during shaking would be to perform a TzQzLiq analysis with a dead load of $Q_f = Q_{dead}$ then reduce the shaft and tip resistance due to the increased excess pore pressures, and then apply cycles of seismic load $(\pm Q_{seismic})$ to the pile head. An illustration of the sequence of loads applied on the pile and the excess pore pressures in the soil while performing a TzQzLiq analysis for seismic loading is shown in Stage 2 of Figure 5.3. During real earthquake shaking, the pile can experience multiple cycles of the seismic load depending upon the ground motion’s duration, intensity, and its predominant period relative to the superstructure. The pile settlement caused by seismic loading is expected to be most prominent in the cycle with the greatest amplitude and significantly less in subsequent and smaller amplitude cycles (Wang et al. 2021). Therefore, applying one cycle of the maximum expected seismic load while the pile capacity is a minimum is suggested to provide a reasonable estimate of pile settlement for most earthquake loading conditions. However, if the superstructure experiences many cycles of seismic load (e.g., in a long duration earthquake), multiple cycles of variable amplitude seismic load should be applied to the piles to assess settlement due to cyclic seismic loads.

Design for Liquefaction-Induced Downdrag

During reconsolidation, it is assumed that the seismic loads have passed, and only the dead load acts on the pile [Figure 5.1 (c), Figure 5.3]. Thus, the proposed approach for estimating the pile settlement during reconsolidation is to consider a dead load ($Q_f = Q_{dead}$) acting on the pile with excess pore pressures decreasing as soil settlement occurs. An illustration of the pile load, the time history of excess pore pressures, and soil settlement considered while performing a TzQzLiq analysis for liquefaction-induced downdrag are shown in Stage 3 of Figure 5.3.

5.3 TzQzLiq Material Properties

The TzQzLiq numerical model uses TzLiq and QzLiq materials [Figure 5.4 (e)] with zero-length elements to model the response of piles in liquefiable soils (Sinha et al. 2021e). These materials account for changes in the shaft and tip capacity of the pile as free-field excess pore pressures develop and dissipate in soil [Figure 5.4 (e)]. The reduced shaft capacity ($t^{r_u}_{ult}$) and tip capacity ($q^{r_u}_{ult}$) is modeled as a function of excess pore pressure ratio (r_u) around the pile's shaft and near the tip as defined in the equations below.

$$t^{r_u}_{ult} = t^{o}_{ult}(1 - r_u)$$

$$q^{r_u}_{t,ult} = q^{o}_{t,ult}(1 - r_u)^{\alpha_t} \tag{5.1}$$

$$\alpha_t = \frac{3 - sin\phi'}{3(1 + sin\phi')}$$

where t^{o}_{ult} is the ultimate shaft capacity when $r_u = 0$, and r_u is the free-field excess pore pressure ratio around the shaft. And $q^{o}_{t,ult}$ is the ultimate tip capacity when $r_u = 0$, α_t is a constant that, according to Knappett and Madabhushi (2009), depends only on the effective friction angle (ϕ') of the soil at the tip. The stiffness of the TzLiq and QzLiq materials in liquefiable soils are scaled proportionally to the respective shaft $\left(t^{r_u}_{ult}\right)$ and tip $\left(q^{r_u}_{ult}\right)$ capacity defined in Equation 1. The ultimate shaft capacity (t^{o}_{ult}) and tip capacity (q^{o}_{ult}) can be obtained empirically using equations and correlations provided in AASHTO (2020) or directly measured from the field or lab tests. Sinha et al. (2021e) describes the selection of stiffness parameter z_{50} (i.e., the displacement corresponding to 50% of ultimate capacity) for the implemented material models TzLiq and QzLiq in OpenSees (McKenna et al. 2010). The stiffness of the TzLiq material can be estimated, assuming a displacement in the order of 3% of the pile diameter can mobilize the interface skin friction capacity (Sinha et al. 2021e). The stiffness (z_{50}) parameter can accordingly be chosen based on the backbone curve of the t-z material. For example, the non-linear backbone curve of the implemented t-z material (Boulanger et al. 1999; Mosher 1984; Reese and O'Niel 1987) in OpenSees is a hyperbolic curve that takes displacement equal to about four times z_{50} to mobilize >90% of the ultimate capacity (t^{o}_{ult}). Thus, a z_{50} of 0.5% of the pile's diameter can be assumed for modeling the stiffness of the TzLiq material.

Determining site-specific QzLiq material stiffness is essential for accurately modeling the pile settlement and drag load accurately. Sinha et al. (2021e) conducted sensitivity studies on the stiffness of TzLiq and QzLiq material on axially loaded piles in liquefiable soils. They found that the QzLiq material's stiffness significantly affected the pile settlement and the development of drag loads. Therefore, the study recommended calibrating the initial capacity and stiffness properties of the QzLiq material against the site-specific pile load test. An empirical pile load test curve was developed to aid the calibration of QzLiq material for cases when a field pile load test is unavailable. Well-documented pile load tests data from the Federal Highway Administration's (FHWA) Deep Foundation Load Test Database (DFLTD) - Version 2.0 (Petek et al. 2016) was used to develop the empirical pile load test curve. Table 5.1 summarizes the projects and the properties of the piles (diameter, slenderness ratio (L/D), Young's Modulus, and bearing layer friction angle (ϕ')) used. Pile load tests from large diameter (>20 inches) cast-in-drilled-hole (CIDH) piles of slenderness ratio (L/D) of about 20 were used to develop the empirical curve. The equation of the empirical pile load test curve is given as

$$\Delta_p = a * exp(b * P/P_{\Delta_p=5\%\,D}) - a * exp(c * P/P_{\Delta_p=5\%\,D}) \qquad 5.2$$

where P is the pile capacity, Δ_p is pile settlement in % of pile's diameter, $P_{\Delta_p=5\%D}$ is the pile capacity corresponding to the settlement equal to 5% of the pile's diameter, and a, b, and c are the constants equal to $a = 0.24, b = 3.3, and\ c = 1.83$, respectively. The empirical pile load test curve and field data are shown in Figure 5.5. It can be seen from the figure that the empirical pile load test curve matches quite well with the field data.

Table 5.1. A summary of the projects, the properties of the piles (diameter, slenderness ratio (L/D), Young's Modulus, and bearing layer friction angle (ϕ')) used in developing the empirical pile load test curve [Figure 5.5].

Projects [a]	***Location***	***Pile Diameter (in)***	***L/D Ratio***	***Pile's Young's Modulus (GPa)***	***Bearing Layer Friction Angle, ϕ'***
176 France	*France*	*30*	*18*	*28*	*28*
192 FHWA File	*Florida, USA*	*24*	*20*	*22*	*26*
193 Barnet Center	*Florida, USA*	*24*	*22*	*31*	*25*
199 Kanapaha	*Florida, USA*	*36*	*20*	*31*	*30*
201 Johannesburg	*South Africa*	*36*	*20*	*28*	*28*
206 FHWA File - BB Site	*Texas, USA*	*24*	*17*	*28*	*30*

[a] *Petek et al. (2016)- FHWA Deep Foundation Load Test Database Version 2.0*

5.4 Proposed Design Procedure Steps

Obtaining design curves relating settlement and drag load to pile length requires multiple steps. The proposed design procedure's steps (a) to (f) are described in Figure 5.4 and in the subsections below.

(a) Perform Soil Liquefaction Hazard Analysis

A soil liquefaction hazard analysis of a site identifies the soil layers which are liquefiable and non-liquefiable. Among many methods (such as Youd et al. (2001), Idriss and Boulanger (2008), Robertson (2015), and Cetin et al. (2018)), the empirical procedure from Idriss and Boulanger (2008) is widely used for performing soil liquefaction hazard analysis for the assumed design earthquake loading. The site's design earthquake loading properties such as magnitude ($\mathrm{M_w}$) and peak ground acceleration (PGA) is first used to compute the cyclic stress ratio (CSR) in the soil layers. Then, liquefaction-triggering correlations developed on normalized overburden corrected "N value" for clean sand (N_{160cs}) obtained from static penetration test (SPT) investigations or normalized overburden corrected cone tip resistance for clean sand (q_{c1Ncs}) obtained from cone penetration test (CPT) investigations are used to estimate the cyclic resistance ratio (CRR) of the soil layers. In the end, a factor of safety against liquefaction $\left(FS_{liq} = \frac{CRR}{CSR}\right)$ is computed to designate the layers as liquefiable and non-liquefiable under the design earthquake loading. $FS_{liq} \leq 1$ refers to a liquefiable layer and $FS_{liq} > 1$ refers to a layer that is non-liquefiable. An illustration on the interpretation of liquefiable and non-liquefiable layers from liquefaction-triggering correlation using N_{160cs} and q_{c1Ncs} is shown in Figure 5.4 (a). The obtained factor of safety (FS_{liq}) from the liquefaction-triggering correlations is then later used in step (c) to estimate the excess pore pressures (u_e) and step (d) to estimate soil settlement from reconsolidation in the liquefiable and non-liquefiable layers.

(b) Evaluate Potential for Surface Manifestation

During shaking, liquefaction in a surficial layer can result in surface manifestation (i.e., ejecta of liquefied material to the surface). The ejecta can travel through the interface of the pile (e.g., interface gaps developed from shaking [Figure 5.1 (c)]) and decrease the pile's shaft resistance in all the affected layers from surface manifestation. The design procedures by Caltrans (2020) uses Ishihara's (1985) (see Figure 5.4 (b)) chart to assess the potential for surface manifestation (depending on the depth and thickness of the liquefiable layer) and assume zero shaft resistance in all layers affected by the surface manifestation for accessing the pile capacity under seismic loading. However, during reconsolidation, the Caltrans (2020) procedure assumes mobilization of the full shaft resistance, even for layers affected by the surface manifestation. The affected layers comprise all the layers above the deepest liquefiable layer, causing surface manifestation. An illustration of the affected layers from surface manifestation is shown in Figure 5.4 (c). The new design procedure also conservatively assumes zero shaft capacity and 100% of the shaft capacity in the affected layers during the seismic loading and liquefaction-induced downdrag, respectively. In the TzQzLiq analysis, the effect of surface manifestation on the pile's shaft resistance is modeled by considering the affected layers as liquefiable layers, resulting in zero shaft capacity during the seismic loading and 100% of shaft capacity (depending upon the relative soil-pile displacement) from liquefaction-induced downdrag.

(c) Estimate Peak Excess Pore Pressures in Soil Layers

The shaking caused by earthquake loading can quickly generate large excess pore pressure in the liquefiable layers. While the excess pore pressure generated from shaking in the non-liquefiable layers is smaller, dissipation of excess pore pressure from the adjacent liquefiable layers can increase excess pore pressures in the non-liquefiable layers. Estimating the peak excess pore pressures from earthquake loading considering redistribution is thus essential for evaluating the minimum shaft and tip capacity following a shaking event. An illustration of peak excess pore pressures in the soil layers is shown in Figure 5.4 (c). Sinha et al. (2021g) developed an approximate procedure to estimate the peak excess pore pressures (u_e^{pk}) in the soil layers considering redistribution. The procedure is described in details with examples in Sinha et al. (2021g). The procedure first estimates the earthquake-induced excess pore pressure ratio (r_u^u) in the liquefiable (defined with subscript "Lu" for example, r_{u-Lu}^u, u_{e-Lu}^u) and non-liquefiable (defined with subscript "NLu" for example, r_{u-NLu}^u, u_{e-NLu}^u) layers using the FS_{liq} (computed in step (a)) as

$$r_{u-Lu}^u \; (or \; r_{u-NLu}^u) = \begin{cases} \frac{2.0}{\pi} arcsin\left(FS_{liq}^{-\frac{1}{2b\beta}}\right), & FS_{liq} > 1 \\ \qquad\qquad 1.0, & FS_{liq} \leq 1 \end{cases} \qquad 5.3$$

where $b \; and \; \beta$ are the parameters in terms of q_{c1Ncs} and N_{160cs} defined by Mele et al. (2021). The peak excess pore pressure ratio (r_{u-liq}^{pk}) in liquefiable layer is taken as r_{u-liq}^{pk} = 1.0. The peak excess pore pressure in the non-liquefiable layer with compressibility (m_{v-NLu}), thickness (H_{NLu}), and initial mean effective stress (σ'_{vo-NLu}) are estimated considering redistribution of excess pore pressures from the adjacent liquefiable layer with compressibility (m_{v-Lu}), thickness (H_{Lu}) and initial mean effective stress (σ'_{vo-NLu}). The peak excess pore pressure ratio in the non-liquefiable layer (r_{u-NLu}^{pk}) depends upon the layer's relative compressibility ratio $\left(\overline{m_v} = \frac{m_{v-Lu}}{m_{v-NLu}}\right)$, thickness ratio $\left(\overline{H} = \frac{H_{NLu}}{H_{Lu}}\right)$, depth to the top of the non-liquefiable layer ($\bar{Z} = \frac{Z}{H_{Lu}}$) and the average earthquake-induced excess pore pressure in the non-liquefiable layer (r_{u-NLu}^{u}). Equation 5.4 summarizes the functional form of the average peak excess pore pressures (u_e^{pk}) in the liquefiable and non-liquefiable layers.

$$r_{u-Lu}^{pk} = 1.0$$

$$r_{u-NLu}^{pk} = f(\sigma'_{vo-NLu}, \sigma'_{vo-Lu}, \overline{H}, \overline{m_v}, \bar{Z}, r_{u-NLu}^{u}) \qquad 5.4$$

$$u_{e-Lu}^{pk} = r_{u-Lu}^{pk}\sigma'_{vo-Lu}\ ;\ u_{e-NLu}^{pk} = r_{u-NLu}^{pk}\sigma'_{vo-NLu}$$

In Equation 5.4, the compressibility m_v of the soil layer is computed estimated using relations by Seed et al. (1976) and Janbu (1985) using the procedure defined in Sinha et al. (2021g) (also described in Chapter 4) [Figure 4.9]. The relation from Seed et al. (1976) is used to compute the relative compressibility (m_v/m_{vo}) of the soils layers in liquefiable soils depending on the relative density (D_R) and the earthquake-induced excess pore pressure ratio (r_u^u) as follows.

$$\frac{m_v}{m_{vo}} = \frac{exp(y)}{1+y+y^2/2}$$

$$y = 5(1.5 - D_R)(r_u^u)^b \qquad 5.5$$

$$b = 3(4)^{-D_R}$$

where m_{vo} is the compressibility at zero excess pore pressure $r_u^u = 0$. The compressibility (m_{vo}) of the normally consolidated sand at mean effective stress (σ'_{vo}) with $r_u^u = 0$ is estimated using empirical correlations from Janbu (1985), as follows

$$m_{vo} = \frac{1}{m\sqrt{P_o \sigma'_{vo}}} \qquad 5.6$$

where m is the modulus parameter depending upon the porosity (n) of the sand layer (determined from Figure 4.9) and P_o is a constant equal to the atmospheric pressure, i.e., P_o =101.3 kPa.

(d) Estimate Soil Settlement from Reconsolidation

The proposed procedure requires the determination of the profile of settlement as a function of depth associated with post-liquefaction reconsolidation. Several empirical methods such as Tokimatsu and Seed (1984), Shamoto et al. (1998), Wu (2002), and Idriss and Boulanger (2008) have been developed for approximately estimating soil settlement from reconsolidation. These empirical methods provide an estimate of reconsolidation settlement with an accuracy of 25-50% (Tokimatsu and Seed 1984). Darby (2018) conducted several centrifuge tests on loose and dense sand under multiple earthquake shakings and found that the estimated reconsolidation settlement using the empirical procedures overestimated the observed measurements. A larger prediction of reconsolidation settlement would be conservative for the pile design. Further research could lead to improved estimates of reconsolidation settlements. Among the listed methods, Idriss and Boulanger's (2008) empirical method gave a conservative estimate and is thus used for estimating reconsolidation settlements. Later in this chapter, a study is performed to evaluate the effect of the magnitude of the reconsolidation settlement on drag load and the associated downdrag settlement caused in a pile. An illustration of the estimated reconsolidation soil settlement profile is shown in Figure 5.4 (d).

(e) Estimate Pile Settlement

The pile settlement during the seismic loading (stage 2) and liquefaction-induced downdrag (stage 3) is estimated by performing a TzQzLiq analysis [Figure 5.4 (e)]. The results from the TzQzLiq analysis on pile settlement and drag load are then used to obtain design curves for the piles. The input parameters of the TzQzLiq numerical model include the pile cross-section and material properties, pile head loads (Q_f), profiles of effective stress and soil settlement, and the TzLiq and QzLiq material properties. Cross-section and material properties are obtained from the dimension of the pile and the material selected for the design. Pile head loads (Q_f) are the design load applied to the pile during seismic loading and liquefaction-induced downdrag (refer to Section 5.2). The effective stress and soil settlement profiles are computed from steps (c) and (d) described above. The TzLiq and QzLiq properties are estimated and calibrated against the pile load test as described in Section 5.3.

(f) Obtain Design Curves

The design curve of the pile includes the plot of pile settlement and drag load against the length of the pile [Figure 5.4 (f)]. Multiple TzQzLiq analyses for different lengths of the piles are performed to obtain the design curves. Figure 5.4 (f) shows the settlement of the pile at the end of seismic loading (stage 2) and the end of liquefaction-induced downdrag (stage 3) for varying lengths of the piles. The figure also shows the drag load developed on the pile (at the end of stage 3) for varying pile lengths. Under the same loading conditions, as the length of the pile increases, the pile settlement decrease. On the other hand, the drag load increases and reaches a saturation equal to the shaft resistance above the lowest reconsolidated liquefied layer.

The design length of the pile is selected from the design curve based on a serviceability criterion on pile settlement. Typically, the allowable settlement is based on the level of movement that the structure can tolerate. Structures such as long-span bridges may accommodate significant amounts of pile settlement without risk of collapse (Law and Wilson 2017). For large diameter piles such as CIDH piles, the serviceability criterion on pile settlement for extreme events generally may be in the range of 5-10% of the pile's diameter. For some structures, the settlement of the pile relative to the ground could serve as the serviceability criteria. For example, the post-earthquake functionality of the superstructure (for example, of the bridges) may be better if the pile settlement is closer to the free-field soil settlement (as described in Section 2.8 of Chapter 2). Figure 5.4 (g) illustrates the selection of pile design length for assumed serviceability criteria. With the selected design length of the pile, the design drag load (Q_{drag}) is estimated, as shown in Figure 5.4 (h). The maximum load acting on the pile $Q_{np} = Q_{dead} + Q_{drag}$ [see Figure 5.1 (f)] is then checked against the pile's structural strength. Suppose the maximum load exceeds the structural strength of the pile. In that case, the cross-section of the pile or its material strength properties are revised, and an associated new design curve is evaluated.

5.5 Comparison of Proposed Design Procedure Results with Centrifuge Test

The proposed design procedure was applied on piles used in centrifuge model tests SKS02 (Sinha et al. 2021c) and SKS03 (Sinha et al. 2021d) for selected shaking events EQM_3 and EQM_4, respectively. The subsections below describe the centrifuge model tests, analysis using the proposed design procedure, and compare the estimated drag load and pile settlement with centrifuge data.

Description of Centrifuge Model Test

The centrifuge models consisted of 21 m of the soil profile with an undrained boundary condition underneath due to the impermeable base of the model container. The relative position of the soil layers with their thicknesses for the SKS02 and SKS03 centrifuge models are shown in Figure 2.1 and Figure 2.4, respectively. The models consisted of identical pipe piles of aluminum with an outer diameter (D) of 635 mm and a thickness of 35 mm (refer to Section 2.3 on pile properties). The centrifuge model test SKS02 consisted of two piles: 0DPile and 5DPile, both with a dead load of Q_{dead}=500 kN. The centrifuge model test SKS03 consisted of three piles: 3DPileS, 3DPileM, and 3DPileL with a dead load of Q_{dead} = 500 kN, 1500 kN, and 2400 kN, respectively. For the centrifuge model test SKS02, the large shaking event EQM_3 was selected. For centrifuge model test SKS03, the large shaking event EQM_4 was selected. The shaking events EQM_3 and EQM_4 were scaled Santa Cruz earthquake motions of M_w = 6.9 from the Loma Prieta 1989 earthquake. EQM_3 was a scaled Santa Cruz motion (third shaking event in sequence applied to SKS02 model) with a peak base acceleration (PBA) of 0.24 g [Figure 2.2]. EQM_4 was the fourth shaking event in sequence applied to the SKS03 model. It consisted of a long-duration modified Santa Cruz motion (Malvick et al. 2002) consisting of one large pulse followed by five small pulses, scaled to produce a PBA of 0.45 g [Figure 2.5]. The measured peak ground acceleration (PGA) produced from the shaking events, EQM_3 and EQM_4, was about 0.2 g and 0.16 g, respectively [Figure 2.2, Figure 2.5]. The normalized overburden corrected cone tip resistance (q_{c1Ncs}) during the shaking events EQM_3 and EQM_4 are shown in Figure 2.3 (a) and Figure 2.6 (a), respectively. Time histories of excess pore pressures (u_e) and soil and pile settlement during shaking and reconsolidation for the two shaking events EQM_3 and EQM_4 are shown in Figure 2.10 and Figure 2.11, respectively. The peak excess pore pressure (u_e^{pk}) profile during shaking and the soil settlement profile after complete reconsolidation is shown in Figure 5.6 and Figure 5.7, respectively. The soil settlement profile was estimated using the inverse analysis method described in Section 3.3 of Chapter 3 [Figure 3.4 and Figure 3.5]. The initial (i.e., before shaking) and final (i.e., after complete reconsolidation) axial load distribution in the piles for the two shaking events, EQM_3 and EQM_4, and their limit load curves are shown in Figure 3.2. The figure shows that the piles had an initial drag load developed from the prior shaking events. After complete reconsolidation, the drag load and thus the axial load in the piles increased at all depths. During the shaking, the piles: 3DPiles (3DPileS, 3DPileM, and 3DPileL), 0DPile, and 5DPile experienced a vertical acceleration of 0.1 g, 0.25 g, and 0.03 g, respectively.

Analysis Using Proposed Design Procedure

The cyclic stress ratio (CSR), the factor of safety against liquefaction (FS_{liq}), peak excess pore pressure (u_e^{pk}), and soil settlement profile obtained for the shaking events EQM_3 and EQM_4 following the proposed design procedure are shown in Figure 5.6 and Figure 5.7, respectively. The figures also compare the estimated peak excess pore pressure with the measurements from pore pressure transducers; and the reconsolidated soil settlement profile with the settlement profile obtained from the inverse analysis of measured excess pore pressures. The subsections below briefly describe the soil liquefaction hazard analysis, estimated peak excess pore pressure, and soil settlement profile for the two shaking events and their comparison with the centrifuge test. A separate subsection describes the TzQzLiq analysis of piles using the estimated peak excess pore pressure and soil settlement profiles.

Soil Liquefaction Hazard Analysis

Soil liquefaction hazard analysis on the soil profiles of centrifuge model tests SKS02 and SKS03 for shaking events EQM_3 and EQM_4 was performed using the CPT-based (q_{c1Ncs}) liquefaction-triggering correlation procedures from Idriss and Boulanger (2008). For the shaking event EQM_3 in centrifuge model test SKS02, the liquefaction-triggering correlation procedure estimated liquefaction ($FS_{liq} \leq 1$) in the loose sand layer between the depth of 5 – 14 m [Figure 5.6]. For the shaking event EQM_4 in the centrifuge model test SKS03, liquefaction was estimated in the loose sand layer and the upper 1.6 m thick medium dense sand layer [Figure 5.7]. The non-liquefiable layers ($FS_{liq} > 1$) consisted dense sand below 14 m in the centrifuge model SKS02 and the medium dense and dense sand below 10.7 m in the centrifuge model SKS03. Empirical curves from Ishihara (1985) predicted no surface manifestation. The predictions were consistent with the results from the centrifuge tests.

The peak excess pore pressure in the non-liquefiable layers was estimated considering the redistribution effects. The peak excess pore pressures in the soil layers estimated for the selected shaking events EQM_3 and EQM_4 are shown in Figure 5.6 (c) and Figure 5.7 (c), respectively. For the shaking event EQM_3 of the centrifuge model test SKS02, the peak excess pore pressure in the non-liquefiable layer was estimated for a compressibility ratio of ($\overline{m_v} = 20$), the thickness ratio of ($\overline{H} = 0.78$), depth to the top of the non-liquefiable layer ($Z = 14\,m$), and the average earthquake-induced excess pore pressure in the non-liquefiable layer ($r^u_{u-NLu} = 0.096$). For the shaking event EQM_4 of the centrifuge model test SKS03, the parameters included a compressibility ratio of ($\overline{m_v} = 12$), thickness ratio of ($\overline{H} = 6.06$), depth to the top of the non-liquefiable layer ($Z = 10.7\,m$), and average earthquake-induced excess pore pressure in the non-liquefiable layer ($r^u_{u-NLu} = 0.1$). The peak excess pore pressure estimated in the non-liquefiable layers for the selected shaking events in centrifuge models SKS02 and SKS03 was were $u_e^{pk} = 98\ kPa\ and\ u_e^{pk} = 75\ kPa$ as shown in Figure 5.6 (c) and Figure 5.7 (c), respectively. The figure shows that the estimated peak excess pore pressures in the non-liquefiable layers match pretty well with the pore pressure transducer measurements.

Soil Settlement from Reconsolidation

The estimated soil settlement profile using the empirical procedures from Idriss and Boulanger (2008) for the two shaking events EQM_3 and EQM_4 are shown in Figure 5.6 (d) and Figure 5.7 (d), respectively. It also includes the soil settlement profile obtained by performing an inverse analysis of measured excess pore pressures for the shaking events EQM_3 and EQM_4 (Sinha et al. 2021e). The estimated soil settlement profile from the inverse analysis was validated with surface settlement measurements. From the figures, it can be seen that the empirical procedures from Idriss and Boulanger (2008) predicted significantly higher (> 400%) magnitudes of soil settlement (in the loose and medium dense sand layers) compared to the estimated settlement from the inverse analysis. At the same time, the estimated soil settlement underpredicted settlements in the dense sand layers. For both the shaking events [Figure 5.6 (d), Figure 5.7 (d)], the soil settlement profile from the inverse analysis showed some small settlements in dense layers. The estimated soil settlement from the inverse analysis (Sinha et al. 2021e) at the tip of 0DPile, 5DPile, and 3DPiles was about 6 mm, 3 mm, and 1.5 mm, respectively. In contrast, Idriss and Boulanger's (2008) empirical procedure estimated no settlement in the dense sand layer. Soil settlements in the dense sand layers and near the pile's tip can significantly affect the settlement of the pile and the development of drag loads. Sinha et al. (2019) studied the effect of reconsolidation strains near the pile's tip and found that it results in more drag loads and pile settlement. TzQzLiq analyses were performed for the two soil settlement profiles: one from the inverse analysis (Sinha et al. 2021e) and the other from the empirical procedure of Idriss and Boulanger (2008) to study and compare the effect of reconsolidation strains in dense sand on pile settlement and drag load.

TzQzLiq Analysis of Piles

A TzQzliq analysis of the piles was performed in OpenSees (McKenna et al. 2010) with a mesh discretization of 0.1 m. The latest version of OpenSees (available from the GitHub repository at https://github.com/OpenSees/OpenSees) with QzLiq material model implemented was used to perform the analysis. The properties of TzLiq and QzLiq material used in the TzQzLiq analysis are summarized in Table 3.1. The material properties were calibrated against the limit load curves and pile load test results (described in Chapter 3). Load transfer backbone curves from Reese and O'Neil (1987) and Mosher (1984) were used to model the TzLiq material behavior in sand and clay layers, respectively. The QzLiq load transfer behavior was modeled with backbone curves from Vijivergiya (1977). The ultimate capacity of the TzLiq material at different depths along the length of the pile was obtained from the limit load curves shown in Figure 3.2. The stiffness parameter (z_{50}) of TzLiq material was taken as 0.3% of the pile's diameter in the clay, silt, loose sand, and medium dense sand layers and 0.15% of the pile's diameter in the dense sand layer. The QzLiq material parameters (capacity ($q^{o}_{t,ult}$) and stiffness (z_{50})) were calibrated against the pile load test results (Figure 2.7). The constant (α_t) was taken as 0.55 calculated using Equation 1 with an effective friction angle of $\phi' = 30^{\circ}$. The pile's seismic load was calculated from the maximum vertical acceleration experienced by the pile during shaking. The seismic load calculated for the 0DPile, 5DPile, 3DPileS, and 3DPileM were 125 kN, 15 kN, 50 kN, and 150 kN, respectively.

A sensitivity study on the magnitude of reconsolidation soil settlement on drag load and pile settlement was performed by analyzing multiple soil settlement profiles scaled to produce surface settlements in the range of 10 – 400 mm. Additionally, two types of TzQzLiq analysis (TzQzLiq Analysis I and TzQzLiq Analysis II) were performed to study the effect of reconsolidation strains in the dense sand layer and near the pile's tip. TzQzLiq Analysis I used the soil settlement profile estimated from the inverse analysis of measured excess pore pressures described in Sinha et al. (2021e). TzQzLiq Analysis II used the soil settlement profile estimated from Idriss and Boulanger (2008) scaled to produce surface settlement equal to the measurement in centrifuge test. Finally, a TzQzLiq analysis using the proposed design procedure (i.e., TzQzLiq Analysis II with unscaled soil settlement profile) named "Proposed Design Procedure" was performed, and results were compared with the centrifuge test (see Table 5.2). Please note that the assumed soil settlement profile was the only difference between TzQzLiq Analyses I, TzQzLiq Analyses II, and TzQzLiq analysis using the proposed design procedure.

Comparison of Estimated Pile Settlement and Drag Load With Centrifuge Test

The TzQzLiq analysis is shown to produce a reasonable estimate of the seismic settlement of piles. The comparison of seismic settlement of the piles with measurements from the centrifuge test is shown in Table 5.2. Since all the different TzQzLiq analyses (TzQzLiq Analysis I, TzQzLiq Analysis II, and Proposed Design Procedure) had the same excess pore pressures profiles and seismic loads, their results on the seismic settlements were the same. The TzQzLiq analyses predicted plunging of 0DPile due to excess pore pressure ratio reaching $r_u = 1.0$ near its tip. The estimated seismic settlement for deeply embedded 5DPile with a small dead load was negligible, similar to results from the centrifuge test. The estimated seismic settlement for the 3DPiles (3DPileS, 3DPileM, and 3DPileL) was slightly smaller than the measured settlements. The predicted seismic settlement in the 3DPileS, 3DPileM, and 3DPileL were about 0.1% D, 3.5% D, and 21.1% compared to the measured settlement of 0.3% D, 4.4% D, and 31.5% D respectively.

The difference in the result could be due to the multiple cycles of seismic load occurring on the piles, compared to the only one cycle of seismic load applied in the TzQzLiq analysis. A separate analysis showed that ten cycles of seismic load on 3DPileM could predict seismic settlements equal to the settlements observed in the centrifuge test. Like the centrifuge test, TzQzLiq analysis showed a substantial settlement of 3DPileL (> 20% D), indicating plunging of the pile in soil. The difference in the seismic settlement prediction for 3DPileL is due to the inability of the TzQzLiq analysis in modeling pile settlement during plunging.

The estimated downdrag settlement in the piles from the TzQzliq analyses matched reasonably well with the centrifuge tests. The downdrag settlement for the different magnitude of soil settlement profiles is shown in Figure 5.8. Results on downdrag settlement from the three TzQzLiq analyses (TzQzLiq Analysis I, TzQzLiq Analysis II, and Proposed Design Procedure) and their comparison with centrifuge test are summarized in Table 5.2. The TzQzLiq analyses showed an increase in downdrag settlement with the magnitude of soil settlement and settlement in dense sand layers. For example, for 3DPileS, downdrag settlement increased from 0% to about 1.5% of the pile diameter when the soil settlement increased from 10 mm to 370 mm. Overall for all the piles (5DPile and 3DPiles), the resulting downdrag settlement was small and was within 2% of the pile's diameter. Results from the TzQzLiq analyses (summarized in Table 5.2) show that for the same magnitude of soil settlement, the downdrag settlement is higher if there are soil settlements near the pile tip (Sinha et al. 2019). TzQzLiq Analysis I (that had soil settlement at the pile's tip) showed consistently higher downdrag settlement compared to TzQLiq Analysis II (that had no soil settlement at the pile's tip). The downdrag settlement of the TzQzLiq Analysis I with the soil settlement profile estimated from the inverse analysis matched quite well with the centrifuge test results. The downdrag settlement results from TzQzLiq analysis following the proposed design procedure were found conservative due to the large magnitude of soil settlement predictions from the empirical procedures of Idriss and Boulanger (2008).

The drag load on the piles also increased with soil settlement; however, it approached saturation at a large magnitude of soil settlements. For example, for 5DPile, drag increased from 100 kN to 1000 kN as soil settlement increased from 10 mm to 370 mm. Among 3DPiles, the drag load was higher for lightly loaded piles (3DPileS) than heavily loaded piles (3DPileM and 3DPileL). The comparison of drag loads in Table 3 for the three different TzQzLiq analyses showed larger drag loads for a larger magnitude of soil settlement. The TzQzLiq analysis following the proposed design procedure gave conservative estimates of drag load compared to the measured drag loads in centrifuge tests.

Overall, the proposed design procedure analysis of piles used in the centrifuge test provided a reasonable estimate of seismic settlement, downdrag settlement, and drag loads on piles. The majority of the pile settlement occurred from seismic loading. Although large drag loads developed on the piles, the resulting downdrag settlement was small (< 2% D). The predictions from TzQzLiq analysis following the proposed design procedure [see Table 5.2] were conservative compared to the results from the centrifuge test. The conservatism in drag load and downdrag settlement estimates was mainly due to the conservatism in predicting the magnitude of soil settlement from reconsolidation.

Table 5.2. Comparison of pile settlement and drag load results obtained from the TzQzLiq analyses of 0DPile, 5DPile, and 3DPiles (3DPileS, 3DPileM, and 3DPileL) for shaking event EQM_3 in centrifuge model test SKS02 and shaking event EQM_4 in centrifuge model test SKS03 against the measurements from the centrifuge test.

Pile	**Methods**	**Soil Settlement**		**Pile Settlement (%D)**		**Drag Load (kN)**
		Surface (mm)	**at the tip (%D)**	**Seismic**	**Downdrag**	
0DPile	*Centrifuge Test*	*54*	*1.0*	*1.7*	*1.4*	*498*
	TzQzLiq Analysis I[a]	*Pile plunged in soil due to r_u = 1.0 near the tip*				
	TzQzLiq Analysis I[b]					
	Proposed Design Procedure[c]					
5DPile	*Centrifuge Test*	*54*	*0.4*	*0.0*	*0.8*	*1068*
	TzQzLiq Analysis I[a]	*54*	*0.4*	*0.0*	*0.8*	*527*
	TzQzLiq Analysis I[b]	*54*	*0.0*	*0.0*	*0.3*	*690*
	Proposed Design Procedure[c]	*370*	*0.0*	*0.0*	*0.6*	*1024*
3DPileS	*Centrifuge Test*	*56*	*0.2*	*0.3*	*0.6*	*600*
	TzQzLiq Analysis I[a]	*56*	*0.2*	*0.1*	*0.8*	*641*
	TzQzLiq Analysis I[b]	*56*	*0.0*	*0.1*	*0.5*	*597*
	Proposed Design Procedure[c]	*225*	*0.0*	*0.1*	*1.4*	*1127*
3DPileM	*Centrifuge Test*	*56*	*0.2*	*4.4*	*0.9*	*620*
	TzQzLiq Analysis I[a]	*56*	*0.2*	*3.5*	*0.9*	*672*
	TzQzLiq Analysis I[b]	*56*	*0.0*	*3.5*	*0.7*	*674*
	Proposed Design Procedure[c]	*225*	*0.0*	*3.5*	*1.7*	*1021*
3DPileL	*Centrifuge Test*	*56*	*0.2*	*31.5*	*1.1*	*-*
	TzQzLiq Analysis I[a]	*56*	*0.2*	*21.1*	*0.9*	*686*
	TzQzLiq Analysis I[b]	*56*	*0.0*	*21.1*	*0.7*	*699*
	Proposed Design Procedure[c]	*225*	*0.0*	*21.1*	*1.7*	*1032*

[a] *TzQzLiq Analysis with soil settlement profile estimated from the inverse analysis of measured excess pore pressures* (Sinha et al. 2021e).

[b] *TzQzLiq Analysis with soil settlement profile estimated from Idriss and Boulanger (2008) and scaled to get a surface settlement equal to measured surface settlement in centrifuge test.*

[c] *TzQzLiq Analysis using Proposed Design Procedure with soil settlement profile estimated from Idriss and Boulanger (2008).*

5.6 Application of Proposed Design Procedure on an Example Design Problem

Problem Description

An example design problem from Caltrans (2020) is taken to demonstrate the proposed design procedures for designing piles in liquefiable soils. The soil profile, soil layer properties, pile properties, the design earthquake, and the design loads on the pile are shown in Figure 5.9 (a). The soil profile consists of 3 m of silty sand, 3 m of thick lean clay ($s_u \approx 72$ kPa), 3 m of poorly graded medium dense sand ($N_{160} = 12$), and dense to very dense silty sand with gravel ($N_{160} = 36$) beneath the depth of 9 m. The groundwater table is located at a depth of 3 m. The design earthquake considered has a magnitude (M_w=7.3) with peak ground acceleration (PGA) of 0.7 g. The pile considered for design is a 1.68 diameter CIDH concrete pile with its tip embedded in the dense silty sand layer, as shown in Figure 5.9 (a). The loads on the pile include a dead load of 3941 kN and a seismic load of 1108 kN.

The design objective is to find the length of the pile that can sustain the given design loads with given serviceability criteria on pile settlement. In practice, the serviceability criterion is usually guided by the structural engineer. For the given example design problem, two serviceability criteria are considered. The first is an absolute pile settlement criterion equal to 10% of pile diameter (D). The second is a relative pile settlement criterion of 0% D with the ground settlement (i.e., the pile settlement is equal to the ground settlement). Based on the serviceability criteria, the design length of the pile is selected. Then the maximum axial load acting on the pile is estimated (from downdrag) and checked against its structural strength. The design length of the pile, the shaft resistance, and the tip capacity of the pile for different lengths are summarized in Table 5.3. The shaft and tip capacities were estimated using the empirical equations provided for the design of drilled shafts in AASHTO (2020). The limit load curve for the pile with zero head load obtained from the cumulative integration of shaft capacity with depth is shown in Figure 5.9 (b).

Table 5.3. Summary of the shaft and tip capacity and the TzLiq and QzLiq material properties used in the TzQzLiq analysis for varying pile lengths ranging 10 - 26 m.

Pile Length (m)	*Capacity (MN)*			*TzLiq Properties*		*QzLiq Properties*	
	Shaft	*Tip*	*Total*	z_{50} *(%D)*	t^{o}_{ult} *(kN)*	z_{50} *(%D)*	q^{o}_{ult} *(kN)*
10	3.3	4.7	8	0.30	Limit Load Curve in Figure 5.9	10	13682
12	4.5	5	9.5				14230
14	5.8	5.2	11.1				15196
16	7.4	5.5	12.9				16119
18	9.2	5.7	14.9				17013
20	11.2	5.9	17				17882
22	13.4	6	19.4				18129
24	15.8	6.2	22				18636
26	18.4	6.4	24.7				19104

Analysis Using Proposed Design Procedure

Results from the proposed design procedure on the cyclic stress ratio (CSR), the factor of safety against liquefaction (FS_{liq}), peak excess pore pressure profile, and soil settlement profile for the example design problem are shown in Figure 5.10. The subsection below briefly describes the design steps.

Soil Liquefaction Hazard Analysis

A soil liquefaction hazard analysis was performed using the SPT-based (N_{160cs}) liquefaction-triggering correlation from Idriss and Boulanger (2008) [Figure 5.10 (a,b)]. Results designated the 3m thick medium dense sand as a liquefiable layer ($FS_{liq} \leq 1$) and the dense silty sand as a non-liquefiable layer ($FS_{liq} > 2$).

Potential for Surface Manifestation

The empirical curves from Ishihara (1985) predicted surface manifestation from the 3 m thick liquefiable layer of medium dense sand. As a result, the pile's shaft resistance up to the depth of 9 m was considered zero during the seismic loading.

Peak Excess Pore Pressure in Soil

The peak excess pore pressure in the liquefiable layer was taken equal to the effective stress of the layer. The peak excess pore pressure in the non-liquefiable dense silty sand layer was estimated considering the redistribution effects using the procedures described in Sinha et al. (2021g). The earthquake-induced excess pore pressure estimated in the non-liquefiable layer (using Equation 3) was about $u^{u}_{e-NLu} = 40\ kPa.$ The compressibility ratio ($\overline{m_v}$) of the liquefiable layer with non-liquefiable layer was estimated to be about $\overline{m_v} = 20.$ Since the thickness of non-liquefiable (dense silty-sand layer) was not available, three thicknesses H_{NLu} = 10 m, 20 m, and 30 m resulting in the thickness ratio $\overline{H} = 3.33$, $\overline{H} = 6.67$, and $\overline{H} = 10$ was considered. These thickness ratios resulted in peak excess pore pressure in the non-liquefiable layer equal to 83 kPa, 78 kPa, and 74 kPa, respectively. The estimated peak excess pore pressure profiles are shown in Figure 5.10 (c). As described in the proposed design procedures, to model the effect of surface manifestation on shaft resistance of the pile, the affected layers from surface manifestation were also considered liquefied with excess pore pressure equal to their effective stress.

Soil Settlement from Reconsolidation

The empirical method of Idriss and Boulanger (2008) resulted in soil settlement of 100 mm in the liquefiable layer. The soil settlement profile is shown in Figure 5.10 (d).

TzQzLiq Analysis

TzQzliq analyses were performed for the three peak excess pore pressure profiles and varying pile lengths ranging from 10 to 26 m. The TzLiq and QzLiq material properties were calibrated against the limit load curves [Figure 5.9 (b)] and the empirical pile load test curve [Figure 5.5], respectively. The TzLiq and QzLiq material properties used in the analysis are summarized in Table 5.3. The TzLiq stiffness parameter (z_{50}) was taken as 0.3% of the pile's diameter for all the layers. The QzLiq material parameters (stiffness (z50) and capacity ($q^{o}_{t,ult}$)) were calibrated using the empirical pile load test curve shown in Figure 5.5, assuming that the estimated tip capacity (as summarized in Table 5.3) corresponded to a pile settlement equal to 5% of the pile's diameter. The constant (α_t) was taken as 0.47 calculated using Equation 1 with an effective friction angle of ϕ' = 42°. The effective friction angle of ϕ' = 42° in the dense silty sand layer was computed using the empirical correlation of effective friction angle (ϕ') with N_{160} given in AASHTO (2020) in design for drilled shafts.

Design Curves

Design curves on seismic settlement, downdrag settlement, seismic+downdrag settlement, and drag load on piles for the three excess pore pressure profiles are shown in Figure 5.11. The figure shows that the seismic settlement and downdrag settlement decreased with the length of the pile. On the other hand, the drag load increased with the length of the pile. The downdrag settlement and drag load on the pile for the three excess pore pressure profiles were almost identical [Figure 5.11 (b,c)]. As expected, the seismic settlement of the pile was affected by u_e^{pk} in dense silty sand layer. The seismic settlement of the pile increased as excess pore pressure increased in the dense silty sand (bearing) layer. The analyses showed that the seismic loading mainly governs the pile's performance (i.e., the settlement). The majority of pile settlements occurred during seismic loading [Figure 5.11 (a)]. The downdrag settlement in the piles was less than 1.5% D [Figure 5.11 (b)]. The estimated settlement of ground from the earthquake event was equal to 6% D [Figure 5.11 (c)]. Table 5.4 summarizes the design length of the pile, design drag load, and the maximum load on the pile based on the two serviceability criteria considered. The design length of the pile was chosen based on the serviceability criteria on total settlement (i.e., seismic + downdrag settlement) as shown in Figure 5.11 (c). The design drag load was chosen from the design curve corresponding to the selected design length of the pile. The maximum axial load on the pile (Q_{np}) was calculated as the sum of the dead load and the design drag load. The maximum axial load on the pile was then checked against the pile's structural strength. For the settlement criteria equal to 10% D, the design length of the pile for the three excess pore pressures profiles with u_e= 83 kPa, 78 kPa, and 74 kPa in the dense silty sand layer came out to be 12.5 m, 12 m, and 11.5 m, respectively. For settlement criteria of 6% D (equal to ground settlement), the design length of the piles came out to be 13.5 m, 13.3 m, and 12.8 m, respectively. In the considered example problem, the serviceability criterion of pile settlement of 10% D was larger than the ground settlement (6% D) by about 67 mm (i.e., about 2.7 inches). If there is a sufficient gap between the pile and the ground, settlement of the pile larger than the ground settlement may be tolerated up to some level. The structural engineers should decide the serviceability criteria accordingly to ensure the post-earthquake functionality of the superstructure. Both the absolute as well as relative serviceability criteria should be considered when selecting the length of the pile.

The design of the piles based on the displacement-based design procedure resulted in saving on the length of the pile compared to the force-based design procedure. Results from the proposed displacement-based design procedure showed that the design length of the pile is governed primarily by the seismic loading as it results in a large settlement of the pile. While significant drag loads developed on the piles from downdrag, the resulting settlement was small (< 2% D). On the contrary, the design length of the pile in the force-based design procedure by Caltrans (2020) was governed by the liquefaction-induced downdrag because of the large drag loads. The force-based design method by Caltrans (2020) resulted in 14 m of design pile length. The % saving in the design length of the pile compared to the force-based design method is summarized in Table 5.4. On average, the pile design from the new displacement-based procedure was found to save the pile length by more than 5-10% compared to the pile design using the force-based design procedure.

Table 5.4. Summary of design pile length, drag load (Q_{drag}), maximum load (Q_{np}) for given serviceability criteria on pile settlement, and % savings in pile's length compared to the Caltrans (2020) force-based approach for the peak excess pore pressures (u_e^{pk}) in the dense silty layer equal to 83 kPa, 78 kPa, and 74 kPa, respectively.

Pile Settlement Criteria (%D)	*u_e in Dense Silty Sand Layer (kPa)*	*Design Pile Length (m)*	*Drag Load Q_{drag} (kN)*	*Max Load[c] Q_{np} (kN)*	*% Saving[d]*
10[a]	*83*	*12.5*	*1920*	*5861*	*11*
	78	*12.0*	*1930*	*5871*	*14*
	74	*11.5*	*1940*	*5881*	*18*
6[b]	*83*	*13.5*	*1940*	*5881*	*4*
	78	*13.3*	*1940*	*5881*	*5*
	74	*12.8*	*1940*	*5881*	*9*

[a] *absolute settlement criteria on pile settlement equal to 10% D*

[b] *relative pile settlement criteria with pile settlement equal to ground settlement*

[c] *Max Load = Total load on the pile + Q_{drag}*

[d] *saving in the pile's length compared to 14 m of design pile length from force-based design procedure by* (Caltrans 2020)

5.7 Conclusions

A new displacement-based design procedure using a TzQzLiq analysis was presented for designing axially loaded piles for earthquake loading and liquefaction-induced downdrag. The proposed design procedure accounts for the initial drag load on the pile, peak excess pore pressures in the non-liquefiable layers following redistribution from the liquefiable layers, and reduction of the shaft and tip capacity from excess pore pressures in the soil around the pile. Steps were provided describing the proposed design procedure for analyzing piles. The results included design curves relating to pile settlement and drag loads for varying pile lengths. The design length of the pile is selected based on a serviceability criterion on the absolute pile settlement and the pile settlement relative to the ground settlement. The maximum load on the pile is then checked against the pile's structural strength. The proposed design procedure was applied to analyze the centrifuge test piles. Analyses results showed that the new design procedure reasonably predicted the seismic settlement, downdrag settlement, and the drag load on the piles. It also showed that most of the pile settlement occurs from seismic loading. While soil settlement from reconsolidation caused large drag loads on the piles, the resulting downdrag settlement was small (< 2% of pile diameter). Finally, an example design problem was considered to demonstrate the procedure of designing piles in liquefiable soils using the proposed design procedure. The design length of the pile using the proposed displacement-based design procedure was found to be governed by the settlement of pile during seismic loading as opposed to the drag load from reconsolidation-induced downdrag in the force-based design procedure by Caltrans (2020). On comparing the design length of the piles from the two methods, the proposed displacement-based design procedure was found to save the length of the pile (for the considered example design problem) by more than 5-10%. Such savings in pile length can significantly reduce the cost of construction projects that involve installing many piles.

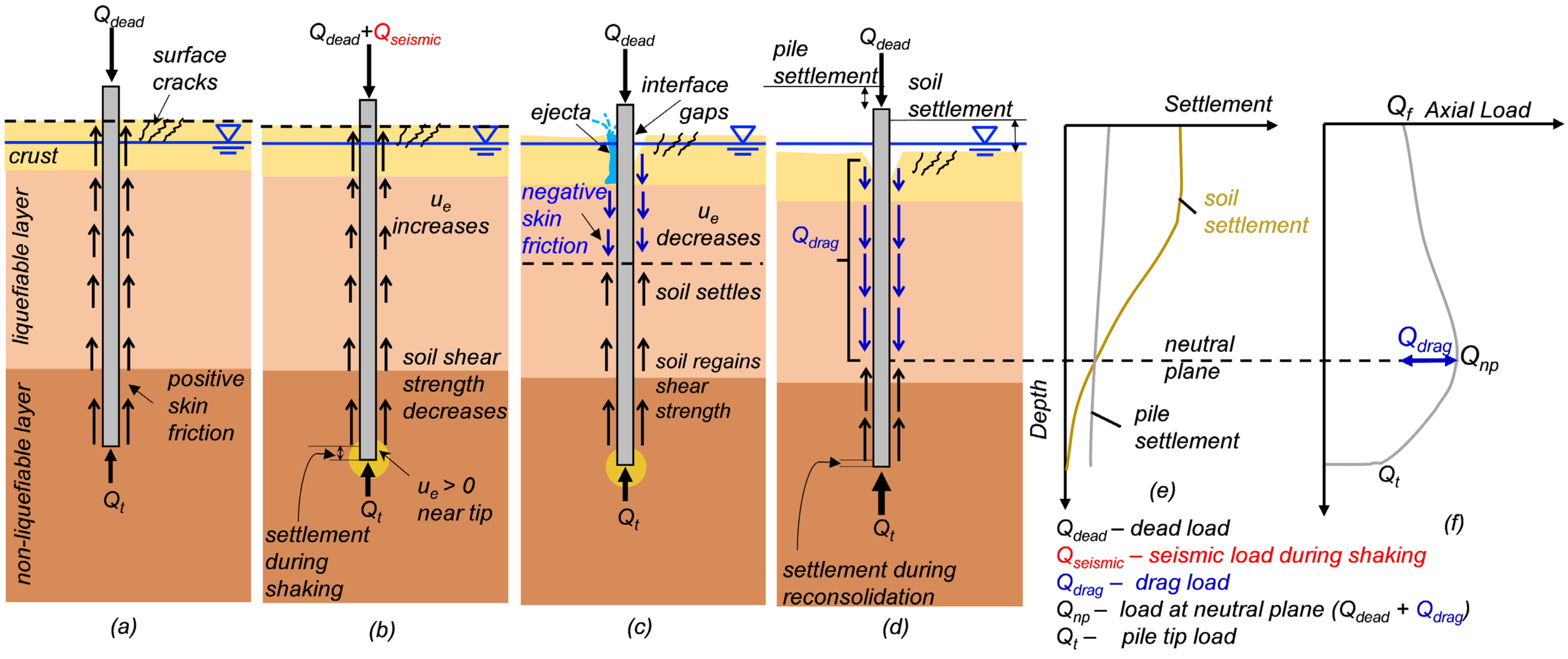

Figure 5.1. Illustration of the mechanisms affecting the axial response of piles in liquefiable soils: (a) Distribution of positive skin friction (shaft resistance) and tip resistance in a pile before shaking. (b) Loss of shaft and tip capacity from generated excess pore pressures (u_e), development of seismic loads, and resulting pile settlement during shaking. (c) Dissipation of excess pore pressures (u_e) and the development of negative skin friction from soil reconsolidation. (d) Developed drag load, final depth of the neutral plane, (e) soil and pile settlement, and (f) the axial load distribution in a pile after complete reconsolidation.

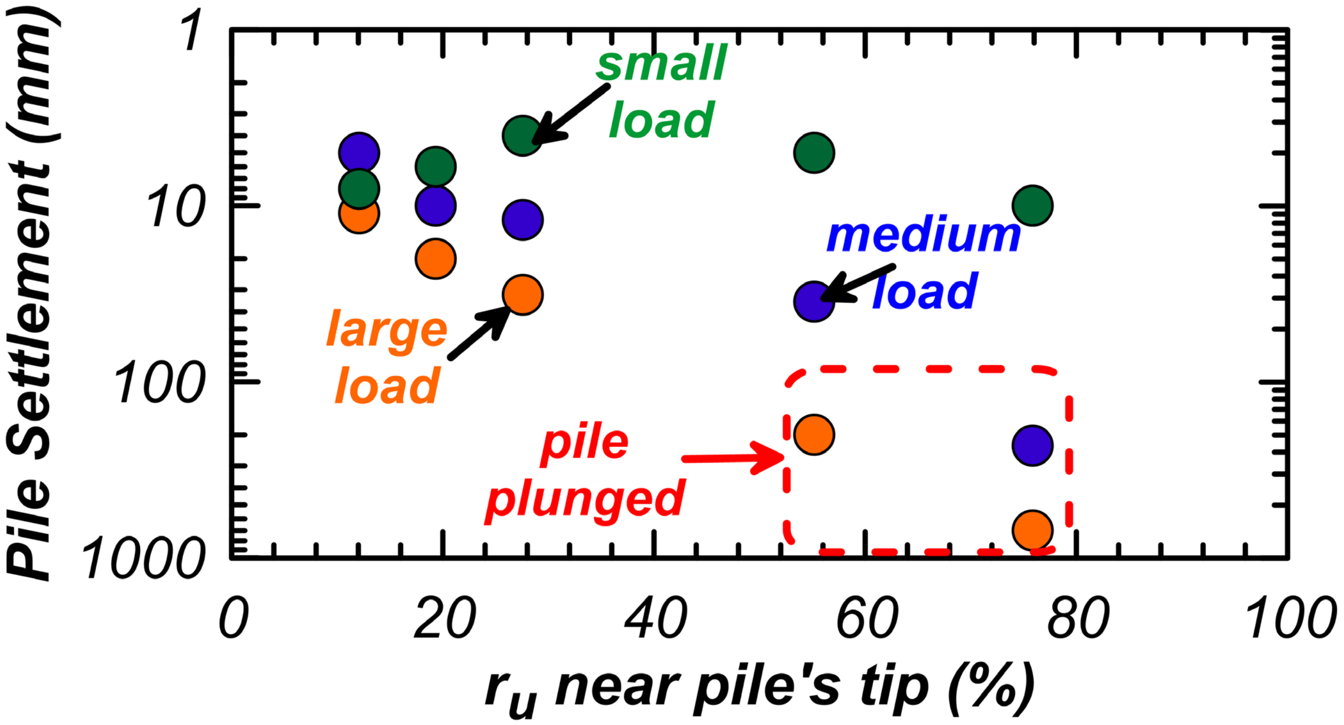

Figure 5.2**.** Effect of excess pore pressure ratio (r_u) near the pile's tip on settlement of three identical piles embedded at the same depth with small, medium, and large pile head loads, resulting in a static factor of safety of 8, 2.6, and 1.6, respectively (Sinha et al. 2021d).

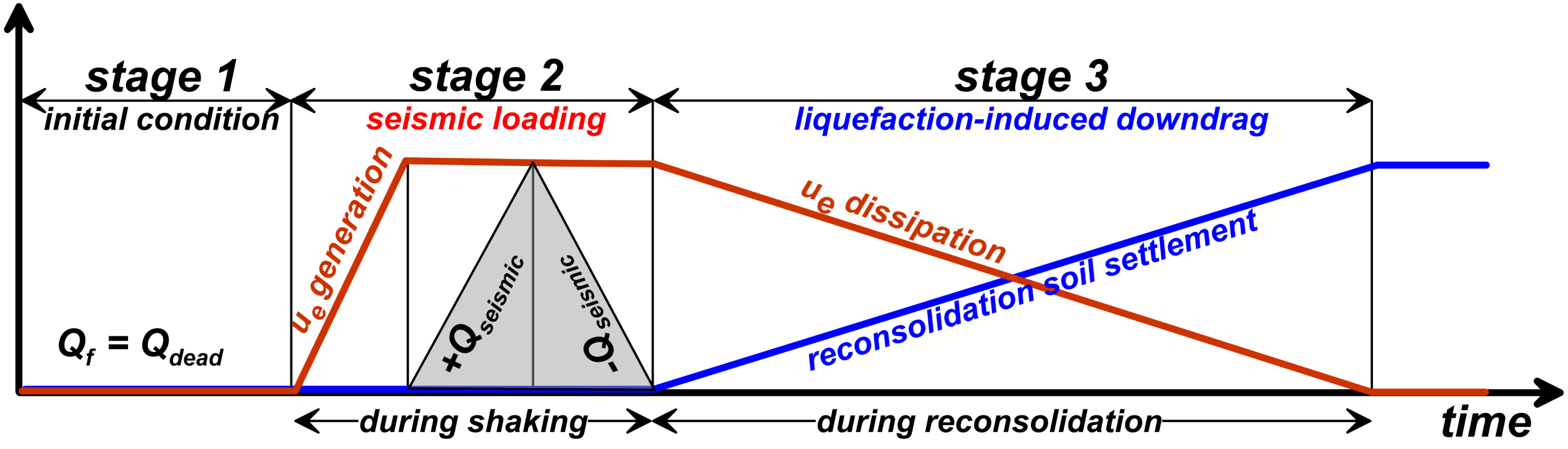

Figure 5.3**.** Stages of modeling in the TzQzLiq analysis.

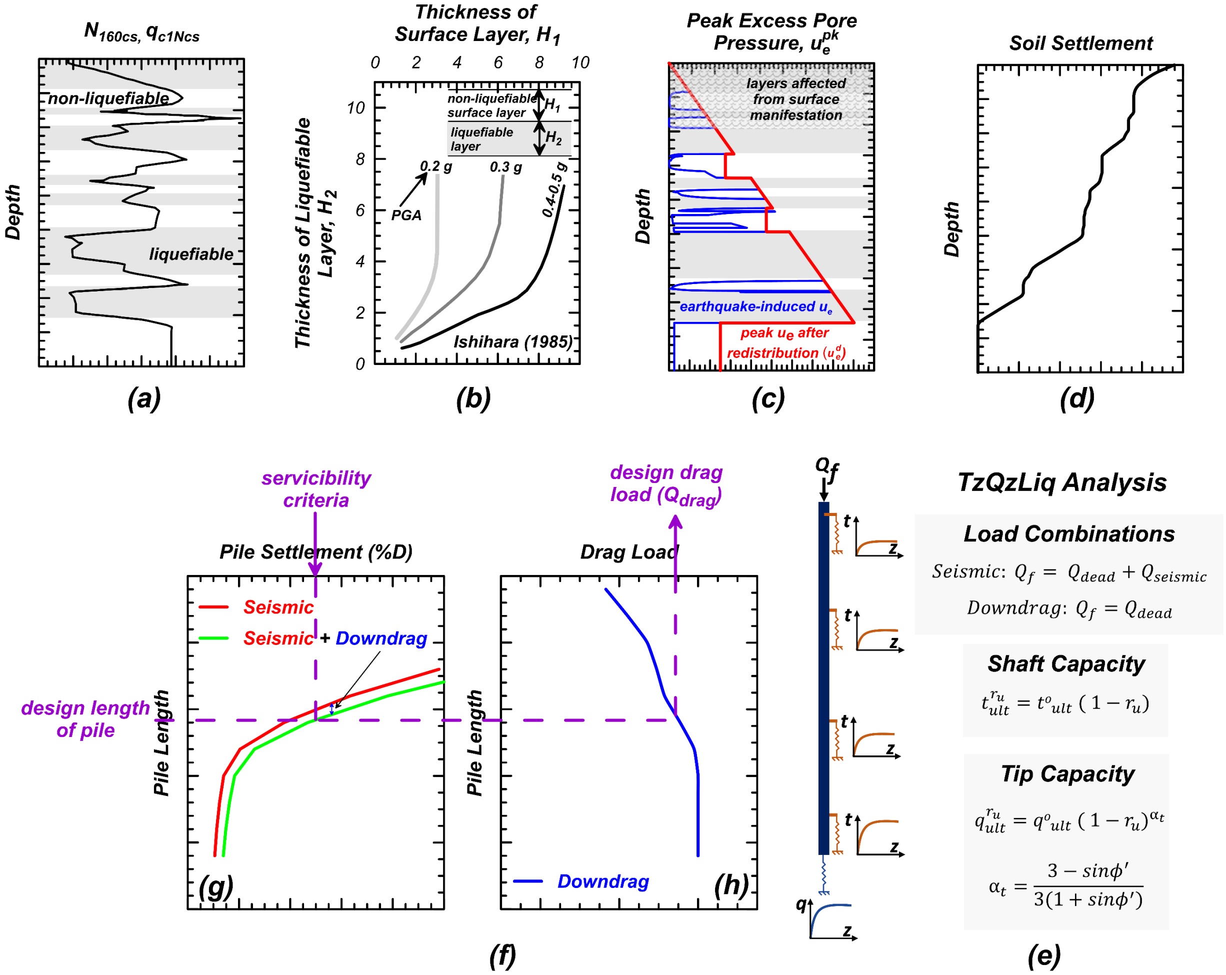

Figure 5.4**.** Illustration of the steps involved in the proposed displacement-based design procedure: (a) perform soil liquefaction hazard analysis, (b) evaluate the potential for surface manifestation, (c) estimate the peak excess pore pressures in soil, (d) estimate soil settlement from reconsolidation, (e) estimate pile settlement by running a TzQzLiq analysis and (f) obtain design curves on (g) pile settlement and (h) drag load for varying lengths of the pile.

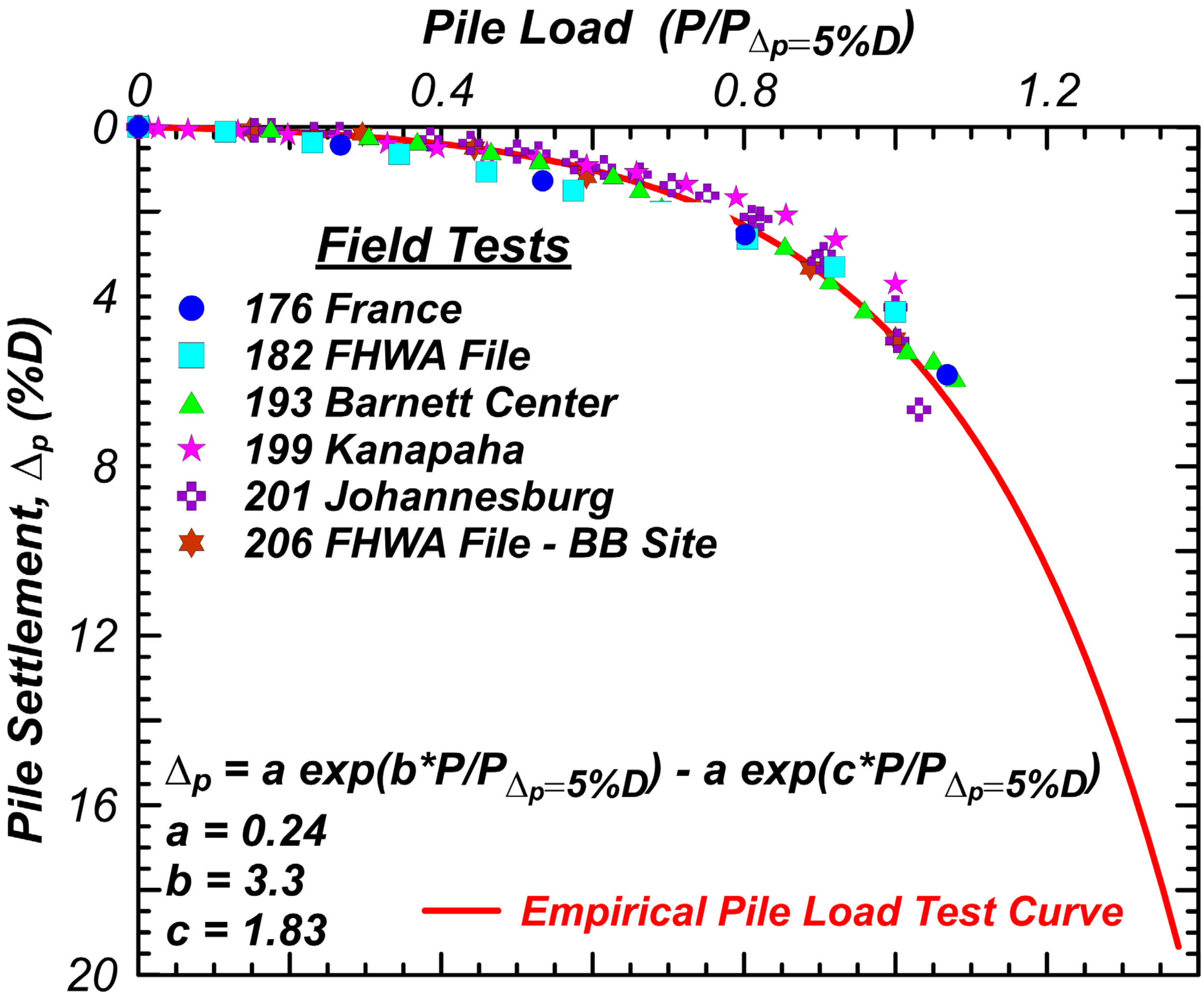

Figure 5.5. An empirical pile load test curve for large diameter (> 20 inches) CIDH piles based on the documented field tests (see Table 5.1) by Petek et al. (2016), where $P_{\Delta=5\%\,D}$ is the pile's load capacity corresponding to the settlement equal to 5% of its diameter.

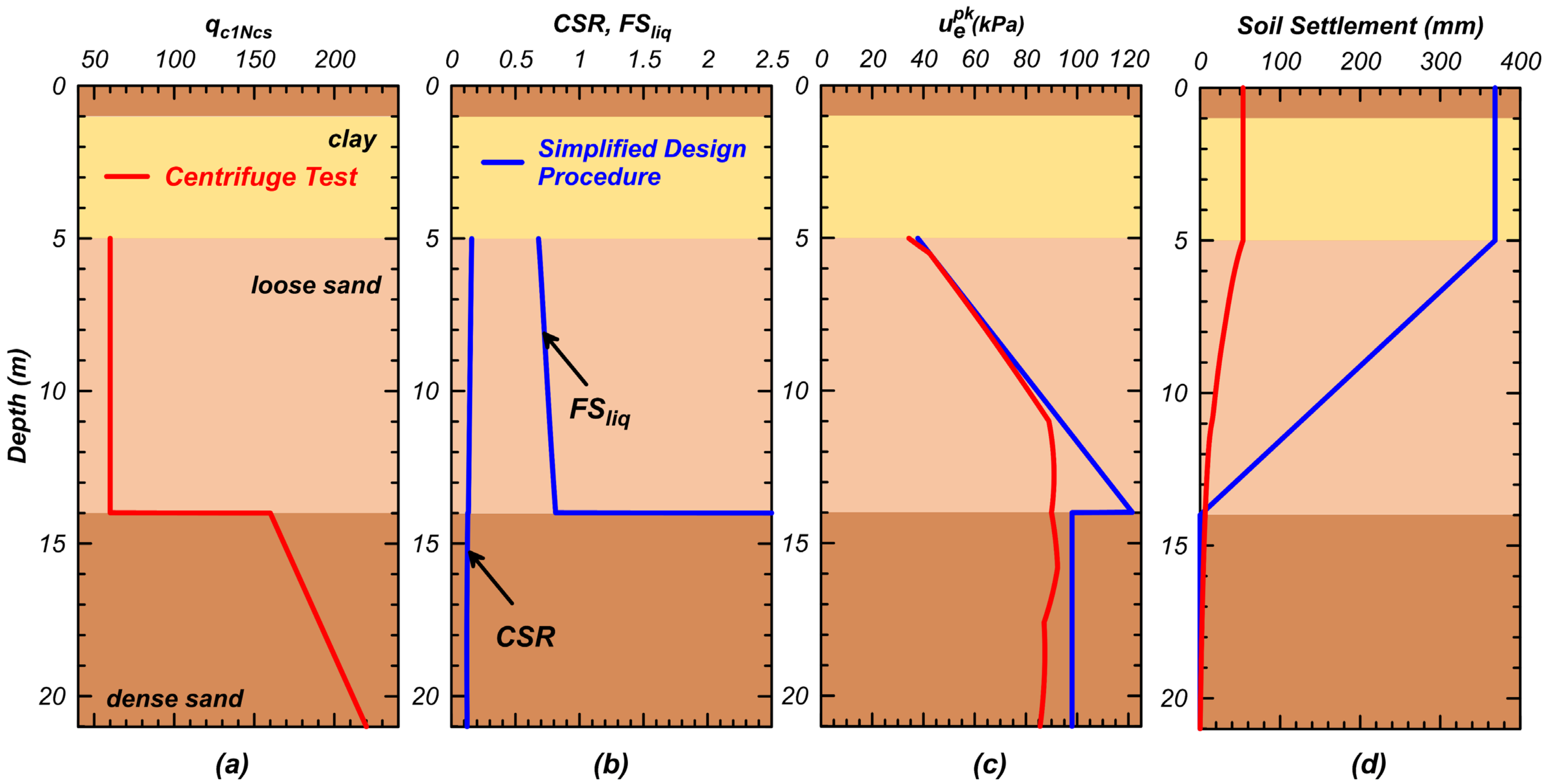

Figure 5.6. Results from the proposed design procedure for shaking event EQM_3 in centrifuge model test SKS02 with (a) normalized overburden corrected cone tip resistance (q_{c1Ncs}) and (b) cyclic stress ratio (CSR) resulting in a factor of safety against liquefaction (FS_{liq}). Comparison of (c) estimated peak excess pore pressures profile against measurements from pore pressure transducers and (d) estimated soil settlement profile against soil settlement profile obtained from the inverse analysis of measured excess pore pressures (Sinha et al. 2021e).

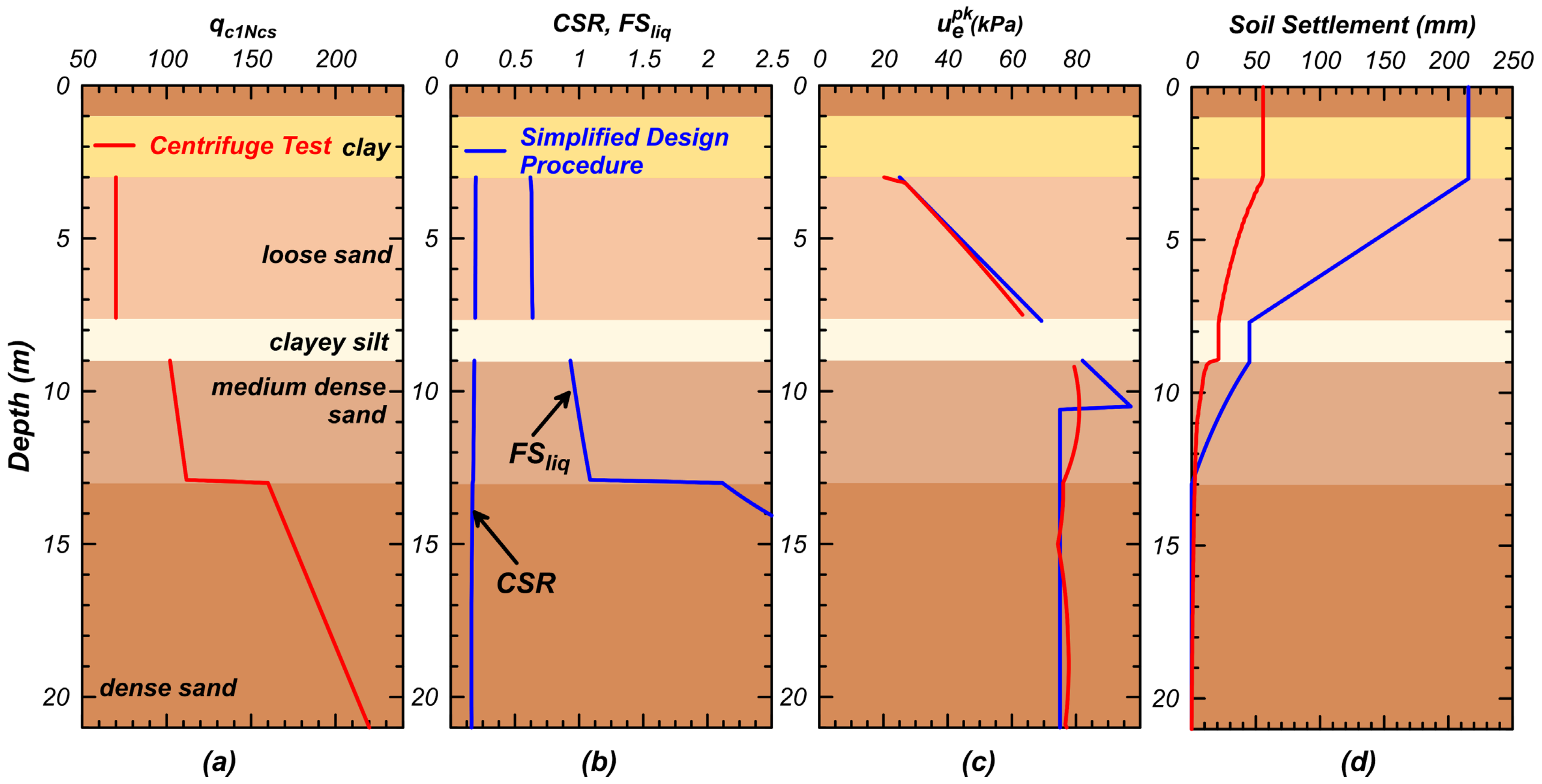

Figure 5.7**.** Results from the proposed design procedure for shaking event EQM_4 in centrifuge model test SKS03 with (a) normalized overburden corrected cone tip resistance (q_{c1Ncs}) and (b) cyclic stress ratio (CSR) resulting in a factor of safety against liquefaction (FS_{liq}). Comparison of (c) estimated peak excess pore pressures profile against measurements from pore pressure transducers and (d) estimated soil settlement profile against soil settlement profile obtained from the inverse analysis of measured excess pore pressures (Sinha et al. 2021e).

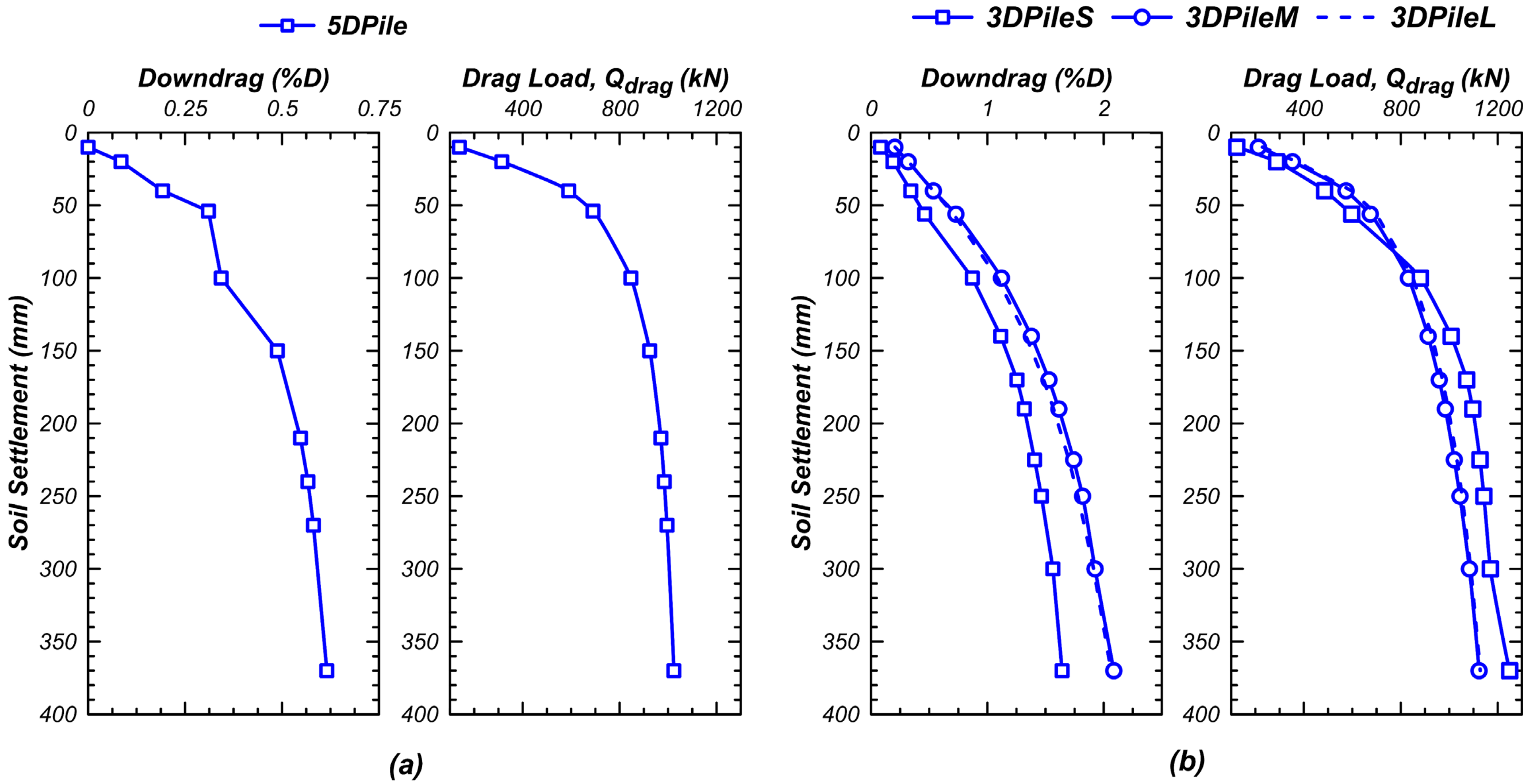

Figure 5.8**.** Results from the proposed design procedure on downdrag settlement and drag load with the magnitude of soil settlement for (a) 5DPile for shaking event EQM$_3$ of the centrifuge model test SKS02 and (b) 3DPileS, 3DPileM, and 3DPileL for shaking event EQM$_4$ of the centrifuge model test SKS03.

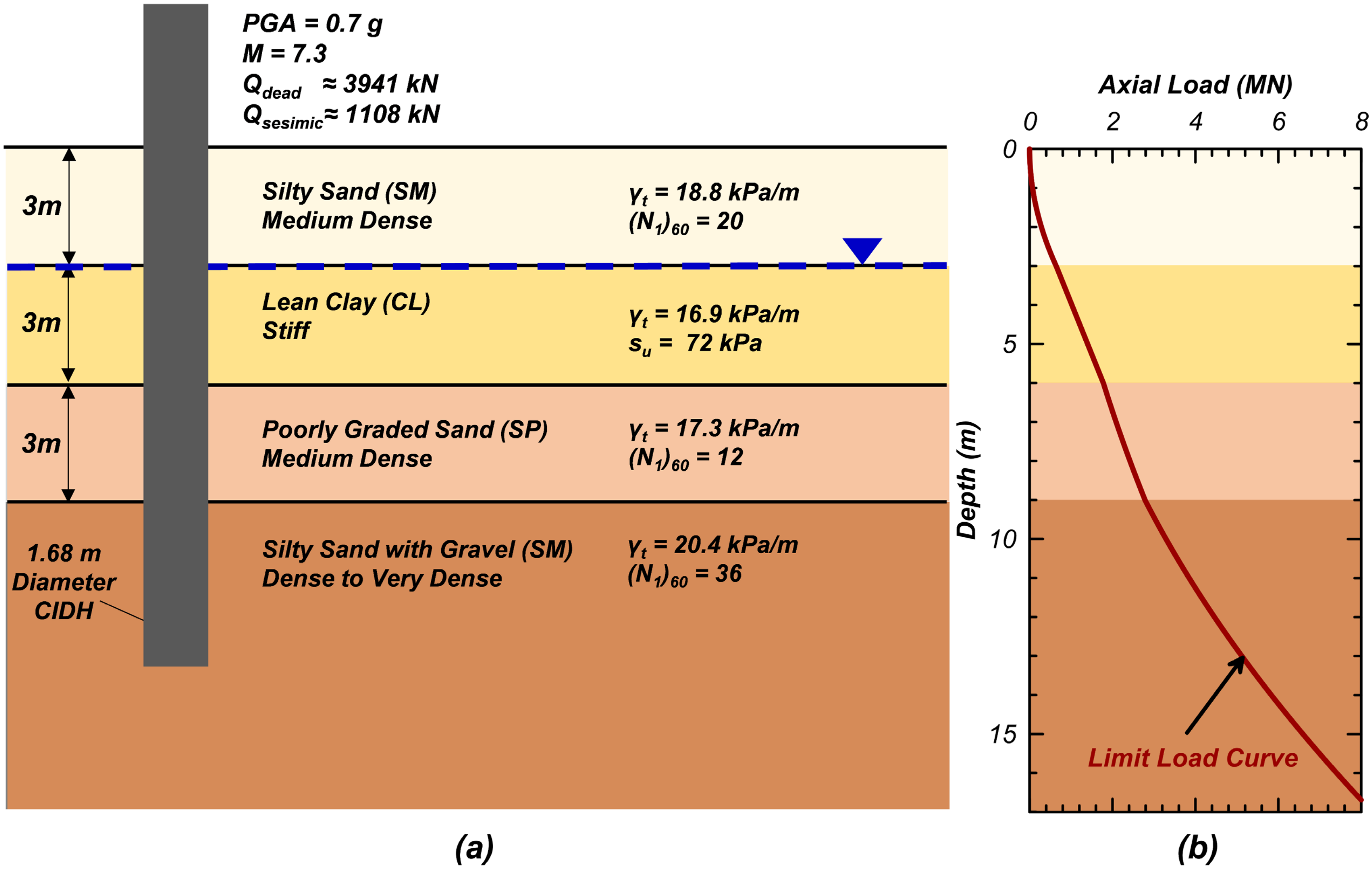

Figure 5.9**.** Illustration of the example design problem with (a) soil properties, pile cross-section properties, dead and seismic loads on pile, design earthquake motion, and (b) the limit load curve for zero head load describing the pile's cumulative shaft capacity with depth.

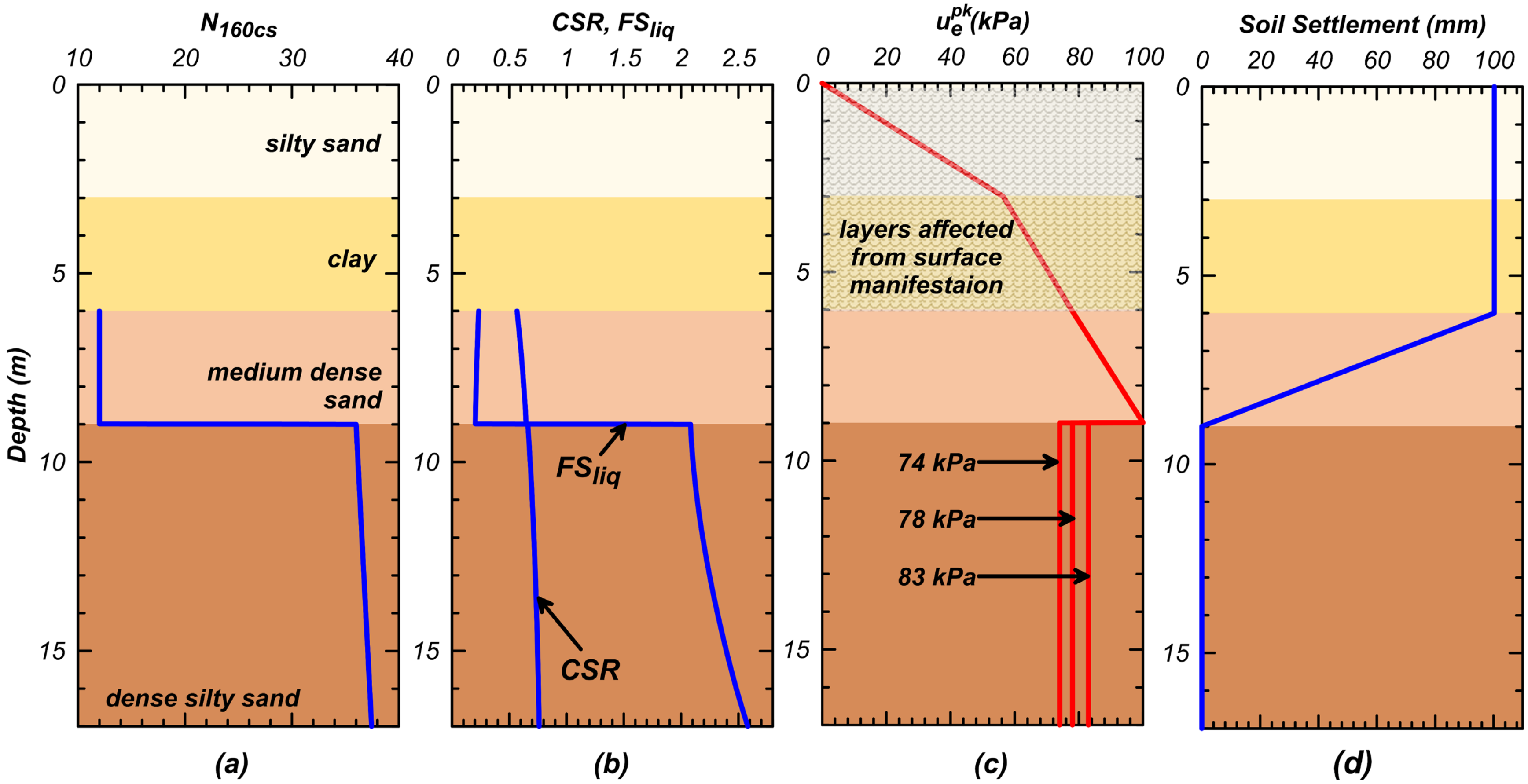

Figure 5.10**.** Illustration of the proposed design procedure on the example design problem with (a) normalized overburden corrected static penetration test blows (N_{160cs}), (b) cyclic stress ratio (CSR), and factor of safety against liquefaction (FS_{liq}). Estimated (c) peak excess pore pressure profiles with u_e^{pk} = 60 kPa and 80 kPa in dense silty sand layer and (d) soil settlement from reconsolidation.

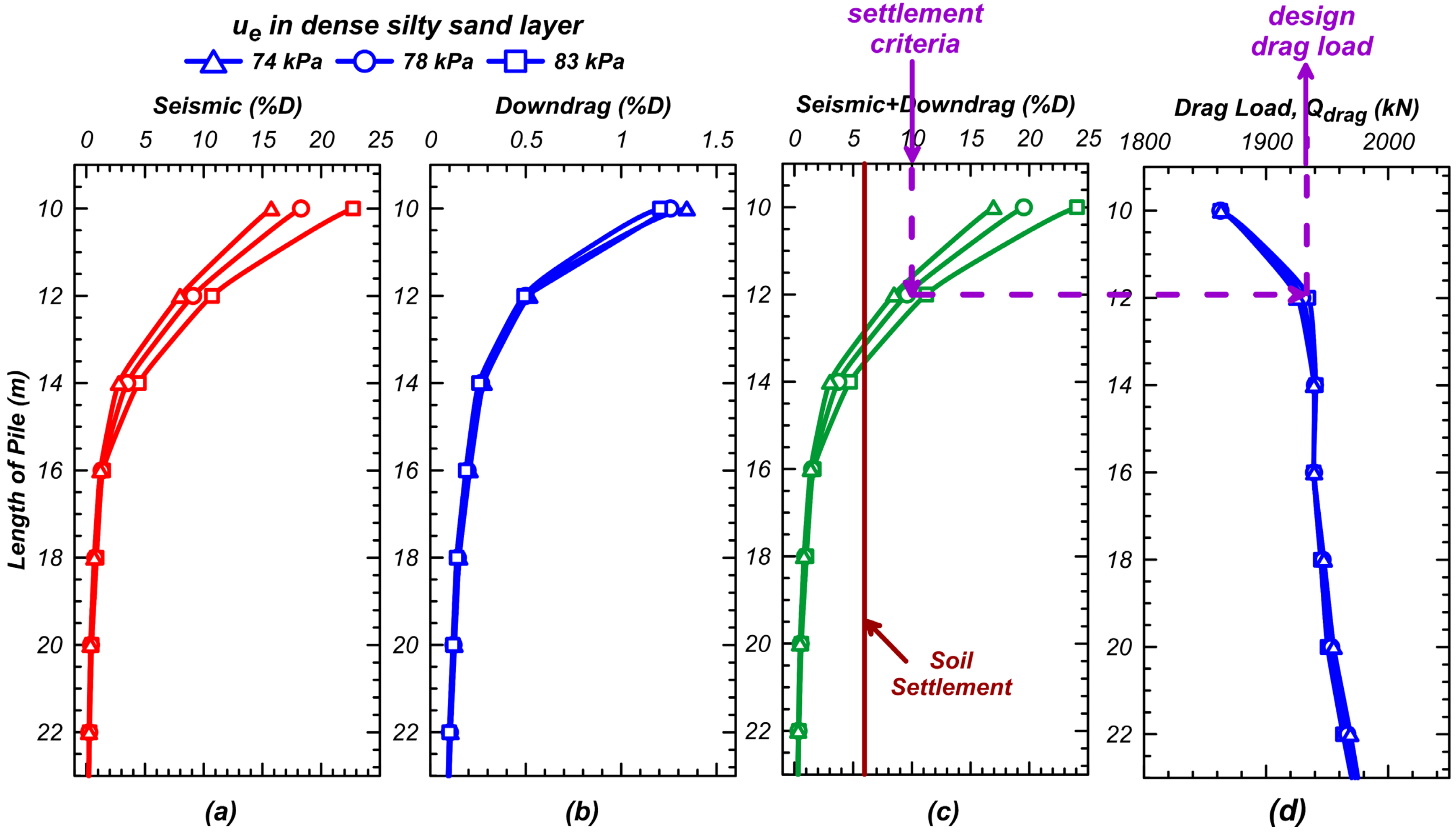

Figure 5.11**.** Design curves for the example design problem on (a) seismic settlement, (b) downdrag settlement, (c) seismic + downdrag settlement, and (d) drag load for varying pile lengths.

CHAPTER 6:

CONCLUSIONS AND FUTURE DIRECTIONS

Pile foundations are designed to transfer superstructure loads through positive skin friction and tip resistance while undergoing acceptable settlements. However, for the piles in liquefiable soils, from a shaking event, they can develop large drag loads (because of the development of negative skin friction) and can undergo significant settlements. During shaking, significant excess pore pressure developed in the soil surrounding the pile reduces the shaft and tip capacity, causing significant pile settlement. Post shaking, reconsolidation-induced soil settlement develops drag load and causes additional pile settlement. Estimating the axial load distribution and pile settlement thus becomes an important criterion for designing and evaluating the performance of piles in liquefiable soils. This dissertation focused on (1) the understanding of mechanisms that affect the response of piles during shaking and from liquefaction-induced downdrag by performing large centrifuge model tests, (2) the development and validation of a numerical modeling approach for modeling piles incorporating the observed mechanisms, (3) developing an approximate procedure for estimating excess pore pressure redistribution and its effects on the liquefiable and non-liquefiable layers, and finally (4) developing a displacement-based design procedure for designing axially loaded piles for seismic loading and for liquefaction-induced downdrag. The following subsections summarize the work, conclusions, and a few recommendations for future research directions.

6.1 Response of Axially Loaded Piles in Liquefiable Soils

A series of densely instrumented large centrifuge model tests were performed to study liquefaction-induced downdrag on piles and understand the interplay and effects of (i) pile embedment, and pile-head load, (ii) excess pore pressure generation and dissipation; and (iii) reconsolidation and ground settlement on pile response during and post shaking. The tests included five heavily instrumented piles installed in two different soil layered profiles with their tip embedment as zero, three, and five times their diameter in the dense sand (bearing) layer. The piles were loaded with different head loads resulting in a static factor of safety ranging from 1.6 to 12.4. The models were shaken with multiple (small, medium, and large) scaled Santa Cruz earthquake motions. Some of the main findings from the centrifuge model tests are described below.

- Soil settlements of the order of 1-3% of the pile diameter relative to the pile are sufficient to mobilize significant negative skin friction.
- Piles can have an initial drag load from negative skin friction developed due to soil reconsolidation from past shaking events or pile installation. In the centrifuge model tests, soil consolidation from centrifuge spin-up caused drag loads on piles.
- During shaking, excess pore pressures generated in the liquefiable layer reduced the negative skin friction, decreasing the drag loads and ultimately diminishing it to zero at complete liquefaction ($u_e \approx \sigma'_v$). However, as pore pressures dissipated and soil settled, the drag loads again increased, approaching or surpassing the drag load that existed before shaking.
- Complete liquefaction ($u_e = \sigma'_v$) is not a prerequisite to developing significant drag loads. Significant drag loads were observed for shaking events that produced excess pore pressures as small as 50% of the initial effective stress. Complete mobilization of negative skin friction equal to 100% of the drained interface shear strength ($\tau = K\ \sigma'_v \tan(\delta)$) can develop in the liquefiable layer. While designing piles for downdrag, the negative skin friction in the liquefiable soils should be taken equal to the interface shear strength.

- Most of the pile settlement occurred during shaking when the excess pore pressures in the soil around the pile resulted in the loss of shaft and tip capacity and their stiffness. Moreover, the pile suffered significant settlement when the tip capacity was reduced due to high excess pore pressures near its tip. While large drag loads developed during reconsolidation, the resulting downdrag settlement was small (< 2% of pile diameter). Furthermore, since most of the pile settlement occurs during shaking, if feasible, piles can be embedded deep into the bearing layer and thus maximizing their resistance and minimizing their settlement during shaking. Therefore, compared to liquefaction mitigation strategies, increasing the embedment of the pile could provide a cost-effective strategy to reduce pile settlements.
- Pile settlements are generally smaller than the free-field soil settlement if the tip capacity does not significantly decrease due to increased pore pressures near the pile's tip in the bearing layer. While designing piles in liquefiable soils, pile settlement should also be considered in the context of free field settlements. In some cases, especially where settlements are of the order of inches, pile settlement close to free-field soil settlements may improve post-earthquake functionality of the superstructure (for example, in bridges). It is possible that if free-field settlement is (let's say) about 4 inches, the bridge would be functional if the pile settlement was 2 inches. However, the bridge would be closed if the pile settlement was 0 inches – due to the differential settlement between the bridge and the approach slab. Perhaps there should be separate serviceability criteria for total pile and differential settlements.

Future Research Direction

a) **What causes drag load to increase after each shaking event?:** The results from the centrifuge test showed a decrease in drag load due to the increase in excess pore pressure during shaking. When the soil liquefied, the drag load was reduced to zero. Post shaking, as excess pore pressure dissipated and soil reconsolidated, the drag load again increased and ultimately became higher than its initial value after achieving complete reconsolidation. Moreover, the drag load kept increasing from the initial value prior to shaking from each shaking event. This increase in drag load could be due to the gradual increase of the effective lateral stress during reconsolidation. Another possible mechanism could be the increased tip stiffness (due to soil stronger or increase in embedment from pile settlement) in each successive event resulting in small downdrag settlement and larger drag load. It remains to be confirmed whether the increase in lateral stress is due to dilatancy of the soil adjacent to the pile producing increased lateral stresses locally around the pile or an artifact of the centrifuge model container flexibility. The mechanism of increasing drag loads with successive shaking events thus needs to be investigated. Investigating the change in lateral stresses around the pile during shaking and reconsolidation could help better understand the development of interface shear strength and thus drag loads.

b) **Investigation of liquefaction-induced downdrag on floating piles:** The present study investigated liquefaction-induced downdrag on end-bearing piles in liquefiable soils and found that while large drag loads develop, the associated downdrag settlement is small. Most of the settlements in the piles occurred during shaking when the shaft and tip capacity were reduced due to excess pore pressures around the pile. The liquefaction-induced downdrag mechanism on a floating pile would likely be different. If the majority length of the pile is in a clay layer, the seismic settlement of the pile during shaking could be smaller due to the small excess pore pressure generated in the clay layer. However, the presence of a deep liquefiable layer may result in a significant drag load and an associated large downdrag settlement in the pile layer. The cyclic softening of clay during shaking and increased undrained shear strength during reconsolidation could have additional effects. The cyclic softening of clay during shaking may decrease undrained shear strength and increase the seismic settlement of the pile. On the other hand, the associated increase in undrained shear strength from reconsolidation may decrease the downdrag settlement. Further complexities may arise from the generation/dissipation of excess pore pressure and settlement pattern. Performing more experimental investigation can increase the current understanding of the liquefaction-induced downdrag mechanism on floating piles.

6.2 Numerical Modeling of Axially Loaded Piles in Liquefiable Soils

A TzQzLiq numerical model was developed to model the mechanism of liquefaction-induced downdrag on piles that were observed in the performed centrifuge model tests. Model input parameters included TzLiq and new QzLiq material properties, time histories of soil settlement and effective stress profiles, and pile properties. The TzLiq and the new QzLiq material (implemented in OpenSees) accounted for the changes in the pile's shaft and the tip capacity as free-field excess pore pressures develop/dissipate in soil. Soil settlement profile and excess pore pressure profiles accounted for sequencing and pattern of excess pore pressure dissipation and soil settlement. The numerical model also accounted for the initial drag load on piles. The developed numerical model was validated against centrifuge tests, and the procedure for obtaining the necessary information for running the TzQzLiq analysis was described.

The TzQzLiq analysis improved the traditional neutral plane solution method by accounting for changes in the stiffness and capacity of the pile's shaft friction and tip resistance in liquefiable soils, offering complete modeling of the liquefaction-induced downdrag phenomenon. The analysis result showed that the proposed TzQzLiq numerical modeling approach reasonably predicts the time histories of axial load distribution and settlement of axially loaded piles in liquefiable soils during shaking and reconsolidation.

A sensitivity study on TzLiq and QzLiq material properties was performed to study their effect on the developed drag load and pile settlement. The sensitivity study showed that the stiffness of the QzLiq material significantly affects the pile settlement. On the other hand, the drag load is affected by both the TzLiq and the QzLiq materials stiffnesses. Therefore, it is crucial to calibrate the initial capacity and stiffness properties of the QzLiq material against results from the pile load test.

A numerical model was also developed and incorporated into the inverse analysis of excess pore pressures to study the water film formation at the sand-clay interface. The formation/drainage of the water film was modeled as the net velocity of water (q_{in} - q_{out}) entering/leaving the interface. The results from the numerical model explained the mechanism behind the observed sequencing of surface settlement in the centrifuge model test SKS02. While the impermeable clay layer hindered drainage, excess pore pressures (and reconsolidation) occurred in the loose sand layer resulting in the formation of a water film. During this period, there was no settlement of the ground. However, once the water established drainage paths through cracks or along edges of the model container, the water film started draining, and the surface settled. Time histories of the numerically simulated surface settlement matched well the recorded measurements from the centrifuge test

Future Research Direction

a) **TzPyQzLiq analysis of piles:** The present work developed a QzLiq material (implemented in OpenSees) that modeled changes in tip capacity of the pile in the presence of excess pore pressures around the tip. A TzPyQzLiq analysis (with TzLiq, PyLiq, and QzLiq materials) can model the complete (axial and bending) response of piles in liquefiable soils. The results on axial load and bending moment distribution and vertical and lateral displacement time histories can help investigate and understand the behavior of piles and design them. Furthermore, the TzPyQzLiq offers a relatively simplified approach (compared to 3-D numerical models) and thus has potential for its application in practice. The continued application of TzPyQzLiq analysis to field case histories and physical model tests will help find areas for further improvement and help incorporate them into practice.

b) **3-D Modeling of piles in liquefiable soils:** The presented TzQzLiq analysis did not model the full 3-D effect on pile behavior, such as the change in the confining and shear stress around the pile from generation/dissipation of excess pore pressures and dilation in the soil. Instead, the interface shear strength and tip capacity around the pile were assumed to vary linearly and as a power function of the excess pore pressure ratio around the shaft and near the tip, respectively. Complete 3-D modeling of piles can help understand the mechanisms occurring at the pile's interface and tip and could further improve the TzQzLiq modeling approach by accurately modeling the observed mechanisms.

6.3 Effects of Excess Pore Pressure Redistribution on Liquefiable and Non-Liquefiable Layers

An approximate analytical framework was developed to study the redistribution of excess pore pressures from a reconsolidating liquefied layer to the adjacent non-liquefiable layer. Redistribution effects were studied primarily for two types of layered systems: non-liquefiable layer below the liquefied layer and non-liquefiable above the liquefied layer, which formed the basis for redistribution effects in multi-layered systems. While redistribution increased excess pore pressure in non-liquefiable layers, it decreased excess pore pressures in the liquefiable layer. As the liquefied soil reconsolidated, the excess pore pressures in the non-liquefiable layer increased and reached a peak value, after which the excess pore pressures in both the layers together decreased. Redistributed excess pore pressures in the soil layers were smaller for thin liquefiable layers with smaller compressibility. Analytical equations were provided to estimate the peak excess pore pressures in the non-liquefiable layer and associated decreased excess pore pressures in the reconsolidated liquefied layer. A criterion was also developed to evaluate the maximum thicknesses of the liquefiable layer below which redistribution could prevent liquefaction in the layer deemed liquefiable according to the liquefaction-triggering procedures. Preventing liquefaction in a deep thin liquefiable layer due to redistribution of excess pore pressures to the adjacent non-liquefiable layer could prove extremely valuable in reducing the risk of liquefaction-related failures and the cost associated with the remediation. Finally, the proposed approximate procedure was applied on selected shakings of centrifuge tests involving liquefaction of layered soil deposits. The excess pore pressure in the soil layers estimated using the proposed approximate procedure matched decently with the centrifuge test results.

Future Research Directions

a) **Further improvements of the analytical procedure:** Several simplifying assumptions were used to present a complete procedure; many of these assumptions may be more conservative than necessary. For example, redistribution of excess pore pressures in the non-liquefiable layer assumed no water drainage outside the liquefied and non-liquefiable layers until redistribution was achieved. This condition would be applicable for the case when the surrounding soil layers are relatively impermeable (such as clay, silt, and sand silt mixtures). For the case of partially or fully drained hydraulic boundary conditions, the presented approximate procedure would result in conservative estimates of redistributed excess pore pressures. The procedure for extending the two-layer systems to multi-layer systems conservatively assumed that the liquefiable layer fully contributed to excess pore pressures above and below the layer. The assumption of a constant compressibility ratio might be overly conservative. The compressibility ratio is nonlinear and maybe more accurately determined by an iterative procedure. Thus, further refinements may better estimate redistribution effects while avoiding excessive conservatism. Additionally, the developed analytical framework needs to be applied to field case histories and other physical tests to build confidence in the procedure and further find areas of improvement.

b) **Push towards incorporating redistribution effects in practice:** Accounting for redistribution effects on increasing excess pore pressure in non-liquefiable layers can help design more resilient piles to earthquake shaking. Also, if a deep thin liquefiable layer is liquefaction resistant due to redistribution effects, it will significantly save the project cost by preventing remediation of that layer. The developed approximate procedure needs to be applied to multiple case studies to build confidence in the procedure and find areas for further improvement.

6.4 Displacement-Based Design Procedure

A displacement-based design procedure using a TzQzLiq analysis was developed for designing axially loaded piles subject to seismic loading and liquefaction-induced downdrag. The new displacement-based design method offered advancements to the state of practice (AASHTO 2020) forced-based design procedure by reasonably accounting for the mechanisms that occur on an axially loaded pile during and post shaking. It accounts for the initial drag load on the pile, redistribution effects resulting in large excess pore pressures in the non-liquefiable layers following reconsolidation from the adjacent liquefied layer, reduction in the pile’s shaft and tip capacity from excess pore pressures in the soil around the pile. The proposed design procedure estimated pile settlement and axial load distribution during shaking and reconsolidation. Design steps were provided describing the procedure for obtaining design curves on the settlement and drag load on the pile with varying pile lengths. The length of the piles is then selected based on the serviceability criteria on pile settlement and the pile's structural strength. The serviceability criteria for pile design should also consider pile settlement relative to the free-field soil settlement. Finally, the proposed design procedure was applied on the piles used in centrifuge tests, and the results were compared. In the end, an example design problem was considered to illustrate the applicability of the new design procedure in practice.

Analyses results showed that the new design procedure reasonably predicted the seismic settlement, downdrag settlement, and the drag load on the piles. It also showed that most of the pile settlement occurs from seismic loading. While soil settlement from reconsolidation caused large drag loads on the piles, the resulting downdrag settlement was small (< 2% of pile diameter). The design length of the pile using the proposed displacement-based design procedure was found to be governed by the settlement of pile during seismic loading as opposed to the drag load from reconsolidation-induced downdrag in the force-based design procedure by Caltrans (2020). On comparing the design length of the piles from the two methods, the proposed displacement-based design procedure was found to save the length of the pile (for the considered example design problem) by more than 5-10%. Such savings in pile length can significantly reduce the cost of construction projects that involve installing many piles.

Future Research Directions

a) **Overprediction in reconsolidation settlements:** The empirical methods for estimating soil settlement from reconsolidation in liquefiable soils such as Tokimatsu and Seed (1984), Shamoto et al. (1998), Wu (2002), and Idriss and Boulanger (2008) have been found to be overly conservative when compared results from centrifuge model test and field case studies. Tokimatsu and Seed (1984) estimate 25-50% accuracy for these empirical procedures. Overprediction of soil settlement, its associated failure, and remedial measures could significantly increase the cost of the projects. For example, in the present study, the overpredicted soil settlement led to large drag loads and downdrag settlement, which could unnecessarily result in increased design length of the pile. One possible reason for overprediction could be not accounting for the redistribution effects on multi-layered soil systems. Redistribution would decrease excess pore pressure in the liquefiable layers resulting in smaller reconsolidation strains. Other factors that affect reconsolidation strains are grain properties such as grain size, angularity, shape and gradation (Lee and Albasia 1974). Continued research could lead to improved estimates of reconsolidation settlements

b) **Push for displacement-based design method in practice:** A displacement-based design method accounting for all the mechanisms can directly provide the performance metric such as movement (settlement and lateral) and loads and help in a better-informed pile design. The proposed design procedure should be applied to multiple case studies to build confidence in the procedure and identify areas of further improvement. Additionally, the proposed design procedure can be expanded to include lateral loading using a TzPyQzLiq analysis. A continuous push towards the use of displacement-based design procedures in practice is required to reduce some of the conservatism in the force-based methods (for example, design for liquefaction-induced downdrag).

REFERENCES

AASHTO (American Association of State Highway and Transportation Officials) (2011). *AASHTO Guide Specifications for LRFD Seismic Bridge Design*. LRFDSEIS-2. Washington, DC: AASHTO.

AASHTO (American Association of State Highway and Transportation Officials) (2020). *AASHTO LRFD Bridge Design Specifications*. LRFDUS-9. Washington, DC: AASHTO.

API (American Petroleum Institute) (2000). *Recommended Practice for Planning , Designing and Constructing Fixed Offshore Platforms — Working Stress Design*. API Recommended Practice 24-WSD. Washington, DC: API.

ASTM (American Society for Testing and Materials) (2013). *Standard Test Methods for Deep Foundations Under Static Axial Compressive Load*. ASTM D1143/D1143M-07. https://doi.org/10.1520/D1143_D1143M-07

Bastidas, A. M. P. (2016). *Ottawa F-65 Sand Characterization*. Ph.D. Dissertation. Davis, CA: Department of Civil and Environmental Engineering, University of California Davis.

Boulanger, B. R. W., Curras, C. J., Kutter, B. L., Wilson, D. W., and Abghari, A. (1999). "Seismic Soil-Pile-Structure Interaction Experiments and Analyses." *Journal of Geotechnical and Geoenvironmental Engineering*, 125(9), 750-759. https://doi.org/10.1061/(ASCE)1090-0241(1999)125:9(750).

Boulanger, R. W., and Brandenberg, S. J. (2004). "Neutral Plane Solution For Liquefaction-Induced Downdrag on Vertical Piles." *GeoTrans,* 470–478. https://doi.org/10.1061/40744(154)32.

Bray, J. D., and Macedo, J. (2017). “Simplified Procedure for Estimating Liquefaction-Induced Building Settlement.” *Soil Dynamic and Earthquake Engineering*, 102, 215-231. https://doi.org/10.1016/j.soildyn.2017.08.026

Caltrans (2020). “Liquefaction-induced downdrag.” In *Caltrans Geotechnical Manual.* https://dot.ca.gov/programs/engineering-services/manuals/geotechnical-manual.

Carey, T., Gavras, A., Kutter, B., Haigh, S. K., Madabhushi, S. P. G., Okamura, M., Kim, D. S., Ueda, K., Hung, W. Y., Zhou, Y. G., Liu, K., Chen, Y. M., Zeghal, M., Abdoun, T., Escoffier, S., and Manzari, M. (2018). “A New Shared Miniature Cone Penetrometer for Centrifuge Testing.” *Physical Modelling in Geotechnics*, 1, 293–298. https://doi.org/10.1201/9780429438660

Carey, T. J., Stone, N., and Kutter, B. L. (2020). “Grain Size Analysis and Maximum and Minimum Dry Density of Ottawa F-65 Sand for LEAP-UCD-2017.” In *Model Tests and Numerical Simulations of Liquefaction and Lateral Spreading*, edited by B. L. Kutter, M. T. Manzari, and M. Zeghal, 31-44: Springer, Cham. https://doi.org/10.1007/978-3-030-22818-7_2.

Cetin, K. O., Seed, R. B., Kayen, R. E., Moss, R. E. S., Bilge, H. T., Ilgac, M., and Chowdhury, K. (2018). “SPT-Based Probabilistic and Deterministic Assessment of Seismic Soil Liquefaction Triggering Hazard.” *Soil Dynamics and Earthquake Engineering*, 115, 698–709. https://doi.org/10.1016/j.soildyn.2018.09.012

Chiaradonna, A., Bilotta, E., D’Onofrio, A., Flora, A., and Silvestri, F. (2018). “A Simplified Procedure for Evaluating Post-Seismic Settlements in Liquefiable Soils.” In *5th Conference on Geotechnical Earthquake Engineering and Soil Dynamics*, edited by S. J. Brandenberg, and M. T. Manzari, 51–59: ASCE. https://doi.org/10.1061/9780784481455.005

Chiaradonna, A., Flora, A., d'Onofrio, A., and Bilotta, E. (2020). "A Pore Water Pressure Model Calibration Based on In-situ Test Results." *Soils and Foundations*, 60(2), 327–341. https://doi.org/10.1016/j.sandf.2019.12.010

Chiaradonna, A., Tropeano, G., d'Onofrio, A., Silvestri, F., and Park, D. (2015). "Application of a Simplified Model for the Prediction of Pore Pressure Build-up in Sandy Soils Subjected to Seismic Loading." In *6th International Conference on Earthquake Geotechnical Engineering*. Christchurch, New Zealand: International Society for Soil Mechanics and Geotechnical Engineering.

Coelho, P. A. L. F., Haigh, S. K., and Madabhushi, S. P. G. (2004). "Centrifuge Modelling of Earthquake Effects in Uniform Deposits of Saturated Sand." In *5th International Conference on Case Histories in Geotechnical Engineering*. New York, NY: University of Missouri Rolla.

Darby, K. M. (2018). *The Use of Centrifuge Model Studies in the Development of CPT-Based Liquefaction Triggering Correlations.* Ph.D. Dissertation. Davis, CA: Department of Civil and Environmental Engineering, University of California Davis.

Darby, K. M., DeJong, J. T., Parra Bastidas, A. M., Boulanger, R. W., and Bronner, J. D. (2016). "Effect of Shaking History on the Cone Penetration Resistance and Cyclic Strength of Saturated Sand." In *Geotechnical and Structural Engineering Congress 2016*, 1460–1471. https://doi.org/10.1061/9780784479742.122

DeJong, J. T., and Westgate, Z. J. (2009). "Role of Initial State, Material Properties, and Confinement Condition on Local and Global Soil-Structure Interface Behavior." *Journal of*

Geotechnical and Geoenvironmental Engineering, 135(11), 1646–1660. https://doi.org/10.1061/(ASCE)1090-0241(2009)135:11(1646).

Elvis, I. (2018). "Liquefaction-Induced Dragload and / or Downdrag on Deep Foundations within the New Madrid Seismic Zone.". Ph.D. Dissertation. Fayetteville, NC: Department of Civil Engineering, University of Arkansas.

Fellenius, B. H. (1972). "Down-drag on Piles in Clay Due to Negative Skin Friction." *Canadian Geotechnical Journal*, 9(4), 321–337.

Fellenius, B. H. (1984). "Negative Skin Friction and Settlement of Piles." In *2nd International Seminar-Pile Foundations*. Singapore: Nanyang Technological Institute.

Fellenius, B. H. (2004). "Unified Design of Piled Foundations with Emphasis on Settlement Analysis."In *Current Practices and Future Trends in Deep Foundations*, 253–275. Los Angeles, CA: Contributions in Honor of George G. Gobel, American Society of Civil Engineers. https://doi.org/10.1061/40743(142)15

Fellenius, B. H. (2006). B*asics of Foundation Design*. Sidney, Canada: Electronic Edition. https://www.fellenius.net/papers/412%20The%20Red%20Book,%20Basics%20of%20Foundation%20Design%202021.pdf.

Fellenius, B. H., Abbasi, B., and Muhunthan, B. (2020). "Liquefaction Induced Downdrag for the Juan Pablo II Bridge at the 2010 Maule Earthquake in Chile." *Geotechnical Engineering Journal of the SEAGS & AGSSEA*, 51(2), 1–8.

Fellenius, B. H., and Siegel, T. C. (2008). "Pile Drag Load and Downdrag in a Liquefaction Event." *Journal of Geotechnical and Geoenvironmental Engineering*, 134(9), 1412–1416.

https://doi.org/10.1061/(ASCE)1090-0241(2008)134:9(1412)

Fiegel, B. G. L., and Kutter, B. L. (1994). “Liquefaction Mechanism For Layered Sands.” *Journal of Geotechnical Engineering*, 120(4), 737–755. https://doi.org/10.1061/(ASCE)0733-9410(1994)120:4(737)

Fleming, K., Weltman, A., Randolph, M., and Elson, K. (2008). *Piling Engineering*. London: CRC press. https://doi.org/10.1201/b22272

Gajan, S., Raychowdhury, P., Hutchinson, T. C., Kutter, B. L., and Stewart, J. P. (2010). “Application and Validation of Practical Tools for Nonlinear Soil-Foundation Interaction Analysis.” *Earthquake Spectra*, 26(1), 111–129. https://doi.org/10.1193%2F1.3263242

Ganainy, H. El, Tessari, A., Abdoun, T., and Sasanakul, I. (2014). “Tactile Pressure Sensors in Centrifuge Testing.” *Geotechnical Testing Journal*, 37(1), 151-163. https://doi.org/10.1520/GTJ20120061

Garnier, J., Gaudin, C., Springman, S. M., Culligan, P. J., Goodings, D., Konig, D., Kutter, B., Phillips, R., Randolph, M. F., and Thorel, L. (2007). “Catalogue of Scaling Laws and Similitude Questions in Geotechnical Centrifuge Modelling.” *International Journal of Physical Modelling in Geotechnics*, 7(3), 01–23. https://doi.org/10.1680/ijpmg.2007.070301

Hannigan, P. J., Rausche, F., Likins, G. E., Robinson, B. R., and Becker, M. L. (2016). *Design and Construction of Driven Pile Foundations*. FHWA-NHI-16-009. Woodbury, MN: Federal Highway Administration.

Idriss, I. M., and Boulanger, R. W. (2008). *Soil Liquefaction During Earthquakes*. Earthquake Engineering Research Institute.

Ilankatharan, M. (2008). "Centrifuge Modeling for Soil-Pile-Bridge Systems with Numerical Simulations Accounting for Soil-Container-Shaker Interaction." Ph.D. Dissertation. Davis, CA: Department of Civil and Environmental Engineering, University of California Davis.

Ishihara, K. (1985). "Stability of Natural Deposits During Earthquakes." In *11th International Conference on Soil Mechanics and Foundation Engineering,* 321–376. San Francisco, CA: International Conference on Soil Mechanics and Foundation Engineering.

Ishihara, K., and Yoshimine, M. (1992). "Evaluation of Settlements in Sand Deposits Following Liquefaction During Earthquakes." *Soils and Foundations*, 32(1), 178–188. https://doi.org/10.3208/sandf1972.32.173

Janbu, N. (1985). "Soil Models in Offshore Engineering." *Geotechnique*, 35(3), 241–281. https://doi.org/10.1680/geot.1985.35.3.241

Knappett, J. A., and Madabhushi, S. P. G. (2008). "Liquefaction-Induced Settlement of Pile Groups in Liquefiable and Laterally Spreading Soils." *Journal of Geotechnical and Geoenvironmental Engineering*, 134(11), 1609–1618. https://doi.org/10.1061/(ASCE)1090-0241(2008)134:11(1609)

Knappett, J. A., and Madabhushi, S. P. G. (2009). "Seismic Bearing Capacity of Piles in Liquefiable Soils." *Soils and Foundations*, 49(4), 525–535. https://doi.org/10.3208/sandf.49.525

Kokkali, P., Abdoun, T., and Zeghal, M. (2018). "Physical Modeling of Soil Liquefaction: Overview of LEAP Production Test 1 at Rensselaer Polytechnic Institute." *Soil Dynamics and Earthquake Engineering*, 113, 629–649. https://doi.org/10.1016/j.soildyn.2017.01.036

Law, H., and Wilson, P. (2017). "Displacement Based Downdrag Analysis for Pile Design." In *3rd International Conference on Performance Based Design (PBD-III)*. Vancouver, Canada: International Conference on Soil Mechanics and Foundation Engineering.

Lee, K. L., and Albasia, A. (1974). "Earthquake Induced Settlements in Saturated Sands." *Journal of Geotechnical Engineeering Division*, 100(4), 387–406. https://doi.org/10.1061/AJGEB6.0000034

Lusvardi, C. M. (2020). *Blast-Induced Liquefaction and Downdrag Development on a Micropile Foundation*. M.S. Thesis. Provo, UT: Department of Civil and Environmental Engineering, Brigham Young University.

Malvick, E. J., Kulasingam, R., Boulanger, R. W., and Kutter, B. L. (2002). *Effects of Void Redistribution on Liquefaction Flow of Layered Soil – Centrifuge Data Report for EJM01*. UCD/CGMDR-02/02. Davis, CA: Center for Geotechnical Modeling, University of California Davis. https://ucdavis.app.box.com/s/evhvz5tzz77bj9teutbr

Malvick, E. J., Kutter, B. L., and Boulanger, R. W. (2008). "Postshaking Shear Strain Localization in a Centrifuge Model of a Saturated Sand Slope." *Journal of Geotechnical and Geoenvironmental Engineering*, 134(2), 164–174. https://doi.org/10.1061/(ASCE)1090-0241(2008)134:2(164)

Martinez, A., and Frost, J. D. (2017). "The Influence of Surface Roughness Form on the Strength of Sand–Structure Interfaces." *Géotechnique Letters*, 7(1), 104–111. https://doi.org/10.1680/jgele.16.00169

McKenna, F., Scott, M. H., and Fenves, G. L. (2010). "Nonlinear Finite-Element Analysis Software Architecture Using Object Composition." *Journal of Computing in Civil*

Engineering, 24(1), 95–107. https://doi.org/10.1061/(ASCE)CP.1943-5487.0000002

Mele, L., Chiaradonna, A., Lirer, S., and Flora, A. (2021). "A Robust Empirical Model to Estimate Earthquake-Induced Excess Pore Water Pressure in Saturated and Non-Saturated Soils." *Bulletin of Earthquake Engineering*, 19, 3865–3893. https://doi.org/10.1007/s10518-020-00970-5

Mosher, R. L. (1984). *Load-Transfer Criteria for Numerical Analysis of Axially Loaded Piles in Sand*. K-84. Vicksburg, MS: US Army Engineer Waterways Experiment Station.

Muhunthan, B., Vijayathasan, N. V, and Abbasi, B. (2017). *Liquefaction-Induced Downdrag on Drilled Shafts*. WA-RD 865.1. Pullman, WA: Washington State Department of Transportation.

Nagase, H., Ishiharai, K., and Ishihara, K. (1988). "Liquefaction-Induced Compaction and Settlement of Sand During Earthquakes." *Soils and Foundations*, 28(1), 65–76. https://doi.org/10.3208/sandf1972.28.65

Nicks, J. (2017). *Liquefaction-induced downdrag on Continuous Flight Auger (CFA) piles from full-scale tests using blast liquefaction*. FHWA-HRT-17-060. McLean, VA: Federal Highway Administration.

O'Neill, M. W. (2001). "Side Resistance In Piles and Drilled Shafts." *Journal of Geotechnical and Geoenvironmental Engineering*, 127(1), 3–16. https://doi.org/10.1061/(ASCE)1090-0241(2001)127:1(3)

Petek, K., Mitchell, R., and Ellis, H. (2016). *FHWA Deep Foundation Load Test Database Version 2.0 User Manual*. FHWA-HRT-17-034. McLean, VA: Federal Highway Administration.

Reese, L. C., and O’Niel, M. W. (1987). *Drilled Shafts: Construction Procedures and Design Methods*. FHWA-IF-99-025. Mclean, Virginia: Federal Highway Administration.

Rituraj, S. S., and Rajesh, B. G. (2022). “Negative Skin Friction on Piles: State of the Art.” *Advances in Geo-Science and Geo-Structures, Lecture Notes in Civil Engineering*, edited by A. K. Choudhary, S. Mondal, S. Metya, and G. L. S. Babu, 323–335: Springer, Singapore. http://doi.org/10.1007/978-981-16-1993-9_34

Robertson, P. K. (2015). “Comparing CPT and Vs Liquefaction Triggering Methods.” *Journal of Geotechnical and Geoenvironmental Engineering*, 141(9), 04015037. https://doi.org/10.1061/(ASCE)GT.1943-5606.0001338

Rollins, K. M. (2017). “Dragload and downdrag on piles from liquefaction induced ground settlement. ” In *U.S.–New Zealand–Japan International Workshop on Liquefaction-Induced Ground Movement Effects,* edited by J. D. Bray, R. W. Boulanger, M. Cubrinovski, K. Tokimatsu, S. L. Kramer, T. O’Rourke, R. A. Green, P. K. Robertson, and C. Z. Beyzaei. Berkeley, CA: Pacific Earthquake Engineering Research Center, University of California Berkeley.

Rollins, K. M., and Hollenbaugh, J. (2015). “Liquefaction Induced Negative Skin Friction from Blast-induced Liquefaction Tests with Auger-cast Piles.” In *6th International Conference on Earthquake Geotechnical Engineering*. Christchurch, New Zealand: International Society for Soil Mechanics and Geotechnical Engineering.

Rollins, K. M., Lusvardi, C., Amoroso, S., and Franceschini, M. (2019). “Liquefaction Induced Downdrag on Full-Scale Micropile Foundation.” In *2nd International Conference on Natural Hazards and Infrastructure*. Chania, Greece: Innovation Center on Natural Hazards and

Infrastructure.

Rollins, K. M., and Strand, S. R. (2006). “Downdrag Forces Due to Liquefaction Surrounding a Pile.” In *8th U.S. National Conference on Earthquake Engineering.* San Francisco, CA: Earthquake Engineering Research Institute.

Rollins, K. M., and Strand, S. R. (2007). *Liquefaction Mitigation Using Vertical Composite Drains: Full-Scale Testing for Pile Applications*. Highway IDEA Project 103. Provo, UT: Transportation Research Board. http://onlinepubs.trb.org/onlinepubs/archive/studies/idea/finalreports/highway/NCHRP103_Final_Report.pdf

Scott, R. F. (1986). “Solidification and Consolidation of a Liquefied Sand Column.” *Soils and Foundations*, 26(4), 23–31. https://doi.org/10.3208/sandf1972.26.4_23

Seed, H. B., and Lee, K. L. (1966). “Liquefaction of Saturated Sands During Cyclic Loading.” *Journal of the Soil Mechanics and Foundation Division*, 92(6), 105–134. https://doi.org/10.1061/JSFEAQ.0000913

Seed, H. B., Martin, P. P., and Lysmer, J. (1976). “Pore-Water Pressure Changes During Soil Liquefaction.” *Journal of Geotechnical Engineeering Division*, 102(4), 323–346. https://doi.org/10.1061/AJGEB6.0000258

Seed, H. B., and Seed, I. M. (1967). “Analysis of Soil Liquefaction: Nigata Earthquake.” *Journal of the Soil Mechanics and Foundation Division*, 93(3), 83–108. https://doi.org/10.1061/JSFEAQ.0000981

Shamoto, Y., Zhang, J., and Tokimatsu, K. (1998). “Methods for Evaluating Settlement Post-

Liquefaction Displacement." *Soils and Foundations*, 38, 69–83. https://doi.org/10.3208/sandf.38.Special_69

Sinha, S. K., Kutter, B. L., Wilson, D. W., Carey, T., and Ziotopoulou, K. (2021a). *Use of Photron Cameras and TEMA Software to Measure 3D Displacements in Centrifuge Tests*. UCD/CGM - 21/01. Davis, CA: Center for Geotechnical Modeling, University of California Davis. https://ucdavis.box.com/s/6hndp2m7mcy5cz8r9g0y6wokzj00hbfb

Sinha, S. K., Kutter, B. L., and Ziotopoulou, K. (2021b). "Measuring Vertical Displacement Using Laser Lines and Cameras." *International Journal of Physical Modelling in Geotechnics*. https://doi.org/10.1680/jphmg.21.00038

Sinha, S. K., Ziotopoulou, K., and Kutter, B. L. (2019). "Parametric Study of Liquefaction Induced Downdrag on Axially Loaded Piles." In *7th lnternational Conference on Earthquake Geotechnical Engineering*. Rome, Italy: International Society for Soil Mechanics and Geotechnical Engineering.

Sinha, S. K., Ziotopoulou, K., and Kutter, B. L. (2021c). *Centrifuge testing of liquefaction-induced downdrag on axially loaded piles : Data Report for SKS02*. UCD/CGMDR - 21/01. Davis, CA. Center for Geotechnical Modeling, University of California Davis. https://doi.org/10.17603/ds2-d25m-gg48

Sinha, S. K., Ziotopoulou, K., and Kutter, B. L. (2021d). *Centrifuge Testing of Liquefaction-Induced Downdrag on Axially Loaded Piles : Data Report for SKS03*. UCD/CGMDR - 21/02. Davis, CA. Center for Geotechnical Modeling, University of California Davis. https://doi.org/10.17603/ds2-wjgx-tb78

Sinha, S. K., Ziotopoulou, K., and Kutter, B. L. (2021e). "Numerical Modeling of Liquefaction-

Induced Downdrag : Validation from Centrifuge Tests." *Journal of Geotechnical and Geoenvironmental Engineering*. Under Review.

Sinha, S. K., Ziotopoulou, K., and Kutter, B. L. (2021f). "Centrifuge Model Tests of Liquefaction-Induced Downdrag on Piles in Uniform Liquefiable Deposits." *Journal of Geotechnical and Geoenvironmental Engineerin*g. Accepted.

Sinha, S. K., Ziotopoulou, K., and Kutter, B. L. (2021g). "Effects of Excess Pore Pressure Redistribution on Liquefiable and Non-Liquefiable Layers." *In Preparation*.

Stringer, M. E., and Madabhushi, S. P. G. (2010). "Effect of liquefaction on pile shaft friction capacity." In 5th *International Conferences on Recent Advances in Geotechnical Earthquake Engineering and Soil Dynamics*. Bangalore, India: Indian Society of Earthquake Technology.

Stringer, M. E., and Madabhushi, S. P. G. (2013). "Re-Mobilization of Pile Shaft Friction After an Earthquake." *Canadian Geotechnical Journal*, 50, 979–988. https://doi.org/10.1139/cgj-2012-0261

Taylor, D. W. (1948). *Fundamentals of Soil Mechanics*. John Wiley and Sons.

Tokimatsu, K., and Seed, H. B. (1984). *Simplified Procedures for the Evaluation of Settlements in Clean Sands.* NSF/CEE- 84027. Berkeley, CA: Earthquake Engineering Research Center, University of Califirnia Berkeley.

Vijayaruban, V. N., Muhunthan, B., and Fellenius, B. H. (2015). "Liquefaction-induced downdrag on piles and drilled shafts." In *6th International Conference on Earthquake Geotechnical Engineering*. Christchurch, New Zealand: International Society for Soil Mechanics and Geotechnical Engineering.

Vijivergiya, V. N. (1977). "Load-Movement Characteristics of Piles." In *4th Symposium of Waterway, Port, Coastal and Ocean Division,* 2, 269–284. Long Beach, CA: American Society of Civil Engineering.

Wang, R., and Brandenberg, S. J. (2013). "Beam on Nonlinear Winkler Foundation and Modified Neutral Plane Solution for Calculating Downdrag Settlement." *Journal of Geotechnical and Geoenvironmental Engineering*, 139(9), 1433–1442. https://doi.org/10.1061/(ASCE)GT.1943-5606.0000888

Wang, S., Lei, X., Meng, Q., Xu, J., Wang, M., and Guo, W. (2021). "Model Tests of Single Pile Vertical Cyclic Loading in Calcareous Sand." *Marine Georesources and Geotechnology*, 39(6), 670–681. https://doi.org/10.1080/1064119X.2020.1744048

Wu, J. (2002). *Liquefaction Triggering and post-Liquefaction deformation of Monterey 0/30 sand under unidirectional cyclic simple shear loading.* Ph.D. Dissertation. Berkeley, CA: Department of Civil and Environmental Engineering, University of California Berkeley.

Yoshimi, Y., and Kuwabara, F. (1973). "Effect of Subsurface Liquefaction on the Strength of Surface Soil." *Soils and Foundations*, 13(2), 67–81. https://doi.org/10.3208/sandf1972.13.2_67

Youd, T. L., Idriss, I. M., Andrus, R. D., Arango, I., Castro, G., Christain, J. T., Dobry, R., Finn, W. D. L., Jr., L. F. H., Hynes, M. E., Ishihara, K., Koester, J. P., Liao, S. S. C., Marcuson, W. F., Martin, G. R., Mitchell, J. K., Moriwaki, Y., Power, M. S., Robertson, P. K., Seed, R. B., and Stokoe, K. H. (2001). "Liquefaction Resistance of Soils: Summary report from the 1996 NCEER and 1998 NCEER/NSF Workshops on Evaluation of Liquefaction Resistance of Soils." *Journal of Geotechnical and Geoenvironmental Engineering*, 127(10), 817–833.

https://doi.org/10.1061/(ASCE)1090-0241(2001)127:10(817)

Zhang, G., Robertson, P. K., and Brachman, R. W. I. (2004). "Estimating Liquefaction-Induced Lateral Displacements Using the Standard Penetration Test or Cone Penetration Test." *Journal of Geotechnical and Geoenvironmental Engineering*, 130(8), 861–871. https://doi.org/10.1061/(ASCE)1090-0241(2004)130:8(861)

APPENDIX A:

SKS02 CENTRIFUGE MODEL TEST RESULTS

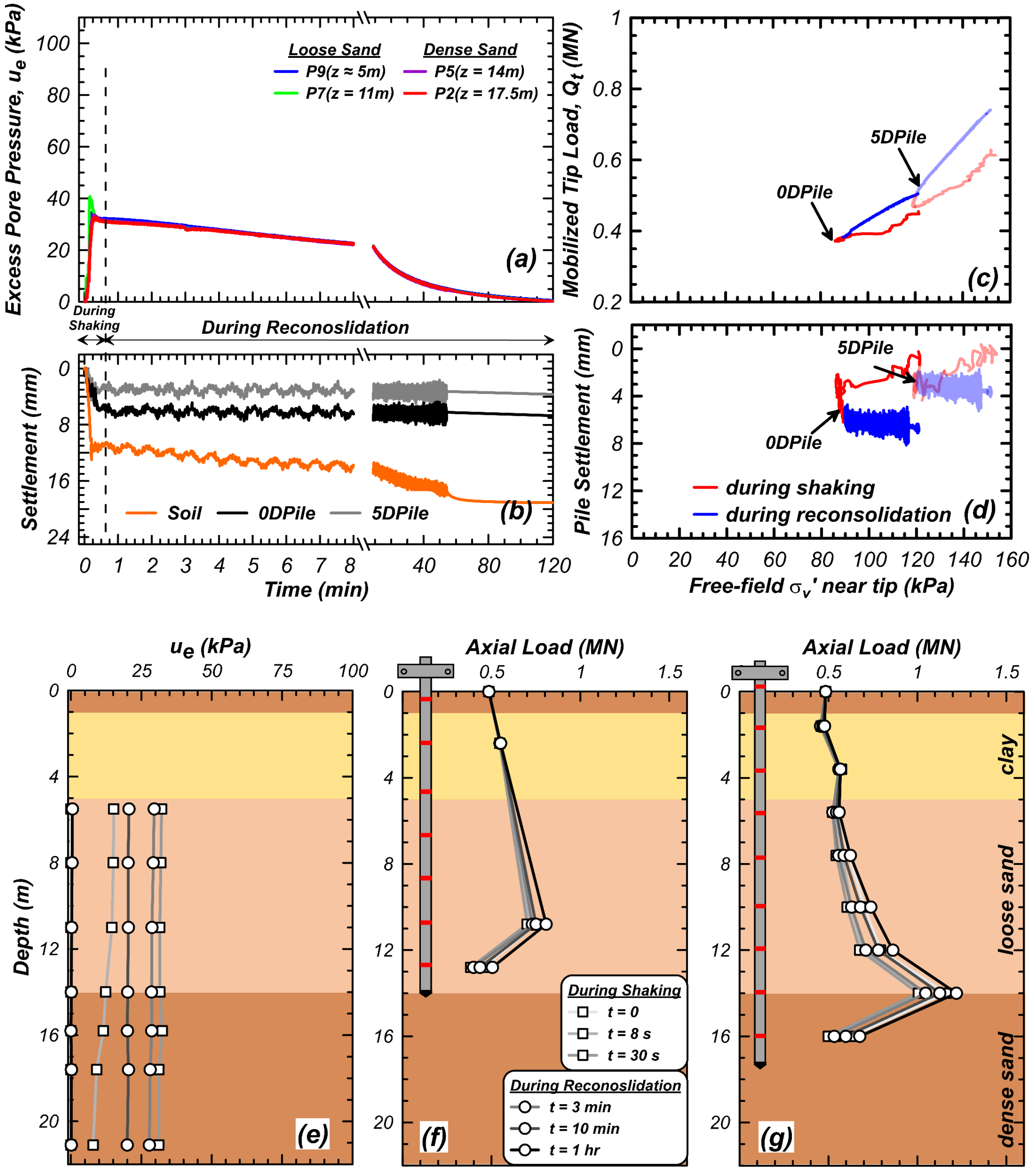

Figure A.1. Results from shaking event EQM_2 of centrifuge model test SKS02: Time histories of (a) u_e and (b) soil and pile settlement. (c) Mobilized tip load (Q_t) and (d) pile settlement as free-field effective stress (σ'_v) changed near the pile's tip. Isochrones of (e) u_e profile and axial load distribution in (f) 0DPile and (g) 5DPile during shaking and reconsolidation.

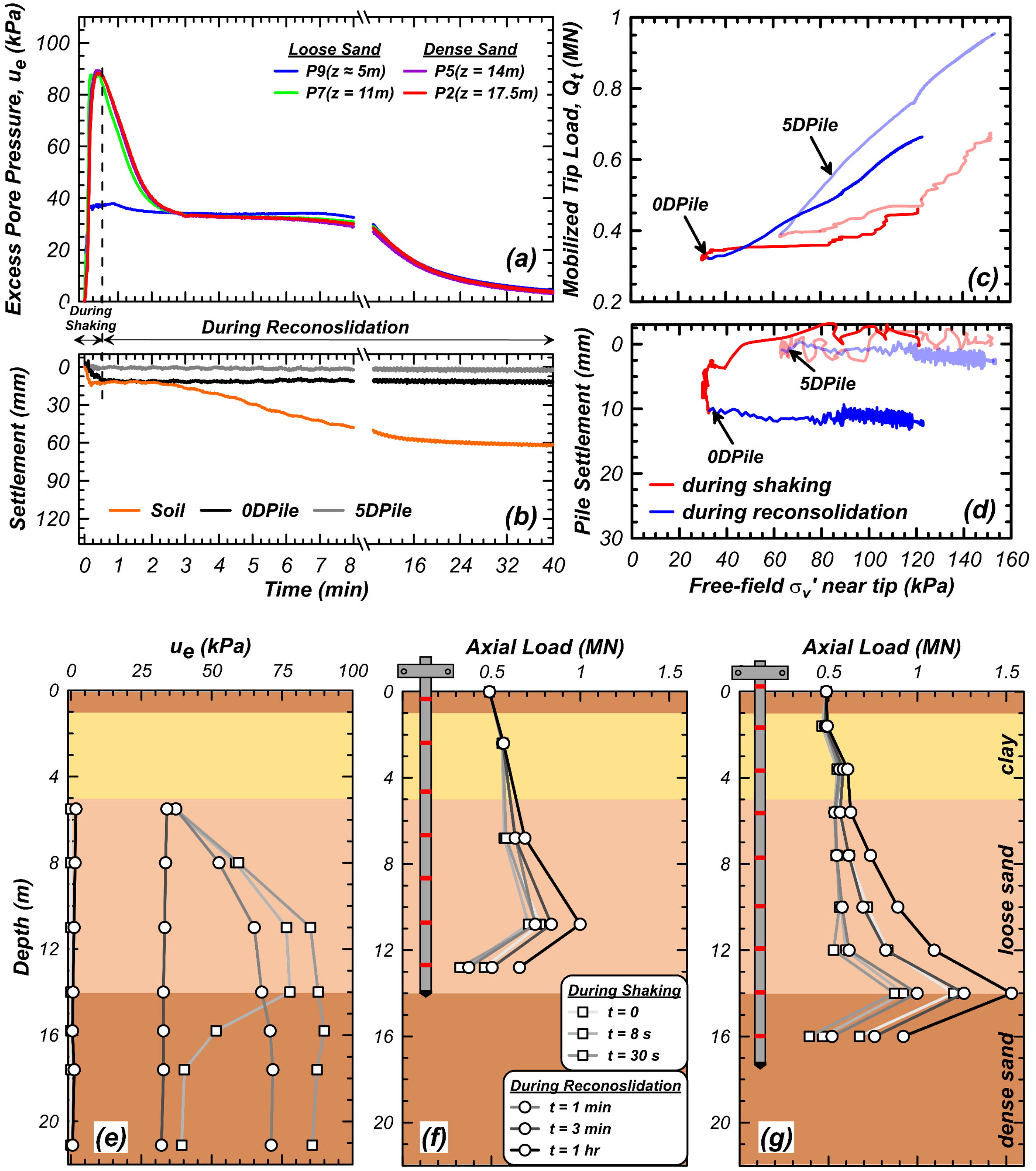

Figure A.2. Results from shaking event EQM$_3$ of centrifuge model test SKS02: Time histories of (a) u$_e$ and (b) soil and pile settlement. (c) Mobilized tip load (Q$_t$) and (d) pile settlement as free-field effective stress (σ'_v) changed near the pile's tip. Isochrones of (e) u$_e$ profile and axial load distribution in (f) 0DPile and (g) 5DPile during shaking and reconsolidation.

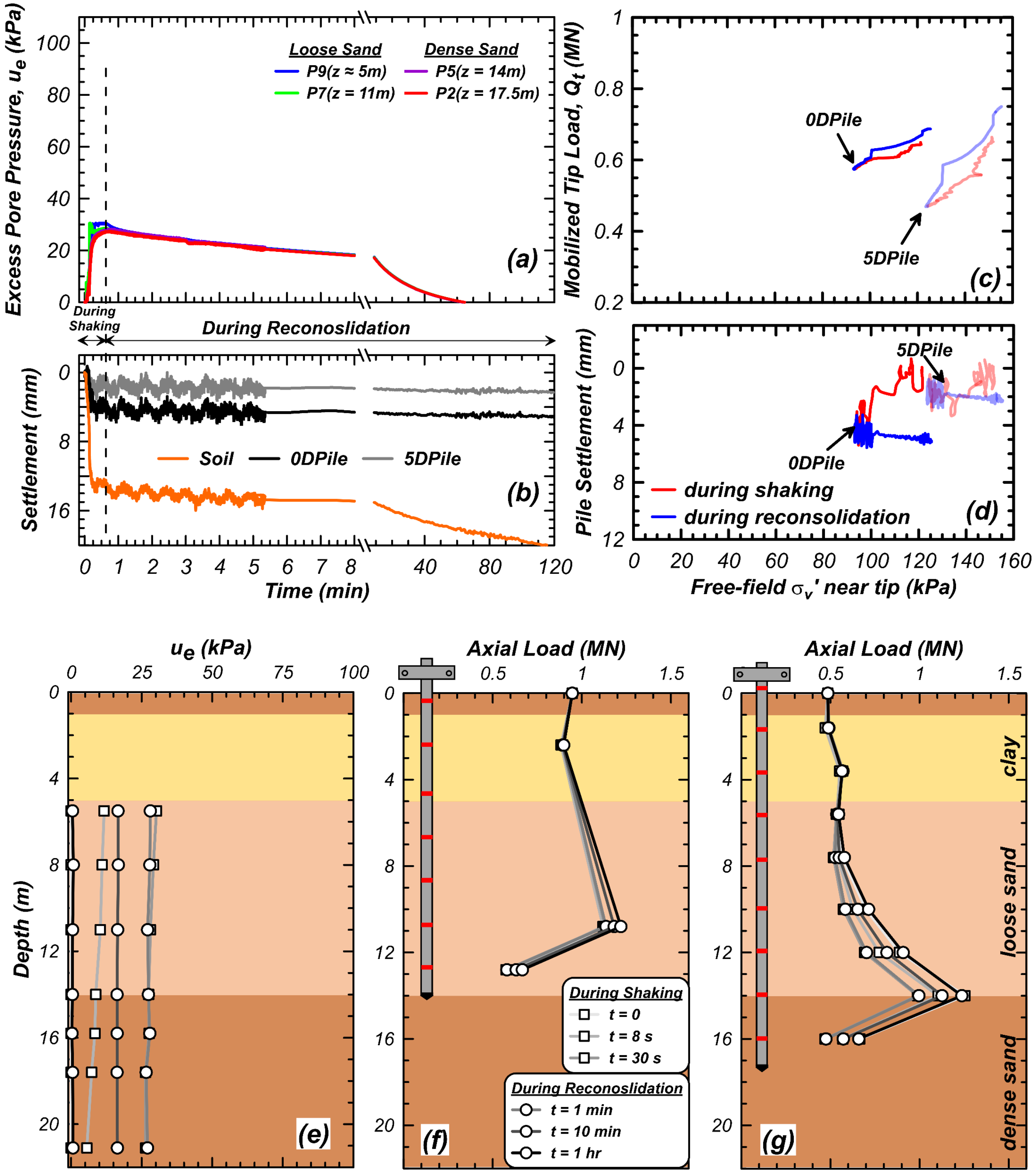

Figure A.3. Results from shaking event EQM_4 of centrifuge model test SKS02: Time histories of (a) u_e and (b) soil and pile settlement. (c) Mobilized tip load (Q_t) and (d) pile settlement as free-field effective stress (σ'_v) changed near the pile's tip. Isochrones of (e) u_e profile and axial load distribution in (f) 0DPile and (g) 5DPile during shaking and reconsolidation.

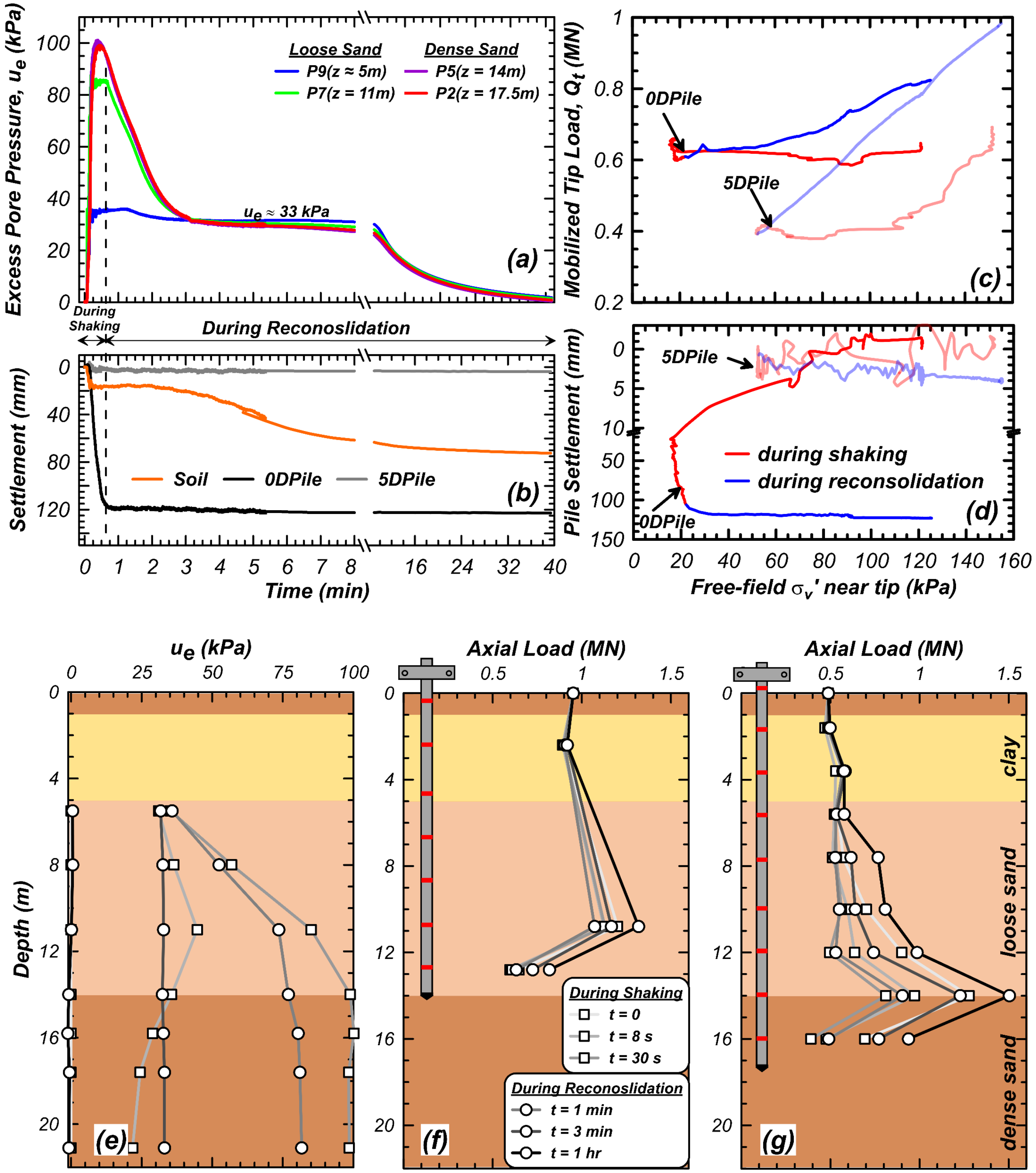

Figure A.4. Results from shaking event EQM$_5$ of centrifuge model test SKS02: Time histories of (a) u_e and (b) soil and pile settlement. (c) Mobilized tip load (Q_t) and (d) pile settlement as free-field effective stress (σ'_v) changed near the pile's tip. Isochrones of (e) u_e profile and axial load distribution in (f) 0DPile and (g) 5DPile during shaking and reconsolidation.

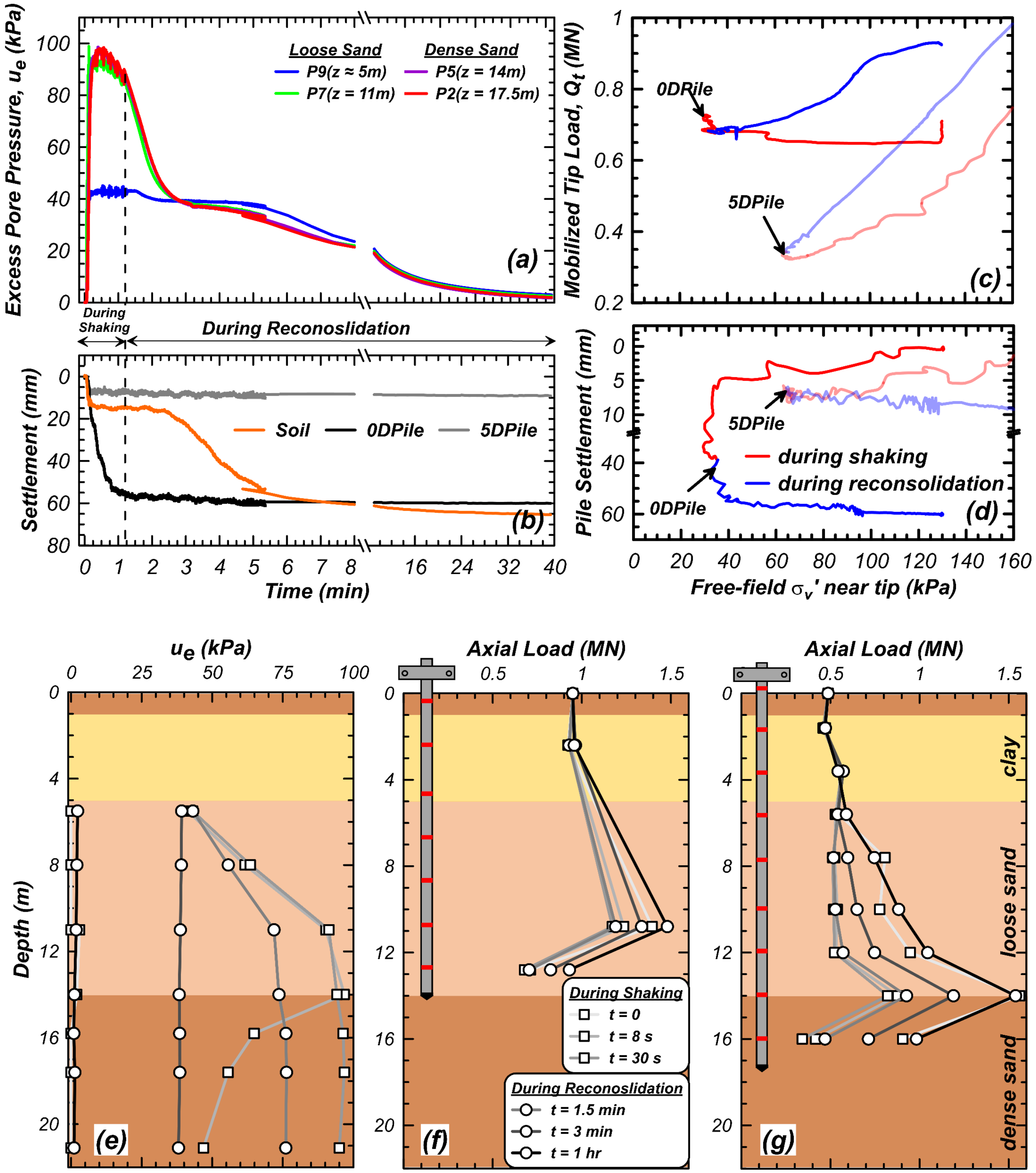

Figure A.5. Results from shaking event EQM$_6$ of centrifuge model test SKS02: Time histories of (a) u_e and (b) soil and pile settlement. (c) Mobilized tip load (Q_t) and (d) pile settlement as free-field effective stress (σ'_v) changed near the pile's tip. Isochrones of (e) u_e profile and axial load distribution in (f) 0DPile and (g) 5DPile during shaking and reconsolidation.

APPENDIX B:

SKS03 CENTRIFUGE MODEL TEST RESULTS

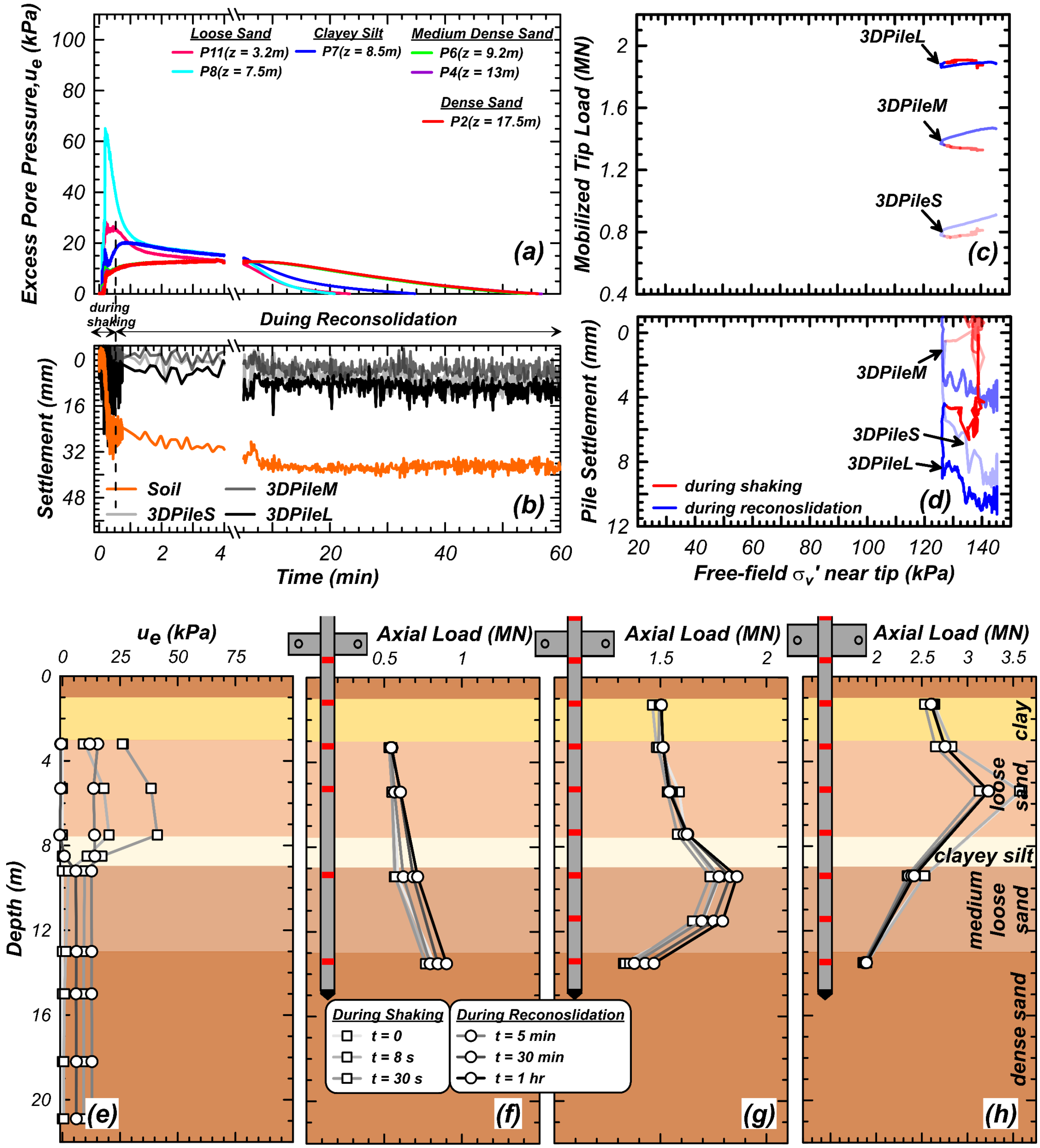

Figure B.1. Results from shaking event EQM1 of centrifuge model test SKS03: Time histories of (a) u_e and (b) soil and pile settlement. (c) Mobilized tip load (Q_t) and (d) pile settlement as free-field effective stress (σ'_v) changed near the pile's tip. Isochrones of (e) u_e profile and axial load distribution in (f) 3DPileS, (g) 3DPileM, and (h) 3DPileL during shaking and reconsolidation.

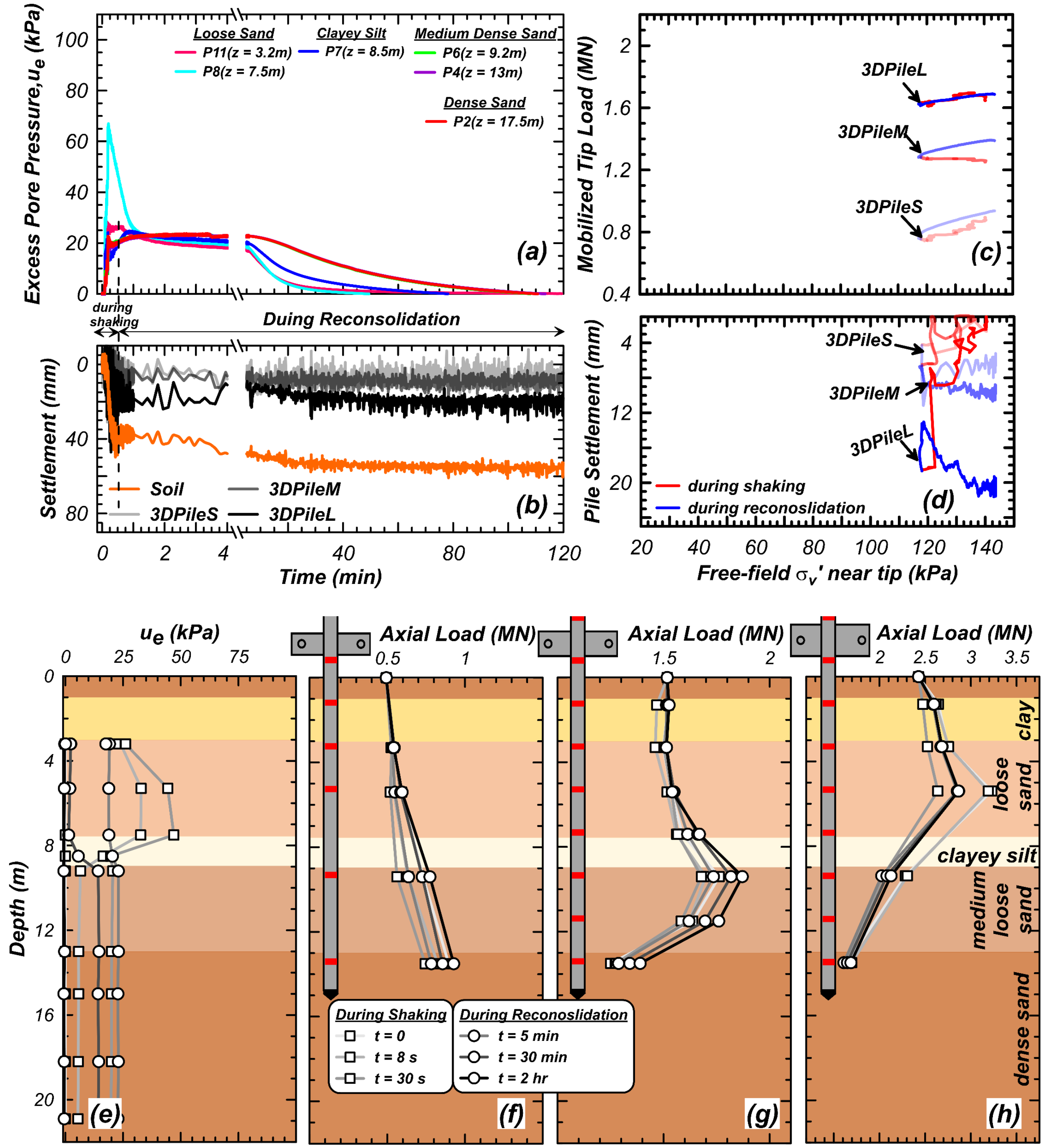

Figure B.2. Results from shaking event EQM2 of centrifuge model test SKS03: Time histories of (a) u_e and (b) soil and pile settlement. (c) Mobilized tip load (Q_t) and (d) pile settlement as free-field effective stress (σ'_v) changed near the pile's tip. Isochrones of (e) u_e profile and axial load distribution in (f) 3DPileS, (g) 3DPileM, and (h) 3DPileL during shaking and reconsolidation.

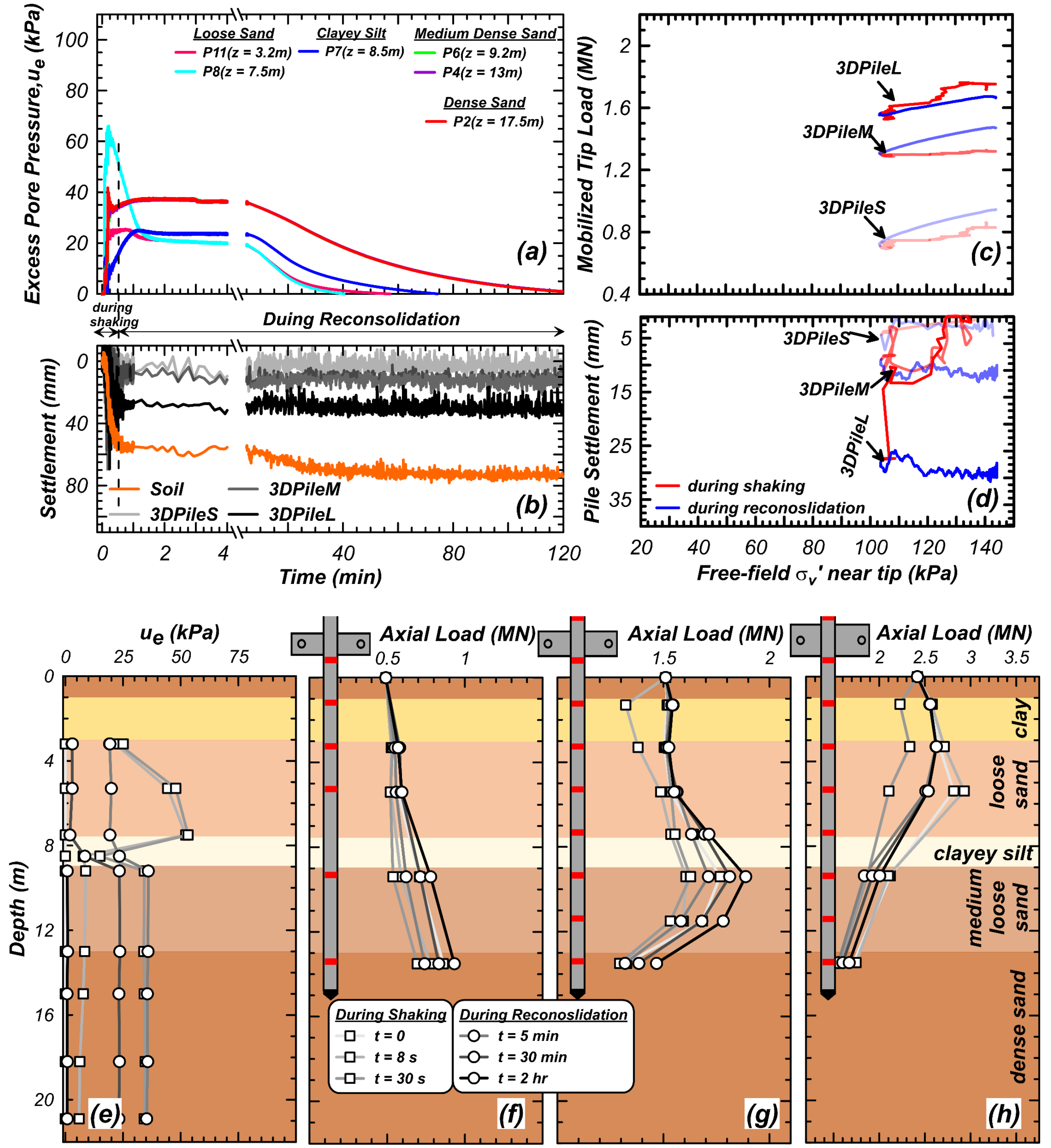

Figure B.3. Results from shaking event EQM$_3$ of centrifuge model test SKS03: Time histories of (a) u_e and (b) soil and pile settlement. (c) Mobilized tip load (Q_t) and (d) pile settlement as free-field effective stress (σ'_v) changed near the pile's tip. Isochrones of (e) u_e profile and axial load distribution in (f) 3DPileS, (g) 3DPileM, and (h) 3DPileL during shaking and reconsolidation.

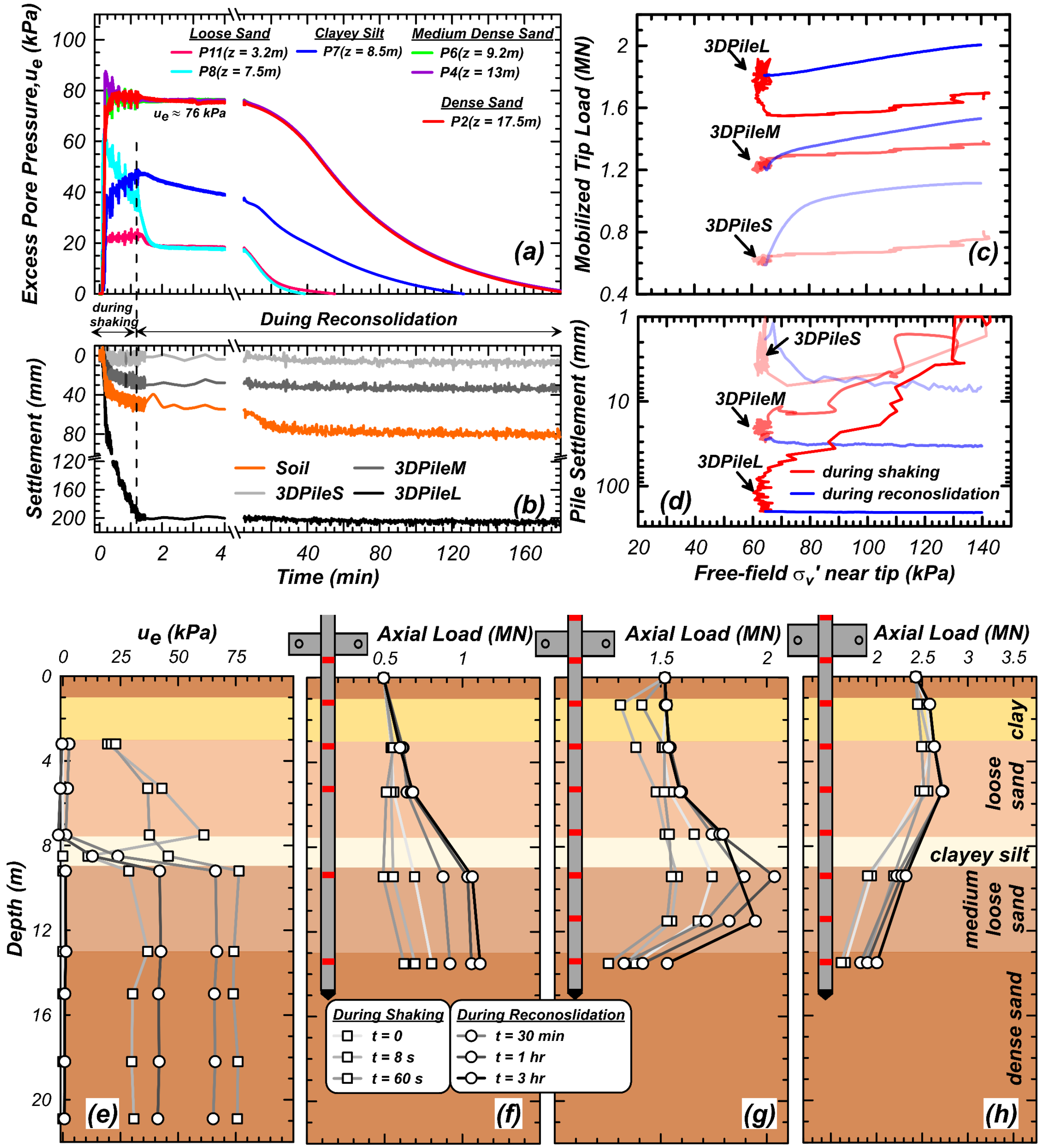

Figure B.4. Results from shaking event EQM4 of centrifuge model test SKS03: Time histories of (a) u$_e$ and (b) soil and pile settlement. (c) Mobilized tip load (Q_t) and (d) pile settlement as free-field effective stress (σ'_v) changed near the pile's tip. Isochrones of (e) u$_e$ profile and axial load distribution in (f) 3DPileS, (g) 3DPileM, and (h) 3DPileL during shaking and reconsolidation.

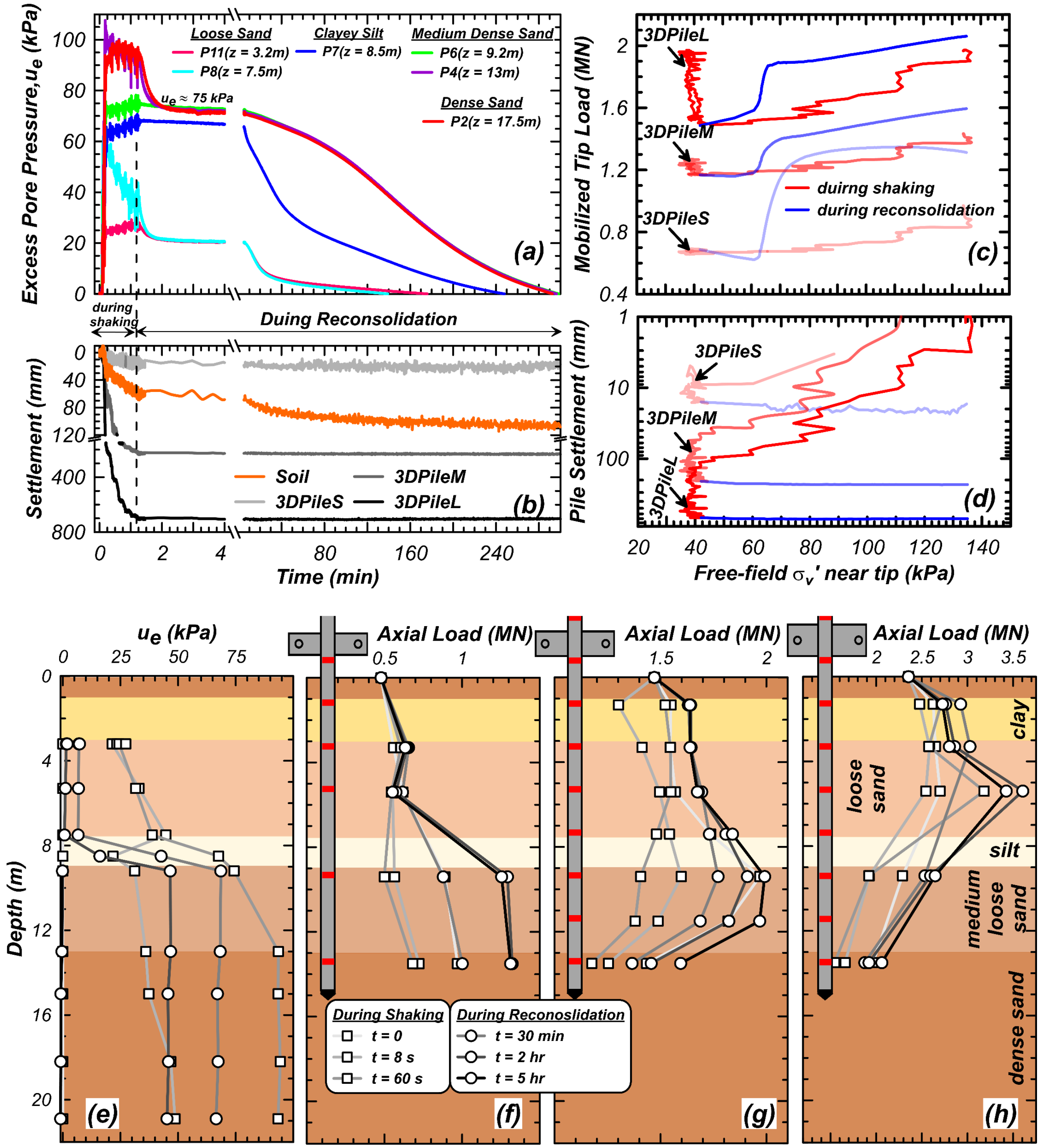

Figure B.5. Results from shaking event EQM$_5$ of centrifuge model test SKS03: Time histories of (a) u$_e$ and (b) soil and pile settlement. (c) Mobilized tip load (Q$_t$) and (d) pile settlement as free-field effective stress (σ′$_v$) changed near the pile’s tip. Isochrones of (e) u$_e$ profile and axial load distribution in (f) 3DPileS, (g) 3DPileM, and (h) 3DPileL during shaking and reconsolidation.